

DESIGN AND REAL-TIME IMPLEMENTATION OF OPTIMAL
MODEL-BASED TORQUE SHAPING AUTOMOTIVE CONTROL SYSTEMS

By

G. V. Prithvi Reddy

A DISSERTATION

Submitted in partial fulfillment of the requirements for the degree of

DOCTOR OF PHILOSOPHY

In Mechanical Engineering - Engineering Mechanics

MICHIGAN TECHNOLOGICAL UNIVERSITY

2022

© 2022 G. V. Prithvi Reddy

This dissertation has been approved in partial fulfillment of the requirements for the Degree of DOCTOR OF PHILOSOPHY in Mechanical Engineering - Engineering Mechanics.

Department of Mechanical Engineering - Engineering Mechanics

Dissertation Co-advisor: *Dr. Mahdi Shahbakhti*

Dissertation Co-advisor: *Dr. Darrell L. Robinette*

Committee Member: *Dr. Wayne W. Weaver Jr.*

Committee Member: *Dr. Tan Chen*

Department Chair: *Dr. Jason R. Blough*

Dedication

To my parents

for their boundless love and support.

Contents

List of Figures	xv
List of Tables	xxv
Preface	xxvii
Acknowledgments	xxxix
List of Abbreviations	xxxiii
Abstract	xli
1 Introduction	1
1.1 Motivation	5
1.2 Literature review	7
1.2.1 Driveline modeling for controls applications	10
1.2.2 Backlash position and size estimators	12
1.2.3 Torque shaping controllers	16
1.3 Limitations in state-of-the-art	18
1.4 Contribution of this Thesis	18

1.5	Thesis structure	20
2	Development of plant models	23
2.1	Full-order model (FOM) - Development	24
2.1.1	Actuator model	24
2.1.1.1	Engine	25
2.1.1.2	Electric Motor	28
2.1.2	Other driveline elements	29
2.1.2.1	Torque converter	29
2.1.2.2	Transmission with backlash	32
2.1.2.3	Propeller shaft	35
2.1.2.4	Final drive with backlash	35
2.1.2.5	Axle shaft	36
2.1.2.6	Tire dynamics	36
2.1.2.7	Longitudinal Vehicle Dynamics	37
2.2	Full-order model - Validation	38
2.3	Control-oriented model - Development	42
2.3.1	Step 1: Lumping model components	43
2.3.2	Step 2: Simplifying the tire model	45
2.3.3	Step 3: Lumping backlash elements	47
2.3.4	Step 4: Validating the COM	47
2.3.5	Step 5: Evaluation of COM for control applications	56

2.3.5.1	Investigation of contact mode dynamics:	59
2.3.5.2	Investigation of backlash mode dynamics:	60
3	Design and validation of backlash position and size estimation algorithms	65
3.1	Development, validation and robustness analyses of backlash position estimator	65
3.1.1	Design of backlash position estimator	66
3.1.2	Contact and backlash mode estimator	68
3.1.3	Validation of backlash position estimator	70
3.1.3.1	Using MIL tests	71
3.1.3.2	Using test vehicle data	72
3.1.4	Robustness analysis of backlash position estimator	74
3.1.4.1	To CAN jitter in speed measurements	74
3.2	Development, validation and robustness analyses of backlash size estimator	79
3.2.1	Switching-free state space representation of COM	80
3.2.2	Estimator development	82
3.2.2.1	Activation	84
3.2.2.2	Estimation	85
3.2.2.3	Steady-state convergence	86
3.2.3	Stability analysis	87

3.2.4	Validation of backlash size estimator	89
3.2.4.1	Using MIL tests	89
3.2.4.2	Using test vehicle data	89
3.2.4.3	Processor-in-the-loop (PIL) testing	90
3.2.5	Robustness analysis	92
3.2.5.1	Varying actuator torque trajectories	93
3.2.5.2	Uncertainty in road load torque calculation	95
3.2.5.3	CAN jitter in actuator and wheel speed signals	97
3.2.5.4	Variation in plant backlash size	99
3.2.5.5	Variation in driveshaft stiffness	99
3.2.5.6	Variation in tire-road interaction	101
3.2.5.7	Variation in driveshaft damping	101
3.2.5.8	Impact of sample time on backlash size estimate	103
4	Design of shuffle and clunk control algorithms	105
4.1	Driveline shuffle controller	106
4.1.1	Design of the pre-compensator	107
4.1.2	Design of the lead compensator	109
4.2	Driveline clunk controller	111
4.2.1	Double integrator backlash model	112
4.2.2	Clunk controller: Design of the baseline controller	113
4.2.3	Clunk controller: Soft-landing reference governor	115

4.2.4	Clunk controller: Maximal output admissible set	120
4.2.5	Clunk controller: Implementation of the reference governor .	121
4.3	Validation of shuffle and clunk control algorithms	121
4.3.1	Performance in MIL tests	122
4.3.2	Performance in PIL tests	124
4.4	Uncertainty analysis of clunk controller	125
4.4.1	Uncertainty in actuator inertia	127
4.4.2	Uncertainty in delivered actuator torque	128
4.4.3	Adaptive clunk controller	133
4.5	Robustness analysis of clunk controller	138
4.5.1	Robustness to various driver torque requests	138
4.5.2	Robustness to variations in backlash size	139
5	Integrating the torque shaping controller with other automotive controllers	143
5.1	Integration with the torque converter torque lag (TCTL) controller	144
5.1.1	Control-oriented model for slipping torque converter	149
5.1.2	TCTL Controller design	156
5.1.2.1	Augmentation of the state space model	158
5.1.2.2	Prediction model	159
5.1.2.3	Actuator and Driveline Constraints	161
5.1.3	Optimization problem	165

5.1.4	Control Results	166
5.1.4.1	MIL results	166
5.1.4.2	PIL results	168
5.1.5	Robustness Analysis of TCTL controller	171
5.1.5.1	Variation in transient fluid path dynamics	172
5.1.5.2	Variation in clutch slip initiation	174
5.2	Integration with an economic nonlinear MPC torque tracking engine controller	176
5.2.1	GT-Power engine model development and validation	178
5.2.2	Design of the economic - nonlinear model predictive engine controller	181
5.2.3	Coordinated control between E-NMPC and torque shaping powertrain controller	183
6	Conclusions and future work	191
6.1	Summary and Conclusions	191
6.2	Recommendations for future work	196
	References	199
A	PhD publications	215
A.1	Peer reviewed journal papers	215
A.1.1	Published journal papers	215

A.1.2	Journal paper in review	216
A.2	Refereed conference papers	216
A.2.1	Conference paper in preparation	217
B	Implementation and testing of the backlash size estimator and the clunk controller in real vehicles	219
C	Letters of permission to republish	221
D	Image and data file summary	231
D.1	Chapter 1	231
D.2	Chapter 2	232
D.3	Chapter 3	233
D.4	Chapter 4	234
D.5	Chapter 5	235

List of Figures

1.1	Schematic showing the main sources of backlash and compliance in an automotive drivetrain with an IC engine.	3
1.2	The points at which clunk and shuffle occur in an automotive drivetrain.	4
1.3	Retail sales distribution between cars and trucks in the United States between 2011 - 2021 [1].	5
1.4	Sales forecast for electric and electrified vehicles in the next few years [2].	7
1.5	Selected literature related to torque shaping control systems.	9
1.6	Summary of previous approaches to backlash position estimation.	13
1.7	Summary of previous approaches to backlash size estimation	15
1.8	Prior studies for clunk control in automotive systems	17
1.9	Organization of this thesis. Citations in this figure indicate original work that was published and work that is in review as a result of this thesis.	22
2.1	Schematic of the FOM with an IC engine as the actuator.	26

2.2	Locations of the sensors used for experimental data acquisition from the test vehicle.	39
2.3	Plot showing experimental validation of the FOM with a locked torque converter clutch in 5th gear. Note that the Y-axis labels of all result plots in this thesis have been substituted by alphanumeric values (e.g., 1T, 12n etc.) to keep the test vehicle parameters confidential. ‘T’ represents T units of actuator torque, ‘n’ represents n units of angular speed, ‘a’ represents a units of acceleration, and ‘t’ represents t units of drive shaft torque.	41
2.4	Plot comparing the simulation outputs obtained with the Pacejka tire model vs. a simplified tire model vs. the experimental test vehicle data.	46
2.5	Plot showing comparative driveline response of COM with 2 individual backlash elements for the transmission and final drive vs. 1 lumped backlash element.	48
2.6	Schematic configuration of reduced-order model with 2 backlash elements.	49
2.7	Schematic configuration of the chosen control-oriented model. . . .	49
2.8	Plot showing the validation of the COM against the outputs of the FOM and the test vehicle data.	53

2.9	Plot showing residuals of the outputs of the FOM and ROM as compared to the measured outputs of the test vehicle, based on the results in Fig 2.8.	54
2.10	Plot showing performance of COM with lumped tire and axle inertias with the actuator inertia.	55
3.1	Estimated and predicted states of the switching backlash position estimator for contact and backlash mode	70
3.2	Schematic of the switching backlash position estimator	71
3.3	Plot showing performance of backlash position estimator in simulations.	73
3.4	Plot showing performance of backlash position estimator with experimental vehicle data.	75
3.5	Probability density function and number of occurrences of CAN jitter in (a) engine speed and (b) wheel speed for an interval of -5 to 5 ms, using data collected from a test vehicle	76
3.6	Plot showing performance of backlash position estimator with CAN jitter injected into engine and wheel speed signals obtained from FOM.	78
3.7	Schematic of the developed backlash size estimator. In this figure, T_{drv} represents the driver requested torque, and the remaining symbols are as defined in the text.	83

3.8	State flow diagram showing the backlash size estimator activation criteria.	85
3.9	Plot showing performance of backlash size estimator in MIL tests. .	88
3.10	Plot showing performance of backlash size estimator using experimental test vehicle data.	91
3.11	Process of PIL validation for the developed backlash size estimator.	93
3.12	Plot showing performance of backlash size estimator in PIL tests. .	94
3.13	Plot showing robustness of the backlash size estimator to different driver torque inputs	96
3.14	Plot showing robustness of the backlash size estimator to road load	97
3.15	Plot showing robustness of the backlash size estimator to CAN jitter.	98
3.16	Plot showing robustness of the backlash size estimator to changes in plant backlash size.	100
3.17	Robustness analysis of the backlash size estimator to variation in tire properties due to changes in the tire-road patch interaction. In this result, a low traction scenario such as an icy road is simulated. . . .	102
3.18	Plot showing robustness of the backlash size estimator at various sample times.	104
4.1	Bode plot of the closed loop shuffle controller showing a dip near the shuffle frequency.	110

4.2	Schematic of the designed torque shaping controller consisting of both contact mode and backlash mode controllers.	119
4.3	The MOAS obtained for an impact velocity constraint of 5s. Color gradation indicates number of feasible solutions. The maximum number of solutions are available in the blue region, which corresponds to the beginning of lash crossing, and they start to reduce in the green and yellow region with the minimum number of solutions in the red region, which corresponds to the end of lash crossing.	120
4.4	Performance of the designed clunk controller during a tip-in event. The controller initially requests significant torque to quickly traverse lash, and then rapidly reduces the torque request to meet the chosen impact velocity constraint (i.e., 5s).	123
4.5	Schematic of the PIL setup used to validate the designed controller for real-time usage.	125

4.6	Difference between (a) original MOAS and (b) reduced MOAS obtained after compensating for uncertainty in actuator delivered torque. The additional constraint in the modified OCP reduces the number of feasible solutions in (b). Color gradation indicates number of feasible solutions. The maximum number of solutions are available in the blue region, which corresponds to the beginning of lash crossing, and they start to reduce in the green and yellow region with the minimum number of solutions in the red region, which corresponds to the end of lash crossing.	130
4.7	Comparison of clunk controller behavior with 25% uncertainty in actuator delivered torque in backlash mode with controllers designed using original and revised MOAS. With the revised MOAS, it is possible to meet impact velocity constraint even with the uncertainty in the delivered actuator torque, albeit with slightly longer lash crossing duration.	132
4.8	Schematic of the proposed adaptive clunk controller. In this schematic, the uncertainty in the delivered actuator torque is being calculated. Note that the remaining elements of the clunk controller as same as shown in Fig. 4.2.	135

4.9	Comparison of clunk controller (CC) behavior with 10% and 40% uncertainty in the delivered actuator torque. The performance of the clunk controller is shown for three cases: (i) with original clunk controller, (ii) with clunk controller developed for 40% uncertainty in the delivered actuator torque, and (iii) with clunk controller developed for 10% and 40% uncertainty in the delivered actuator torque. Additional plots show zoomed portions of the tip-ins.	137
4.10	Performance of the designed clunk controller when backlash size changes in the vehicle but the controller does not have the updated backlash size information. During the first and second tip-in events, the size of the backlash in the vehicle is larger than the size of the backlash known to the controller. This leads to a violation of the impact velocity constraint (as evident in plot (c1)). The backlash size estimator learns the increase in the backlash size and updates the known backlash size (observed in plot (b2)) by the third tip-in event between $t = 14$ s and $t = 16$ s. Even though the reference governor's MOAS is not updated, the impact velocity constraint is met as seen in plot (c2).	141
5.1	Torque lag in a vehicle powertrain due to a slipping torque converter.	146
5.2	Comparison of FOM and ROM outputs with a slipping torque converter.	147

5.3	Schematic of a torque converter equipped with a lock-up clutch. The fluid path and the mechanical path of torque transmission are illustrated.	150
5.4	Schematic of the COM designed to capture the torque lag dynamics.	150
5.5	Schematic of torque converter torque lag (TCTL) controller designed in this work.	157
5.6	Response of a drivetrain during torque delivery with locked and slipping torque converter clutch (TCC).	167
5.7	Comparison of the observed expediency and connectedness with the designed drivetrain controller for slipping torque converters.	169
5.8	Schematic showing the PIL test setup for the TCTL controller	171
5.9	Comparison of the drivetrain controller with varying first order lag constants for the fluid dynamics of the torque converter.	173
5.10	Comparison of the drivetrain controller for different clutch slip positions.	175
5.11	High-fidelity engine model developed in GT-Power for use in MIL testing of the E-NMPC engine controller [3].	179
5.12	Schematic showing the coordinated control between the E-NMPC engine controller and the clunk and shuffle torque shaping driveline controller.	185

5.13	Driveline response when the engine and the driveline controllers <u>do not have proper coordination</u> . At $t = 8.4$ sec, the engine controller fails to reach convergence for the torque commanded by the driveline controller. The simulation abruptly stops at this point.	187
5.14	Plot showing the coordinated control between the engine and driveline controller to deliver the shaped torque command during a tip-in scenario.	188
5.15	Plot showing the engine controller commands in the engine actuators to deliver the driveline controller commanded torque shown in Fig. 5.14.	190

List of Tables

2.1	Summary of evaluations on COM for shuffle and clunk control. . . .	64
3.1	MicroAutoBox II real-time performance timers	92
4.1	Summary of PIL performance of the designed torque shaping controller on dSPACE MicroAutoBox II.	126
4.2	Summary of closed-loop stability analysis of the backlash mode system with uncertainties.	128
4.3	Summary of performance of the designed clunk controller for variations in ramp rate of driver torque request. Note that the impact velocities are reported in alphanumerical representation ('s') to keep test vehicle parameters confidential.	139

5.1	Performance comparison of driveline metrics with and without the developed controller. The term <i>Expediency</i> is defined as the time taken by the vehicle to reach an acceleration of 0.4 m/s^2 and the term <i>Connectedness</i> is defined as the maximum acceleration attained within 1 second of the tip-in occurring. Moreover, the percentage difference is computed with respect to the corresponding variables for the locked TCC scenario.	170
5.2	TCC slipping positions for robustness analysis	174
D.1	Chapter 1 figure files	231
D.2	Chapter 2 figure files	232
D.3	Chapter 2 model files	232
D.4	Chapter 3 figure files	233
D.5	Chapter 3 model files	233
D.6	Chapter 4 figure files	234
D.7	Chapter 4 model files	234
D.8	Chapter 5 figure files	235
D.9	Chapter 5 model files	236

Preface

The contents of the PhD dissertation are mainly based on two published journal papers, one journal paper under review, four conference papers, and one conference paper under preparation (Appendix A). Publishers of these papers have granted permission for reuse of material (Appendix C). The contributions of the authors in these papers are as follows:

- ◇ Chapter 2 [4]: The full-order and control-oriented models for the vehicle driveline were collaboratively developed and analyzed by Prithvi Reddy and Kaushal Darokar, an alumni of Michigan Technological University and former member of Energy Mechatronics Laboratory. Mary Farmer and her colleagues at Ford Motor Company provided vehicle test data which was used for validating the developed models. Dr. Jeff Doering provided regular technical feedback which helped during the validation of the models. Dr. Darrell Robinette helped with the initial set up and development of the driveline models, and Dr. Darrell Robinette and Dr. Jason Blough participated in the research discussions related to this work. Dr. Mahdi Shahbakhti and Dr. Maruthi Ravichandran were instrumental in guiding and directing the research and writing efforts for this paper.-

- ◇ Chapter 3 [5, 6, 7]: The backlash position estimator was mainly developed by Kaushal Darokar with modeling and validation help from Prithvi Reddy. Robustness analysis for the backlash position estimator was performed by Kaushal Darokar. The backlash size estimator was mainly developed by Prithvi Reddy with modeling and validation help from Kaushal Darokar. Dr. Jeff Doering provided regular technical feedback which helped during the validation and analyses of the estimation algorithms. Jon Furlich, an alumni of Michigan Technological University, Dr. Darrell Robinette and Dr. Jason Blough participated in the research discussions related to this work. Dr. Mahdi Shahbakhti and Dr. Maruthi Ravichandran directed the research and writing efforts for the papers in this Chapter.

- ◇ Chapter 4 [8]: The torque shaping clunk and shuffle controller was developed and analyzed by Prithvi Reddy, with technical inputs from Dr. Maruthi Ravichandran, Dr. Mahdi Shahbakhti and Dr. Jeff Doering. The same team also participated in the uncertainty analysis for developing the robust reference governor. Syed Ahmad Nadeem, an alumni of Michigan Technological University and a former member of Energy Mechatronics Laboratory assisted with the robustness analyses for the torque shaping controller. Dr. Mahdi Shahbakhti and Dr. Maruthi Ravichandran supported the writing efforts for the papers in this Chapter.

- ◇ Chapter 5 [3, 9]: The torque converter torque lag controller was developed and

analyzed by Syed Ahmad Nadeem, with technical and modeling collaboration with Prithvi Reddy. Dr. Mahdi Shahbakhti, Dr. Darrell Robinette, Dr. Maruthi Ravichandran and Dr. Jeff Doering provided technical guidance in the design of this controller. Prithvi Reddy, Dr. Mahdi Shahbakhti and Dr. Maruthi Ravichandran supported the writing efforts for one of the papers [9] in this chapter. The engine controller used in this Chapter was developed by Dr. Xin Wang, an alumni of Michigan Technological University, as part of his PhD dissertation. The modeling changes and analysis required for the coordinated control of the engine and driveline controllers was done by Prithvi Reddy, with technical inputs from Dr. Mahdi Shahbakhti.

Acknowledgments

This work would not have been possible without the patient and dedicated guidance of my academic advisors, Dr. Mahdi Shahbakhti and Dr. Darrell Robinette. I am indebted to Dr. Shahbakhti for giving me an opportunity to work in the automotive controls domain, and for the time and effort he invested in improving both my technical and non-technical knowledge. I am also thankful to the Dept. of Mechanical Engineering - Engineering Mechanics for supporting my PhD work through Teaching Assistantships, and to the Graduate School for providing support through the Finishing fellowship program.

I am sincerely thankful to Dr. Maruthi Ravichandran and Dr. Jeff Doering of the Ford Motor Company for their timely technical inputs and feedback through the duration of this work. Thanks are also due to the members of Vehicle Controls and Systems Engineering (VCSE) department of Ford Research and Advanced Engineering organization, for their help in obtaining the driveline parameters. I am also thankful to Dr. Rajit Johri, who was my supervisor at the Ford Motor Company during my summer intership, for his support and feedback on my work.

I am obliged to Dr. Wayne Weaver and Dr. Tan Chen for agreeing to be a part of my PhD committee, and for their time and efforts in providing feedback on this work.

Their participation will help add a new perspective to this work and provide feedback for future work in this domain.

I am also thankful to Michigan Tech alumni Prince Lakhani, Kaushal Darokar and Syed Ahmad Nadeem, for their collaboration on and contributions to various parts of this work. I am grateful for the support and encouragement I received from my friends and roommates, Sampath Rallapalli, Vishnu Durgam, Chethan Reddy and Pradeep Bhat.

I owe everything in my life to the love and support I received from my parents, Radha and Prakash, my brother, Kedar, and my wife, Hasitha. Their belief in my abilities has always motivated me to continue improving myself, and for that I cannot thank them enough.

Nomenclature

List of symbols and abbreviations used in this work:

Symbols

T_{drv}	Driver requested torque [Nm]
T_{act}	Torque delivered by the actuator [Nm]
T_{s}	Torque delivered at the lumped shaft [Nm]
T_{w}	Torque delivered at the wheels [Nm]
T_{load}	Road load torque on the vehicle [Nm]
θ_{act}	Angular position of the actuator [rad]
θ_{s}	Angular position of the lumped shaft [rad]
θ_{b}	Angular position in the lumped backlash [rad]
θ_{fd}	Angular position of the final drive [rad]
θ_{w}	Angular position of the wheel [rad]
J_1	Lumped inertia of the actuators, torque converter, transmission, propeller shaft, and final drive [kgm ²]
J_2	Lumped inertia of the axle shafts and tires [kgm ²]
J_3	Lumped inertia of the wheels and the vehicle body [kgm ²]

k_s	Stiffness of lumped propeller and axle shafts [Nm/rad]
c_s	Damping coefficient of lumped propeller and axle shafts [Nm/(rad/s)]
k_w	Stiffness of lumped tires [Nm/rad]
c_w	Damping coefficient of lumped tires [Nm/(rad/s)]
α	Half of the lumped backlash size [rad]
i_t	Gear ratio of the transmission [-]
i_{fd}	Gear ratio of the final drive [-]
$\theta_{b,size}$	Size of the backlash [rad]
K	Kalman filter gain matrix [-]
P	Error covariance matrix [-]
Q	Process noise covariance matrix [-]
R	Measurement noise covariance matrix [-]
e_1	Error in estimated actuator-side twist angle [rad]
e_2	Error in estimated wheel-side twist angle [rad]
$T_{act,init}$	Initial value of actuator torque at tip-in [Nm]
t_{init}	Time instance at which tip-in starts [s]
C_1	Calibration threshold to determine the beginning of tip-in [N/s]
C_2	Calibration threshold to determine steady-state convergence of estimated backlash size [rad/s]

$\hat{\theta}_{b,\text{size,reported}}$	Estimated size of the backlash reported to the supervisory controller [rad]
k_p	Proportional gain of the PD controller [–]
k_D	Derivative gain of the PD controller [–]
q	Modified backlash position reference controlled by the reference governor [rad]
t_c	Current time instant [sec]
t_{im}	Time instant at which impact occurs [sec]
v_{im}	Impact velocity limit when backlash reaches positive contact [rad/s]
T_{sat}	Actuator torque limit during lash crossing [Nm]
δ_1	Uncertainty in actuator inertia [–]
δ_2	Uncertainty in actuator delivered torque [–]
K_{cap}	Capacity Factor for torque converter model [(rad/s)/($\sqrt{\text{Nm}}$)]
$T_{\text{act rate,low}}$	Lower limit on rate of delivered actuator torque [Nm/s]
$T_{\text{act rate,up}}$	Upper limit on rate of delivered actuator torque [Nm/s]
$T_{\text{TCC rate,low}}$	Lower limit on rate of change of TCC capacity [Nm/s]
$T_{\text{TCC rate,up}}$	Upper limit on rate of change of TCC capacity [Nm/s]
N_c	Control horizon [–]
N_p	Prediction horizon [–]
SR	Speed ratio for torque converter model [–]

TR	Torque ratio for torque converter model [–]
$\alpha_{1,act}$	2 nd coeff. of Kotwicki eq. for impeller torque in torque multiplication mode [Nm/(rad/s) ²]
$\alpha_{2,act}$	2 nd coeff. of Kotwicki eq. for impeller torque in torque multiplication mode [Nm/(rad/s) ²]
$\alpha_{3,act}$	3 rd coeff. of Kotwicki eq. for impeller torque in torque multiplication mode [Nm/(rad/s) ²]
$\alpha_{1,tu}$	1 st coeff. of Kotwicki eq. for turbine torque in torque multiplication mode [Nm/(rad/s) ²]
$\alpha_{2,tu}$	2 nd coeff. of Kotwicki eq. for turbine torque in torque multiplication mode [Nm/(rad/s) ²]
$\alpha_{3,tu}$	3 rd coeff. of Kotwicki eq. for turbine torque in torque multiplication mode [Nm/(rad/s) ²]
$\alpha_{1,fc}$	1 st coeff. of Kotwicki eq. for impeller torque in fluid coupling mode [Nm/(rad/s) ²]
$\alpha_{2,fc}$	2 nd coeff. of Kotwicki eq. for impeller torque in fluid coupling mode [Nm/(rad/s) ²]
$\alpha_{3,fc}$	3 rd coeff. of Kotwicki eq. for impeller torque in fluid coupling mode [Nm/(rad/s) ²]
Φ	Slack variable vector [–]
Q	Weight matrix (Chapter 5) [–]

S	Tuning parameters matrix for manipulated variables [–]
θ_{thr}	Throttle angle [°]
θ_{IGN}	Spark timing [°]
θ_{IVC}	Intake valve closing timing [°]
θ_{EVO}	Exhaust valve opening timing [°]
θ_{WG}	Turbocharger wastegate opening [°]
θ_{CA50}	Crank angle of 50% of fuel burned [°]
P_{TIP}	Throttle inlet pressure [kPa]
P_{Man}	Intake manifold pressure [kPa]

Abbreviations

FOM	Full-order model
COM	Control-oriented model
ROM	Reduced-order model
CM	Contact mode
BM	Backlash mode
BL	Backlash
AJC	Anti-jerk control
CAN	Controller-area network

PDF	Probability density function
ECU	Electronic control unit
PD	Proportional-derivative (controller)
PID	Proportional-integral-derivative (controller)
OCP	Optimal control problem
MIL	Model-in-the-loop
PIL	Processor-in-the-loop
MPC	Model predictive controller
TCTL	Torque converter torque lag
SIP	Slip initiation point
SR	Speed ratio
TC	Torque converter
TCC	Torque converter lockup clutch
TR	Torque ratio
E-NMPC	Economic nonlinear model predictive control
GTDI	Gasoline turbocharged direct injection
SI	Spark ignition
NO _x	Oxides of Nitrogen
IMEP	Indicated mean effective pressure
CA ₅₀	Crank angle of 50% fuel burn
MAP	Manifold absolute pressure

ATDC	After top dead center
IVC	Intake valve closing
EVO	Exhaust valve opening
COV	Coefficient of variation
KI	Knock index
WG	Wastegate

Abstract

The presence of backlash and compliance in automotive drivelines can lead to undesirable NVH phenomena known as *clunk* and *shuffle*, respectively, which severely deteriorates the drivability of the vehicle. Since the backlash and compliance are design choices for automotive drivelines, they cannot be completely eliminated. Therefore, torque shaping control systems are used to appropriately modulate the torque commands sent to automotive actuators under different operating conditions in order to reduce clunk and shuffle. Model-based controllers provide good control performance without the need for cumbersome calibrations and long development time. Consequently, this dissertation centers on the design and real-time implementation of an optimal, model-based torque shaping control system for mitigating clunk and shuffle from the driveline.

In this PhD dissertation, Kalman filter-based estimation algorithms and soft landing reference governor-based control algorithms are designed to provide the shaped torque commands to the actuators. A high fidelity plant model and control-oriented models are developed for use in the model-based torque shaping controller, and they are validated using experimental data. Both the high fidelity plant model and the control-oriented model capture the frequency and phase of the shuffle oscillations with an average error of less than 10%.

For effective performance of the torque shaping controller up-to-date backlash position and backlash size information is needed, and estimators are designed using Kalman filter techniques which make use of readily available driveline sensors to provide this information. The backlash position estimator is shown to be accurate in estimating the plant backlash position with a delay of up to 2 sample periods. The backlash size estimator is demonstrated to estimate the plant backlash size in various operating conditions with an error of less than 10%.

The torque shaping shuffle and clunk control algorithms are designed using a pre-compensator and lead compensator-based feedback controller, and a reference governor-based optimal controller which work using information from existing driveline sensors, and provide a smooth and connected driving experience. This model-based shuffle and clunk controller reduces the number of calibrations by more than 90% compared to a rule-based controller, and is easily implementable on embedded processors. Finally, the impact of model uncertainties on the performance of the shuffle and clunk controller is analyzed, and the controller is shown to be robust in multiple use cases. Additionally, the torque shaping controller is integrated with two separate model-based, optimal controllers. One of the controllers reduces torque lag caused during the transition of the torque converter clutch from locked to slipping condition from 13.5% to 2.1%.

Chapter 1

Introduction

Ever since the first automobiles started appearing in the late 19th century, there have been tens of thousands of developmental changes and improvements in all aspects of an automobile. Today, automobile buyers take into account a variety of factors such as safety, efficiency, comfort, performance, etc. into their purchase decision. Comfort and, to some degree, performance of an automobile is typically defined by the Noise, Vibration and Harshness (NVH) characteristics of the vehicle. An important aspect of the vehicle's NVH characteristics is drivability which, by definition, is the smoothness and steadiness with which the vehicle is able to accelerate. The topic of drivability has been thoroughly researched in the past few decades and certain phenomena affecting the drivability of a vehicle, such as clunk, shuffle, rattle, judder, etc., have been identified by the researchers [10, 11, 12]. These phenomena materialize in the form of

undesirable audible noises, and/or uncomfortable jerks and oscillations in the vehicle. In this thesis, the focus is on the phenomena of clunk and shuffle.

Clunk is an undesirable audible noise caused due to adjacent gear teeth hitting one another when the direction of torque traversal in the drivetrain is reversed (e.g., when a tip-in event occurs from coasting). It is caused due to the presence of *backlash* in gears, which is the clearance between adjacent gear teeth to ensure lubrication and proper mating of the gears. An event causing a clunk can also lead to an unwanted jerk in the drivetrain. *Shuffle* is a low-frequency longitudinal oscillation that occurs due to the *compliance* of driveshafts used for transmitting the torque from the actuators to the wheels of the automobile. The driveshafts are typically manufactured to be compliant (or flexible) to improve their durability while transferring large amount of torque. Low-frequency vibrations such as shuffle are extremely uncomfortable for the human body [13], and need to be reduced to improve driving comfort. Both backlash and compliance are design choices and cannot be completely eliminated from the powertrain. Automobiles today can have different powertrain configurations with various propulsion sources and torque flow paths (e.g., conventional internal combustion (IC) engine vehicle, hybrid electric vehicle, battery electric vehicle, etc.). The common elements in all these configurations are the presence of gears and driveshafts, and, therefore, backlash and compliance, respectively. Fig. 1.1 shows a schematic of an automotive drivetrain highlighting the main sources of backlash and compliance.

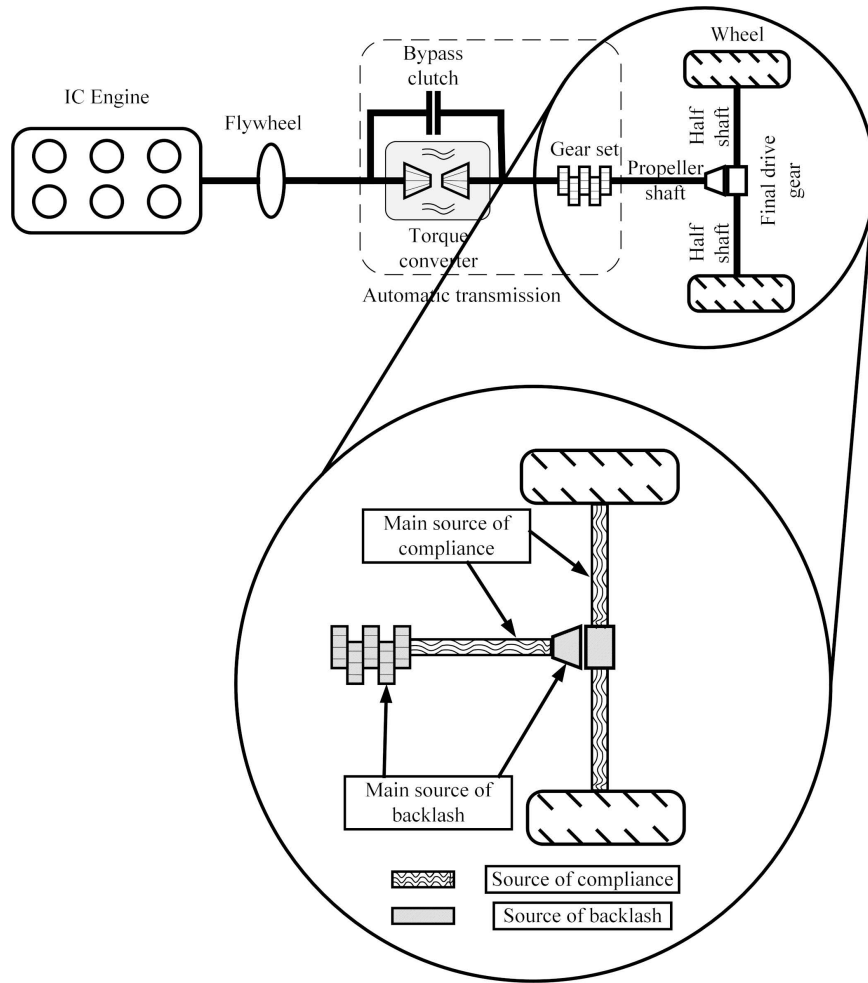


Figure 1.1: Schematic showing the main sources of backlash and compliance in an automotive drivetrain with an IC engine.

For an in-depth analysis into the clunk and shuffle phenomenon, Fig. 1.2 illustrates a tip-in scenario, wherein the vehicle is initially in coasting condition and, after a few seconds, the driver presses the accelerator pedal causing the driver requested torque to increase. In this scenario, the propeller shaft torque and the backlash position is represented as being in the negative domain when the vehicle is coasting. As the torque delivered by the actuator starts to ramp up, first the driveshafts start to untwist and then the backlash traversal starts to take place. During backlash

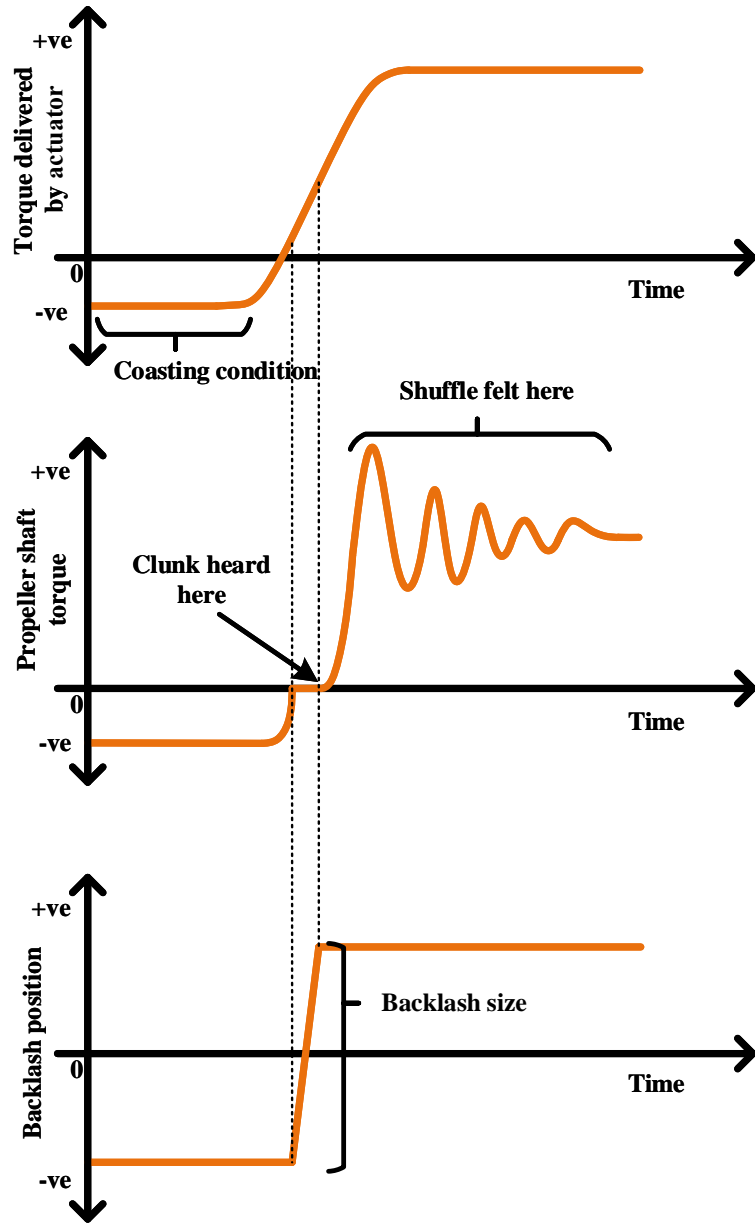


Figure 1.2: The points at which clunk and shuffle occur in an automotive drivetrain.

traversal, it is noticed that the propeller shaft torque remains approximately 0 Nm, since there is no physical contact between the actuator and the wheels. At the end of backlash traversal, the clunk is heard and the propeller shaft torque starts to ramp up.

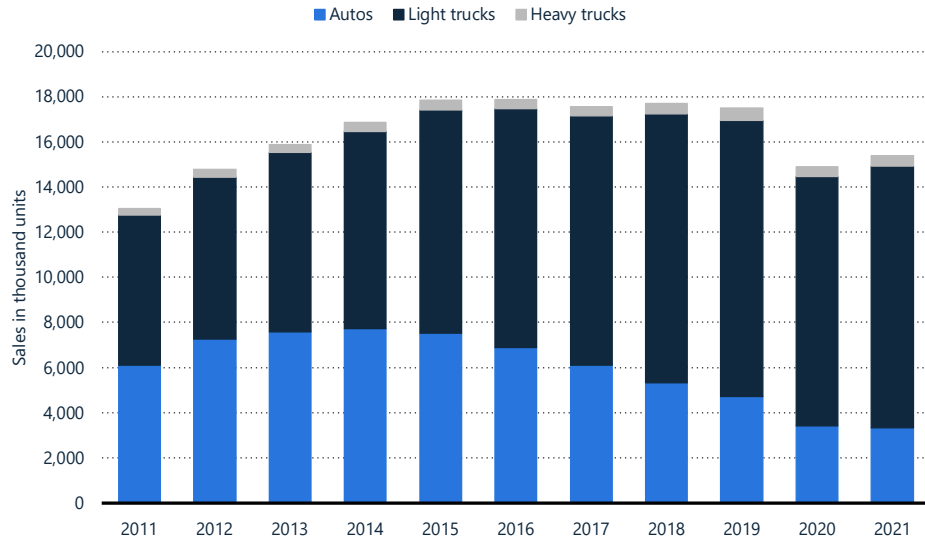


Figure 1.3: Retail sales distribution between cars and trucks in the United States between 2011 - 2021 [1].

However, a low frequency oscillation is also noticed in the propeller shaft torque which is caused due to the twisting of the driveshafts, and this is the shuffle phenomenon.

1.1 Motivation

There are multiple reasons for interest in improving the drivability of a vehicle, especially by reducing NVH phenomenon such as clunk and shuffle:

1. In recent years, the sales trend of larger passenger vehicles such as pick-up trucks and SUVs has been rising in North America [1] (see Fig. 1.3). These vehicles typically have larger displacement engines with relative high torque outputs, and rear wheel drive (RWD) or all wheel drive (AWD) drivetrain configurations.

The impact of clunk and shuffle is more prominently perceived in such vehicles. In addition, customer expectations and demands of vehicle comfort have been increasing.

2. Since the past decade, there has been a paradigm shift in automotive propulsion from linear torque producing internal combustion engines to instant torque delivering electric motors [2] (see Fig. 1.4). While the compact and relatively simple electric motor architecture makes it possible to have various powertrain configurations in an automobile, the torque characteristics of the electric motor also make it much more prone to the clunk and shuffle phenomenon. While most automobiles with an electric motor do not need a transmission, they still have reducer gears between the motors and wheels, and they utilize driveshafts for transmitting the propulsion torque to the wheels. On the other hand, faster and more precise torque control opportunities with electric motors makes it easier to implement more advanced and effective torque shaping algorithms.
3. With an exponential increase in the available computation power in an automotive control unit (a.k.a. an ECU), there is a growing scope to implement complex, optimal control logic in automobiles today. Such control algorithms have better performance compared to legacy, heuristic control algorithms. Moreover, legacy control algorithms typically have hundreds of calibration parameters and need long development time. Optimal, model-based control algorithms have relatively less calibration parameters and reduce vehicle

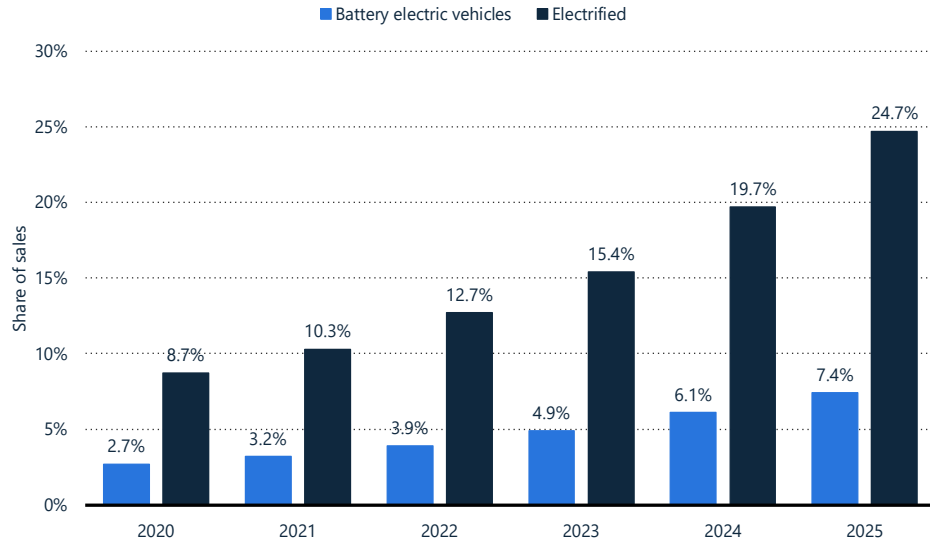


Figure 1.4: Sales forecast for electric and electrified vehicles in the next few years [2].

development time.

In the next section, the current state-of-the-art in reducing clunk and shuffle is discussed, and an overview of relevant research in driveline torque shaping algorithms is provided.

1.2 Literature review

The topic of automotive powertrain control has been of significant interest in the past to many researchers both in academia and research. While the field of powertrain control is quite large, we can broadly categorize the literature in this field into three areas based on research area: (i) development of high-fidelity and

reduced order automotive plant models for use in model-based estimation and control applications, (ii) design and validation of estimation algorithms for automotive driveline applications, and (iii) design and validation of control algorithms for automotive driveline applications. In this chapter, past research in these categories and their advantages and disadvantages are discussed. A timeline showing selected works in the topic of powertrain clunk and shuffle is shown in Fig. 1.5.

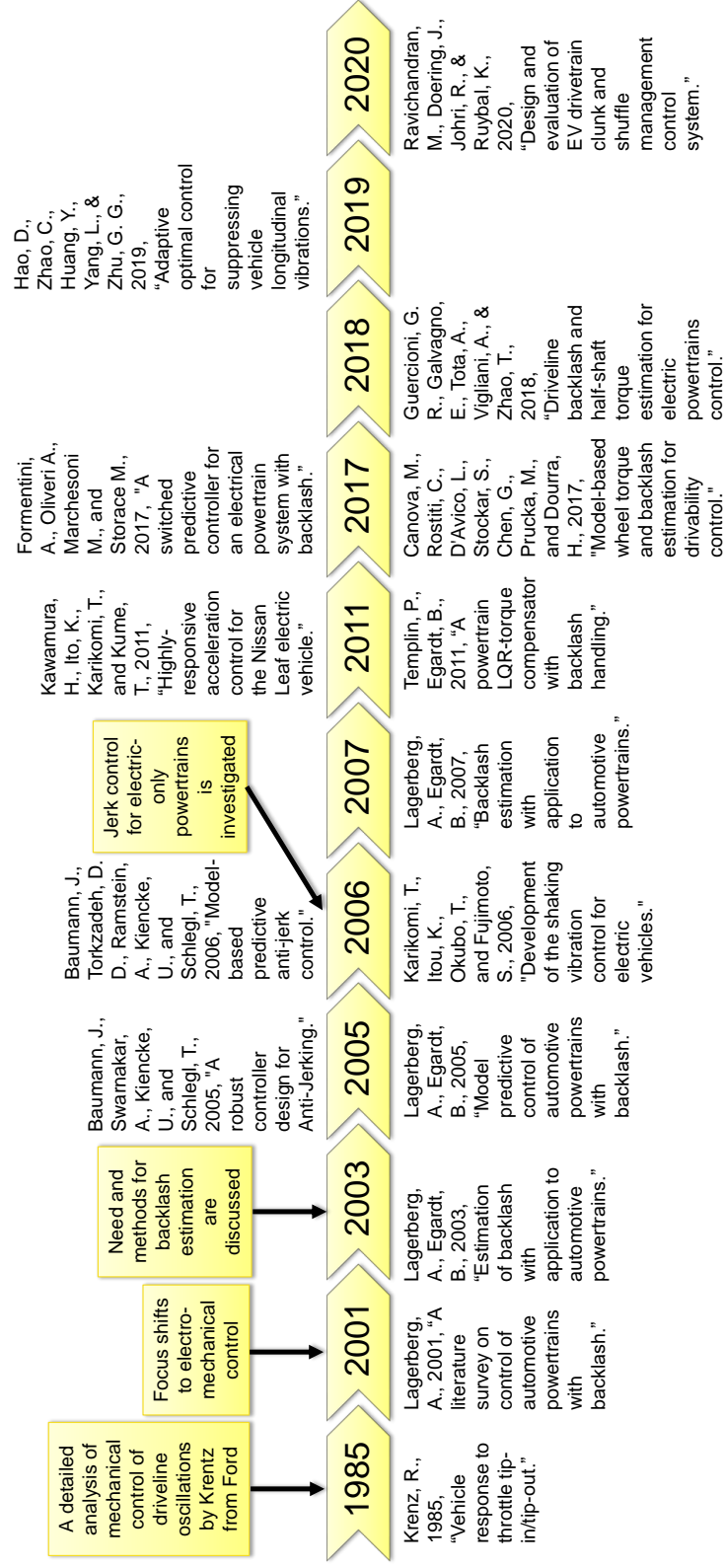


Figure 1.5: Selected literature related to torque shaping control systems.

1.2.1 Driveline modeling for controls applications

Various types of plant models have been previously developed for controls applications based on the dynamics of interest to the researchers. Since this work deals with driveline NVH problems, driveline models developed for estimation and control algorithm development were reviewed and they are presented here.

In [14], an eight state mathematical model was developed based on engine, transmission and driveline states for powertrain dynamics. This model was experimentally validated, and was found to be suitable for developing closed-loop control systems. This technique had the advantage of being easily configurable for any vehicle. In [15], the suitability of a cylinder-by-cylinder engine model and a mean value engine model is compared for use in powertrain control applications. This work suggests that the mean value engine model is a good choice for powertrain simulations and control especially when computational demand needs to be low. In [16], three models of various complexities were designed and they provide a good source for understanding the basic principles of powertrain modeling for control applications. The first model was a linear model with the transmission and final drive including viscous friction, and the clutch, propeller shaft and driveshafts modeled as stiff elements. For the other two models, flexibility was added to the clutch and included static nonlinearity in the clutch, respectively.

In [17], a bond graph-based simple driveline model is developed for analyzing shuffle oscillations in a manual transmission vehicle. Their work includes components that are relevant for observing dominant shuffle modes in an automobile. Further, this work was experimentally validated and showed good agreement with the developed model. In [18], the performance of a nonlinear automotive model developed using Bond Graph and Block Diagram technique is compared, and it is found that both the approaches showed approximately similar accuracy while representing the vehicle speed for an electrical powertrain.

In [19], a dynamic model for automotive powertrain simulations was developed in AMESim. This model was validated through laboratory data for different operating conditions of an IC engine. In [20], an in-depth analysis is presented on various models that are best suited for different aspects of drivability (e.g., tip-in or tip-out, take off, and during gear shifts). This work also propose different modeling techniques based on the stage of vehicle design cycle. A full-order linear model is proposed during the design and development phase. A reduced order model is proposed for the control strategy formulation phase, and a full-order nonlinear model is proposed for the validation phase of the vehicle development. In [21], five nonlinear models of the vehicle driveline were developed. The stiffness of the driveshaft and half-shafts were identified to be the main factors affecting the low-frequency vibrations in the vehicle. In [22], the relation between road surface and vibrations in the driveline was studied. It was observed that depending on the road conditions, there may be significant effect

on the oscillation amplitude and frequency of a driveline.

1.2.2 Backlash position and size estimators

Various models of backlash have been discussed in the literature (see, e.g., [23]) for application in automotive systems. Past researchers have utilized some of these models for developing different methods of backlash position estimation. In [24], the researchers split the driveline into different operating modes based on the position of the backlash, and developed extended Kalman filter-based estimators for determining the position of the backlash. However, they assume the availability of angular position information of the engine and the wheels in their work, whereas obtaining angular position of the wheels from their angular speed measurement is difficult on production vehicles. In [25], a Loop Transfer Recovery (LTR) method is developed for use during contact mode operation, and system simulation is used during backlash mode operation for estimating the backlash position. However, this approach is not validated using experimental vehicle data.

Canova et al., [26] and Guercioni et al., [27] estimate the backlash position using a discrete Kalman filter. Both their approaches use the speed measurements of the engine and wheels as the measured variables, and the torque input to the driveline as the control input. However, there are certain key differences when compared to the

Backlash position estimation		
<p>Extended Kalman filter</p> <p>Lagerberg, Adam, and Bo Egardt. "Backlash estimation with application to automotive powertrains." <i>IEEE Transactions on Control Systems Technology</i> 15.3 (2007): 483-493.</p> <p>Measured states: Engine and wheel position</p> <p>Shortcomings: Difficult to obtain initial engine position information using available production sensors on the vehicle</p>	<p>Loop Transfer Recovery and system simulation</p> <p>Templin, Peter, and Bo Egardt. "A powertrain LQR-torque compensator with backlash handling." <i>Oil & Gas Science and Technology—Revue d'IFP Energies nouvelles</i> 66.4 (2011): 645-654</p> <p>Measured states: Engine and wheel speed</p> <p>Shortcomings: Accuracy of backlash position estimation is not discussed due to lack of test vehicle data</p>	<p>Discrete Kalman filter</p> <p>Canova, Marcello, et al. "Model-based wheel torque and backlash estimation for drivability control." <i>SAE International Journal of Engines</i> 10.3 (2017): 1318-1326.</p> <p>Guercioni, Guido Ricardo, et al. <i>Driveline backlash and half-shaft torque estimation for electric powertrains control</i>. No. 2018-01-1345. SAE Technical Paper, 2018.</p> <p>Measured states: Engine and wheel speed</p> <p>Shortcomings: Uses 1 ms time step and does not verify for robustness to CAN jitter</p>

Figure 1.6: Summary of previous approaches to backlash position estimation.

current work, namely: (i) the plant model considered in [27] uses a two-mass reduced-order model, which might not capture the clunk and shuffle dynamics accurately, and (ii) these works do not analyze the impact of CAN jitter [28] on their estimator's performance, while jitter is present in the measured signals obtained over CAN in production vehicles.

Past literature in automotive backlash size estimation is limited. Lagerberg et al., [24] developed a size estimator using Kalman filter methodology, assuming the availability of engine and wheel angular position measurements. However, this approach is difficult to implement due to the non-availability of wheel angular position information in production vehicles. Templin [29] proposed a prediction-based estimation approach for obtaining drivetrain parameters, including the lash size, though the effectiveness and robustness of this approach are not investigated.

Researchers in other fields such as manufacturing, robotics, and wind turbines are also interested in estimating the backlash size. Using angular position measurement, Hovland et al., [30] design an extended Kalman filter to identify the size of backlash in robotic transmissions. Prajapat et al., [31] make use of an unscented Kalman filter to estimate the size of the lash present in gearboxes of wind turbines. Here, the inputs to the estimator are the generator speed and power. Merzouki et al., [32] and Papageorgiou et al., [33] develop sliding-mode observers that use position and speed measurements to estimate the backlash size in electromechanical systems and machine tools, respectively. Stein et al., [34] introduce a bounce estimation technique, based on momentum transfer analysis, for estimating the size of the backlash present in industrial machinery. However, their approach places certain limitations on the amount of compliance present in the system. In addition, the estimator also requires calibration on each and every machine that it is applied to. Tjahjowidodo et al., [35] propose a nonlinear parameter estimation technique for obtaining the backlash size. This technique is computationally intensive and, therefore, needs to be performed offline. An overview of different approaches to estimate backlash size, previously proposed by researchers, is illustrated in Fig. 1.7.

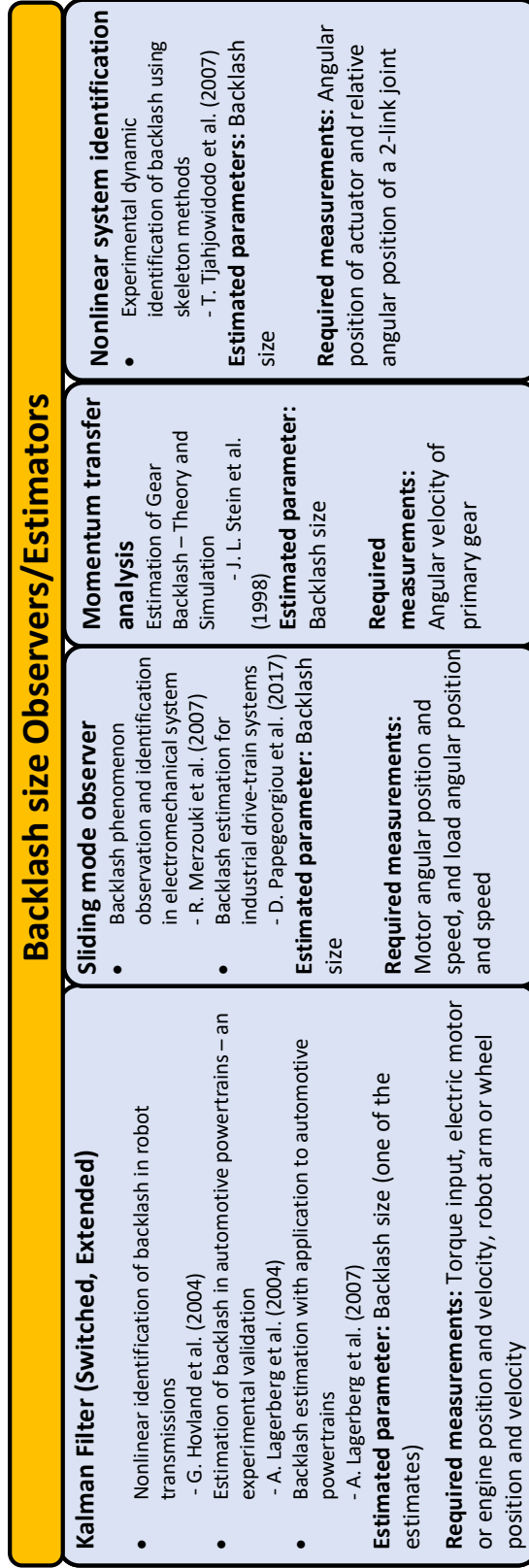


Figure 1.7: Summary of previous approaches to backlash size estimation

1.2.3 Torque shaping controllers

Past researchers have shown interest in controlling drivetrain clunk and they have proposed a number of rule-based and model-based control techniques. In [25], a Linear Quadratic Regulator (LQR) torque compensator is used for finding a constant torque value to saturate the controller output during lash traversal to reduce clunk. While this helps in controlling clunk, saturating actuator torque output during lash traversal would increase the time taken to cross lash, and may cause the driver to perceive the vehicle to be sluggish. In [36], a bang-bang controller is proposed for reducing clunk in an electric vehicle architecture. Fixed upper and lower torque commands are chosen based on an estimation of the backlash position. While this approach is straightforward, it requires significant calibration efforts to obtain optimal upper and lower bounds for all operating conditions. In [37], a sliding mode controller is used for minimizing the relative speed between the actuator and the wheels. While simulation results show good performance, the authors do not discuss the feasibility of implementing this controller on an automotive electronic control unit (ECU). In [38], a mixed H_2/H_∞ servo controller is used for reducing vibrations in an automobile. A backlash reducer and anti-windup feature is included with this controller to compensate for the presence of backlash in the system. However, the use cases discussed have relatively small backlash size values when compared to the typical backlash size observed in passenger automobiles. Other researchers have used Model

<p>Linear Quadratic Regulator (LQR) [25] Approach: Calculating constant torque command during lash traversal using cost function Limitation: Limited performance due to monotonic torque shaping during lash traversal</p>	<p>Bang-bang control [36] Approach: Saturating actuator torque to an upper and lower bound during lash traversal Limitation: Difficult to calibrate for all possible operating conditions</p>
<p>Automotive clunk control</p>	
<p>Sliding mode controller [37] Approach: Reducing the relative speed between actuator and wheel while traversing lash using sliding mode controller Limitation: No discussion on feasibility for implementing real-time on automotive ECU</p>	<p>Model Predictive Controller (MPC) [39, 41] Approach: (i) Keeping actuator torque close to zero at end of backlash traversal (ii) Reducing variation of kinetic energy across relative ends of driveshafts Limitation: High computational load for real-time application</p>

Figure 1.8: Prior studies for clunk control in automotive systems

Predictive Control (MPC) for shaping the torque during lash traversal [39, 40, 41]. While MPC has shown promising results in simulations, one of its major drawback has been the high computational demand for a production ECU, which makes it difficult to implement on real-time controllers without making compromises in performance. A brief summary of past research in automotive clunk control is shown in Fig. 1.8.

1.3 Limitations in state-of-the-art

From the literature review in the previous section, it is evident that there are certain limitations in the current state-of-the-art for torque shaping control algorithms used in reducing the clunk and shuffle phenomena. These can be summarized as:

- † Difficulty in obtaining accurate backlash position and size information, both real-time and over the life of the vehicle.
- † Satisfying the competing requirements of crossing lash quickly while limiting impact velocity.
- † Ensuring model-based, optimal torque shaping algorithms are suitable for real-time implementation.
- † Lack of coordination between optimal driveline controller and engine torque controller.

1.4 Contribution of this Thesis

This PhD thesis aims to address the challenges and limitations identified in Section 1.3. To that end, the main contributions of this thesis are:

1. **Development of high-fidelity and control-oriented driveline models for controls application:** Both high-fidelity and control-oriented models for a passenger vehicle's driveline are developed and validated using experimental test vehicle data with the primary intention of using in model-based estimator and controller development. Co-simulation between MATLAB and AMESim is setup to connect the plant models with estimation and control algorithms.
2. **Design of Kalman filter-based backlash size and position estimation algorithms:** To provide the torque shaping controller with up-to-date backlash position and size data, estimation algorithms are developed using readily available powertrain sensors, and validated using experimental test vehicle data.
3. **Design of an optimal torque shaping control algorithm that is easy to implement on automotive control units:** Using pre-compensators, lead compensators and soft landing reference governor approach, a model-based, optimal torque shaping controller which is easily calibratable is developed and validated.
4. **Analysis of the estimators and controller developed for torque shaping:** Detailed robustness analysis within the operating conditions of an automobile are performed for the designed estimation and control algorithms.
5. **Design and analysis of an optimal control algorithm for reducing torque lag caused due to the fluid path of a torque converter:** An

optimal, model-based torque lag controller is designed for cases when the torque converter lock-up clutch is allowed to slip. This controller is integrated with the driveline torque shaping controller to provide smooth and connected driveline torque in all driving scenarios.

- 6. Integration of the designed torque shaping controller with an optimal, model-based engine controller to demonstrate coordinated control between two complex, model-based controllers:** The driveline torque shaping controller is integrated with an engine torque controller, and coordinated control between these two complex controllers is demonstrated to show that both the controllers are able to meet their individual control objectives.

1.5 Thesis structure

This thesis is organized as follows: Chapter 2 discusses the development and validation of the high-fidelity and control-oriented driveline models and the co-simulation setup between MATLAB and AMESim. Details about the experimental vehicle data collection used for validating the models is also discussed in this chapter.

Chapter 3 delves into the design of the backlash position and size estimators. The activation, deactivation and the tuning process for these estimators is also discussed

in this Chapter. Later, robustness analysis of both the backlash size and backlash position estimators are discussed.

The design and validation of the model-based, optimal torque shaping controller for a locked torque converter are discussed in Chapter 4. The setup of the optimal control problem and the tuning of the torque shaping controller are also discussed in this Chapter.

Chapter 5 discusses the integration of the torque shaping controller from Chapter 4 with other model-based, automotive controllers. Two applications are discussed in this chapter: (i) the design and integration of an optimal controller for reducing the impact of torque lag in scenarios where the torque converter lock-up clutch starts to slip, and (ii) the design and integration of an economic nonlinear MPC engine controller with the torque shaping controller. Chapter 6 summarizes the conclusions from this thesis and provides ideas to further expand the studies from this thesis. The organization of this thesis is illustrated in Fig. 1.9.

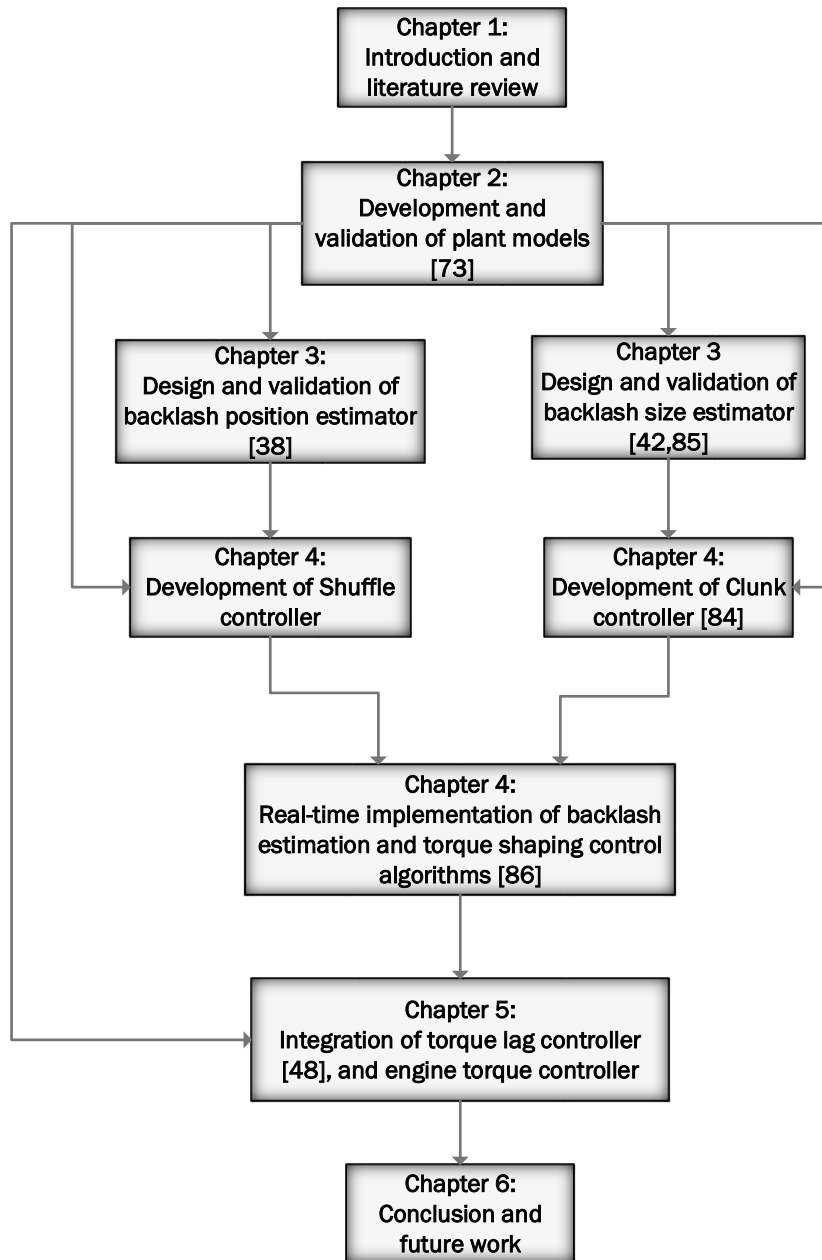


Figure 1.9: Organization of this thesis. Citations in this figure indicate original work that was published and work that is in review as a result of this thesis.

Chapter 2

Development and validation of plant models¹

The first step in developing model-based estimation and control algorithms is to develop a high-fidelity, full-order physics-based model of the vehicle driveline. Since the focus of this work is on reducing clunk and shuffle in the driveline, the physics-based model needs to accurately capture these dynamics. After the model is developed, it has to be validated using experimentally collected test vehicle data. Later, for reducing computational load, the full-order model (FOM) has to be condensed into a simplified, representative control-oriented model (COM) and this COM also needs to be validated using the test vehicle data.

¹Contents of this chapter first appeared in SAE conference paper [4]. Letter of permission from SAE to republish is available in Appendix C.

In this chapter, the development and validation of FOM and COM is discussed in detail. MATLAB Simulink software was used for developing a model of the actuators, and Simcenter AMESim software was used for developing the remaining driveline components starting for the torque converter to the wheels. A co-simulation interface was setup between these two modeling environments with data exchange occurring in both directions.

2.1 Full-order model (FOM) - Development

The FOM was developed to capture the clunk and shuffle dynamics in a passenger vehicle of the Ford Motor Company, and its driveline component parameters were provided by the Ford Motor Company. These parameters were obtained or calculated through supplier data, computer-aided-engineering (CAE) analysis, and internal testing of the driveline components at the Ford Motor Company. The individual components making up the FOM in this work are as follows:

2.1.1 Actuator model

The high-level dynamics of both an internal combustion engine and an electric motor actuator were captured in this work. The torque delivery dynamics of the engine

and the electric motor were represented using a combination of the inertias of the actuators, first order transfer functions and pure time delays. The input to the actuator was the commanded torque request from the controller and the outputs were torque delivered and the rotational speed of the actuator.

2.1.1.1 Engine

The dynamics of the engine model in the FOM can be classified as: (i) slow dynamics, caused due to the intake of the air-charge; and (ii) fast dynamics, caused due to the change in spark timing. The slow dynamics are also referred to as the *base path* dynamics and are represented as a lag, using a first order transfer function with a time constant of $\tau_{e,base}$, whose approximate value is obtained through experimental engine testing. The engine torque delivery in the base path is also affected by a combustion time delay $t_{d,base}$, which is assumed to be one complete rotation of the engine crankshaft [42]. The equation for calculating the delivered base path engine torque, $T_{e,base,ind}$, in indicated domain, is given as:

$$\dot{T}_{e,base,ind}(t) = \frac{1}{\tau_{e,base}} [T_{e,base,ind}^*(t - t_{d,base}) - T_{e,base,ind}(t)], \quad (2.1)$$

where $T_{e,base,ind}^*$ is the commanded base path engine torque, in the indicated domain.

Since the base path dynamics are dependent on air flow, these dynamics are relatively slow at changing the engine torque. On the other hand, the spark timing affects the *instantaneous path* dynamics which, as the name suggests, can vary the engine torque relatively quickly. The spark delay associated with the firing of each cylinder, $t_{d,inst}$, is a function of engine speed and number of cylinders in the engine. In general, this delay $t_{d,inst}$ also depends on the phase of the engine combustion. However, for simplicity, this dependency is ignored here.

A torque ratio, TR_{spk} , is defined based on spark timing of the engine. This TR_{spk} is in the range of $[0.3,1]$, where the lower bound is set such that unacceptable emissions and combustion instability is avoided, and the upper bound is set such that maximum engine brake torque (MBT) spark timing is achieved. The commanded torque ratio, TR_{spk}^* , is computed using the commanded instantaneous torque and delivered base torque, and is given as:

$$TR_{spk}^* = \frac{T_{e,inst,ind}^*(t)}{T_{e,base,ind}(t)}. \quad (2.2)$$

The delivered torque ratio, TR_{spk} , is given as:

$$TR_{spk}(t) = TR_{spk}^*(t - t_{d,inst}), \quad (2.3)$$

where $t_{d,inst}$ is the above mentioned spark delay.

Finally, the torque delivered by the engine, $T_{e,\text{inst,brake}}$, can be represented as:

$$T_{e,\text{inst,brake}}(t) = T_{e,\text{base,ind}}(t) TR_{\text{spk}}(t) - T_{\text{fric}}(t), \quad (2.4)$$

where T_{fric} is the engine friction torque, which is a function of engine speed.

2.1.1.2 Electric Motor

The torque delivery dynamics of the electric motor are modeled as a rate-limited, first order transfer function. The time constant, $\tau_{e-\text{mot}}$, of the first order transfer function, and the motor rate limits are chosen based on experimental test data for the modeled electric motor. Therefore, the delivered electric motor torque is given as:

$$\dot{T}_{e-\text{mot}}(t) = \frac{1}{\tau_{e-\text{mot}}} [T_{e-\text{mot}}^*(t) - T_{e-\text{mot}}(t)], \quad (2.5)$$

where $T_{e-\text{mot}}^*$ is the commanded motor torque and $T_{e-\text{mot}}$ is the delivered motor torque.

The rest of the driveline equations for the FOM have the same equations of motion irrespective of the actuator. Therefore, in the forthcoming sections, the delivered engine torque, $T_{e,\text{inst,brake}}$, and the delivered motor torque, $T_{e-\text{mot}}$, are interchangeably referred to as delivered actuator torque, T_{act} .

2.1.2 Other driveline elements

The torque delivered by the actuator, $T_{\text{act}}(t)$, is used to calculate its angular speed, $\dot{\theta}_{\text{act}}$, using the rotational inertia, J_a , at the actuator:

$$J_a \ddot{\theta}_{\text{act}} = T_{\text{act}} - T_{\text{im}}, \quad (2.6)$$

where $\ddot{\theta}_{\text{act}}$ is the angular acceleration of the actuator, and T_{im} is the load torque at the impeller of the torque converter.

2.1.2.1 Torque converter

The torque converter consists of an impeller, stator, turbine, and a lock-up clutch with damper springs set inside a metal housing. The lock-up clutch can operate in one of its three modes when the vehicle is running: locked, open, or slipping. In general, when the vehicle starts from a stationary state, the lock-up clutch is open and complete torque transmission takes place through the fluid between the impeller and turbine. When the vehicle reaches a set of pre-defined conditions (e.g., impeller speed, vehicle speed and transmission fluid temperature), the lock-up clutch can operate in either slipping or locked positions. The transmission control unit (TCU) defines the position

of the lock-up clutch based on drivability target while minimizing fuel consumption [43]. The modeled torque converter includes both the fluid path dynamics (due to the fluid inside the converter), and the lock-up clutch dynamics. The fluid path dynamics are represented using look-up tables which define the torque ratio and capacity factor of the converter based on its speed ratio. The lock-up clutch dynamics are modeled based on its assumed clutch capacity. Additionally, the hysteresis caused by the damper springs of the lock-up clutch inside the torque converter are also modeled.

When the torque converter lock-up clutch operates in locked condition, it is assumed that there are no losses in torque transmission, and that the impeller torque, T_{im} , is completely transmitted to the torque converter turbine:

$$T_{tu} = T_{im} \quad (2.7)$$

where T_{tu} is the turbine torque of the torque converter.

The speed ratio (SR), torque ratio (TR) and capacity factor (K) of the torque converter are defined as:

$$SR = \frac{\dot{\theta}_{tu}}{\dot{\theta}_{im}} \quad (2.8)$$

where, $\dot{\theta}_{tu}$ is the angular speed of the torque converter turbine and $\dot{\theta}_{im}$ is the angular speed of the torque converter impeller.

$$TR = \frac{T_{tu}}{T_{im}} \quad (2.9)$$

$$K = \frac{\dot{\theta}_{im}(9.55)}{\sqrt{T_{im}}} \quad (2.10)$$

where, $\dot{\theta}_{im}$ is the angular speed of the torque converter impeller.

When the torque converter lock-up clutch operates in open condition, the turbine torque, T_{tu} , is given by:

$$T_{tu} = \left(\frac{\dot{\theta}_{act}(9.55)}{K(SR)} \right)^2 (TR(SR)) \quad (2.11)$$

where $\dot{\theta}_{act}$ is the angular speed of the actuator which is equal to the angular speed of the torque converter impeller, K is the capacity factor of the torque converter as a function of speed ratio, SR , and TR is the torque ratio as a function of speed ratio, SR , of the torque converter.

When the torque converter lock-up clutch operates in slipping condition, the equation is a combination of fluid path dynamics and clutch path dynamics and the turbine torque, T_{tu} , is given by:

$$T_{\text{tu}} = T_{\text{tcc}} + \left(\frac{\dot{\theta}_{\text{act}}(9.55)}{K(\text{SR})} \right)^2 (TR(\text{SR})) \quad (2.12)$$

where T_{tcc} is the torque through the lock-up clutch.

It is important to note that the equations for the torque converter discussed in this chapter are simplified equations, and do not consider the effect of geometrical parameters (like number of blades on the impeller and turbine, and their blade angles) and fluid properties of the converter.

2.1.2.2 Transmission with backlash

The transmission model in this work consists of a 10-speed automatic transmission with a backlash element, and the effect of the latter is included before the torque multiplication of the gear. The effect of gear changes on driveline dynamics is out of scope of this thesis, and, therefore, a fixed gear state is assumed for the tip-in scenarios. The dynamics of the backlash are modeled using the ‘Physical Model’ from [23].

Let $\theta_{\text{d,trans}}$ be the displacement of the torque converter output shaft, $\theta_{\text{b,trans}}$ be the position in transmission backlash, $\theta_{\text{transbl,in}}$ be the angular position of the transmission input shaft at the beginning of the backlash, and $\theta_{\text{transbl,out}}$ be the angular position of

the transmission input shaft at the end of the backlash. Then,

$$\theta_{d,\text{trans}} = \theta_{\text{tc},\text{out}} - \theta_{\text{transbl},\text{out}}, \quad (2.13)$$

$$\theta_{b,\text{trans}} = \theta_{\text{transbl},\text{in}} - \theta_{\text{transbl},\text{out}}. \quad (2.14)$$

The torque at the output of the backlash is given by:

$$T_{\text{transbl},\text{out}} = k_{\text{tc},\text{out}}[\theta_{d,\text{trans}} - \theta_{b,\text{trans}}] + c_{\text{tc},\text{out}}[\dot{\theta}_{d,\text{trans}} - \dot{\theta}_{b,\text{trans}}], \quad (2.15)$$

where $k_{\text{tc},\text{out}}$ is the stiffness of the torque converter output shaft and $c_{\text{tc},\text{out}}$ is the damping of the torque converter output shaft. Let 2α be the size of the transmission backlash; then, the dynamics of the speed of lash traversal, $\dot{\theta}_{b,\text{trans}}$, can be expressed as:

$$\dot{\theta}_{b,trans} = \begin{cases} \max\left\{0, \dot{\theta}_{d,trans} + \frac{k_{tc,out}}{c_{tc,out}} [\theta_{d,trans} - \theta_{b,trans}]\right\}, & \text{if } \theta_{b,trans} = -\alpha, \\ \dot{\theta}_{d,trans} + \frac{k_{tc,out}}{c_{tc,out}} [\theta_{d,trans} - \theta_{b,trans}], & \text{if } |\theta_{b,trans}| < \alpha, \\ \min\left\{0, \dot{\theta}_{d,trans} + \frac{k_{tc,out}}{c_{tc,out}} [\theta_{d,trans} - \theta_{b,trans}]\right\}, & \text{if } \theta_{b,trans} = +\alpha, \end{cases} \quad (2.16)$$

where $\theta_{d,trans}$ and $\theta_{b,trans}$ are defined in equations (2.13) and (2.14).

The torque loss within the transmission (including transmission pump loss) is included at the input of the transmission model. These losses are a function of the engaged gear and the actuator speed. Therefore, the torque at the output of the transmission, T_t , is given by:

$$T_t = [T_{transbl,out} - T_{gearloss}] i_t, \quad (2.17)$$

where i_t is the gear ratio of the engaged gear.

2.1.2.3 Propeller shaft

The torque at the output of the propeller shaft, T_{ps} , is given by:

$$T_{ps} = k_{ps}[\theta_t - \theta_{ps}] + c_{ps}[\dot{\theta}_t - \dot{\theta}_{ps}], \quad (2.18)$$

where θ_t is the angular position of the transmission output shaft, and θ_{ps} is the angular position of the propeller shaft on its output side.

2.1.2.4 Final drive with backlash

Let 2β be the size of the final drive backlash; then, the dynamics of the speed of lash traversal, $\dot{\theta}_{b,fd}$, can be expressed similar to the previous equations (2.13 - 2.16). The torque output on the wheel side of the final drive, T_{fd} , is given by:

$$T_{fd} = T_{fd,bl,out} \cdot i_{fd}, \quad (2.19)$$

where i_{fd} is the final drive ratio.

2.1.2.5 Axle shaft

Let k_{ax} be the stiffness of the axle shaft, c_{ax} be the damping of the axle shaft, θ_{fd} be the angular position of the final drive backlash output, θ_{ax} be the angular position of the axle shaft on the tire end, $\dot{\theta}_{\text{fd}}$ be the angular speed of the final drive backlash output, and $\dot{\theta}_{\text{ax}}$ be the angular speed of the axle shaft at the tire end. Then, the torque on the wheel side of the axle shaft, T_{ax} , is given by:

$$T_{\text{ax}} = k_{\text{ax}}[\theta_{\text{fd}} - \theta_{\text{ax}}] + c_{\text{ax}}[\dot{\theta}_{\text{fd}} - \dot{\theta}_{\text{ax}}]. \quad (2.20)$$

2.1.2.6 Tire dynamics

The tire dynamics is modeled using Pacejka's magic formula [44]. Let κ be the longitudinal slip percentage of the tire, C be the shape factor, D be the peak factor, BCD be the stiffness factor, E be the curvature factor, Sh be the horizontal shift and Sv be the vertical shift used for calculating the tire force in the magic formula. Then the longitudinal force on the tire, F_{ti} , is given by:

$$F_{\text{ti}} = D \cdot \sin(C \cdot \arctan(\psi)) + Sv, \quad (2.21)$$

where

$$\psi = B \cdot [\kappa + Sh] - E[B \cdot [\kappa + Sh]] - \arctan(B \cdot [\kappa + Sh]), \quad (2.22)$$

$$B = \frac{BCD}{C \cdot D}. \quad (2.23)$$

Let F_z be the vertical force (i.e., weight) on one tire of the vehicle, R_{roll} be the rolling radius of the tire, and R_c be the rolling resistance coefficient of the tire. Then, the rolling resistance torque of the tire, T_{res} , is given by:

$$T_{\text{res}} = R_{\text{roll}} \cdot F_z \cdot R_c. \quad (2.24)$$

Let J_{wheel} represent the lumped inertia at the wheel and $\dot{\omega}_{\text{wheel}}$ be the angular acceleration of the wheel. Then the dynamics of the wheel are given by:

$$J_{\text{wheel}} \cdot \dot{\omega}_{\text{wheel}} = T_{\text{ax}} - T_{\text{res}} - R_{\text{roll}} F_{\text{ti}}. \quad (2.25)$$

2.1.2.7 Longitudinal Vehicle Dynamics

The aerodynamic force, involved in the dynamics of the vehicle body, is given by [45]:

$$F_{\text{aero}} = \frac{1}{2} \cdot \rho \cdot A_f \cdot C_D \cdot V^2, \quad (2.26)$$

where ρ is the air density, A_f is the frontal area of the vehicle, C_D is the drag coefficient, and V is the longitudinal velocity of the vehicle.

The acceleration of the vehicle, a_{veh} , is calculated according to the following equation:

$$a_{\text{veh}} = \frac{F_{\text{ti}} - F_{\text{aero}}}{m_{\text{veh}}}, \quad (2.27)$$

where m_{veh} is the mass of the vehicle. In Fig. 2.1, T_{load} represents the road load acting on the vehicle, which includes the combined effect of the resistive forces acting on the vehicle, and is given by:

$$T_{\text{load}} = T_{\text{res}} + [F_{\text{aero}} \cdot R_{\text{roll}}]. \quad (2.28)$$

2.2 Full-order model - Validation

It is imperative that the FOM is able to correlate shuffle and clunk with respect to the vehicle behavior; thus a set of vehicle states is required to be chosen, which can quantify shuffle and clunk so that the accuracy of the FOM can be evaluated. Clunk

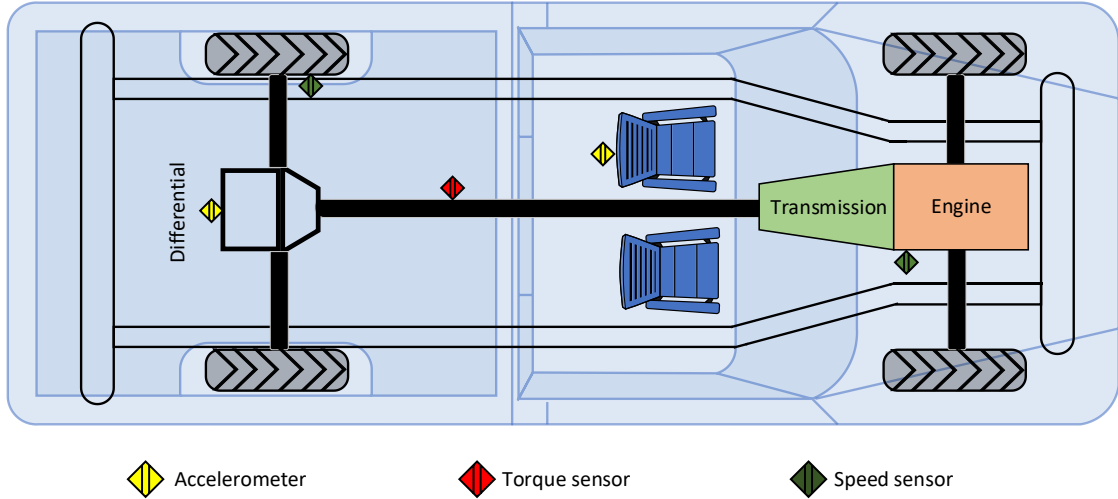


Figure 2.2: Locations of the sensors used for experimental data acquisition from the test vehicle.

can be quantified as a function of the lash crossing speed. The lash crossing speed can be evaluated as the difference of the actuator speed and wheel speed when brought in the same domain. Similarly, shuffle can be quantified using the frequency and amplitude of oscillations in the longitudinal vehicle acceleration and in the driveshaft torque. Thus, the vehicle acceleration and propeller shaft torque are recorded and analyzed using a test vehicle, whose driveline architecture is similar to the FOM. Physical properties of the driveline components (i.e., inertia, stiffness, mass, drag coefficient, etc.) are used to parameterize the FOM.

Fig. 2.2 illustrates the positions of the sensors on a test vehicle belonging to the Ford Motor Company. In addition to production level sensors such as engine speed sensor, wheel speed sensor, etc., this vehicle is also instrumented with a telemetry torque sensor on the propeller shaft, accelerometers on the driver's seat and on the

rear differential. Other data such as driver requested torque, actuator speed, vehicle speed, etc., is obtained from the vehicle's powertrain ECU. The torque converter lock-up clutch is explicitly commanded to be in the locked position throughout the validation experiments.

The data collected from the vehicle is post-processed, and compared with the simulation results of the FOM. Fig. 2.3 shows the comparative results when the driver tips in from coasting and the transmission is in 5th gear. Fig. 2.3(a) shows the ECU estimated crankshaft torque from the vehicle and the simulation output from the engine model. A 10% error is assumed in the estimated engine torque to account for the uncertainties in the ECU's engine charge estimation and the variations in tuning of the engine torque controller. Due to this assumed uncertainty, there is an offset in the estimated and simulated crankshaft torque signals. Fig. 2.3(b) shows the measured and simulated engine speeds and vehicle speeds on the left and right axis, respectively. Fig. 2.3(c) shows the measured acceleration at the driver's seat and the simulated acceleration obtained from the FOM. The measured acceleration has significant amount of noise in it. However, the frequency and amplitude of shuffle oscillations from the simulated data matches with the measured data. Fig. 2.3(d) compares the torque at the propeller shaft, measured on the vehicle using the telemetry torque sensor, with the simulated propeller shaft torque that is obtained from the model. It is observed that the simulated and measured propeller shaft torques are in good agreement. Additionally, it can be seen that the oscillations in

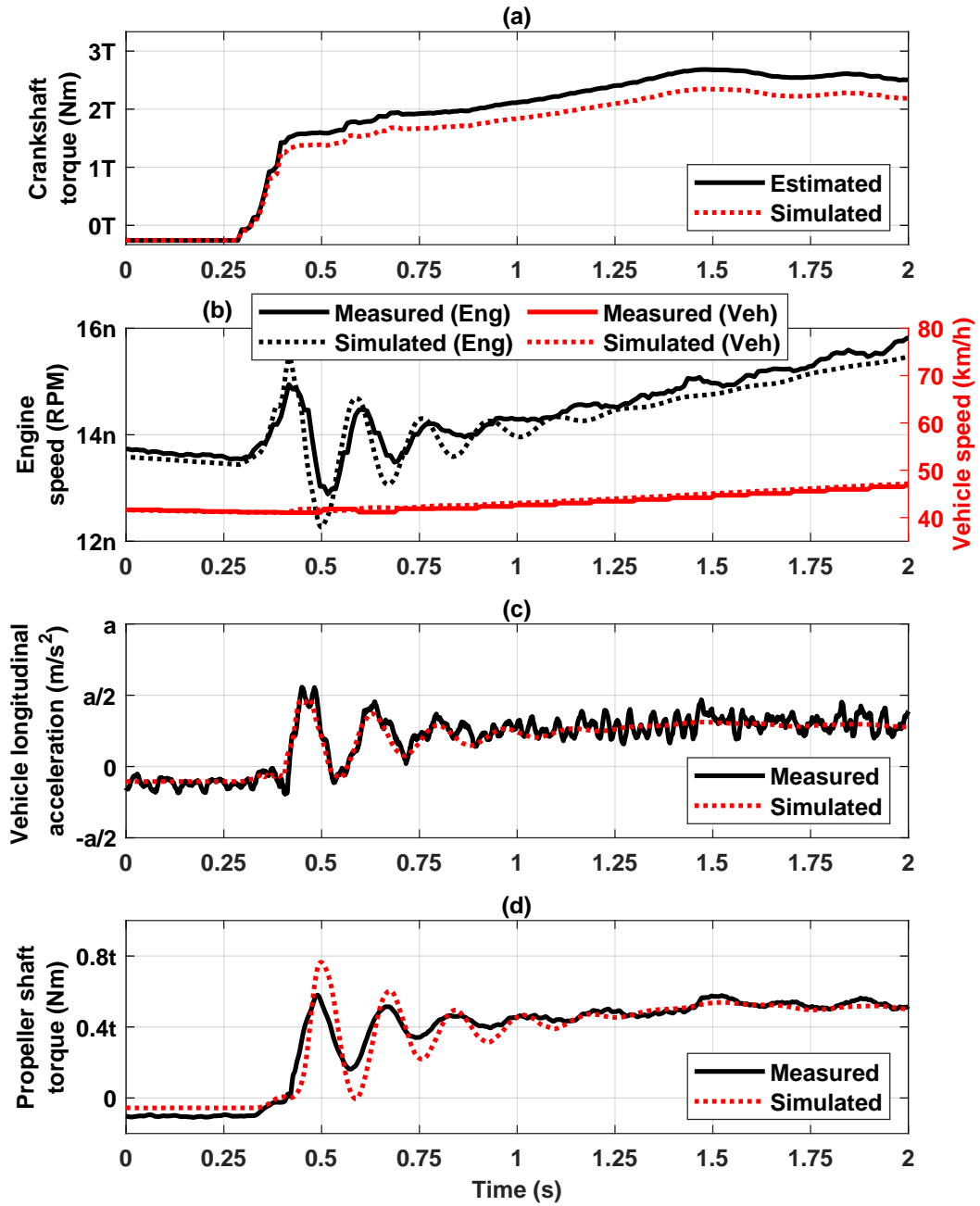


Figure 2.3: Plot showing experimental validation of the FOM with a locked torque converter clutch in 5th gear. Note that the Y-axis labels of all result plots in this thesis have been substituted by alphanumeric values (e.g., 1T, 12n etc.) to keep the test vehicle parameters confidential. ‘T’ represents T units of actuator torque, ‘n’ represents n units of angular speed, ‘a’ represents a units of acceleration, and ‘t’ represents t units of drive shaft torque.

the measured data die down faster than the oscillations in the simulated data. This variation may be attributed to the uncertainty in damping offered by the torque converter clutch damper.

2.3 Control-oriented model - Development

FOMs are computationally expensive and not ideal for use in real-time model-based estimation or control algorithms. Therefore, the complexity of the FOM is reduced by condensing it into a control-oriented model (COM). This COM is then validated with simulation results from the FOM and the experimental test vehicle data. Note that the COM may also be referred to as reduced-order model (ROM) in literature and in this thesis. The steps involved in building the COM in this thesis are:

† Step 1: Lump FOM blocks in terms of inertias, stiffness, and damping;

† Step 2: Simplify the tire model in the FOM;

† Step 3: Lump backlash elements;

† Step 4: Validate the COM;

† Step 5: Evaluate the COM for control applications.

2.3.1 Step 1: Lumping model components

The FOM in this thesis consists of 24 inertia elements, 4 stiffness and damping elements, and 2 backlash elements. However, only some of these elements have a major effect on the response of the driveline. Therefore, the less significant elements are lumped with the more significant ones by taking the physics of the model's sub-components into account. Out of the 24 inertia elements, the inertias of actuator, torque converter, tires, and vehicle body are most significant. Consequently, the model is divided into three inertia elements. Similarly, the stiffness and damping are also lumped into two elements. However, the backlash elements are not lumped at this stage.

The equivalent inertia of two separate inertia elements is obtained by simply adding the inertias together. While lumping the inertia elements, the effect of gear ratio (i.e., transmission gear ratio and final drive gear ratio) is taken into consideration. As an example, the procedure followed for lumping moment of inertias of the propeller shaft, axle shafts, and tires is shown below:

$$J_{\text{axle shafts}} = J_{\text{left axle}} + J_{\text{right axle}}, \quad (2.29)$$

$$J_{\text{lumped axle and tire}} = J_{\text{axle shafts}} + J_{\text{tires}}, \quad (2.30)$$

$$J_{\text{lumped propeller, axle and tire}} = J_{\text{prop shaft}} + \frac{J_{\text{lumped axle and tire}}}{i_{\text{fd}}^2}. \quad (2.31)$$

Similarly, the stiffness of the left and right axle shafts is lumped as follows:

$$k_{\text{axle shafts}} = k_{\text{left axle}} + k_{\text{right axle}}. \quad (2.32)$$

For lumping the combined stiffness of the axle shafts with the propeller shaft, the gear ratio of the final drive (i_{fd}) is taken into account. Moreover, the propeller shaft and the lumped axle shafts are connected in series. Therefore, the lumped shaft stiffness as reflected at the propeller shaft is calculated as follows:

$$\frac{1}{k_{\text{lumped shafts}}} = \frac{1}{k_{\text{prop shaft}}} + \frac{i_{\text{fd}}^2}{k_{\text{axle shafts}}}. \quad (2.33)$$

The damping elements are also lumped in a similar fashion. Using equations (2.29 - 2.33), a COM is derived from the FOM.

2.3.2 Step 2: Simplifying the tire model

The Pacejka tire model is accurate in representing the tire dynamics during a variety of tire slip scenarios. However, the downside is that it requires significant amount of parameter data, i.e., the values of the various Pacejka coefficients, to begin with. Moreover, it also incurs significant computational cost because it considers the variation in tire longitudinal force due to change in tire slip.

Based on the premise that clunk and shuffle control are not prioritized during significant tire slip events, it can be assumed that the scenario of the vehicle driving in non tire-slip conditions is sufficient for developing the torque shaping control system. With this motivation, the Pacejka tire model is replaced with a simple stiffness and damping model of the tire. A comparison between the driveline response with the Pacejka tire model and the simple, compliance tire model is shown in Fig. 2.4. The frequency of shuffle oscillations remains the same with both the tire models, for a non-slip drive scenario. Therefore, the simple tire model is accurate in representing the dynamics of the system. Using Simulink's solver profiler, it can be observed that the simple tire model is approximately 19% faster than the Pacejka model for the scenario illustrated in Fig. 2.4. This reduces the overall computational cost of the COM.

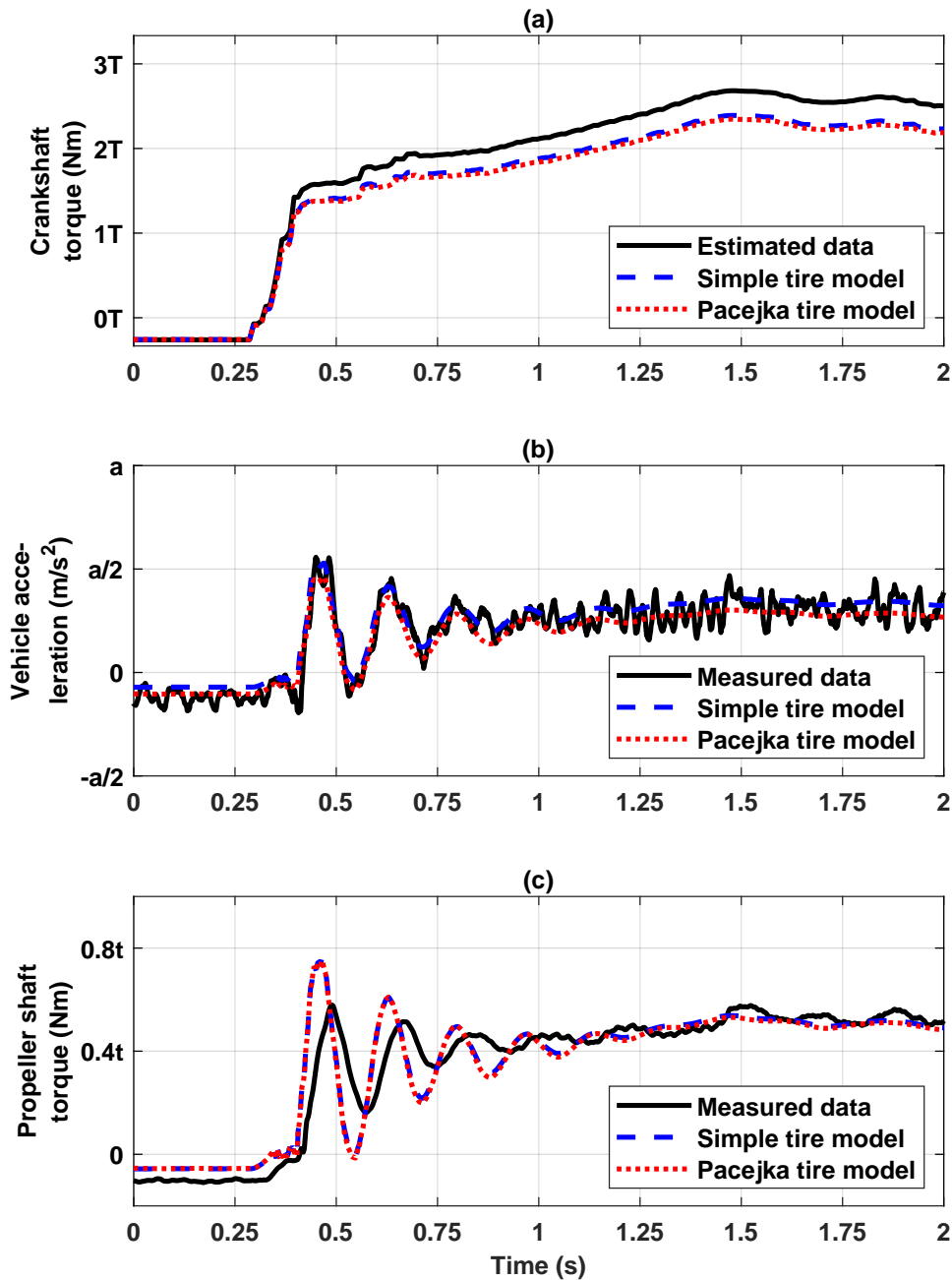


Figure 2.4: Plot comparing the simulation outputs obtained with the Pacejka tire model vs. a simplified tire model vs. the experimental test vehicle data.

2.3.3 Step 3: Lumping backlash elements

The backlash elements in the driveline lead to nonlinearities in the driveline response. Having distributed backlash elements makes the model complicated and difficult to use for control design applications. It is desirable to lump backlash elements as long as the response of the model is not affected adversely. Therefore, a comparative analysis is performed between two COMs, one with individual transmission and final drive backlash (see Fig. 2.6), and one with lumped transmission and final drive backlash, reflected before the final drive (see Fig. 2.7). The results of this analysis is illustrated in Fig. 2.5. The position of the backlash elements with respect to time is shown in Fig. 2.5(b). It is observed that the time taken for lash crossing is the same in both the lumped and individual cases. Fig. 2.5(c) shows the propeller shaft torque from both models. It is further observed that the frequency and amplitude of driveline oscillations from both the COMs are the same. Therefore, a lumped backlash element is chosen for the control-oriented model.

2.3.4 Step 4: Validating the COM

The schematic of the COM obtained after lumping the inertia, compliance, and backlash elements is shown in Fig. 2.7. This COM consists of the following three

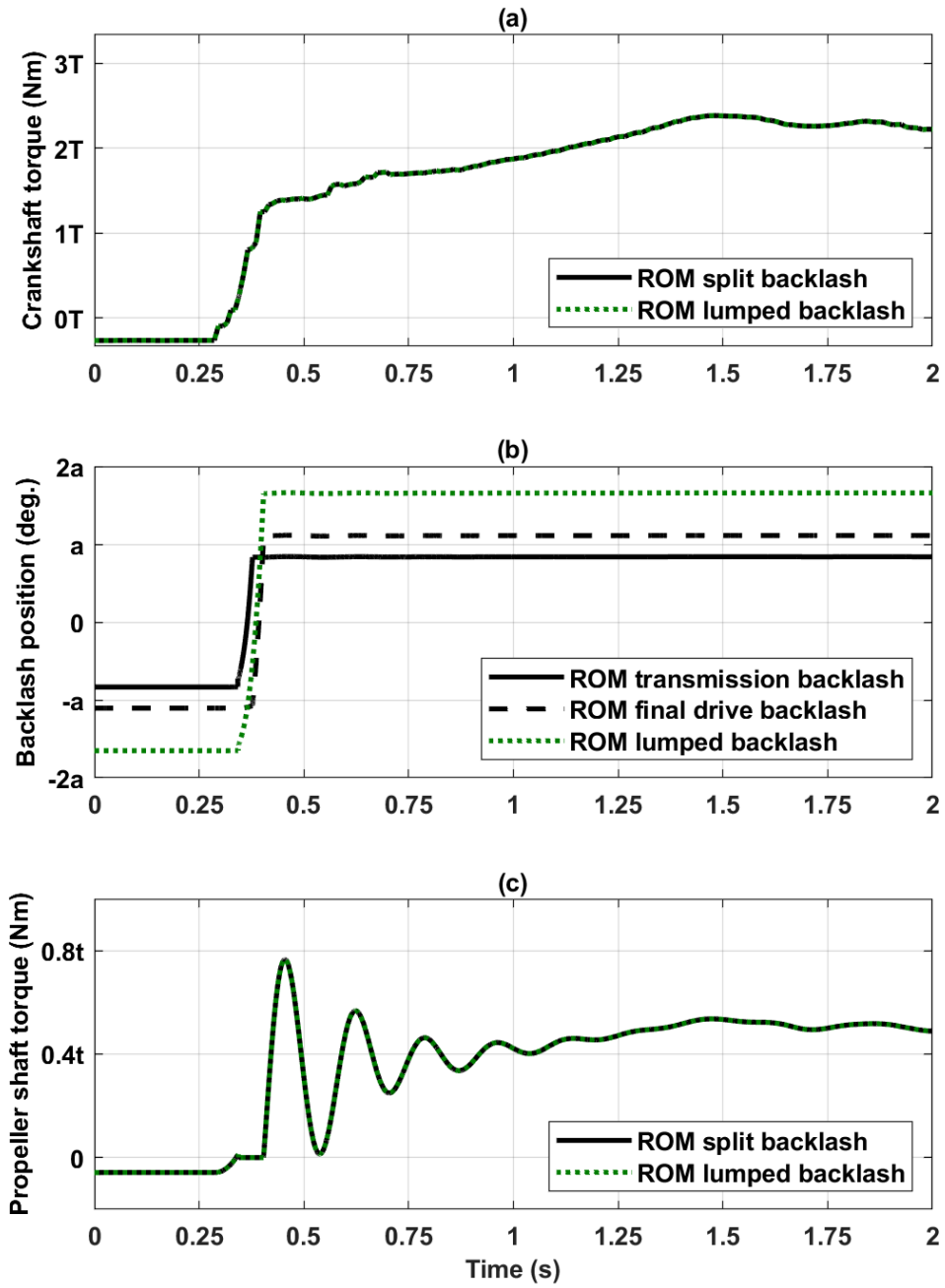


Figure 2.5: Plot showing comparative driveline response of COM with 2 individual backlash elements for the transmission and final drive vs. 1 lumped backlash element.

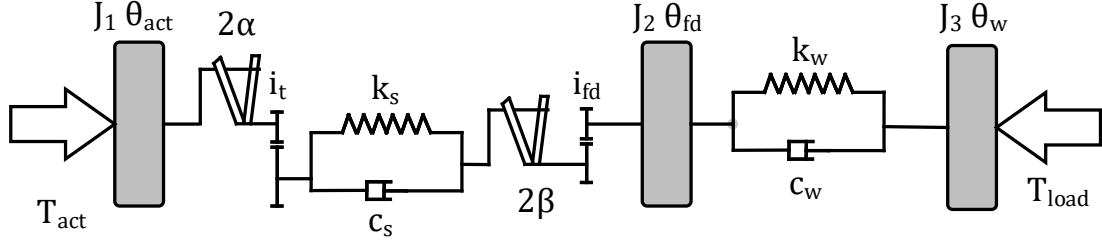


Figure 2.6: Schematic configuration of reduced-order model with 2 backlash elements.

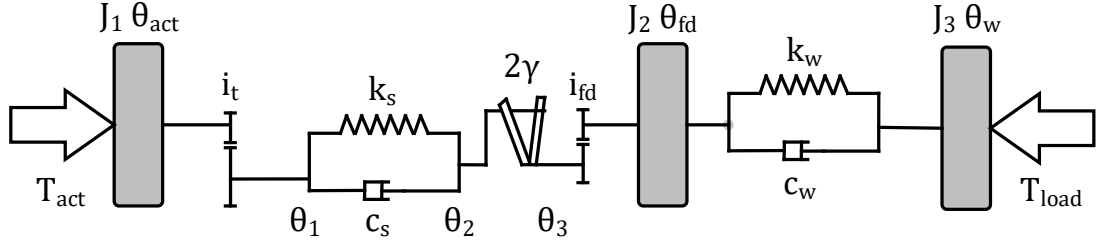


Figure 2.7: Schematic configuration of the chosen control-oriented model.

inertia elements: J_1 , representing the lumped inertia of the actuator, torque converter, transmission, and propeller shaft, J_2 , representing the lumped inertia of the tires and the axle shafts, and J_3 , representing the lumped inertia of the wheels and the vehicle body. The COM also consists of two compliant elements, represented by the stiffness and damping values k_s , c_s , k_w , and c_w . The backlash is lumped before the final drive, and has a size of 2γ , which is calculated as:

$$2\gamma = \frac{2\alpha}{i_t} + 2\beta. \quad (2.34)$$

The equations of motion of the COM are:

$$J_1 \ddot{\theta}_{\text{act}} = T_{\text{act}} - \frac{T_s}{i_t}, \quad (2.35)$$

$$T_s = k_s(\theta_s - \theta_b) + c_s(\dot{\theta}_s - \dot{\theta}_b), \quad (2.36)$$

$$J_2 \ddot{\theta}_{\text{fd}} = T_s i_{\text{fd}} - T_w, \quad (2.37)$$

$$T_w = k_w(\theta_{\text{fd}} - \theta_w) + c_w(\dot{\theta}_{\text{fd}} - \dot{\theta}_w), \quad (2.38)$$

$$J_3 \ddot{\theta}_w = T_w - T_{\text{load}}, \quad (2.39)$$

where: T_{act} , T_s , T_w , and T_{load} are the torques at the actuator, lumped shaft, tire, and road load, respectively; i_t and i_{fd} are the transmission and final drive gear ratios, respectively; k_s and k_w are the stiffnesses of the shafts and the tires, respectively; and c_s and c_w are the damping coefficients of the shafts and the tires, respectively. The displacement of the lumped shaft, θ_s , and its position in the lash, θ_b , are given by:

$$\theta_s = \theta_1 - \theta_3, \quad (2.40)$$

$$\theta_b = \theta_2 - \theta_3, \quad (2.41)$$

where θ_1 , θ_2 , and θ_3 (see Fig. 2.7) represent positions of the transmission shaft output, propeller shaft output, and the final drive input after the lumped backlash, respectively. As mentioned in the FOM section, the dynamics of the lumped backlash

is governed according to [23], i.e.,

$$\dot{\theta}_b = \begin{cases} \max\{0, \dot{\theta}_s + \frac{k_s}{c_s}[\theta_s - \theta_b]\}, & \text{if } \theta_b = -\gamma, \\ \dot{\theta}_s + \frac{k_s}{c_s}[\theta_s - \theta_b], & \text{if } |\theta_b| < \gamma, \\ \min\{0, \dot{\theta}_s + \frac{k_s}{c_s}[\theta_s - \theta_b]\}, & \text{if } \theta_b = +\gamma. \end{cases} \quad (2.42)$$

For ensuring accuracy in representing driveline oscillations, the simulation outputs of the COM are compared against that of the FOM and the experimental test vehicle data. In Fig. 2.8(b), the actuator speeds and vehicle speeds obtained from the test vehicle, the FOM and COM show that the frequency of the driveline oscillations is the same in both the models. There is an average offset of 5% between the amplitudes of the FOM and COM signals. Similar trends are observed in Fig. 2.8(c) and Fig. 2.8(d), where the longitudinal acceleration and propeller shaft torque from FOM and COM are compared. The residuals of the FOM and COM outputs in relation to the vehicle measurements are plotted in Fig. 2.9. These residuals may be attributed to: (i) the noise in the measured acceleration signal caused by chassis vibrations while driving on the road, and (ii) errors in the estimated engine torque from the ECU. Figures 2.8 and 2.9 confirm that: i) the FOM and COM vehicle acceleration and propeller shaft torque predict accurately the beginning and the end of the lash traversal; ii) the FOM and COM engine speed behavior reflects appropriately a rapid increase during lash crossing, as mentioned above; iii) the frequency and phase of the shuffle in these three

FOM and COM signals match well with those from the test vehicle, with an average error of less than 10%, and (iv) the amplitudes of these three FOM and COM signals do not always match their counterparts from the test vehicle, but they are reasonably close for the purpose of this work.

As a verification exercise, the complexity of the COM is further reduced by lumping the tire and axle shaft inertias with the actuator inertia, and tire stiffness and damping with the shaft stiffness and damping. Therefore, while J_3 remains the same as in the previous case (see Fig. 2.7), J_2 is lumped with J_1 , and k_w and c_w are lumped with k_s and c_s respectively. Fig. 2.10 illustrates the response of this model, compared to the response of the FOM. It is clear that this model is not suitable because the driveline oscillation frequency and amplitude do not match in any of the observed signals.

To verify that the COM (of Fig. 2.7) is computationally less demanding compared to the FOM (of Fig. 2.1), both the FOM and COM are simulated using the same initial conditions. A laptop computer with a 64-bit Intel Core-i7 processor and 16 GB RAM is utilized for this analysis using the same AMESim and Simulink interface. Simulations are run using a variable-step solver for a time period of 10 seconds, involving one tip-in scenario. Using Simulink's solver profiler, it is observed that the COM runs approximately 4 times faster than the FOM. Specifically, a 10 second simulation for a tip-in event takes approximately 28 seconds to run on the FOM, whereas it takes approximately 7 seconds to run on the COM.

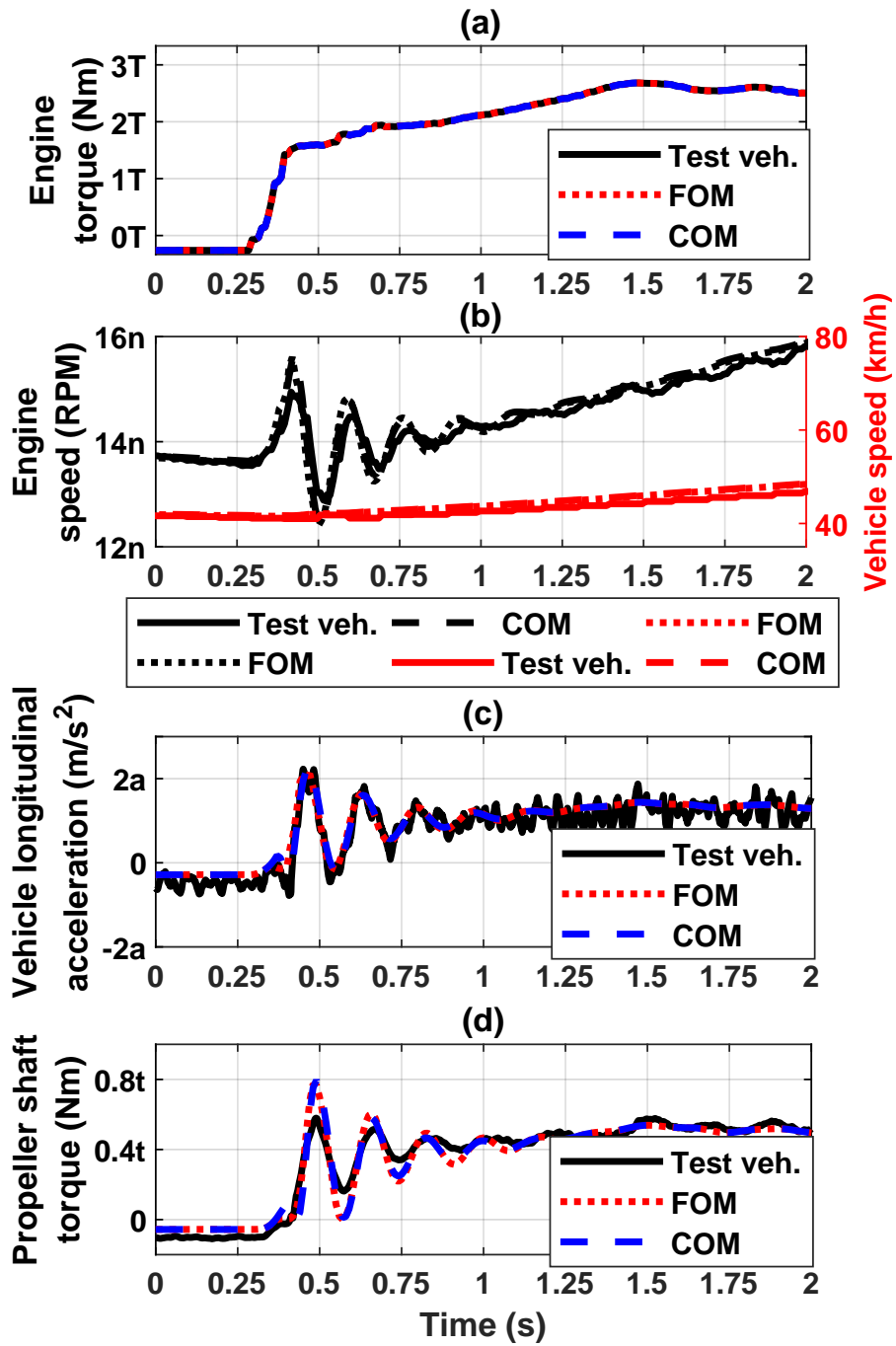


Figure 2.8: Plot showing the validation of the COM against the outputs of the FOM and the test vehicle data.

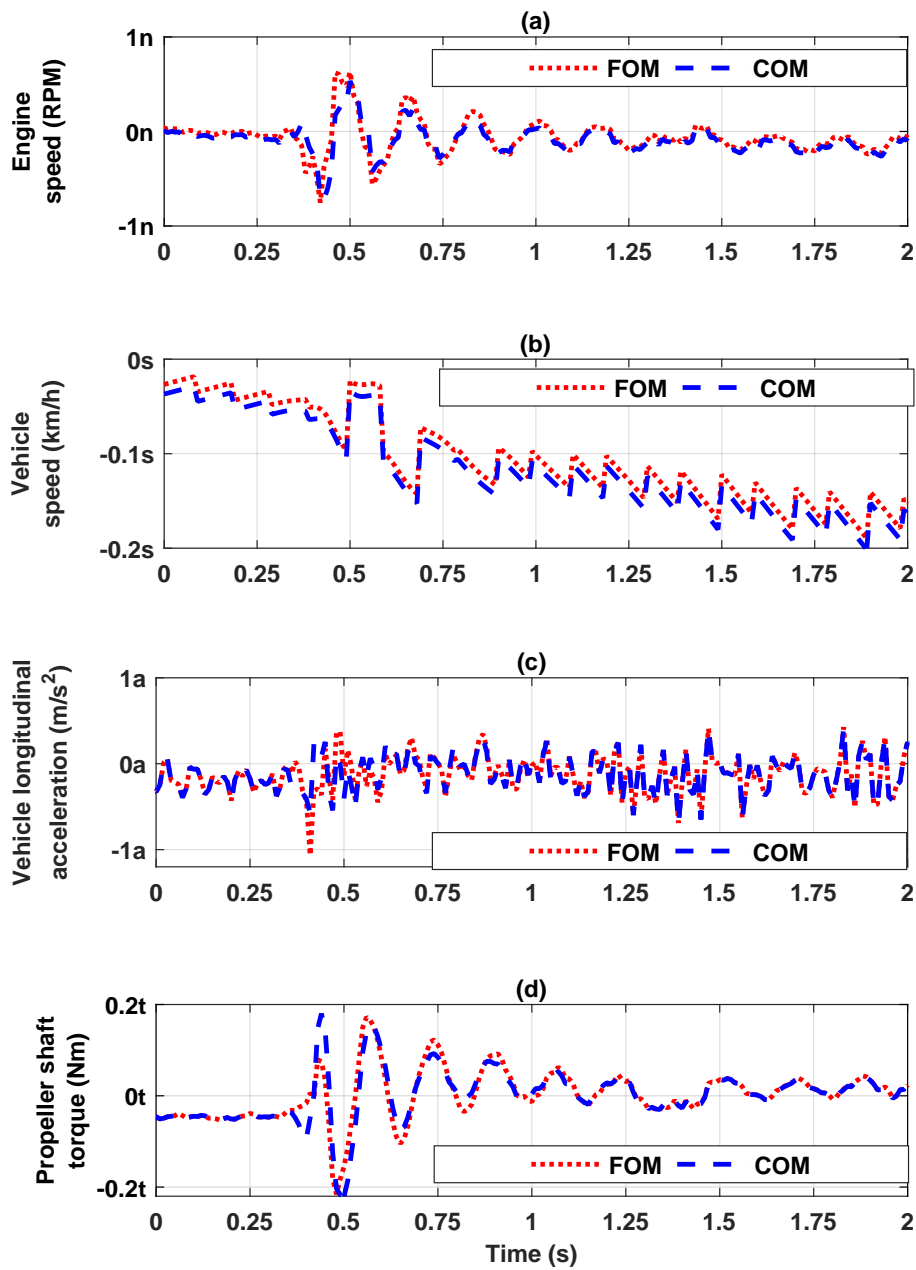


Figure 2.9: Plot showing residuals of the outputs of the FOM and ROM as compared to the measured outputs of the test vehicle, based on the results in Fig 2.8.

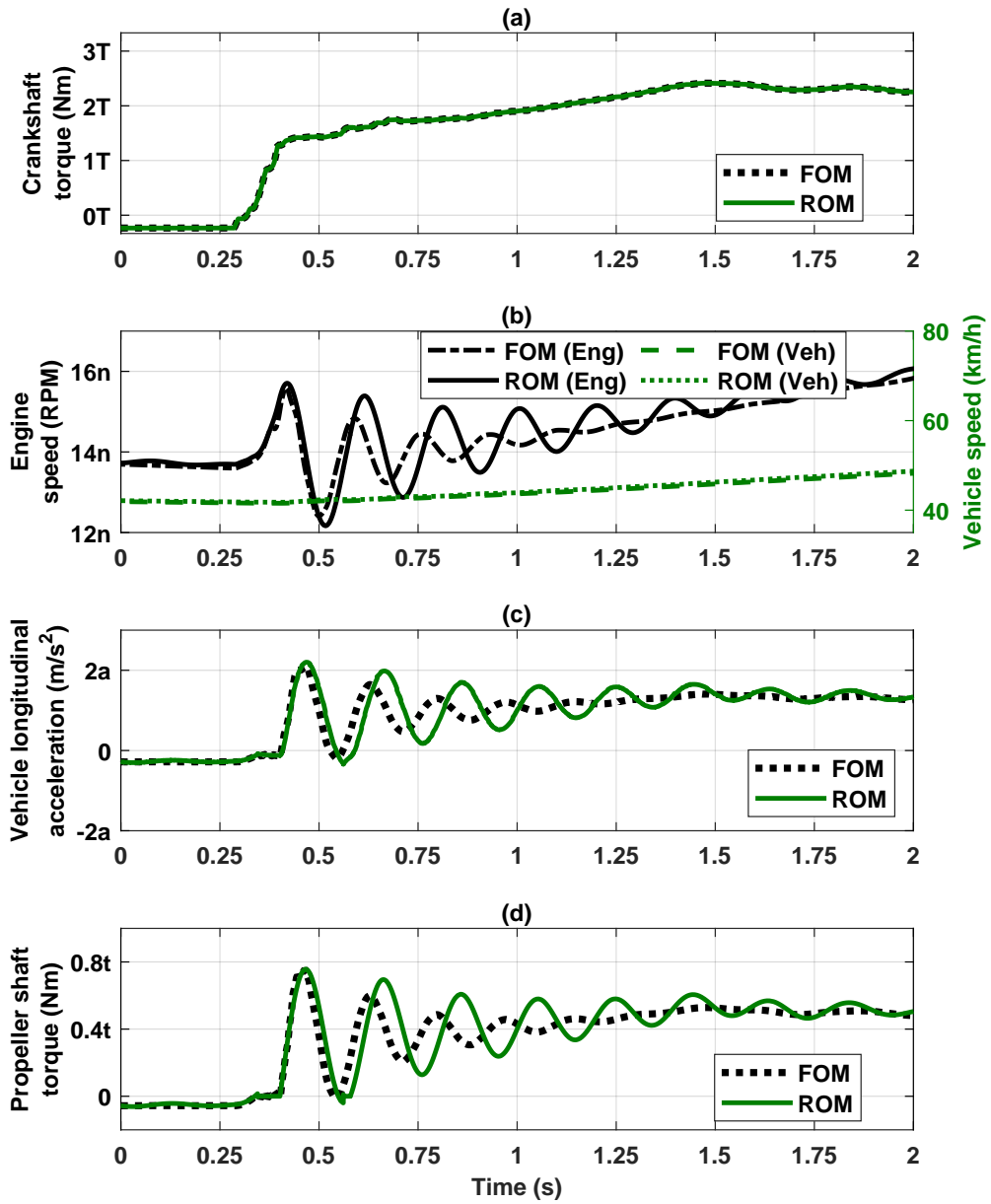


Figure 2.10: Plot showing performance of COM with lumped tire and axle inertias with the actuator inertia.

2.3.5 Step 5: Evaluation of COM for control applications

In this subsection, the dynamics of the COM of Fig. 2.7 is described as a switched linear time invariant (LTI) system, consisting of two modes. Additionally, the controllability and observability properties of each of these two modes is also investigated.

Due to the backlash nonlinearity, the dynamics of the model are categorized into two modes: (i) contact (cm) mode and (ii) backlash (bm) mode. The system is in contact mode when the gear teeth are in contact, i.e., the backlash position is either $+\gamma$ (positive contact) or $-\gamma$ (negative contact), and the entire driveline is connected without any discontinuities. On the other hand, the system is in backlash mode when the gear teeth are not in contact, i.e., the backlash position is in the range $(-\gamma, +\gamma)$, implying that the backlash traversal has started.

The switched LTI representation of the COM dynamics is given by:

$$\text{Plant : } \begin{cases} \dot{\mathbf{x}}_{\text{cm}} = \mathbf{A}_{\text{cm}}\mathbf{x}_{\text{cm}} + \mathbf{B}_{\text{cm}}\mathbf{u} + \mathbf{G}_{\text{cm}}\mathbf{d}, & \text{in cm mode,} \\ \dot{\mathbf{x}}_{\text{bm}} = \mathbf{A}_{\text{bm}}\mathbf{x}_{\text{bm}} + \mathbf{B}_{\text{bm}}\mathbf{u} + \mathbf{G}_{\text{bm}}\mathbf{d}, & \text{in bm mode,} \end{cases} \quad (2.43)$$

$$\mathbf{y} = \begin{cases} \mathbf{C}_{\mathbf{cm}}\mathbf{x}_{\mathbf{cm}}, \\ \mathbf{C}_{\mathbf{bm}}\mathbf{x}_{\mathbf{bm}}, \end{cases} \quad (2.44)$$

$$\text{Switching rule : } \begin{cases} \mathbf{cm} \text{ mode : } |\theta_b| \geq \gamma \text{ AND } \theta_b \cdot \dot{\theta}_b \geq 0, \\ \mathbf{bm} \text{ mode : } |\theta_b| < \gamma \text{ OR } (|\theta_b| = \gamma \text{ AND } \theta_b \cdot \dot{\theta}_b < 0), \end{cases} \quad (2.45)$$

where

$$\mathbf{x}_{\mathbf{cm}} = \begin{bmatrix} \left(\frac{\theta_{\text{act}}}{i_t} - \theta_{\text{fd}}i_{\text{fd}} - \theta_b\right) & \dot{\theta}_{\text{act}} & (\theta_{\text{fd}} - \theta_w) & \dot{\theta}_{\text{fd}} & \dot{\theta}_w \end{bmatrix}^T, \quad (2.46)$$

$$\mathbf{x}_{\mathbf{bm}} = \begin{bmatrix} \left(\frac{\theta_{\text{act}}}{i_t} - \theta_{\text{fd}}i_{\text{fd}}\right) & \dot{\theta}_{\text{act}} & (\theta_{\text{fd}} - \theta_w) & \dot{\theta}_{\text{fd}} & \dot{\theta}_w & \theta_b \end{bmatrix}^T, \quad (2.47)$$

$$\mathbf{y} = \begin{bmatrix} \dot{\theta}_{\text{act}} \\ \dot{\theta}_w \end{bmatrix}, \quad (2.48)$$

$$\mathbf{u} = \begin{bmatrix} T_{\text{act}} \end{bmatrix}, \quad (2.49)$$

$$\mathbf{d} = \begin{bmatrix} T_{\text{load}} \end{bmatrix}. \quad (2.50)$$

In the above equations (2.46-2.50), $\left(\frac{\theta_{\text{act}}}{i_t} - \theta_{\text{fd}}i_{\text{fd}} - \theta_b\right)$ is the twist angle on the actuator side, $\dot{\theta}_{\text{act}}$ is the angular speed of the actuator, $(\theta_{\text{fd}} - \theta_w)$ is the twist angle on the wheel side, $\dot{\theta}_{\text{fd}}$ is the angular speed of the final drive, $\dot{\theta}_w$ is the angular speed of wheel, $\left(\frac{\theta_e}{i_t} - \theta_{\text{fd}}i_{\text{fd}}\right)$ is the relative angular position of the input end of the lumped shaft with

respect to its output end, θ_b is the backlash angle, T_{act} is the engine delivered torque, and T_{load} is the road load on the vehicle. Furthermore, the A, B, C, and G matrices of eq. (2.43) and (2.44) are given by:

$$\mathbf{A}_{\text{cm}} = \begin{bmatrix} 0 & \frac{1}{i_t} & 0 & -i_{\text{fd}} & 0 \\ -\frac{k_s}{J_1 i_t} & -\frac{c_s}{J_1 i_t^2} & 0 & \frac{c_s i_{\text{fd}}}{J_1 i_t} & 0 \\ 0 & 0 & 0 & 1 & -1 \\ \frac{k_s i_{\text{fd}}}{J_2} & \frac{c_s i_{\text{fd}}}{J_2 i_t} & -\frac{k_w}{J_2} & -\frac{a}{J_2} & \frac{c_w}{J_2} \\ 0 & 0 & \frac{k_w}{b} & \frac{c_w}{b} & -\frac{c_w}{b} \end{bmatrix}, \quad (2.51)$$

$$\mathbf{A}_{\text{bm}} = \begin{bmatrix} 0 & \frac{1}{i_t} & 0 & -i_{\text{fd}} & 0 & 0 \\ 0 & 0 & 0 & 0 & 0 & 0 \\ 0 & 0 & 0 & 1 & -1 & 0 \\ 0 & 0 & -\frac{k_w}{J_2} & -\frac{c_w}{J_2} & \frac{c_w}{J_2} & 0 \\ 0 & 0 & \frac{k_w}{b} & \frac{c_w}{b} & -\frac{c_w}{b} & 0 \\ \frac{k_s}{c_s} & \frac{1}{i_t} & 0 & -i_{\text{fd}} & 0 & -\frac{k_s}{c_s} \end{bmatrix}, \quad (2.52)$$

$$\mathbf{B}_{\text{cm}} = \begin{bmatrix} 0 & \frac{1}{J_1} & 0 & 0 & 0 \end{bmatrix}^T, \quad (2.53)$$

$$\mathbf{B}_{\text{bm}} = \begin{bmatrix} 0 & \frac{1}{J_1} & 0 & 0 & 0 & 0 \end{bmatrix}^T, \quad (2.54)$$

$$\mathbf{G}_{\mathbf{cm}} = \begin{bmatrix} 0 & 0 & 0 & 0 & \frac{-r_w}{b} \end{bmatrix}^T, \quad (2.55)$$

$$\mathbf{G}_{\mathbf{bm}} = \begin{bmatrix} 0 & 0 & 0 & 0 & \frac{-r_w}{b} & 0 \end{bmatrix}^T, \quad (2.56)$$

$$\mathbf{C}_{\mathbf{cm}} = \begin{bmatrix} 0 & 1 & 0 & 0 & 0 \\ 0 & 0 & 0 & 0 & 1 \end{bmatrix}, \quad (2.57)$$

$$\mathbf{C}_{\mathbf{bm}} = \begin{bmatrix} 0 & 1 & 0 & 0 & 0 & 0 \\ 0 & 0 & 0 & 0 & 1 & 0 \end{bmatrix}, \quad (2.58)$$

where a and b are defined as:

$$a = c_s i_{\text{fd}}^2 + c_w, \quad b = J_3 + Mr_w^2.$$

2.3.5.1 Investigation of contact mode dynamics:

In cm mode, the measured actuator and wheel speeds provide sufficient information to estimate all the state variables in eq. (2.46). In other words, the pair $(\mathbf{A}_{\mathbf{cm}}, \mathbf{C}_{\mathbf{cm}})$ is observable. Furthermore, since the actuator is connected without discontinuities to the driveline and the wheels, all the state variables in eq. (2.46) can also be regulated. In other words, the pair $(\mathbf{A}_{\mathbf{cm}}, \mathbf{B}_{\mathbf{cm}})$ is controllable.

2.3.5.2 Investigation of backlash mode dynamics:

In bm mode, since the actuator is disconnected from the driveline and wheels, it is not possible to estimate and regulate all the state variables in eq. (2.47). In other words, $(A_{\text{bm}}, C_{\text{bm}})$ is not observable and $(A_{\text{bm}}, B_{\text{bm}})$ is not controllable.

To alleviate this lack of observability and controllability, the bm system is divided into two subsystems, one wherein a subset of the state variables from eq. (2.47) can be estimated and another wherein another subset from eq. (2.47) can be regulated. Specifically, in the first subsystem, the dynamics of the backlash position are ignored, which is unobservable, and in the second subsystem, the same dynamics are included, which is controllable.

Bm Subsystem 1

Consider the following subsystem:

$$\mathbf{x}_{\text{bm},1} = \begin{bmatrix} \dot{\theta}_{\text{act}} & (\theta_{\text{fd}} - \theta_{\text{w}}) & \dot{\theta}_{\text{fd}} & \dot{\theta}_{\text{w}} \end{bmatrix}, \quad (2.59)$$

$$\mathbf{A}_{\text{bm},1} = \begin{bmatrix} 0 & 0 & 0 & 0 \\ 0 & 0 & 1 & -1 \\ 0 & \frac{-k_w}{J_2} & \frac{-c_w}{J_2} & \frac{c_w}{J_2} \\ 0 & \frac{k_w}{b} & \frac{c_w}{b} & \frac{-c_w}{b} \end{bmatrix}, \quad (2.60)$$

$$\mathbf{B}_{\text{bm},1} = \begin{bmatrix} \frac{1}{J_1} & 0 & 0 & 0 \end{bmatrix}^\top, \quad (2.61)$$

$$\mathbf{G}_{\text{bm},1} = \begin{bmatrix} 0 & 0 & 0 & \frac{-r_w}{b} \end{bmatrix}^\top, \quad (2.62)$$

$$\mathbf{C}_{\text{bm},1} = \begin{bmatrix} 1 & 0 & 0 & 0 \\ 0 & 0 & 0 & 1 \end{bmatrix}. \quad (2.63)$$

Clearly, $(\mathbf{A}_{\text{bm},1}, \mathbf{C}_{\text{bm},1})$ is observable.

Bm Subsystem 2

Since the ratio $\frac{k_s}{c_s}$ is large, the engine side twist angle, $(\frac{\theta_{\text{act}}}{i_t} - \theta_{\text{fd}}i_{\text{fd}} - \theta_b)$, will settle rapidly to 0. This phenomenon takes place due to the following dynamics in the bm mode:

$$\left(\frac{\dot{\theta}_{\text{act}}}{i_t} - \dot{\theta}_{\text{fd}}i_{\text{fd}} - \dot{\theta}_b\right) = -\frac{k_s}{c_s}\left(\frac{\theta_{\text{act}}}{i_t} - \theta_{\text{fd}}i_{\text{fd}} - \theta_b\right). \quad (2.64)$$

Consequently, the backlash velocity can be approximated as:

$$\dot{\theta}_b \approx \left(\frac{\dot{\theta}_{\text{act}}}{i_t} - \dot{\theta}_{\text{fd}}i_{\text{fd}}\right). \quad (2.65)$$

Furthermore, since the inertia J_2 is small and the ratio $\frac{k_w}{c_w}$ is large, the final drive velocity $\dot{\theta}_{fd}$ can be approximated as:

$$\dot{\theta}_{fd} \approx \dot{\theta}_w. \quad (2.66)$$

Finally, since the inertia J_3 is large and the time spent in bm mode is small, the wheel velocity during lash traversal can be assumed constant, i.e.,

$$\ddot{\theta}_w \approx 0. \quad (2.67)$$

Under these approximations (eq. (2.65)-(2.67)), the dynamics of the second bm mode subsystem can be expressed in terms of the following double-integrator plant:

$$\mathbf{x}_{bm,2} = \left[\theta_b \quad \left(\frac{\dot{\theta}_{act}}{i_t} - \dot{\theta}_{fd} i_{fd} \right) \right]^T, \quad (2.68)$$

$$\mathbf{A}_{bm,2} = \begin{bmatrix} 0 & 1 \\ 0 & 0 \end{bmatrix}, \quad (2.69)$$

$$\mathbf{B}_{bm,2} = \begin{bmatrix} 0 & \frac{1}{J_1 i_t} \end{bmatrix}^T, \quad (2.70)$$

$$\mathbf{G}_{bm,2} = \begin{bmatrix} 0 & \frac{-r_w i_{fd}}{b} \end{bmatrix}^T, \quad (2.71)$$

$$\mathbf{C}_{bm,2} = \begin{bmatrix} 0 & 1 \end{bmatrix}. \quad (2.72)$$

Clearly, the pair $(A_{\text{bm},2}, B_{\text{bm},2})$ is controllable.

The backlash position, θ_b , cannot be ascertained using the measured engine and wheel speeds alone, since it is not possible to determine the initial position of the engine crankshaft using the speed signal. Therefore, in bm mode, the initial value of θ_b is assigned using the delivered engine torque as:

$$\theta_b(k_{\text{lash enter}}) = \begin{cases} -\gamma, & \text{if } T_{\text{act}}(k_{\text{ti,to}}) < 0, \\ +\gamma, & \text{if } T_{\text{act}}(k_{\text{ti,to}}) > 0, k_{\text{lash enter}} > k_{\text{ti,to}} \end{cases} \quad (2.73)$$

where $k_{\text{lash enter}}$ is the time corresponding to lash entry and $k_{\text{ti,to}}$ is the time at which the tip-in/tip-out began. Further, the future values of θ_b can be predicted using the dynamics (see eq. (2.65) and (2.68)-(2.72)):

$$\hat{\theta}_b(k+1) = \hat{\theta}_b(k) + T_s \left[\frac{\dot{\theta}_{\text{act}}(k)}{i_t} - \dot{\theta}_{\text{fd}}(k) i_{\text{fd}} \right], \quad k = k_{\text{lash enter}}, k_{\text{lash enter}} + 1, k_{\text{lash enter}} + 2, \dots, \quad (2.74)$$

where T_s is the fixed-step discrete time interval. Thus, the pair $(A_{\text{bm},2}, C_{\text{bm},2})$ is predictable. The above investigations into controllability, observability, and predictability are summarized in Table 2.1.

Recall that the switching rule (eq. (2.45)) involves conditions on θ_b and $\dot{\theta}_b$. As described above, both θ_b and $\dot{\theta}_b$ are predictable in bm mode. In cm mode, θ_b

Table 2.1

Summary of evaluations on COM for shuffle and clunk control.

Mode	Pairs	Controllable	Observable	Predictable
cm mode	$(\mathbf{A}_{\text{cm}}, \mathbf{B}_{\text{cm}})$	Yes	-	-
	$(\mathbf{A}_{\text{cm}}, \mathbf{C}_{\text{cm}})$	-	Yes	-
bm mode	$(\mathbf{A}_{\text{bm},1}, \mathbf{B}_{\text{bm},1})$	No	-	-
	$(\mathbf{A}_{\text{bm},1}, \mathbf{C}_{\text{bm},1})$	-	Yes	-
	$(\mathbf{A}_{\text{bm},2}, \mathbf{B}_{\text{bm},2})$	Yes	-	-
	$(\mathbf{A}_{\text{bm},2}, \mathbf{C}_{\text{bm},2})$	-	No	Yes

can be predicted using the engine torque, similar to eq. (2.73). Moreover, $\dot{\theta}_b$ can also be predicted using the dynamics of states $\mathbf{x}_{\text{cm}}(1)$, $\mathbf{x}_{\text{cm}}(2)$, and $\mathbf{x}_{\text{cm}}(4)$ (see eqs. (2.51),(3.11), and (2.55)). Thus, the switching between cm mode and bm mode, and vice versa, is predictable as well.

Chapter 3

Design and validation of backlash position and size estimation algorithms¹

3.1 Development, validation and robustness analyses of backlash position estimator

As evident from the driveline models in Chapter 2, the driveline exhibits different dynamics depending on whether it is in contact mode or backlash mode. Therefore,

¹Contents of this chapter first appeared in [5, 6, 7]. Letter of permission to republish from IEEE is available in Appendix C.

the availability of accurate backlash position information, consequently providing information about driveline mode, has a significant impact on the effectiveness of a driveline torque shaping clunk and shuffle controller. Calculation of the backlash position is dependent on the relative angular positions of the actuator and the wheel. It is not straightforward to calculate the backlash position because it is difficult to obtain accurate angular position information for an IC engine. Therefore, an estimation algorithm provides a reasonable solution for obtaining the backlash position information. Historically, heuristic algorithms have been used for predicting the backlash position in automotive drivelines, and these approaches are, generally, calibration intensive. Development of model-based algorithms for estimating the backlash position has the potential to provide comparatively more accurate estimates within shorter development times.

3.1.1 Design of backlash position estimator

In this section, a switching backlash position estimator is developed that uses the delivered actuator torque as the control input, and the actuator and wheel speeds as the measured variables. These three signals are typically available on the vehicle CAN bus. Due to the presence of estimation uncertainties in the ECU, sensor noise, CAN arbitration delays, and quantization errors, these three signals are generally imperfect. In order to obtain a relatively accurate estimate using these imperfect

signals, a discrete, time-varying Kalman filter approach is chosen for designing the switching estimator. Moreover, choosing a time-varying Kalman filter allows the designed estimator to perform well in the presence of time-varying delays, which could occur due to CAN arbitration in the measured signals. Since the dynamics of the driveline are split into contact and backlash modes, two estimation schemes are developed; one for the contact mode using contact mode dynamics (Eq. 2.51), and one for the backlash mode using backlash mode dynamics (Eq. 2.52). A switching rule for these estimation schemes is developed based on the estimated backlash position and the estimated backlash traversal speed. The prediction and measurement update equations used for the discrete, time-varying Kalman filter are given by:

Prediction update

$$\begin{aligned}\hat{\mathbf{x}}_{\psi[k+1|k]} &= \mathbf{A}_{\psi}\hat{\mathbf{x}}_{\psi[k|k]} + \mathbf{B}_{\psi}\mathbf{u}_{\psi[k]}, \\ \mathbf{P}_{\psi[k+1|k]} &= \mathbf{A}_{\psi}\mathbf{P}_{\psi[k|k]}\mathbf{A}_{\psi}^{\mathbf{T}} + \mathbf{Q}.\end{aligned}\tag{3.1}$$

Measurement update

$$\begin{aligned}\hat{\mathbf{x}}_{\psi[k+1|k+1]} &= \hat{\mathbf{x}}_{\psi[k+1|k]} + \mathbf{K}_{\psi[k+1]}(\mathbf{y}_{\psi[k+1]} - \mathbf{C}_{\psi}\hat{\mathbf{x}}_{\psi[k+1|k]}), \\ \mathbf{K}_{\psi[k+1]} &= \mathbf{P}_{\psi[k+1|k]}\mathbf{C}_{\psi}^{\mathbf{T}}(\mathbf{R} + \mathbf{C}_{\psi}\mathbf{P}_{\psi[k+1|k]}\mathbf{C}_{\psi}^{\mathbf{T}})^{-1}, \\ \mathbf{P}_{\psi[k+1|k+1]} &= (\mathbf{I} - \mathbf{K}_{\psi[k+1]}\mathbf{C}_{\psi})\mathbf{P}_{\psi[k+1|k]}.\end{aligned}\tag{3.2}$$

where ψ refers to either ‘cm’ (i.e. contact mode) or ‘bm’ (i.e. backlash mode), \mathbf{A} ,

\mathbf{B} , \mathbf{C} are the respective state-space matrices of the driveline, \mathbf{u} and \mathbf{y} are the input and output vectors, $\hat{\mathbf{x}}$ is the estimated state vector, \mathbf{K} is the time-varying Kalman gain matrix, \mathbf{P} is the error covariance matrix, \mathbf{Q} is the process noise covariance matrix which is obtained through recursive tuning and analysis of the performance of the designed estimator, and \mathbf{R} is the measurement noise covariance matrix which is obtained based on the performance specification of the speed sensors on the vehicle.

3.1.2 Contact and backlash mode estimator

From Chapter 2, it is known that the contact mode has full observability. Therefore, the states, \mathbf{x} , in the contact mode are estimated using both prediction and measurement updates (Eq. 3.1 - 3.2). However, as discussed in Chapter 2, the backlash mode is not completely observable and, consequently, the Kalman filter approach cannot be directly applied in this mode. Therefore, the unobservable states in backlash mode, i.e., the actuator-side twist angle and the backlash position, are estimated using only prediction update (Eq. 3.1). The observable states, i.e., the angular speed of the actuator, the wheel-side twist angle, the angular speed of final drive and the angular speed of wheel, are estimated using both prediction and measurement update (Eq. 3.1 - 3.2). After estimation, the observable and unobservable states are augmented to obtain the estimated state vector, $\hat{\mathbf{x}}$, in the backlash mode. Fig. 3.1 illustrates how each of the states in contact and backlash

mode is estimated.

The transition between the contact mode and the backlash mode estimation algorithms takes place based on a set of conditions:

Cm activation condition:=

$$\{ |(\hat{\theta}_b)_{[t|t-1]}| \geq \gamma \} \text{ AND } \{ (\hat{\theta}_b)_{[t|t-1]}(\dot{\hat{\theta}}_b)_{[t|t-1]} \geq \text{Threshold value} \} \quad (3.3)$$

Bm activation condition:=

$$\{ |(\hat{\theta}_b)_{[t|t-1]}| < \gamma \} \text{ OR } \{ (\hat{\theta}_b)_{[t|t-1]}(\dot{\hat{\theta}}_b)_{[t|t-1]} < \text{Threshold value} \} \quad (3.4)$$

In both Eq. 3.3 and 3.4, $\hat{\theta}_b$, $\dot{\hat{\theta}}_b$ and γ represent the estimated backlash position, the estimated backlash traversal speed and known backlash size respectively. It is worth noting that the backlash position is only updated when the backlash mode estimator is active. When the contact mode estimator is active, the backlash position is not updated, and is only used for determining the transition conditions of the estimator. Fig. 3.2 shows a schematic of the switching backlash position estimator along with its inputs and outputs. It is assumed that the driveline has some positive torque (e.g., creep torque) at the instant the switching estimator is turned on and, therefore, the estimation is initiated in the positive contact mode. Furthermore, the estimator runs on a discrete solver with 10 ms sample time, as indicated by T_s in Fig. 3.2.

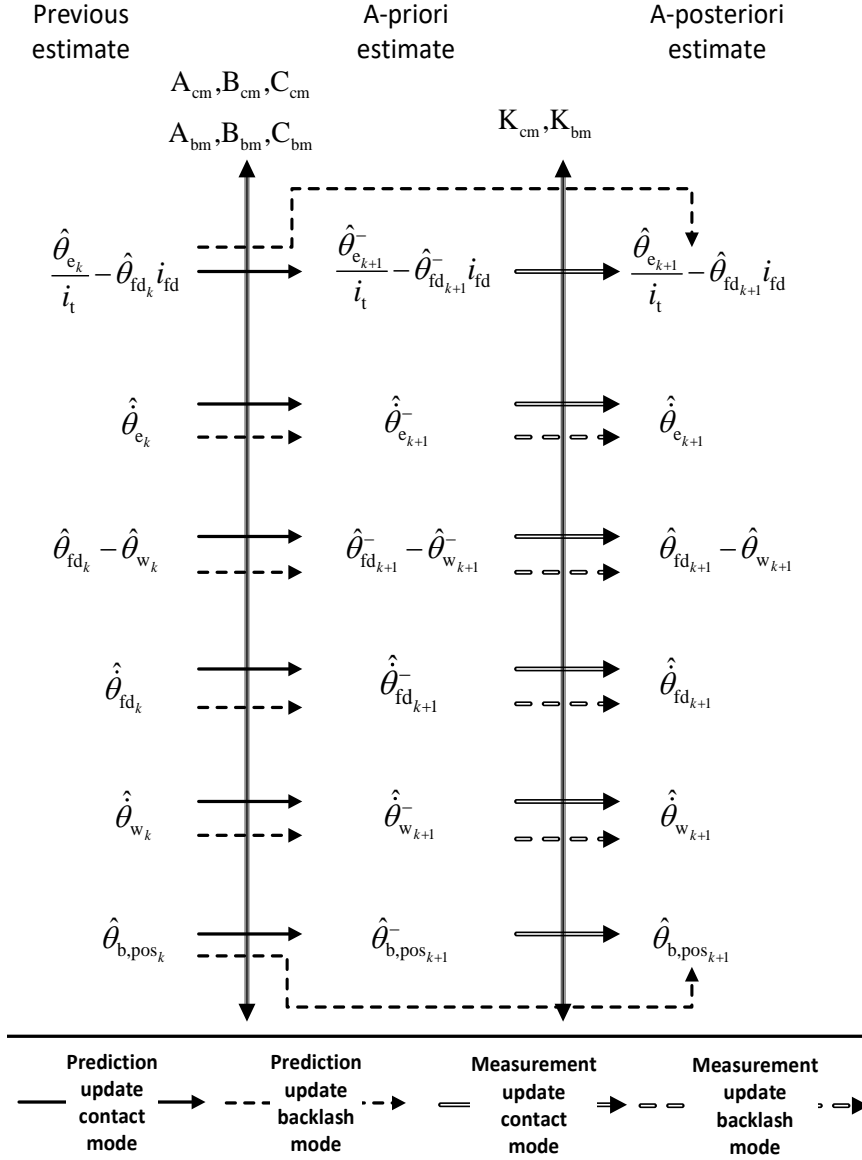


Figure 3.1: Estimated and predicted states of the switching backlash position estimator for contact and backlash mode

3.1.3 Validation of backlash position estimator

The backlash position estimator is validated using both model-in-the-loop (MIL) tests and experimental data collected from a test vehicle.

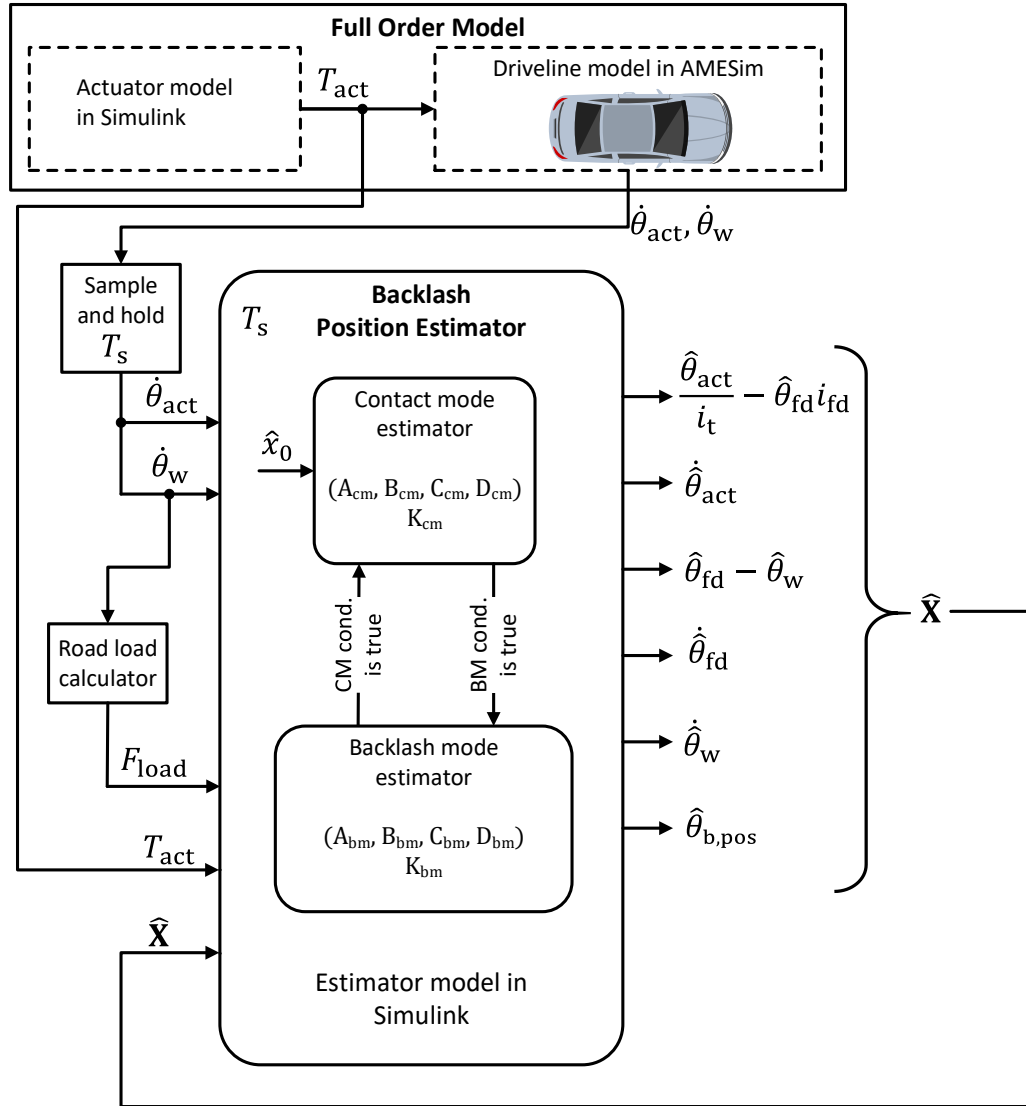


Figure 3.2: Schematic of the switching backlash position estimator

3.1.3.1 Using MIL tests

The developed backlash position estimator is evaluated for a torque input representing a tip-in from coasting scenario. The FOM from Chapter 2 is used as the high-fidelity plant model for this evaluation. The response of the driveline and the

performance of the backlash position estimator is shown in Fig. 3.3. In this figure, the estimated engine and wheel speed signals show good agreement with the FOM engine and wheel speed signals, with an average error of less than 0.1%. Therefore, the lash traversal estimated by the switching estimator also matches well with the lash traversal in the plant model. There is a 10 ms time delay in the instant at which the estimated backlash position reaches positive contact, which is due to the 10 ms sampling time of the discrete solver used in the simulation. Note that the labels on the Y-axis of all result plots in this chapter have been modified to alphanumeric representation (e.g., 2T, 15N, 1b etc.) to keep vehicle parameters confidential. ‘T’ represents T units of torque in Nm, ‘N’ represents N units of angular speed in RPM, and ‘b’ represents b units of angular position in degrees.

3.1.3.2 Using test vehicle data

The performance of the switching estimator using experimental test data is shown in Fig. 3.4. The estimated engine and wheel speeds are compared against the measured speeds, and they show a good match in both amplitude and frequency of the signals with an average error of less than 0.1%. Since it is not possible to directly measure the traversal of lash on the vehicle, the estimated backlash position is evaluated against the behavior of the measured propeller shaft torque in Fig. 3.4 (d). During lash traversal, since the driveline is disconnected, the propeller shaft torque is expected to

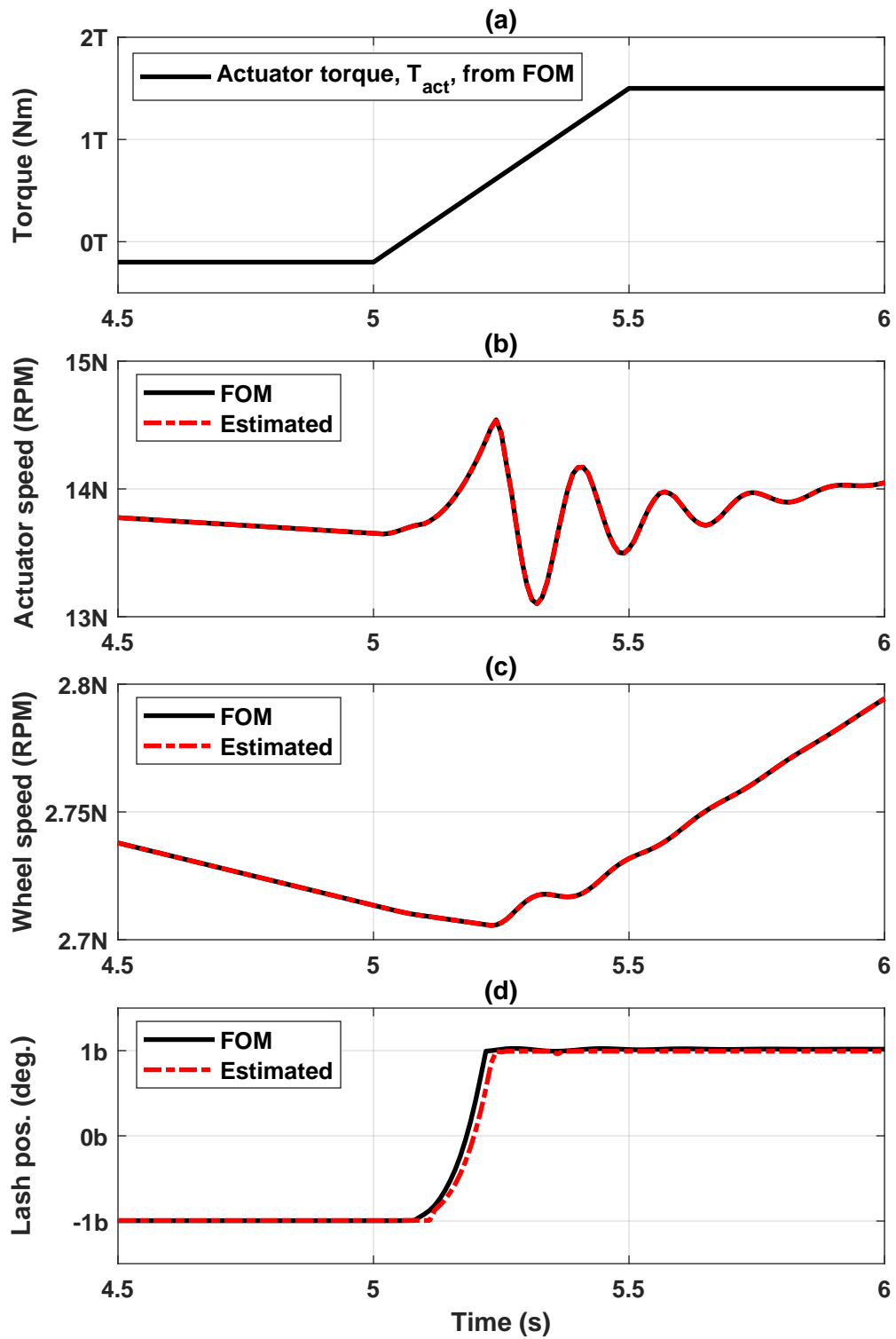


Figure 3.3: Plot showing performance of backlash position estimator in simulations.

take a constant value of 0 (or close to 0, due to measurement bias). As seen in the zoomed inset of Fig. 3.4 (d), the behavior of the shaft torque during lash traversal agrees with this expectation. As part of the evaluation dotted vertical lines are also included, which represent the start and end of the lash traversal reported by the estimator. It is observed that when compared against the shaft torque signal, the estimator predicts the start of the lash traversal correctly, but it predicts the end of the traversal with a 20 ms delay. This delay may be attributed to the error in the ECU-estimated engine torque used as the input of the estimator and CAN delays in the measured engine and wheel speed.

3.1.4 Robustness analysis of backlash position estimator

3.1.4.1 To CAN jitter in speed measurements

Message arbitration in CAN bus can sometimes cause the actuator speed and wheel speed signals to exhibit jitter behavior [28]. In this subsection, an approximate model of the jitter is developed using vehicle data, and the robustness of the backlash position estimator is evaluated for this jitter.

The CAN jitter manifests as delays and advances in the measured actuator and wheel speeds in relation to the sample time of the estimator. These delays and advances

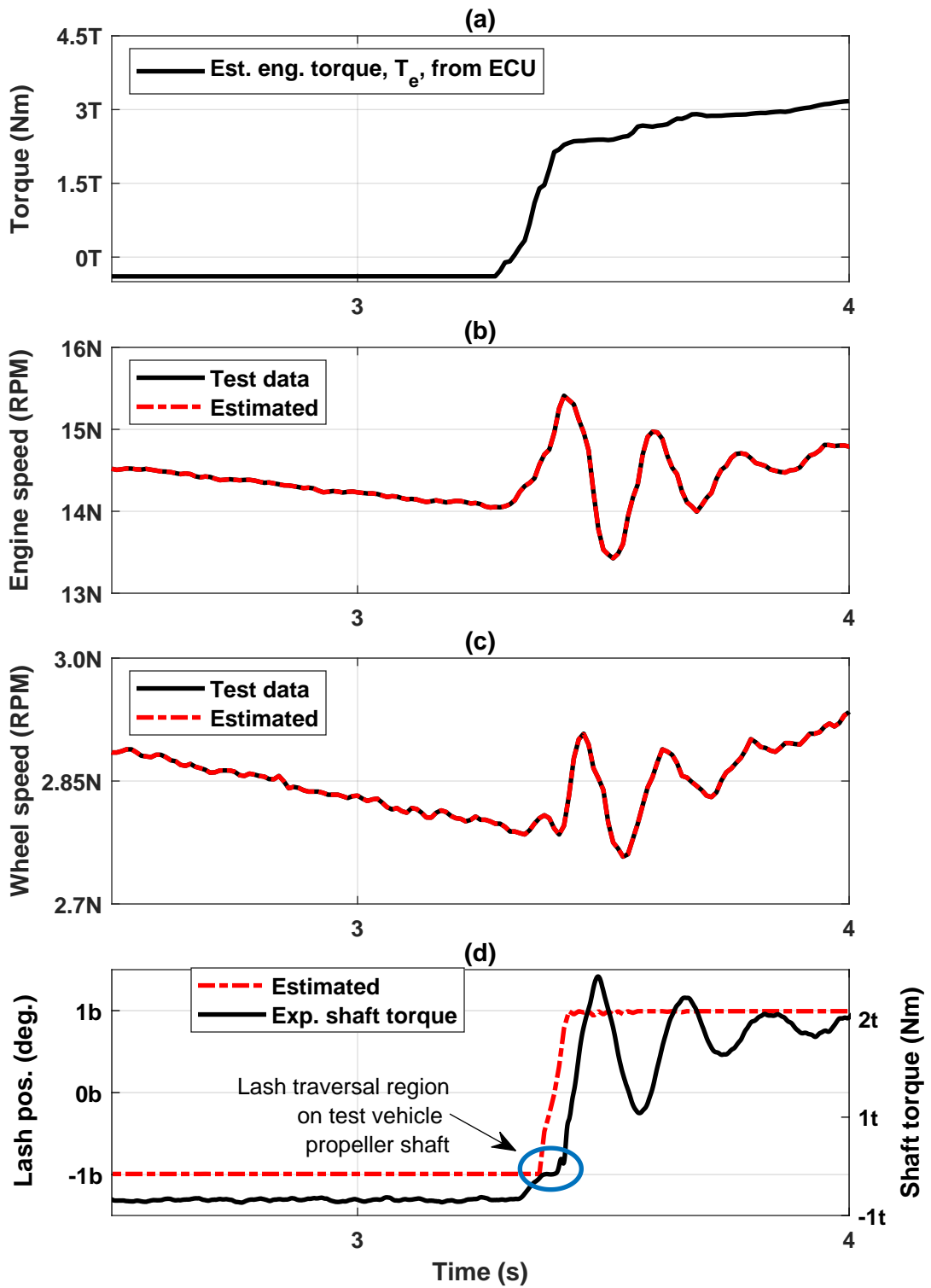


Figure 3.4: Plot showing performance of backlash position estimator with experimental vehicle data.

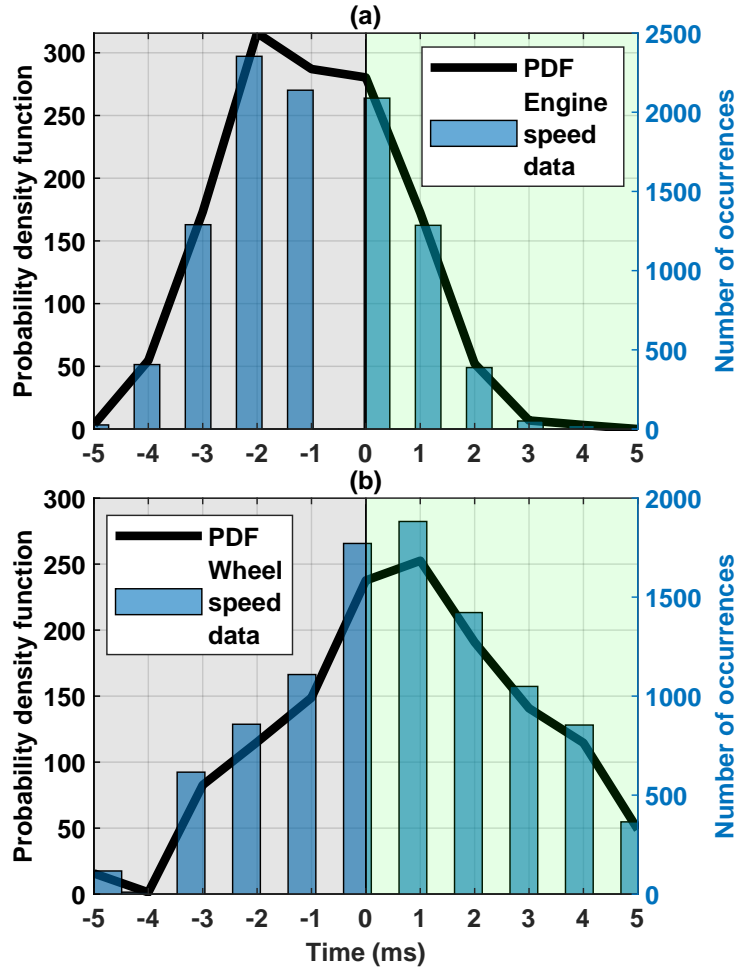


Figure 3.5: Probability density function and number of occurrences of CAN jitter in (a) engine speed and (b) wheel speed for an interval of -5 to 5 ms, using data collected from a test vehicle

are modeled as random variables, and their probability density functions (PDFs) are approximated using the CAN speed signals and illustrated in Fig. 3.5. The PDFs of the jitter are categorized into signal advance zone, where the measurement is received before the sample time and signal delay zone, where the measurements are received after the sample time. To evaluate the robustness, the FOM is utilized and this random jitter (whose delays and advances are generated based on the obtained PDFs) is injected in

the FOM's actuator speed and wheel speed signals. For the purpose of illustration, the effect of the jitter on the actuator speed is shown in an inset plot in Fig. 3.6. As indicated in this figure, the effect of the jitter is that certain actuator speed samples are missed by, i.e., not reported to, the estimator. Specifically, the estimator misses a speed sample when, due to the jitter, a consecutive delay and advance take place in between two samples of the estimator. In this scenario, the initial delayed speed sample is missed by the estimator.

The performance of the developed estimator with jitter injected in the measured engine and wheel speeds is shown in Fig. 3.6. A torque input representing a tip-in from coasting scenario is used in this analysis. The estimated engine and wheel speed signals show a good match with the jitter injected signals obtained from the FOM. Therefore, the estimated backlash position also shows good agreement with the backlash position obtained from the FOM. There is a 10 ms time delay in the instant at which the estimated lash position reaches positive contact, which is similar to the case when simulation data is used for testing the estimator. Therefore, the estimator performs well in the presence of CAN jitter in measured engine and wheel speed signals. This good performance can be partially attributed to the right selection of the process noise co-variance matrix, \mathbf{Q} , of the estimator which is already tuned to deal with such uncertainties. It is worth noting that the test vehicle dataset used in this analysis is from another test vehicle of same vehicle type that was used for experimental validation of the backlash position estimator. This demonstrates that

the performance of the estimator remains accurate without any additional tuning.

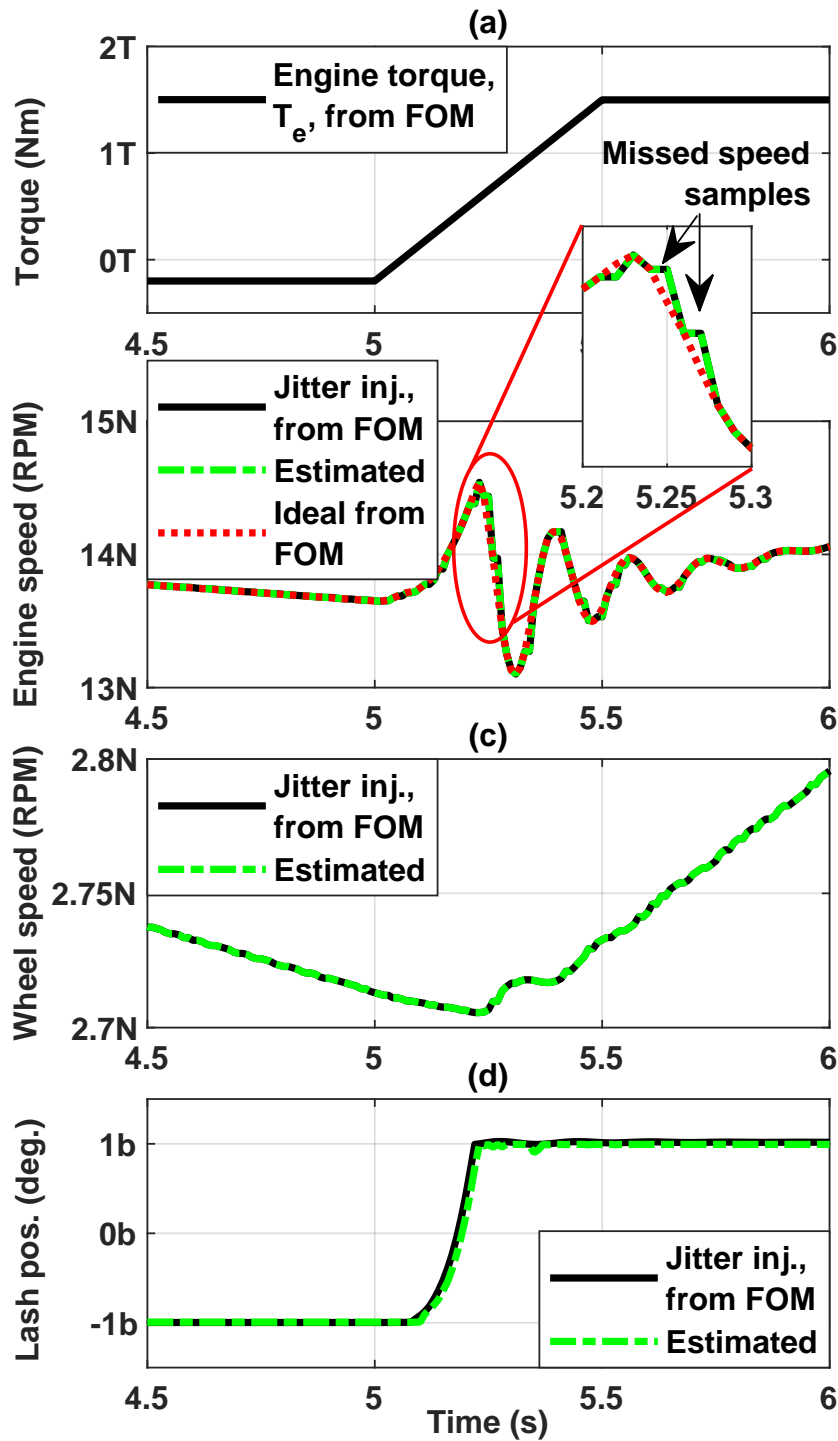


Figure 3.6: Plot showing performance of backlash position estimator with CAN jitter injected into engine and wheel speed signals obtained from FOM.

3.2 Development, validation and robustness analyses of backlash size estimator

The size of the backlash is defined as the angular displacement between mating gear tooth faces, which come into contact during torque delivery. This size parameter varies from vehicle-to-vehicle due to manufacturing tolerances of the drivetrain components and wear caused during regular operation. In fact, the backlash size may increase by as much as 80% - 100% over the lifetime of the vehicle. Manually measuring this increase as the vehicle ages is impractical. Alternatively, ignoring this increase causes the performance of the torque shaping controller to degrade (as indicated by the increase in clunk and shuffle) as the vehicle ages. To mitigate this degradation, control engineers may include adaptive schemes that modify the controller calibrations as a function of vehicle mileage. However, this option may not be effective because the variation in backlash size is unique to each vehicle's operating conditions. Therefore, in order to maintain the efficacy of the torque shaping control system, it is necessary to develop algorithms that automatically estimate and update the size of the backlash in real-time. The development of the backlash size estimator starts with developing the reduced-order model required for building the model-based estimator.

3.2.1 Switching-free state space representation of COM

For developing the backlash size estimator, switching between the backlash and contact mode dynamics of the driveline (as seen in the backlash position estimator) is no longer required. The COM of Eq. (2.35) - (2.41) is used as the state space model, while ignoring the switching dynamics associated with the traversal of the backlash. When these switching dynamics are ignored, and the model outputs and measured outputs are compared, a clear difference in these outputs is observed. This difference is used to estimate the size of the backlash. Accordingly, the lash size is included as one of the states in the switching-free state space representation, i.e.,

$$\dot{\mathbf{x}} = \mathbf{A}\mathbf{x} + \mathbf{B}\mathbf{u}, \quad (3.5)$$

$$\mathbf{y} = \mathbf{C}\mathbf{x} + \mathbf{D}\mathbf{u}, \quad (3.6)$$

where

$$\mathbf{x} = \left[\frac{\theta_{\text{act}}}{i_t} - \theta_{\text{fd}} i_{\text{fd}} \quad \dot{\theta}_{\text{act}} \quad \theta_{\text{fd}} - \theta_{\text{w}} \quad \dot{\theta}_{\text{fd}} \quad \dot{\theta}_{\text{w}} \quad \theta_{\text{b,size}} \right]^T, \quad (3.7)$$

$$\mathbf{u} = \left[T_{\text{act}} \quad T_{\text{load}} \right]^T, \quad (3.8)$$

$$\mathbf{y} = \left[\dot{\theta}_{\text{act}} \quad \dot{\theta}_{\text{w}} \right]^T, \quad (3.9)$$

$\mathbf{A} =$

$$\begin{bmatrix} 0 & \frac{1}{i_t} & 0 & -i_{fd} & 0 & 0 \\ -\frac{k_s}{J_1 \dot{i}_t} & -\frac{c_s}{J_1 \dot{i}_t^2} & 0 & \frac{c_s \dot{i}_{fd}}{J_1 \dot{i}_t} & 0 & \frac{k_s}{J_1 \dot{i}_t} \\ 0 & 0 & 0 & 1 & -1 & 0 \\ \frac{k_s \dot{i}_{fd}}{J_2} & \frac{c_s \dot{i}_{fd}}{J_2 \dot{i}_t} & -\frac{k_w}{J_2} & -\frac{a}{J_2} & \frac{c_w}{J_2} & -\frac{k_s \dot{i}_{fd}}{J_2} \\ 0 & 0 & \frac{k_w}{b} & \frac{c_w}{b} & -\frac{c_w}{b} & 0 \\ 0 & 0 & 0 & 0 & 0 & 0 \end{bmatrix}, \quad (3.10)$$

$$\mathbf{B} = \begin{bmatrix} 0 & \frac{1}{J_1} & 0 & 0 & 0 & 0 \\ 0 & 0 & 0 & 0 & \frac{-1}{b} & 0 \end{bmatrix}^T, \quad (3.11)$$

$$\mathbf{C} = \begin{bmatrix} 0 & 1 & 0 & 0 & 0 & 0 \\ 0 & 0 & 0 & 0 & 1 & 0 \end{bmatrix}, \quad (3.12)$$

$$\mathbf{D} = 0. \quad (3.13)$$

The a and b involved in Eq. (3.10) and (3.11) represent:

$$a = c_s i_{fd}^2 + c_w, \quad b = J_3 + m r_t^2,$$

where m is the vehicle mass, r_t is the tire radius, and c_s , c_w , J_3 , and i_{fd} are the same parameters described in Section II. The state variables in Eq. (3.7) are the actuator-side twist angle, $\frac{\theta_{act}}{i_t} - \theta_{fd} i_{fd}$, the actuator speed, $\dot{\theta}_{act}$, the wheel-side twist angle,

$\theta_{\text{fd}} - \theta_{\text{w}}$, the final drive speed, $\dot{\theta}_{\text{fd}}$, the wheel speed, $\dot{\theta}_{\text{w}}$, and the size of the backlash, $\theta_{\text{b,size}}$. The inputs to the state-space model in Eq. (3.8) are the actuator torque, T_{act} , and the road load torque, T_{load} .

3.2.2 Estimator development

The assumption made about the state space being switching-free would lead to differences (errors) in the measured and estimated speed signals, and consequently, to errors in the estimated twist angles, i.e.,:

$$\frac{\theta_{\text{act,meas}}}{i_{\text{t}}} - \theta_{\text{fd,meas}} i_{\text{fd}} = \frac{\hat{\theta}_{\text{act}}}{i_{\text{t}}} - \hat{\theta}_{\text{fd}} i_{\text{fd}} + e_1, \quad (3.14)$$

$$\theta_{\text{fd,meas}} - \theta_{\text{w,meas}} = \hat{\theta}_{\text{fd}} - \hat{\theta}_{\text{w}} + e_2, \quad (3.15)$$

where the subscript ‘meas’ represents measured variables and e_1 and e_2 represent errors in the estimated actuator-side and wheel-side twist angles, respectively. The (\mathbf{A}, \mathbf{C}) pair (see Eq. 3.10 and 3.12) of the state-space model is observable, which allows the estimator to attribute the errors e_1 and e_2 to the size of the backlash.

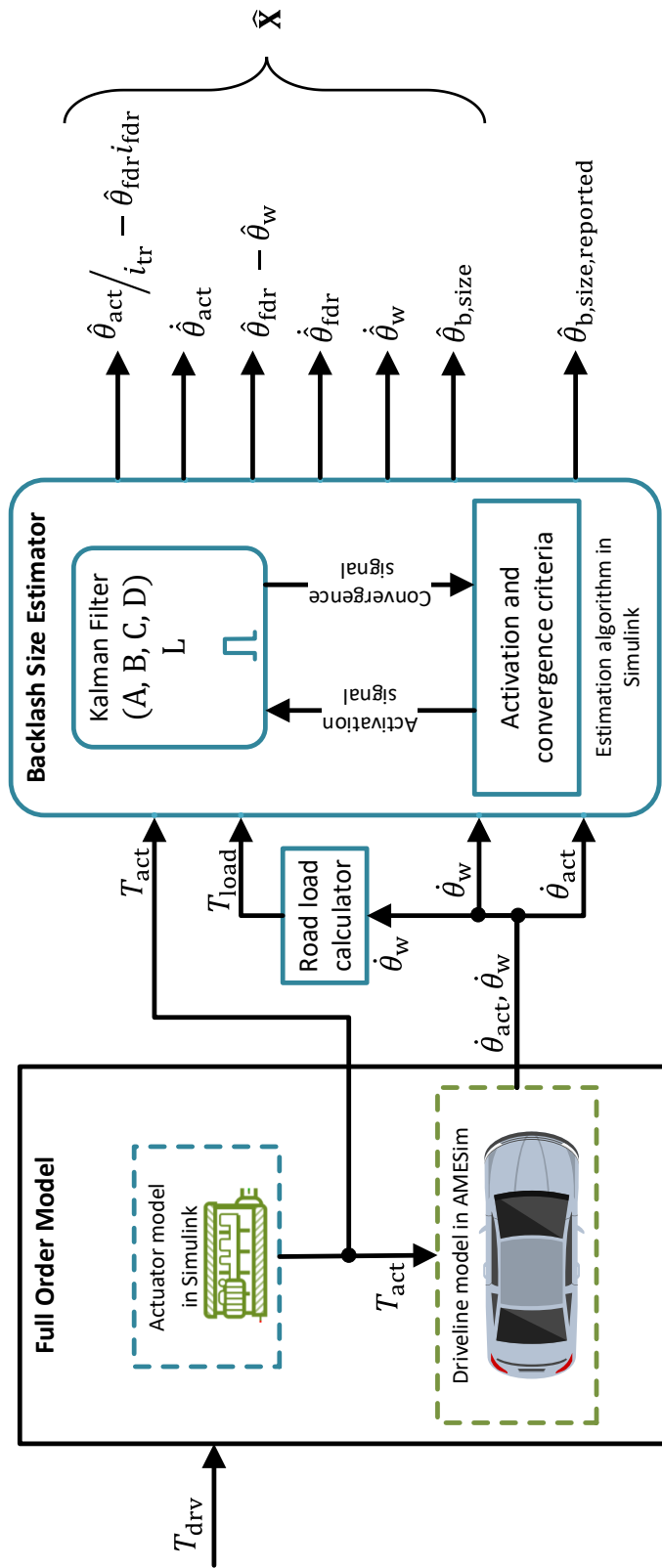


Figure 3.7: Schematic of the developed backlash size estimator. In this figure, T_{drv} represents the driver requested torque, and the remaining symbols are as defined in the text.

The backlash size estimator (see Fig. 3.7) is designed as a Kalman filter, whose operation is governed by the following sequence of steps: 1) activation, 2) estimation, and 3) steady-state convergence. These three steps involved in the backlash size estimator calculations are described below and summarized in Algorithm 1.

3.2.2.1 Activation

For simplicity, an activation criterion is considered that accounts for tip-in from coasting maneuvers. Specifically, let $T_{\text{act,init}}$ be the initial value of the actuator torque, which is latched onto at the time of the tip-in, i.e.,

$$T_{\text{act,init}} = T_{\text{act}}(t_{\text{init}}), \quad (3.16)$$

where the time t_{init} is characterized by

$$\dot{T}_{\text{act}}(t_{\text{init}}) > C_1, \quad (3.17)$$

where C_1 is a calibration threshold. Then, using the above $T_{\text{act,init}}$, the estimator activation criteria can be defined as:

$$\begin{aligned} &T_{\text{act,init}} < 0 \text{ AND } T_{\text{act}}(t) > 0 \text{ AND} \\ &\text{Convergence criteria not met, } t > t_{\text{init}} > 0, \end{aligned} \quad (3.18)$$

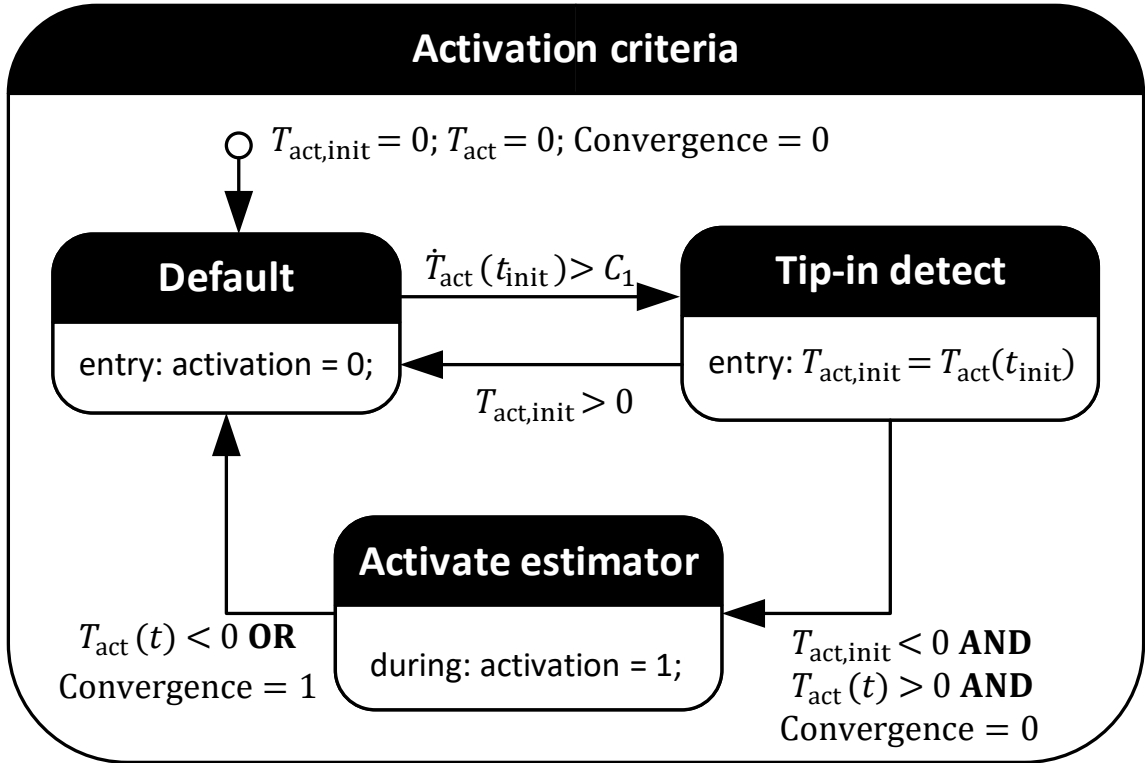


Figure 3.8: State flow diagram showing the backlash size estimator activation criteria.

where this convergence criteria is given below. The size estimator activation criteria is also shown as a state flow diagram in Fig. 3.8.

3.2.2.2 Estimation

As long as the estimator is active, the state estimates of the system (3.5) - (3.13) are obtained through the following equation:

$$\dot{\hat{\mathbf{x}}} = \mathbf{A}\hat{\mathbf{x}} + \mathbf{B}\mathbf{u} + \mathbf{L}[\mathbf{y} - \mathbf{C}\hat{\mathbf{x}}], \quad (3.19)$$

where \mathbf{A} , \mathbf{B} , \mathbf{C} are the state-space matrices, \mathbf{u} and \mathbf{y} are the input and output vectors, $\hat{\mathbf{x}}$ is the estimated state vector, and \mathbf{L} is the steady-state Kalman gain, calculated using the Kalman filter equations. While the process noise covariance matrix of the Kalman filter, \mathbf{Q} , is tuned manually based on model uncertainty, the measurement noise covariance matrix, \mathbf{R} , is fixed and the values are chosen based on known noise information for the speed sensors. The \mathbf{Q} matrix is tuned by initially starting off with an identity matrix and using knowledge about the process noise to choose a trend for the diagonal elements of the matrix. For instance, it is known from the validation studies (e.g., see Fig. 2.9) that the measured engine and wheel speeds may not match COM-simulated engine and wheel speeds. Therefore, a relatively larger value is chosen for the diagonal elements that affect these speed signals. Using this iterative approach, the \mathbf{Q} matrix elements are chosen such that the error in the estimated backlash size is reduced.

3.2.2.3 Steady-state convergence

The third step of the estimation procedure involves monitoring the backlash size estimate and stopping the Kalman filter once the rate of change of the estimated size is below a small threshold, C_2 , i.e.,:

$$\dot{\hat{\theta}}_{\text{b,size}} \leq C_2. \quad (3.20)$$

Algorithm 1 Steps involved in operating backlash size estimator

```
1: while Activation criterion (3.18) is satisfied do
2:   Execute Kalman filter dynamics (3.19);
3:   if Convergence criterion (3.20) is met then
4:      $\hat{\theta}_{b,\text{size,reported}} \leftarrow \hat{\theta}_{b,\text{size}}$ ;
5:     Activation signal  $\leftarrow 0$ ;
6:     break;
7:   else
8:     Activation signal  $\leftarrow 1$ ;
9:     continue;
10:  end if
11: end while
```

3.2.3 Stability analysis

For ensuring that the Kalman gain used in Eq. (3.19) results in a stable steady-state estimator, it is verified that a stabilizing solution exists for the Algebraic Riccati Equation of the system. To this end, the steady-state Kalman filter stability analysis theorems in [46] are utilized, and it is observed that: (i) the (\mathbf{A}, \mathbf{C}) pair is observable, and (ii) the $(\mathbf{A}, \sqrt{\mathbf{Q}})$ pair is controllable. This confirms that the steady-state Kalman gain, \mathbf{L} , that is used in Eq. (3.19) results in a stable Kalman filter.

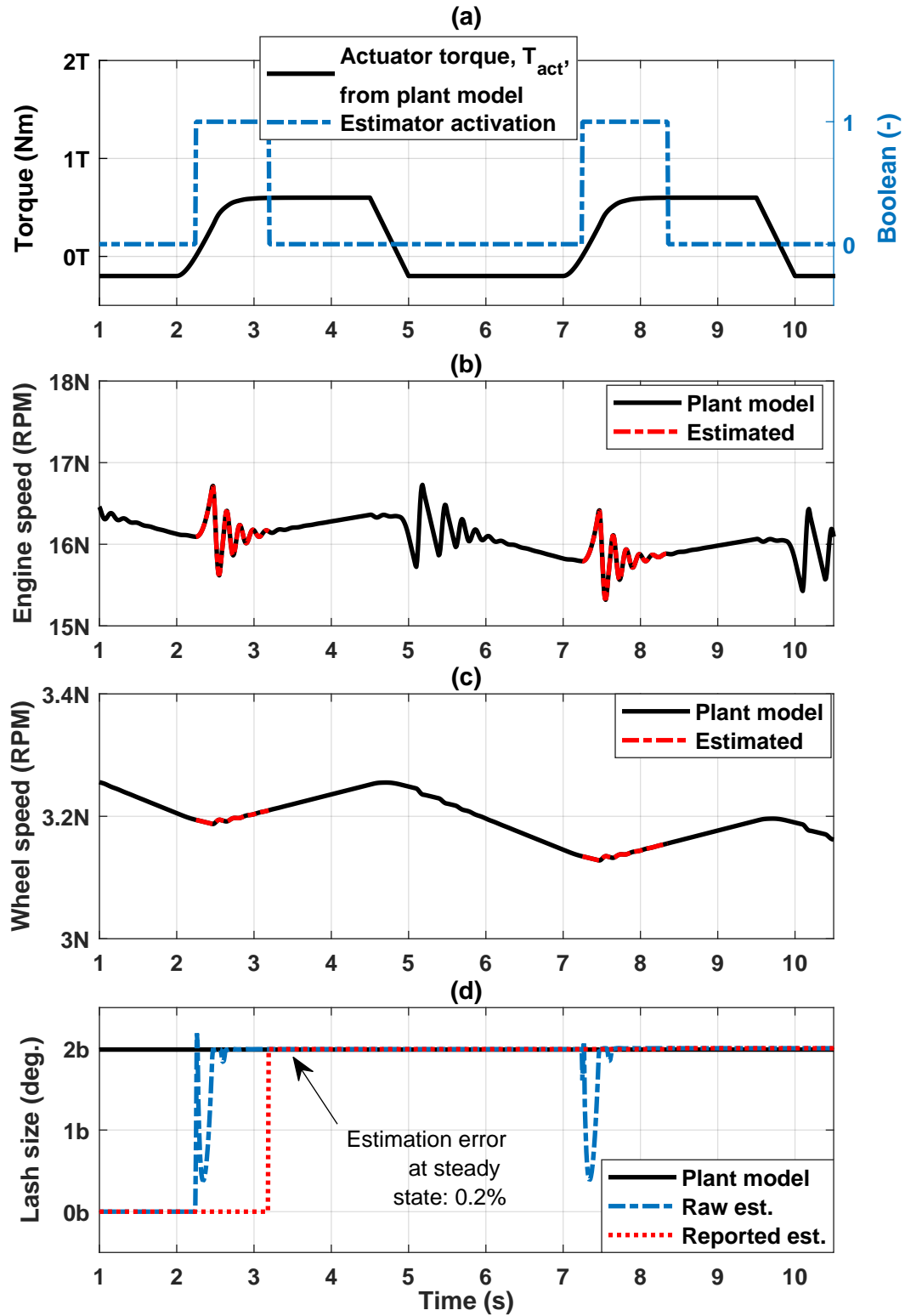


Figure 3.9: Plot showing performance of backlash size estimator in MIL tests.

3.2.4 Validation of backlash size estimator

3.2.4.1 Using MIL tests

The performance of the backlash size estimator is first validated through MIL tests by comparing outputs obtained from the FOM discussed in Chapter 2 with that of the outputs from the estimator. A tip-in from coasting torque profile is provided as an input to the FOM, and the resulting engine and wheel speeds from the FOM are utilized as the measured parameters by the estimator. The performance of the backlash size estimator is illustrated for a tip-in from coasting maneuver in Fig. 3.9. The estimator activates and deactivates according to the specified activation and convergence criteria. Consequently, it is observed that the estimated engine and wheel speeds in Fig. 3.9(b) and (c), respectively, are updated only when the estimator is active. The final size estimate reported to the ECU is shown in Fig. 3.9(d), and it is observed that this estimated size is within 1% of the known plant backlash size.

3.2.4.2 Using test vehicle data

Next, the performance of the backlash size estimator is validated using experimental test vehicle data. The size estimation for this experimental data is shown in Fig. 3.10.

Note that the estimator remains active throughout the first maneuver, (which takes place from 2.5 to 6 seconds). During this maneuver, it is noticed that the intermediate estimation shown in Fig. 3.10 (d) ramps up from ‘0b’ up to ‘2b’ relatively slowly as compared to the FOM simulations in Fig. 3.9. This additional time taken by the estimator to converge may be attributed to the measurement noise in the speed signals and uncertainty in the estimated engine torque. The final size estimate is reported to the ECU only after the second tip-in (which takes place at around 12 seconds). During this tip-in, the estimator converges to the final value quite quickly due to the memory from the previous maneuver. Here, the steady-state estimation error in the reported backlash size is 2%.

3.2.4.3 Processor-in-the-loop (PIL) testing

To evaluate the computational load of the developed estimation algorithm on embedded processors, PIL tests of the backlash size estimator are performed using a dSPACE MicroAutoBox II system. These tests also help us to identify potential road blocks for integration of the developed algorithms with other estimation and control strategies that share the same resources on the embedded processor. For implementing the estimator, the state-space of the system is discretized using Tustin’s method with a sample time of 10 ms. The workflow for PIL validation is shown in Fig. 3.11. In the simulation layer, a driver request is sent to the FOM and the

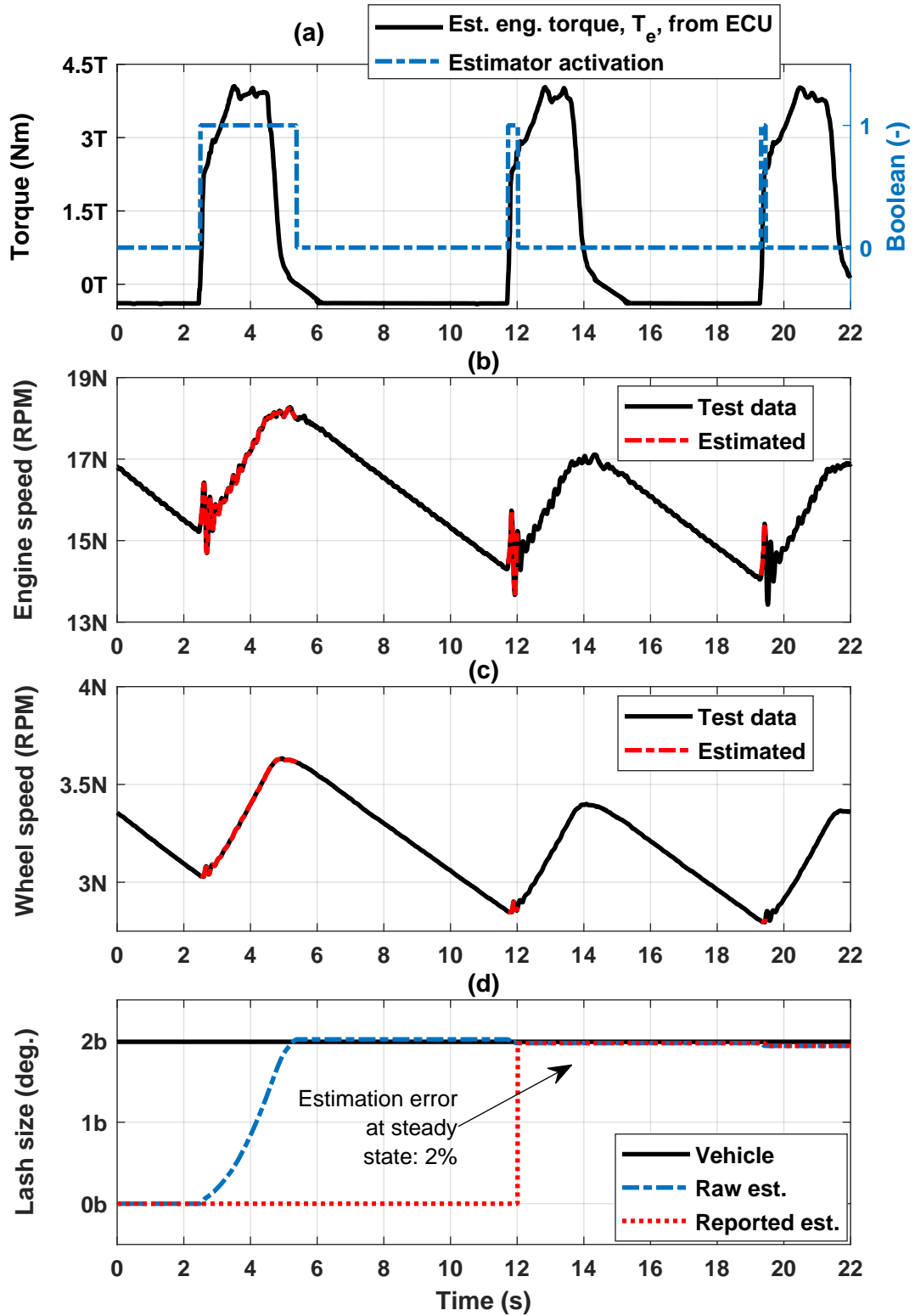


Figure 3.10: Plot showing performance of backlash size estimator using experimental test vehicle data.

Table 3.1
MicroAutoBox II real-time performance timers

Parameter	Value (in seconds)
Simulation run time	7
Solver sample time	1e-2
Processor turnaround time	6e-5

resulting actuator torque, actuator speed, and wheel speed signals are obtained from the FOM. These signals are provided as inputs to the dSPACE MicroAutoBox II, which contains the discretized backlash size estimator. As illustrated in Fig. 3.12, the reported backlash size here has an error of 1.4%. Furthermore, the turnaround time of the estimation algorithm, given in Table 3.1, indicates that the computation time at each sample instant is 1000 times smaller than the sample time. Clearly, the algorithm does not consume substantial processing power and is suitable for running on embedded systems.

3.2.5 Robustness analysis

In this section, the robustness of the backlash size estimator is analyzed using MIL tests for various use cases and uncertainties that are expected to take place in vehicle applications.

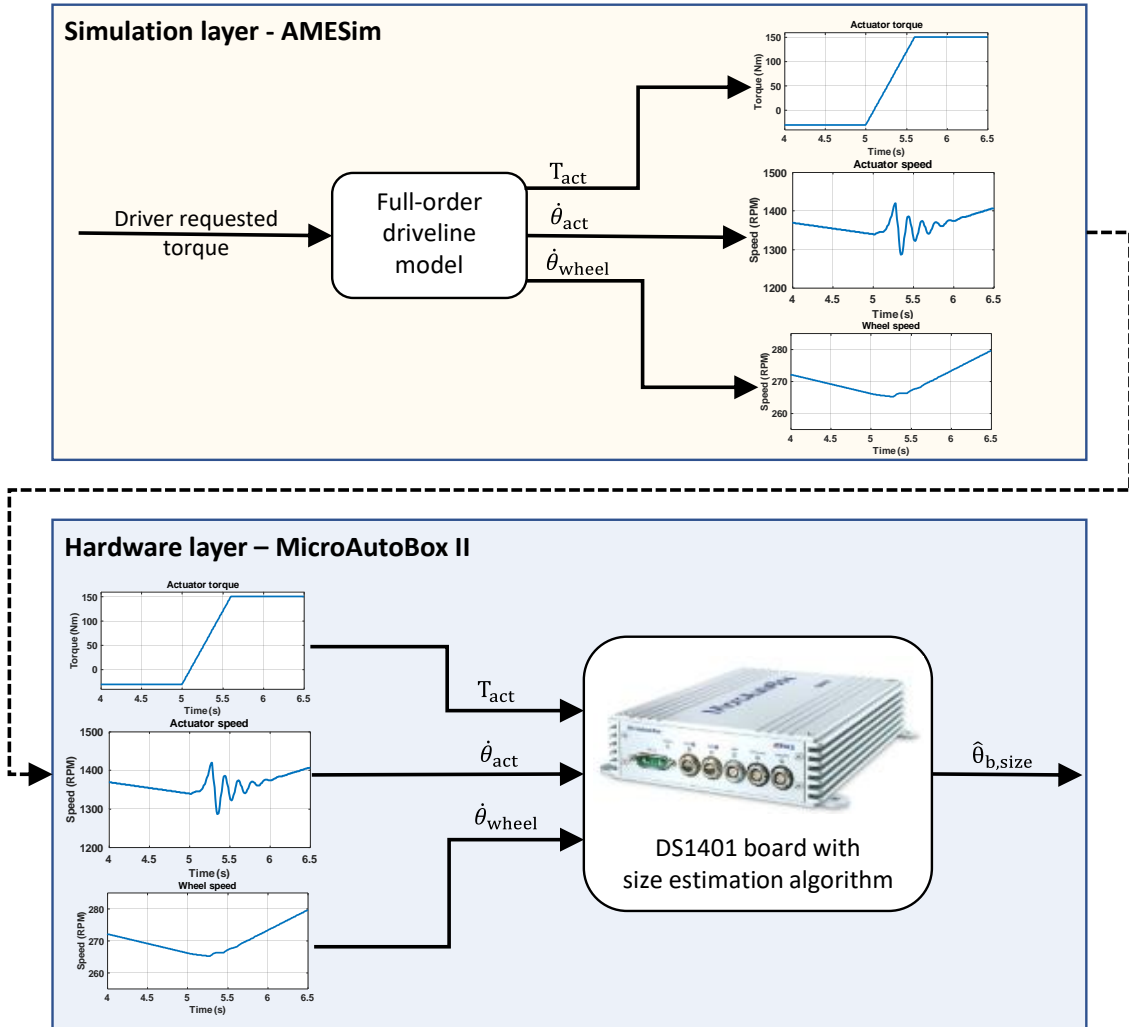


Figure 3.11: Process of PIL validation for the developed backlash size estimator.

3.2.5.1 Varying actuator torque trajectories

In order to account for different driving conditions and driving styles, the estimator needs to work accurately for various torque magnitudes and ramp-rates. Fig. 3.13 shows the behavior of the backlash size estimator when the torque input changes

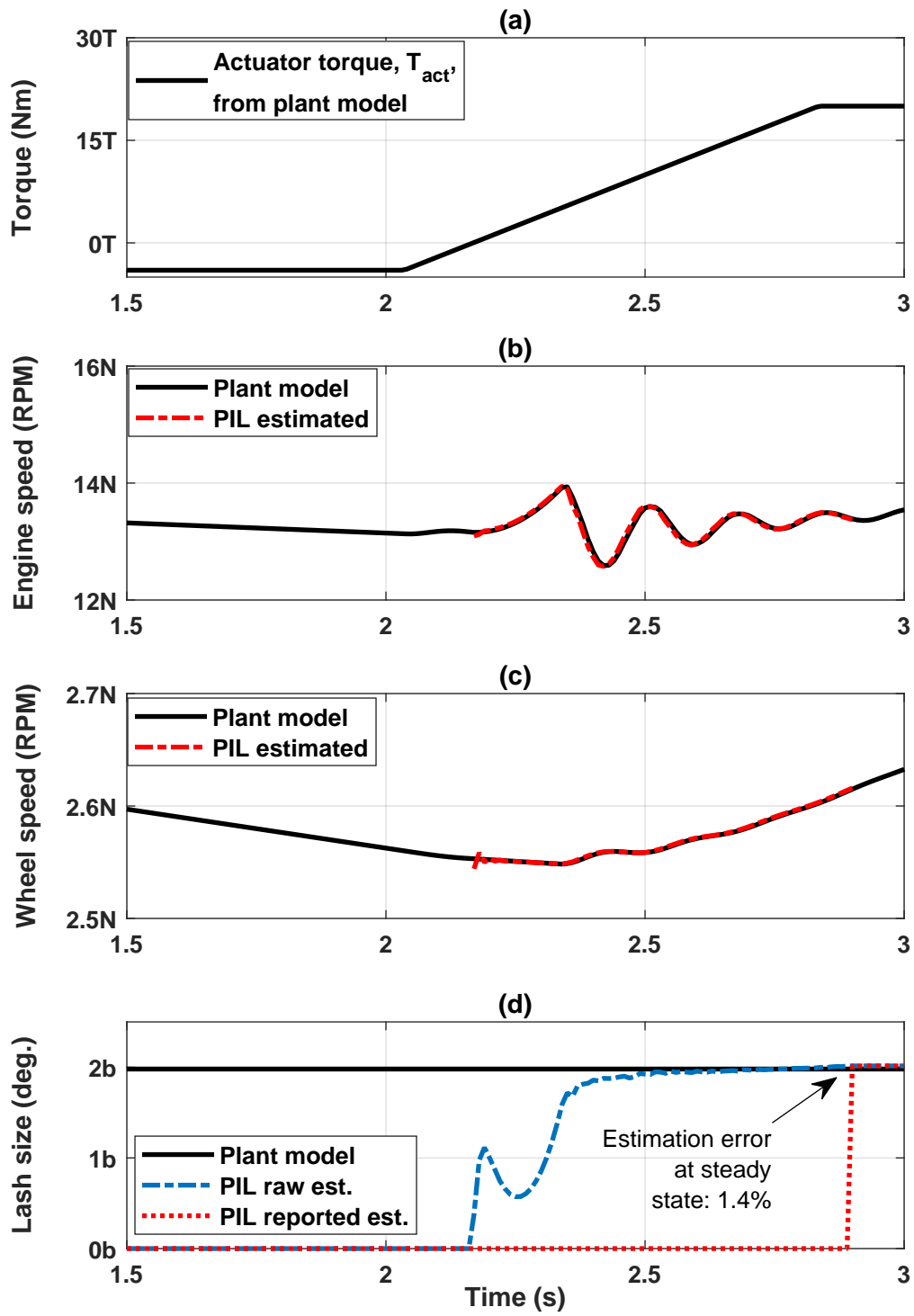


Figure 3.12: Plot showing performance of backlash size estimator in PIL tests.

from one tip-in scenario to another. It is observed that the estimator is able to converge quickly and accurately during each of these tip-ins. Overall, there is a steady state estimation error of less than 1% in the reported lash size estimate making the estimator robust to various torque input profiles.

3.2.5.2 Uncertainty in road load torque calculation

Since the road load torque is one of the inputs to the estimator, the parameters affecting its calculation are varied and its impact on the backlash size estimation is observed. As illustrated in Fig. 3.14, a 25% variation in these parameters causes an average error of less than 10% in the estimated backlash size, with the uncertainty in vehicle mass having the largest impact on the estimation error. The performance of the estimator for road grades up to 15% (without the grade information available to the size estimator) is also tested and an error of up to 8% is observed in the reported backlash size.

It is worth noting that it is possible to obtain high confidence estimates of the vehicle mass and other road load parameters from the vehicle ECU, which will help in reducing the uncertainty in road load torque calculations.

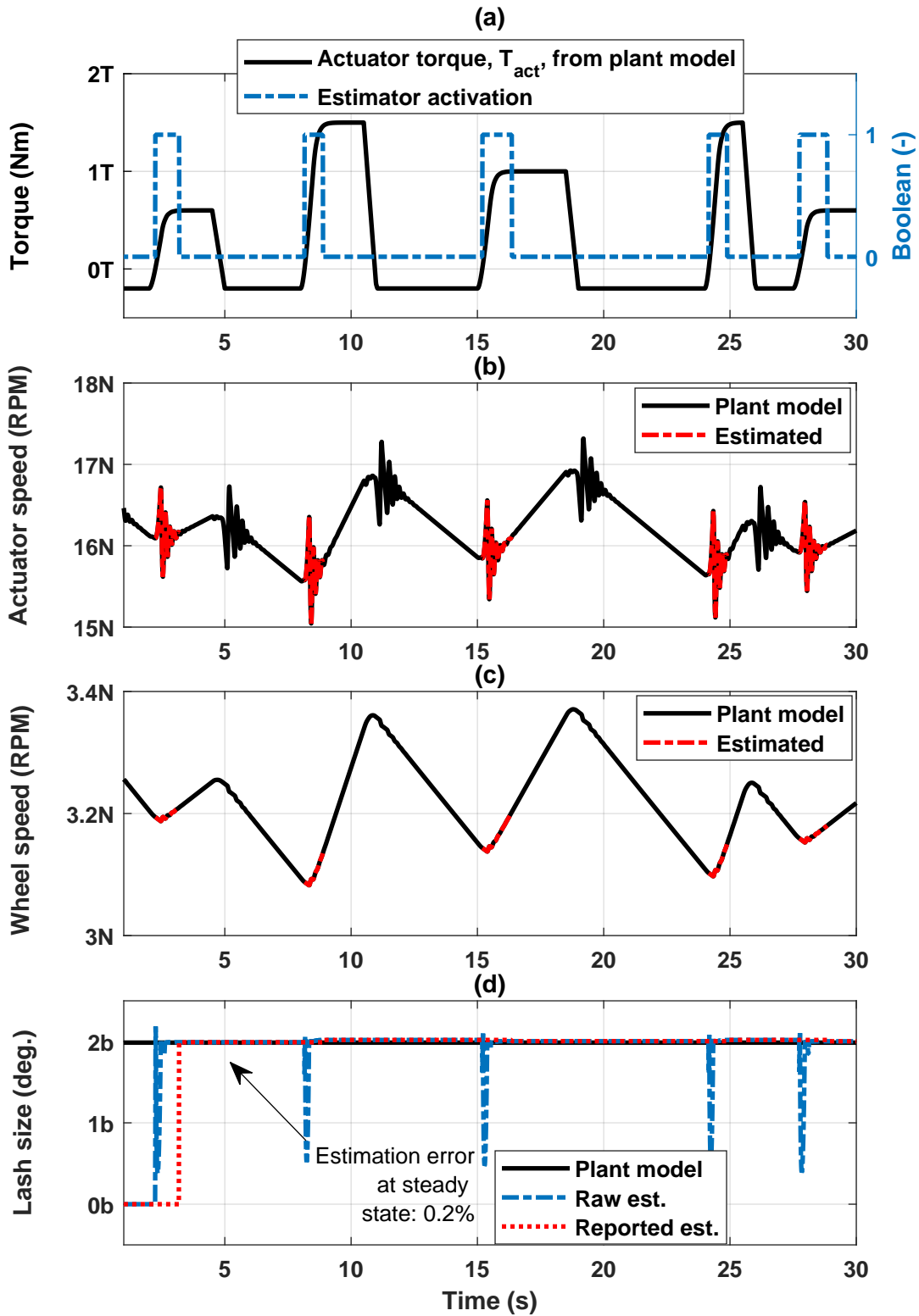


Figure 3.13: Plot showing robustness of the backlash size estimator to different driver torque inputs

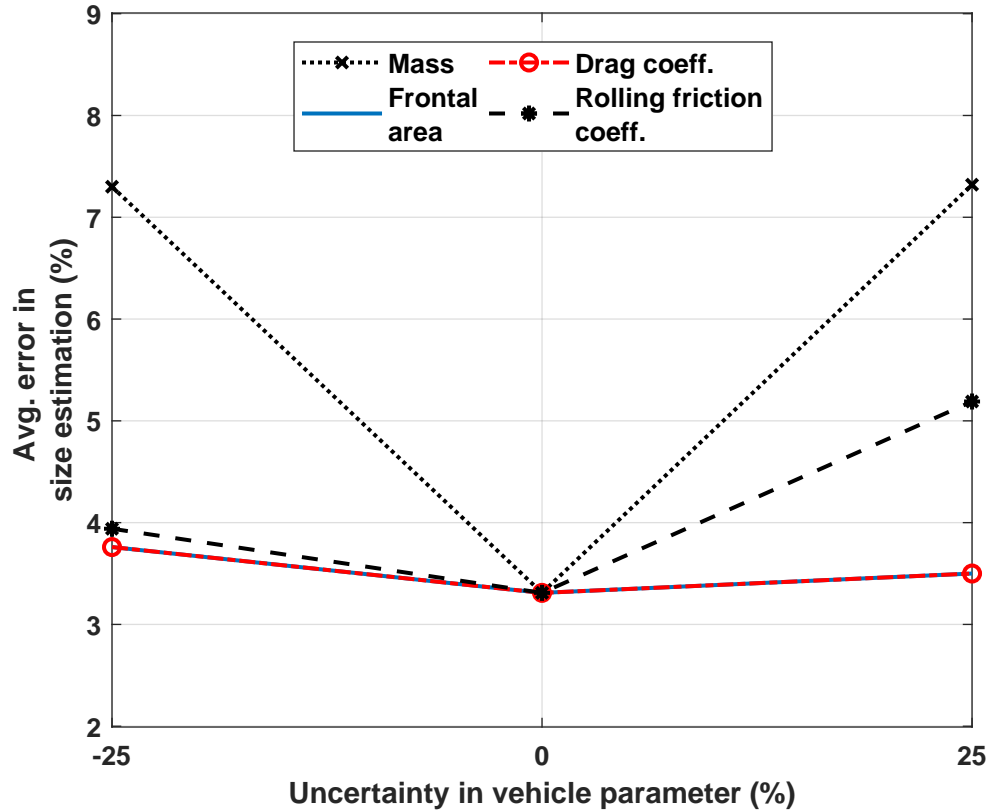


Figure 3.14: Plot showing robustness of the backlash size estimator to road load

3.2.5.3 CAN jitter in actuator and wheel speed signals

Due to message arbitration on the CAN bus, the actuator and wheel speed signals reaching the estimator may be affected by time-varying delays, called jitter. Due to this CAN jitter, a random subset of samples of the measured engine and wheel speeds are missed from being reported to the estimator. As part of the robustness study, the experimental data obtained from the test vehicle was analyzed and a probability density function (PDF) was developed for the jitter delays.

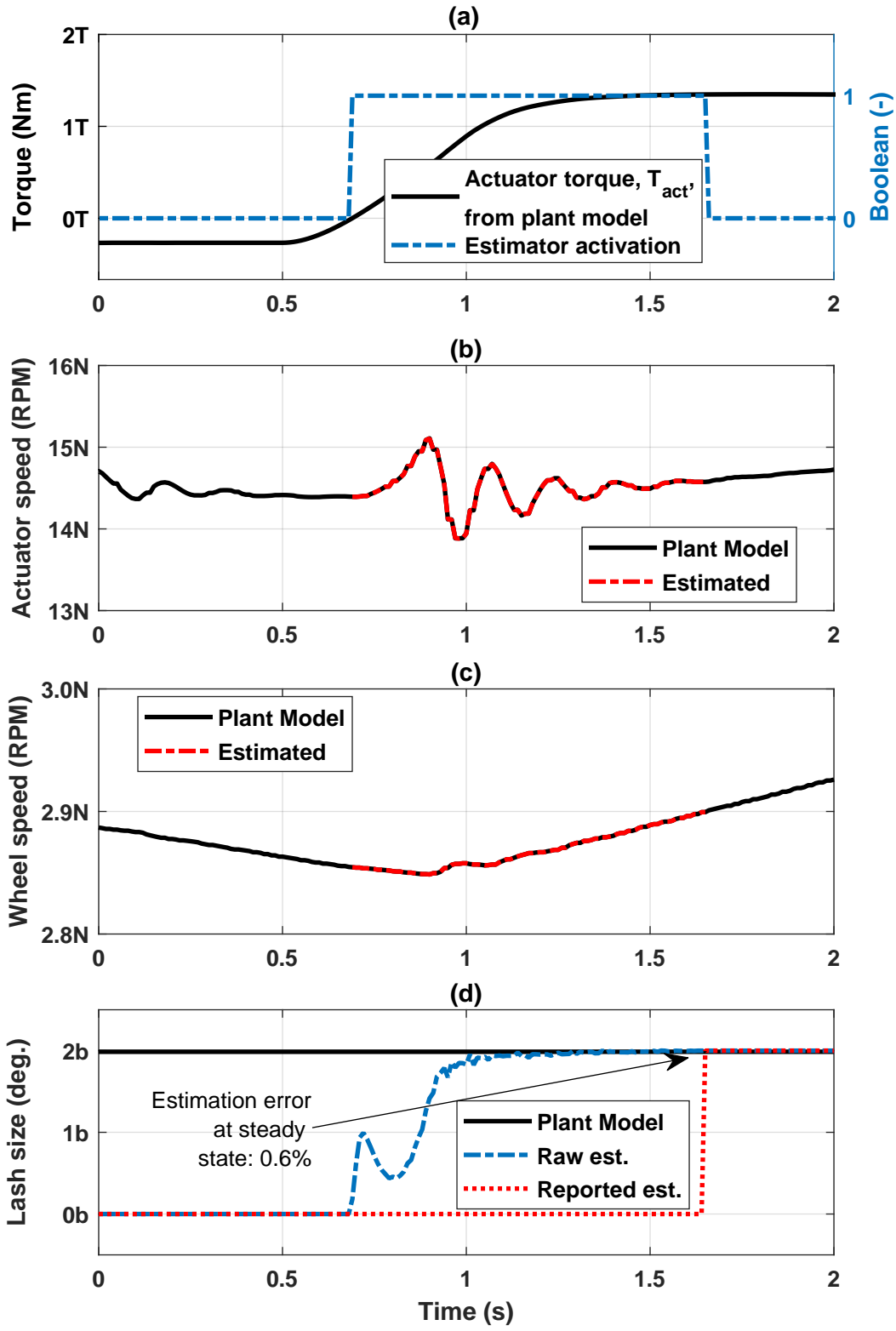


Figure 3.15: Plot showing robustness of the backlash size estimator to CAN jitter.

Using the PDF obtained in [6], random jitter is injected into the engine and wheel speed signals of the FOM. In Fig. 3.15 it is observed that the estimator is able to work well even with jitter affecting these measured speed signals. An error of less than 1% is observed in the estimated lash size.

3.2.5.4 Variation in plant backlash size

As mentioned at the beginning of this section, the backlash size in an automotive drivetrain may vary substantially over the lifetime of the vehicle and/or from vehicle-to-vehicle. Therefore, in order to evaluate robustness, the backlash size in the FOM is increased by up to 100% and the performance of the estimator is evaluated (under the assumption that the estimator has no prior information about the increase in the plant backlash size). As illustrated in Fig. 3.16(a), the estimation error is within 2%, despite the substantial increases in the size of the drivetrain backlash. Moreover, the estimation error also decreases as the lash size increases, since the estimator is active for longer time duration, thus receiving larger number of samples of the input signals.

3.2.5.5 Variation in driveshaft stiffness

Another driveline parameter that may vary due to part-to-part manufacturing variations is the effective stiffness of the driveshaft. This stiffness accounts for the

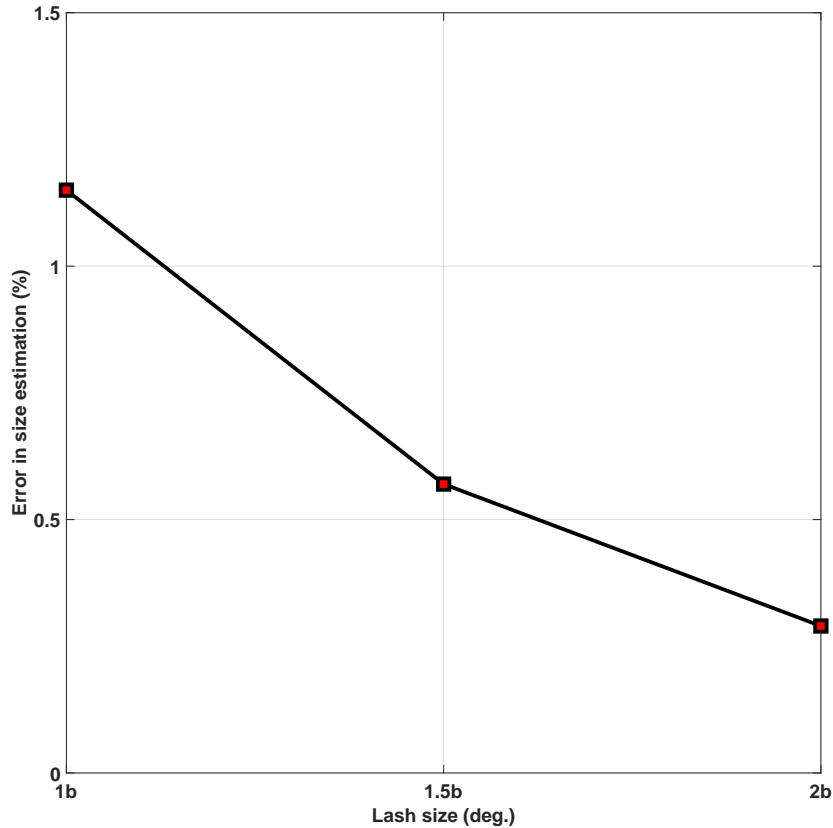


Figure 3.16: Plot showing robustness of the backlash size estimator to changes in plant backlash size.

stiffnesses of both propeller and axle shaft. These variations can lead to changes in the twist angles of the shafts, which may affect the backlash size estimate. Therefore, assuming that the variation in stiffness is within $\pm 25\%$, the performance of the estimator is evaluated as described below.

It is expected that as the shaft stiffness increases the twisting in the shafts will reduce and vice versa. Along these lines, in Fig. 3.16(b) it is observed that the estimator underestimates the backlash size by 8% when the shaft stiffness increases and overestimates the size by 7% when the shaft stiffness decreases. However,

the relatively small magnitudes of errors suggest that the developed backlash size estimator is reasonably accurate for stiffness variations up to $\pm 25\%$ in the driveshafts.

3.2.5.6 Variation in tire-road interaction

The interaction between the tire and the road may change significantly when the operating conditions, such as ambient temperature, tire pressure, and type of road, change (see [47, 48, 49]). The engine and wheel speeds of the vehicle on high-traction (e.g., dry tarmac) surfaces is expected to represent the outputs observed previously in Fig. 3.9. However, under low-traction surfaces (such as icy roads), the magnitudes of these speeds increase and the frequency of shuffle oscillations decreases (see Fig. 3.17 vs. Fig. 3.9). These changes in behavior are a direct consequence of the change in tire stiffness and damping due to slippery road conditions. Even under these operating conditions, the designed estimator is able to estimate the backlash size with a steady-state error of approximately 9% after the first tip-in event, as seen in Fig. 3.17.

3.2.5.7 Variation in driveshaft damping

Another parameter that may vary significantly is the effective driveshaft damping. For up to $\pm 25\%$ change in this parameter, it is observed that there is no significant impact on the accuracy of the designed backlash size estimator.

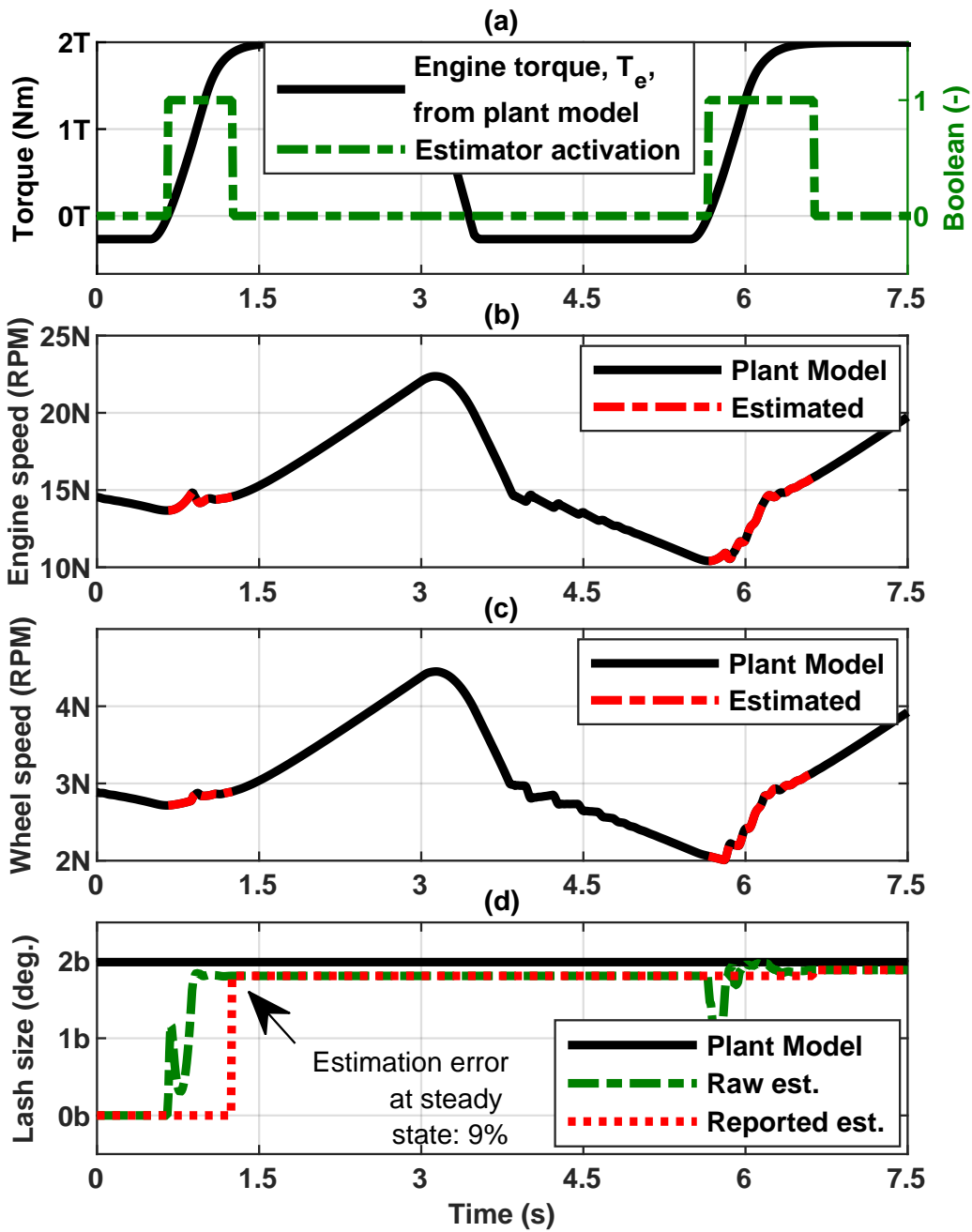


Figure 3.17: Robustness analysis of the backlash size estimator to variation in tire properties due to changes in the tire-road patch interaction. In this result, a low traction scenario such as an icy road is simulated.

3.2.5.8 Impact of sample time on backlash size estimate

The backlash size estimator is dependent on lash traversal taking place in order to estimate the size of the lash. Such events are typically in the order of tens of milliseconds. Therefore, the sample time of the estimator affects the accuracy of the estimated value. In all the previous robustness analysis results, a 10 ms sample time is used as that was the sample time in the ECU of the test vehicle. Here, the benefit of using a smaller sample time is analyzed since future ECUs are expected to run at a sample time less than 10 ms.

Fig. 3.18 shows the distribution of percentage error in the estimated lash size for 3 sample times: (i) 1 ms, (ii) 5 ms, and (iii) 10 ms. The percentage error is the least when the sample time is the smallest, i.e., 1 ms.

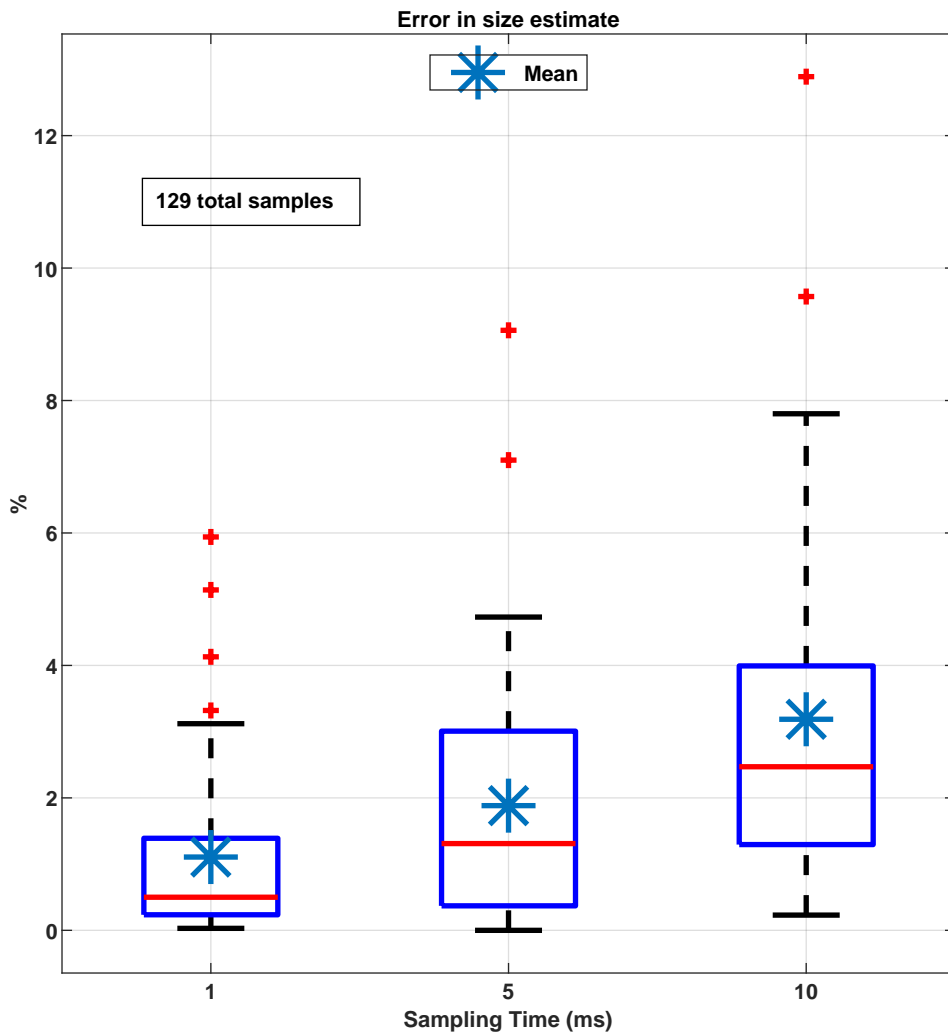


Figure 3.18: Plot showing robustness of the backlash size estimator at various sample times.

Chapter 4

Design of shuffle and clunk control algorithms¹

After developing and validating the plant models and the estimation algorithms, the next step in designing the clunk and shuffle torque shaping controller is to develop the control algorithms. As discussed in Chapter 1, the goal of the shuffle controller is to reduce the unwanted longitudinal oscillations caused due to the rapid twisting and untwisting of the driveshafts, and the goal of the clunk controller is to reduce the impact between adjacent gear teeth while traversing lash as soon as possible.

While the goal of this work is to develop optimal, model-based controllers, it is also

¹Contents of this chapter first appeared in [8]. Letter of permission to republish from IFAC is available in Appendix C.

necessary to be cognizant of the computation load that these control algorithms would demand. Therefore, a pre-compensator and a lead compensator combination is chosen as the shuffle controller, while a reference governor-based controller is chosen as the clunk controller. The details of these controllers, and the motivation behind choosing them are discussed in the next sections.

4.1 Driveline shuffle controller

From previous research studies [10, 50], it is evident that engine torque rate rise contributes to an increased severity of shuffle. Therefore, the control objectives of the driveline shuffle controller are to: (i) reduce the severity of the longitudinal oscillations, and (ii) robustly smoothen the remaining oscillations. The first objective is met through the use of a pre-compensator which acts as a filter to smoothen the driver requested torque such that this torque request does not excite the driveline shuffle mode. The second objective is handled using feedback control through the lead compensator. Since it is also imperative that new sensors are not required for this controller, the feedback parameter is chosen such that it can be easily calculated or estimated through the use of readily available CAN signals. To this end, the rate of change of propeller shaft torque is used as a metric for measuring and mitigating driveline shuffle. The propeller shaft torque can be estimated using the actuator and wheel speed signals which removes the need for additional sensors on the vehicle.

4.1.1 Design of the pre-compensator

The pre-compensator is designed as a Butterworth low pass filter, since this type of filter offers lower band pass ripple in the frequency response [51]. The contact mode transfer function describing the relation between the commanded actuator torque, T_{act}^* , and the propeller shaft torque, T_{prop} , is given by:

$$TF_{cm}(s) = \frac{T_{prop}(s)}{T_{act}^*(s)} = \frac{0.18s^3 + 2606s^2 + 5.84e05s^1 + 1.7e07}{0.15s^5 + 35.17s^4 + 1967s^3 + 7.09e04s^2 + 2.12e06s + 1.15e07} \quad (4.1)$$

The poles of the above transfer function indicate that the damped frequency of the complex poles of $TF_{cm}(s)$ is at approximately 5 Hz. This transfer function represents the plant transfer function for designing the pre-compensator.

For designing the Butterworth low pass filter the following performance considerations are taken into account:

1. The rise time of the shaft torque ≤ 175 milliseconds. This is based on internal Ford research where having a rise time larger than 1 period of the shuffle oscillations results in unacceptable vehicle response.
2. The overshoot in the shaft torque has to be $\leq 10\%$, for avoiding unintended vehicle acceleration.

3. The settling time of the shaft torque has to be ≤ 350 milliseconds, for maintaining the driveline shuffle at acceptable limits.

Additionally, the pass band frequency, f_p , of the filter has to be $\gg f_{\text{shuffle}}$, and the stop band frequency, f_s , of the filter has to be $\ll f_{\text{shuffle}}$ to satisfy the performance requirements of the filter. The pass band ripple limit, $1 - \delta_p$, and stop band ripple limit, δ_s , are assigned the standard values used for the Butterworth low pass filter, i.e., 0.8 and 0.2, respectively. While fixing the stop band frequency, f_s , at 6 Hz, a sweep of step responses is carried out for $f_p = 2$ Hz through 5 Hz. The most smoothest response meeting the performance criteria is obtained with a combination of $f_p = 2$ Hz and $f_s = 6$ Hz, and this yields the following pre-compensator:

$$\text{PC}(s) = \frac{201.5}{s^2 + 20.07s + 201.5} \quad (4.2)$$

Including a zero and modifying the pre-compensator can further improve its rise time while meeting the remaining performance criteria. Therefore, using the SISO tool in MATLAB, an additional zero that improves the performance of the pre-compensator is determined and the modified pre-compensator is given as:

$$\text{PC}_{\text{mod}}(s) = \frac{10.57s + 201.5}{s^2 + 20.07s + 201.5} \quad (4.3)$$

4.1.2 Design of the lead compensator

As mentioned earlier, the feedback control by the lead compensator is based on feedback of the estimated propeller shaft torque in the driveline. Since, the rate of change of propeller shaft torque is used as the metric for shuffle oscillation, the transfer function between the time derivative of the propeller shaft torque and the commanded actuator torque is given by:

$$\text{TF}_{\text{cm,mod}}(s) = \frac{sT_{\text{prop}}(s)}{T_{\text{act}}^*(s)} = \frac{(s)(0.18s^3 + 2606s^2 + 5.84e05s + 1.7e07)}{0.15s^5 + 35.17s^4 + 1967s^3 + 7.09e04s^2 + 2.12e06s + 1.15e07} \quad (4.4)$$

$\text{TF}_{\text{cm,mod}}(s)$ is the plant transfer function for the lead compensator controller design.

The lead compensator, $C(s)$, is selected as:

$$C(s) = c \frac{1+a}{1+b}, c > 0, a > 0, b > 0. \quad (4.5)$$

The zero of $C(s)$ pulls the lightly damped poles from $\text{TF}_{\text{cm,mod}}(s)$, thereby, increasing the damping of the combined system. The gain c is used as a calibration knob to fine tune the lead compensator's response. Using the SISO tool in MATLAB, the numerical values of c, a, b are obtained as $c = 0.013$, $a = 20.85$, and $b = 26.45$.

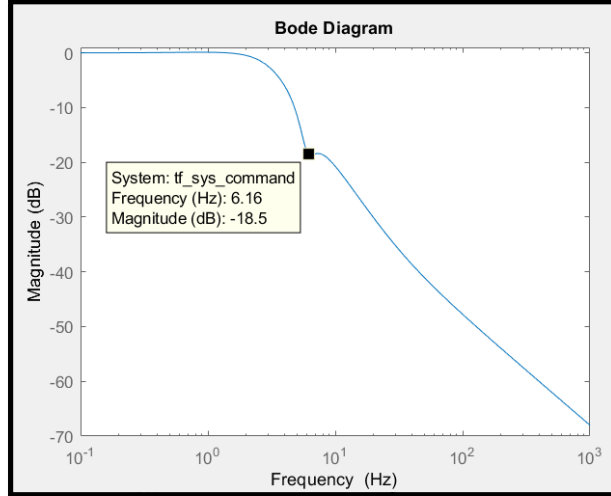


Figure 4.1: Bode plot of the closed loop shuffle controller showing a dip near the shuffle frequency.

The combined transfer function between the shuffle controller-shaped actuator torque command and the driver torque request of the closed-loop system can be given as:

$$\frac{T_{\text{act}}^*(s)}{T_{\text{drv}}(s)} = \frac{PC_{\text{mod}}(s)}{1 + TF_{\text{cm,mod}}(s) \cdot C(s)} \quad (4.6)$$

The frequency response of the closed-loop system is shown through a Bode plot in Fig. 4.1. This response is similar to what is seen in a low pass filter, indicating that the high frequency content exciting the driveline has been prevented from propagating into the system. The magnitude dips close to the shuffle frequency which further indicates the damping effect being added through the designed shuffle controller.

4.2 Driveline clunk controller

For controlling the clunk phenomenon a reference governor-based design is chosen for the clunk controller. The reference governor is a predictive, model-based control algorithm which continually monitors the reference and states of a system and only intercedes when an unsupervised reference may lead to a violation of predefined constraints. While a reference governor approach shares some similarities with MPC, it is primarily different in the fact that it uses one-step ahead prediction instead of MPC's n -steps ahead. This decreases the computational load of the reference governor approach and makes it easier to be implemented on embedded processors. Typically, reference governors are designed to supplement a new or an existing feedback controller (denoted as the baseline controller in this work). These feedback controllers might have been designed using conventional control techniques and might already be providing acceptable performance for use cases in which constraint violation is of no concern. The reference governor improves the performance of the baseline controller by adding the capabilities of handling state and control constraints, especially in transient conditions. Additionally, it reduces processing time, and provides comprehensive calibrations for various operating conditions of the baseline controller.

4.2.1 Double integrator backlash model

The clunk phenomenon can be represented in terms of the relative speed between the actuator and wheels, taken in the same domain, at the end of lash traversal. This is called as the impact velocity in this thesis. From the discussions in Chapter 1 and Fig. 1.2, it is evident that the magnitude of impact velocity, and, consequently, clunk is a direct result of the dynamics of the backlash mode. Therefore, the backlash mode dynamics are of primary interest for developing the clunk controller.

In the backlash mode, when lash traversal is taking place the link between the actuator and wheel is disconnected for a brief amount of time. Therefore, the actuator speed increases proportionally with the actuator torque, but the large inertia of the vehicle causes the wheel speed to remain approximately constant during this duration of disconnectedness. Moreover, for the plant considered in this thesis, the ratio of driveshaft damping with respect to driveshaft stiffness is small. This allows the assumption that the driveshaft is neither twisting nor untwisting when the drivetrain is in the backlash mode. Therefore, during this period, the dynamics of the backlash can be approximated to a double integrator system and can be represented in state space form as:

$$x_1 = \theta_b; \quad x_2 = \dot{\theta}_b, \quad (4.7)$$

$$\begin{bmatrix} \dot{x}_1 \\ \dot{x}_2 \end{bmatrix} = \begin{bmatrix} x_2 \\ \frac{T_{\text{act}}}{J_1} \end{bmatrix}, \quad (4.8)$$

where θ_b is the position in backlash, $\dot{\theta}_b$ is the speed of lash traversal (which is the relative speed of the actuator and the wheels), T_{act} is the actuator delivered torque, and J_1 is the lumped inertias of the actuator, torque converter, transmission, propeller shaft, and final drive. In addition to the drivetrain dynamics in backlash mode, the control algorithm also utilizes the real-time information about the size and position of the backlash. This information is obtained using estimation algorithms developed in Chapter 3. Additionally, a backlash position predictor is also used which helps in reducing the delays and errors in the estimated backlash position. These details are discussed in the next section.

4.2.2 Clunk controller: Design of the baseline controller

The control objectives of the clunk controller are: (i) to traverse lash from negative contact to positive contact as soon as possible, (ii) to hit positive contact at or less than a chosen threshold velocity, and (iii) to meet the physical constraints of the drivetrain. To satisfy such competing objectives, the soft landing reference governor approach is chosen as the preferred choice and the objectives are formulated as an optimal control problem (OCP).

The baseline controller is used to set the control law for the clunk controller and is chosen to: (i) move the backlash towards positive contact, and (ii) be easily calibratable and implementable on an embedded processor. Thus, a Proportional-Derivative (PD) baseline controller is designed which tracks a reference backlash position. When the drivetrain is in lash, the desired reference backlash position is to reach positive or negative contact. The PD controller tracks this reference by shaping the torque command sent to the actuator. The gains of this PD controller are chosen such that they provide fast and stable tracking performance. Time intensive calibrations for different operating conditions are not required since a reference governor is being used with the PD controller, which modifies the reference backlash position to be tracked if it predicts a chance of constraint violation. Therefore, the baseline control law, u , is chosen as:

$$u = T_{\text{act}} = k_p[q - \theta_b] - k_d\dot{\theta}_b, \quad k_d > 0, \quad (4.9)$$

where, k_p is the proportional gain and k_d is the derivative gain of the PD controller, q is the modified backlash position reference controlled by the reference governor, θ_b is the predicted backlash position of the plant, and $\dot{\theta}_b$ is the calculated speed of lash traversal.

4.2.3 Clunk controller: Soft-landing reference governor

Now the OCP is defined which encapsulates the control objectives. As mentioned earlier, the clunk controller is required to cross lash as quickly as possible while meeting certain constraints: (i) the reference position should be within the negative and positive contact positions of the backlash, (ii) the commanded torque should be within a pre-defined range of values which are chosen to limit undesirable changes in the torque command during lash crossing, and (iii) the speed of lash traversal when the lash reaches positive contact (a.k.a. impact velocity) should be within the predefined limit. While the first and second constraints are straightforward to setup, a Lyapunov function candidate is utilized for setting up the third constraint:

$$V(x) = \frac{1}{2}k_p[q - \theta_b]^2 + \frac{1}{2}\dot{\theta}_b^2, \quad (4.10)$$

where the terms carry the same definition as Eq. (4.9). This equation satisfies the positive semi-definite condition for all scenarios when $k_p > 0$. Taking the Lie derivative of Eq. (4.10) and substituting the value for T_{act} , the following relation is

obtained:

$$\dot{V}(x) = \nabla V f(x), \quad (4.11)$$

$$\dot{V}(x) = \begin{bmatrix} \partial V / \partial x_1 & \partial V / \partial x_2 \end{bmatrix} \begin{bmatrix} x_2 \\ \frac{k_p(q - x_1) - k_d x_2}{J_1} \end{bmatrix}, \quad (4.12)$$

$$\dot{V}(x) = - \begin{bmatrix} k_d \\ \frac{1}{J_1} x_2^2 \end{bmatrix}, \quad (4.13)$$

which proves that the Lie derivative of the candidate Lyapunov function is negative semi-definite for all scenarios when $k_d > 0$. Therefore, the function in Eq. (4.10) can be considered as a suitable Lyapunov function for the controller's requirements.

Let t_c and t_{im} represent the current time instant and the time at which impact occurs on positive contact, respectively. From Eq. (4.13), it can be stated that:

$$V(t_{im}) \leq V(t_c). \quad (4.14)$$

Assuming that the lash position reference, q , does not change in the time interval $t_c \leq t \leq t_{im}$, the expression of Lyapunov function from Eq. (4.10) can be used in

Eq. (4.14) to get:

$$\frac{1}{2}k_p[q - \theta_b(t_{im})]^2 + \frac{1}{2}\dot{\theta}_b^2(t_{im}) \leq \frac{1}{2}k_p[q - \theta_b(t_c)]^2 + \frac{1}{2}\dot{\theta}_b^2(t_c), \quad (4.15)$$

which can be rewritten as:

$$\dot{\theta}_b^2(t_{im}) \leq k_p[q - \theta_b(t_c)]^2 - k_p[q - \alpha]^2 + \dot{\theta}_b^2(t_c). \quad (4.16)$$

If it is assumed that:

$$k_p[q - \theta_b(t_c)]^2 - k_p[q - \alpha]^2 + \dot{\theta}_b^2(t_c) \leq v_{im}^2, \quad (4.17)$$

then:

$$\dot{\theta}_b^2(t_{im}) \leq v_{im}^2, \quad (4.18)$$

where v_{im} is the impact velocity limit that can be chosen as required. The relation obtained in Eq. (4.17) and (4.18) can be used for defining the second constraint. Therefore, the OCP for obtaining a governed reference backlash position, q , during tip-in scenarios is setup as:

$$\text{maximize } q(t_c) \quad (4.19)$$

subject to

$$- \alpha \leq q \leq +\alpha, \quad (4.20)$$

$$-T_{\text{sat}} \leq k_p[q - \theta_b] - k_d[\dot{\theta}_b] \leq T_{\text{sat}}, \quad (4.21)$$

$$k_p[q - \theta_b(t_c)]^2 - k_p[q - \alpha]^2 + \dot{\theta}_b^2(t_c) \leq v_{\text{im}}^2. \quad (4.22)$$

This OCP is solved offline on a desktop computer, and the obtained solutions are visualized in the form of a Maximal Output Admissible Set (MOAS). For getting these solutions, the clunk control algorithm performs one step ahead prediction for each combination of θ_b and $\dot{\theta}_b$, and then selects a feasible q .

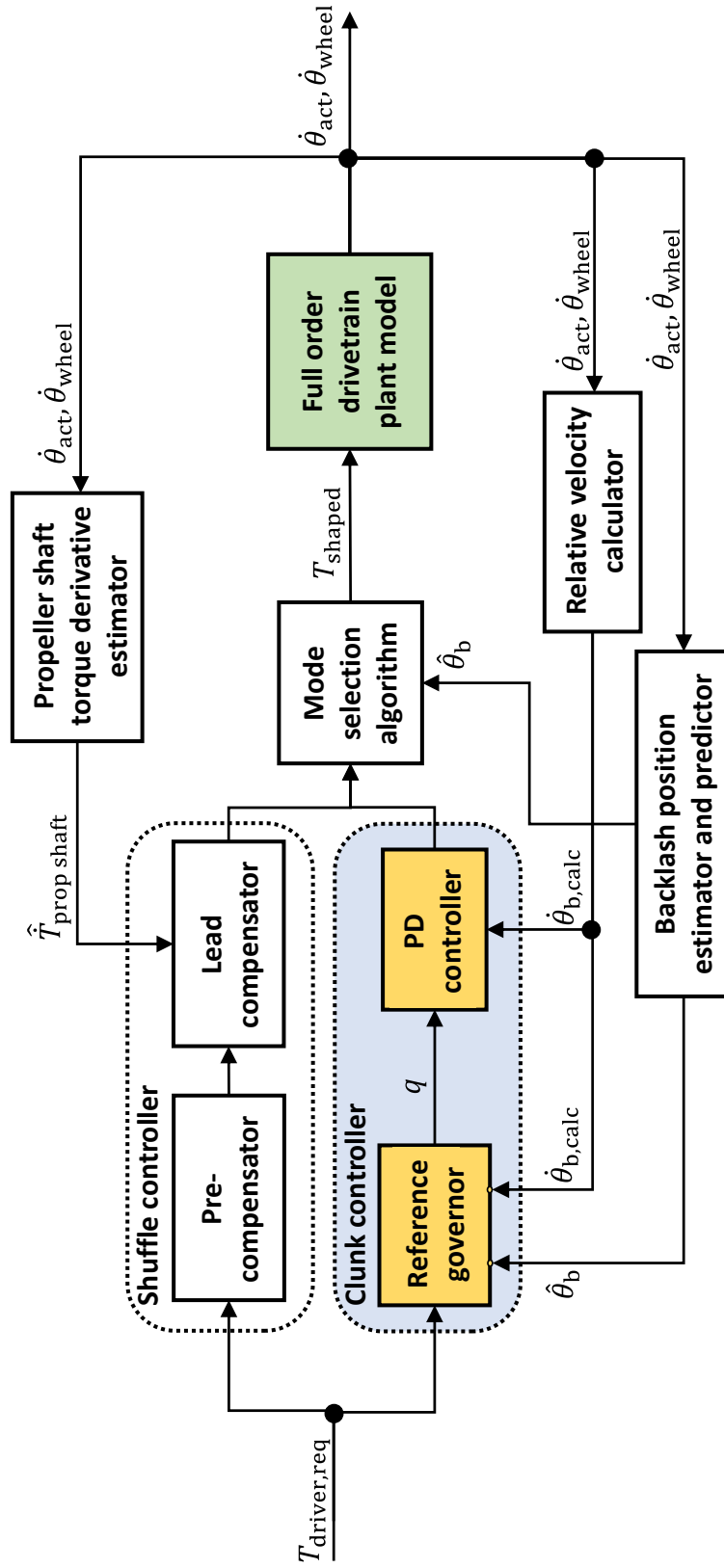


Figure 4.2: Schematic of the designed torque shaping controller consisting of both contact mode and backlash mode controllers.

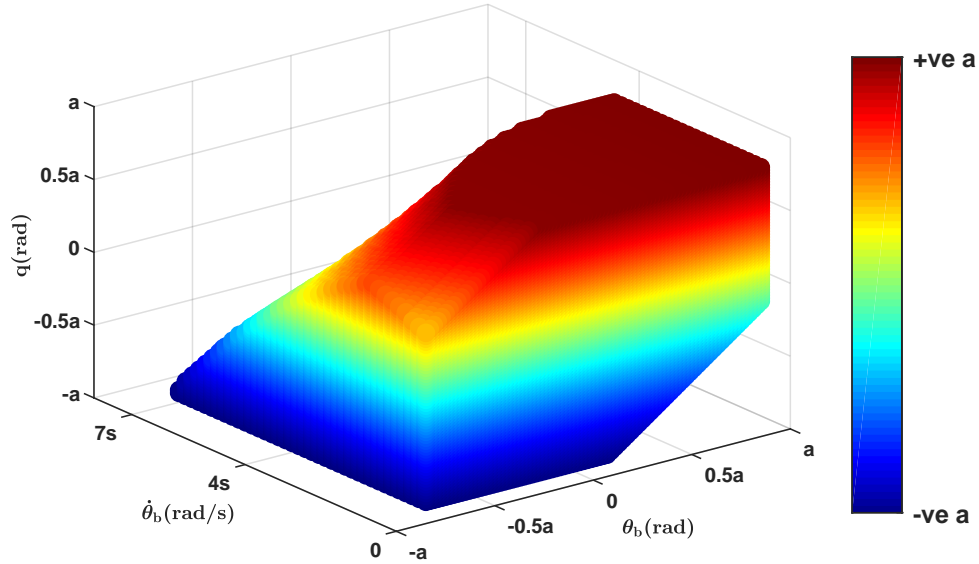


Figure 4.3: The MOAS obtained for an impact velocity constraint of 5s. Color gradation indicates number of feasible solutions. The maximum number of solutions are available in the blue region, which corresponds to the beginning of lash crossing, and they start to reduce in the green and yellow region with the minimum number of solutions in the red region, which corresponds to the end of lash crossing.

4.2.4 Clunk controller: Maximal output admissible set

The MOAS is defined as the set of all feasible values of states and inputs of a system such that the predicted response of the system with these initial states and constant inputs satisfy the constraints set for the system; see [52]. The states of the backlash mode system are $\theta_b, \dot{\theta}_b$ and the reference modified by the reference governor is q . All possible combinations of these three parameters satisfying the constraints listed above give the MOAS for the defined OCP, and this can be visualized as illustrated in Fig. 4.3. The density of the MOAS can be changed by changing the number of ticks on each axis, when defining the range of each axis before solving the OCP.

4.2.5 Clunk controller: Implementation of the reference governor

For implementing the designed reference governor, a lookup table (LUT) with the computed maximal value of q , for each combination of θ_b and $\dot{\theta}_b$, is generated. When the predicted backlash position, $\hat{\theta}_b$, and speed of lash crossing, $\dot{\theta}_b$ are provided as inputs to this LUT, the modified reference backlash position, q , is obtained as the output (see Fig. 4.2). Implementing the reference governor as an LUT is an attractive option because this makes it feasible to run real-time on embedded processors (automotive ECUs). All the computation-intensive calculations are performed offline and this reduces the computational footprint of the clunk controller. Moreover, multiple LUTs can be quickly generated offline and implemented on the ECU for different operating conditions.

4.3 Validation of shuffle and clunk control algorithms

The performance of the shuffle and clunk torque shaping system is verified in both model-in-the-loop (MIL) as well as processor-in-the-loop (PIL) tests. The FOM

and the ROM are used as the plant models in the MIL and PIL validation tests, respectively.

4.3.1 Performance in MIL tests

A tip-in scenario is simulated with the driver torque request ramping up from a slightly negative torque at 1000 Nm/s using the co-simulation model (see Fig. 4.4). It is noticed that the relative speed between the actuator and the wheel starts to ramp up rapidly at the beginning of the backlash traversal (see Fig. 4.4(d)). It is also noticed that the clunk controller does not intervene at the start of lash traversal to facilitate quick lash crossing. However, once the lash is closer to positive contact and there is a chance of violating impact velocity, the clunk controller modifies the reference backlash position to keep the impact velocity within the predefined constraint (see Fig. 4.4(c)). Consequently, it is noticed that the torque shaping system keeps clunk and shuffle at a minimum and quickly delivers the driver requested torque (see propeller shaft torque signal in Fig. 4.4(c)).

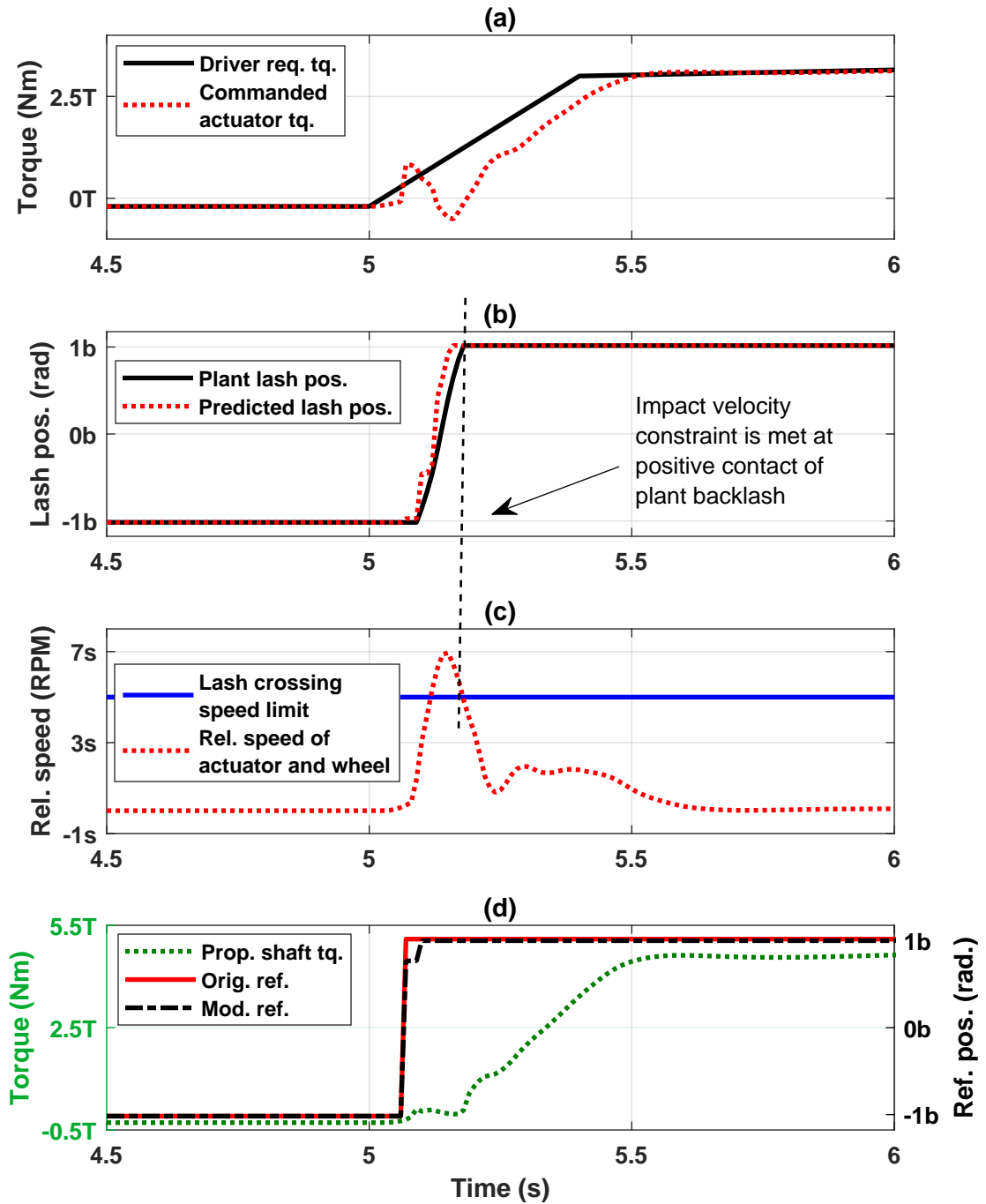


Figure 4.4: Performance of the designed clunk controller during a tip-in event. The controller initially requests significant torque to quickly traverse lash, and then rapidly reduces the torque request to meet the chosen impact velocity constraint (i.e., 5s).

4.3.2 Performance in PIL tests

To ensure that the controller works on real-time embedded processors, PIL testing is performed using a dSPACE MicroAutoBox II platform. In this implementation, both the plant model and the controller are flashed on to the MicroAutoBox II. dSPACE ControlDesk software is used as the user interface for sending a torque request and for recording the actuator and wheel speed outputs. The schematic of the PIL setup used for this validation is shown in Fig. 4.5. The reduced-order model is used as the plant model and the performance of the torque shaping controller for various driver torque requests, and various controller and plant sampling rates is tested. Through these PIL tests, the turnaround time and task overrun information is obtained for the designed controller. The turnaround time is defined as the computation time of the embedded processor to process the algorithms at each time step. Task overrun is defined as the number of times that the turnaround time is larger than the sample time. Typically, intensive PIL computations can cause task overruns which could cause an error in the algorithm and prevent from running real time. The testing results are shown in Table 4.1. It is observed that the designed controller is able to perform well at both 5 ms and 10 ms sample time without any task overruns. For 1 ms sample time, 2 task overruns are noticed. Therefore, it is concluded that the designed controller is able to work well in embedded processors up to a sample time of 5 ms.

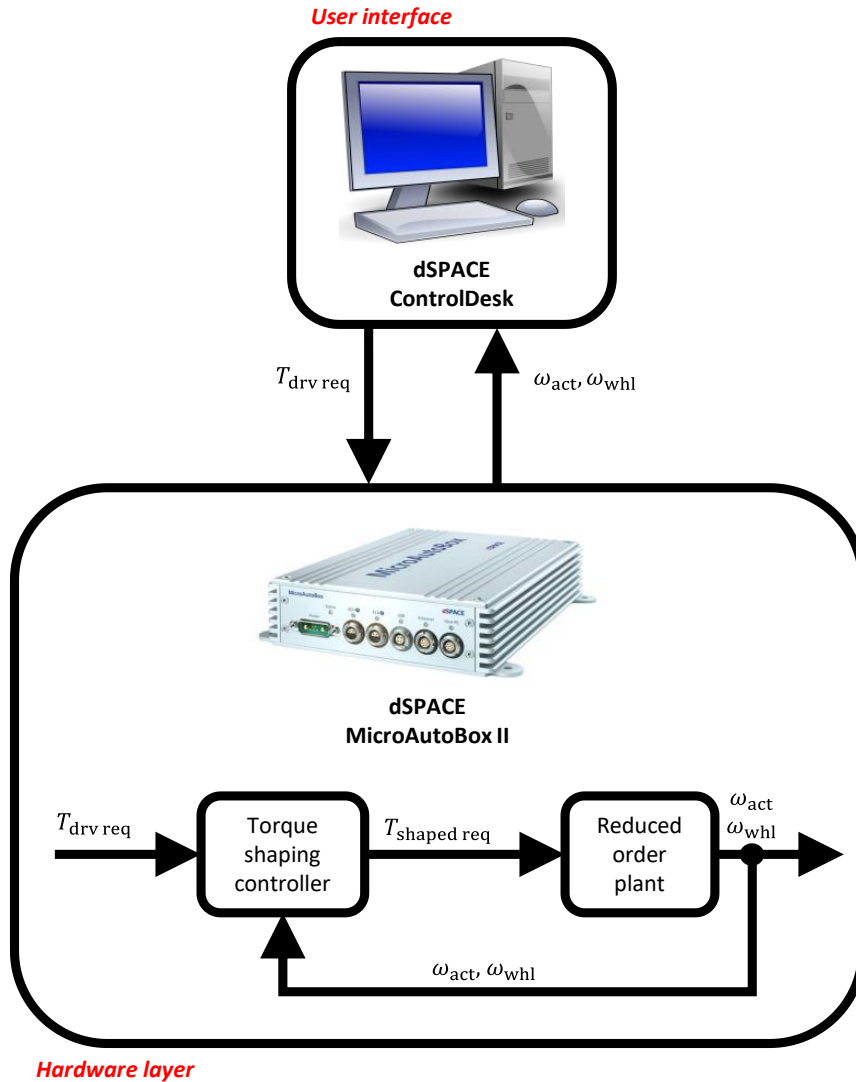


Figure 4.5: Schematic of the PIL setup used to validate the designed controller for real-time usage.

4.4 Uncertainty analysis of clunk controller

In this section, the impact of uncertainty in key vehicle parameters that could affect the performance of the clunk controller is analyzed and methods through which the

Table 4.1

Summary of PIL performance of the designed torque shaping controller on dSPACE MicroAutoBox II.

Controller and plant time (ms)	sample	Turnaround time (ms)	Task overruns (-)
10		1.4e-4	0
5		1.4e-4	0
1		1.4e-4	2

desired behavior of the controller could be maintained are proposed.

Typically, the available model parameters may deviate from the actual parameters of the vehicle for two reasons: (i) part-to-part variations due to manufacturing tolerances, and (ii) changes in certain vehicle parameters due to component wear. Since the backlash mode dynamics for the clunk controller is simplified to a double integrator system, there are only two parameters for which the uncertainty analysis needs to be performed, i.e., the actuator inertia and the estimated torque delivered by the actuator. Uncertainty in the actuator inertia could be due to part to part variations, whereas uncertainty in the estimated torque delivered by the actuator could be due to estimation errors (which itself could be a consequence of the two reasons mentioned above). Uncertainty in either of these parameters might lead to a violation of the impact velocity constraint. Therefore, the effect of each of these uncertainties on the performance of the clunk controller is analyzed.

4.4.1 Uncertainty in actuator inertia

The variation in actuator inertia is characterized as an additive uncertainty [53] which modifies the backlash mode dynamics of the double integrator system as follows:

$$\begin{Bmatrix} \dot{x}_1 \\ \dot{x}_2 \end{Bmatrix} = \begin{bmatrix} 0 & 1 \\ 0 & 0 \end{bmatrix} \begin{Bmatrix} x_1 \\ x_2 \end{Bmatrix} + \begin{bmatrix} 0 \\ 1 \\ \hline J_1(1 \pm \delta_1) \end{bmatrix} \left\{ T_{\text{act}} \right\}, \quad (4.23)$$

where δ_1 represents the uncertainty in the actuator inertia. For this analysis it is assumed that $\delta_1 \in [-0.15, 0.15]$.

First, a closed-loop stability analysis of the system in Eq. (4.23) is performed with the baseline PD controller. The results in Table 4.2 show that the system is closed-loop stable with sufficient stability margin. Next, the effect of this additive uncertainty on the Lyapunov function selected in Eq. (4.10) is checked, and it is observed that the function is valid as long as it is assumed that $\delta_1 < J_{\text{act,model}}$, where $J_{\text{act,model}}$ is the actuator inertia used in the model while performing the reference governor calculations. Since this is a reasonable assumption, it can be concluded that a 15% deviation in the known actuator inertia does not adversely affect the performance of the designed clunk controller.

Table 4.2

Summary of closed-loop stability analysis of the backlash mode system with uncertainties.

Parameter	Type of uncertainty	Closed-loop stable	Gain Margin	Phase margin
Actuator inertia	Additive	Yes	∞	$\approx 65^\circ$
Delivered actuator torque	Multiplicative	Yes	∞	$\approx 65^\circ$

4.4.2 Uncertainty in delivered actuator torque

Next, the variation in actuator delivered torque is represented as multiplicative uncertainty [53] which leads to the following modification in the double integrator system:

$$\begin{Bmatrix} \dot{x}_1 \\ \dot{x}_2 \end{Bmatrix} = \begin{bmatrix} 0 & 1 \\ 0 & 0 \end{bmatrix} \begin{Bmatrix} x_1 \\ x_2 \end{Bmatrix} + \begin{bmatrix} 0 \\ \frac{1 \pm \delta_2}{J_1} \end{bmatrix} \left\{ T_{\text{act}} \right\}, \quad (4.24)$$

where δ_2 is the fractional uncertainty in the delivered actuator torque and it is assumed that $\delta_2 \in [-0.25, 0.25]$. The numerical value of this fractional uncertainty may vary based on the type of actuator (i.e., IC engine or electric motor). However, this does not affect the crux of this analysis. The closed-loop stability analysis of this system with the baseline controller confirms that the system is closed-loop stable (see Table 4.2). Due to the multiplicative uncertainty in Eq. 4.24, the Lie derivative of

the Lyapunov function candidate in Eq. 4.10 changes to:

$$\dot{V}(x) = \begin{bmatrix} \partial V / \partial x_1 & \partial V / \partial x_2 \end{bmatrix} \quad (4.25)$$

$$\begin{bmatrix} x_2 \\ \frac{(k_p(q - x_1) - k_d x_2)(1 \pm \delta_2)}{J_1} \end{bmatrix}, \quad (4.26)$$

$$\dot{V}(x) = \begin{bmatrix} k_d & k_p \\ -\frac{k_d}{J_1} x_2^2 (1 \pm \delta_2) + \frac{k_p}{J_1} (q - x_1) \delta_2 x_2 \end{bmatrix}. \quad (4.27)$$

To ensure negative semi-definiteness of Eq. 4.27 and, consequently, the validity of the chosen Lyapunov function, an additional constraint needs to be added to the initial OCP. Therefore, the revised OCP can be expressed as:

$$\begin{aligned} & \text{maximize} && q(t_c) \\ & \text{subject to} && \\ & && -\alpha \leq q \leq +\alpha, \\ & && -T_{\text{sat}} \leq k_p[q - \theta_b] - k_d[\dot{\theta}_b] \leq T_{\text{sat}}, \\ & && k_p[q - \theta_b(t_c)]^2 - k_p[q - \alpha]^2 + \dot{\theta}_b^2(t_c) \leq v_{\text{im}}^2, \\ & && \left| \frac{k_p}{J_1} (q - x_1) \delta_2 x_2 \right| < \left| \frac{k_d}{J_1} x_2^2 (1 \pm \delta_2) \right|. \end{aligned} \quad (4.28)$$

Adding the additional constraint leads to an expected reduction in the number of

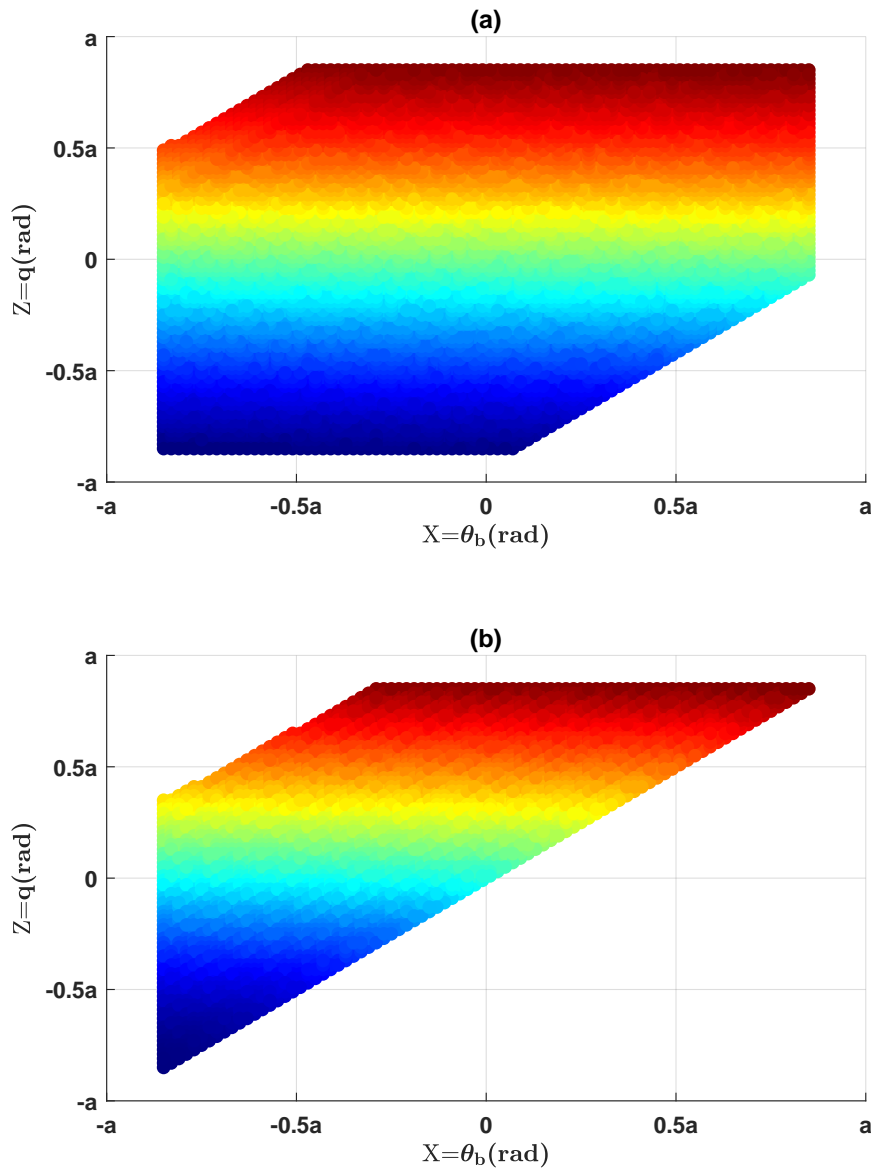


Figure 4.6: Difference between (a) original MOAS and (b) reduced MOAS obtained after compensating for uncertainty in actuator delivered torque. The additional constraint in the modified OCP reduces the number of feasible solutions in (b). Color gradation indicates number of feasible solutions. The maximum number of solutions are available in the blue region, which corresponds to the beginning of lash crossing, and they start to reduce in the green and yellow region with the minimum number of solutions in the red region, which corresponds to the end of lash crossing.

feasible solutions of the OCP, as illustrated by the modified MOAS in Fig. 4.6. Moreover, a reduction in the MOAS also leads to a comparatively conservative behavior of the reference governor. In Fig. 4.7, the behavior of a clunk controller designed using the original MOAS is compared with that of the one designed using the revised MOAS. In the case shown, the actuator is over delivering torque by 25% during the lash crossing scenario. This translates to larger torque values during the start of lash crossing and smaller negative torque value when the lash traversal is about to end. Consequently, with the original controller, the relative speed between the actuator and wheel is comparatively higher during lash crossing and violation of the impact velocity constraint occurs at positive contact.

On the other hand, it is observed that the controller designed with the modified MOAS is: (i) intervening and modifying the reference position earlier than the original controller, (ii) meeting the desired impact velocity constraint and keeping the maximum lash crossing velocity smaller than the original controller, and (iii) traversing lash comparatively slower than the original controller. The slower lash traversal is a result of the smaller MOAS obtained with the additional constraint.

The above analysis shows that making the reference governor robust to the uncertainty in the delivered actuator torque will limit its performance. Since it is assumed that the delivered actuator torque uncertainty takes a range of $[-0.25, 0.25]$, designing the reference governor considering one particular value of δ_2 might not

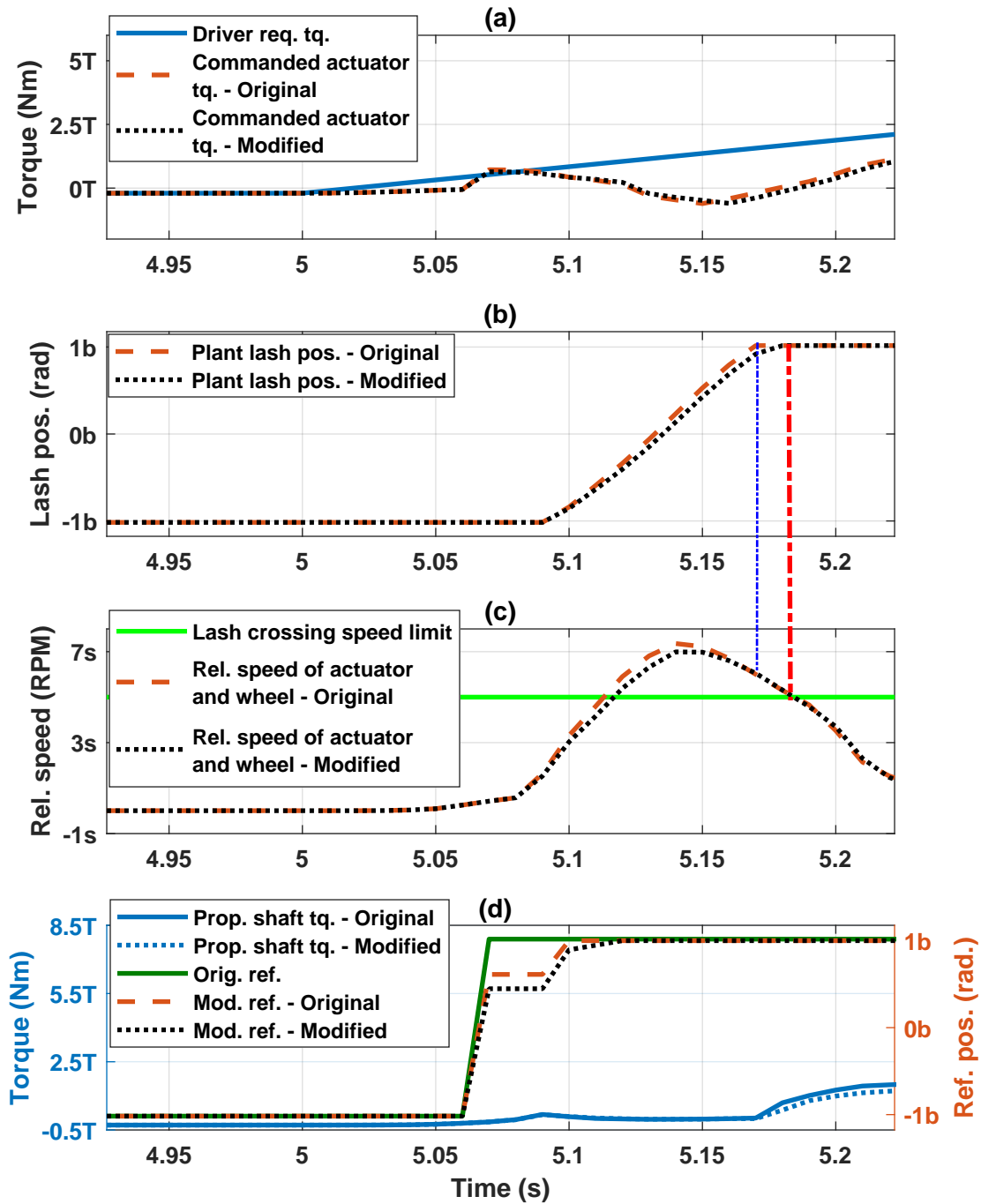


Figure 4.7: Comparison of clunk controller behavior with 25% uncertainty in actuator delivered torque in backlash mode with controllers designed using original and revised MOAS. With the revised MOAS, it is possible to meet impact velocity constraint even with the uncertainty in the delivered actuator torque, albeit with slightly longer lash crossing duration.

result in an optimal output if the true uncertainty is different from the assumed value. To improve optimality, the uncertainty in the actuator torque delivered could be calculated using principles of model-reference adaptive control (MRAC) [53], and multiple LUTs could be developed for different values of uncertainty. Then, at each time step, the calculated uncertainty could be used to decide which reference governor LUT to use for obtaining the modified reference.

4.4.3 Adaptive clunk controller

To illustrate the benefit of designing an adaptive clunk controller, a scenario is assumed where the uncertainty in the delivered actuator torque is initially 10% and increases to 40% as the actuator ages. If the reference governor is designed to compensate only for the initial uncertainty, the clunk controller will start violating the constraints as soon as the uncertainty increases. On the other hand, if the reference governor is designed to compensate the larger uncertainty, the clunk controller will perform conservatively over a majority of the vehicle's life. Therefore, an adaptive clunk controller is proposed that consists of: (i) algorithm to calculate the uncertainty in the delivered actuator torque at each time step, and (ii) multiple MOAS designed for compensating a range of uncertainty in the delivered torque and a switching heuristic to select between these MOAS based on the calculated uncertainty at each time step. The schematic of the proposed adaptive clunk controller is shown in

Fig. 4.8. The remaining components of the torque shaping controller are the same as shown previously in Fig. 4.2.

The uncertainty in the actuator delivered torque is calculated using concepts of MRAC [53]. Using a reference model that consists of actuator torque delivery dynamics (modeled as a 1st order transfer function with rate limits) and lash crossing dynamics from Eq. (4.8), and assuming that the inertia of the actuator is known and constant, the uncertainty, δ_2 , in the delivered actuator torque can be calculated as:

$$T_{\text{del,ideal}} = J_1 \ddot{\theta}_{\text{act,ideal}}, \quad (4.29)$$

$$T_{\text{del,actual}} = T_{\text{del,ideal}} + \delta_2 = J_1 \ddot{\theta}_{\text{act,meas}}, \quad (4.30)$$

$$\delta_2 = J_1 (\ddot{\theta}_{\text{act,meas}} - \ddot{\theta}_{\text{act,ideal}}), \quad (4.31)$$

where $\ddot{\theta}_{\text{act,meas}}$ is the time derivative of measured actuator speed from the actual vehicle, $T_{\text{del,ideal}}$ is the ideal delivered torque calculated using commanded torque and actuator torque delivery dynamics, and $\ddot{\theta}_{\text{act,ideal}}$ is the calculated actuator acceleration obtained from the reference model.

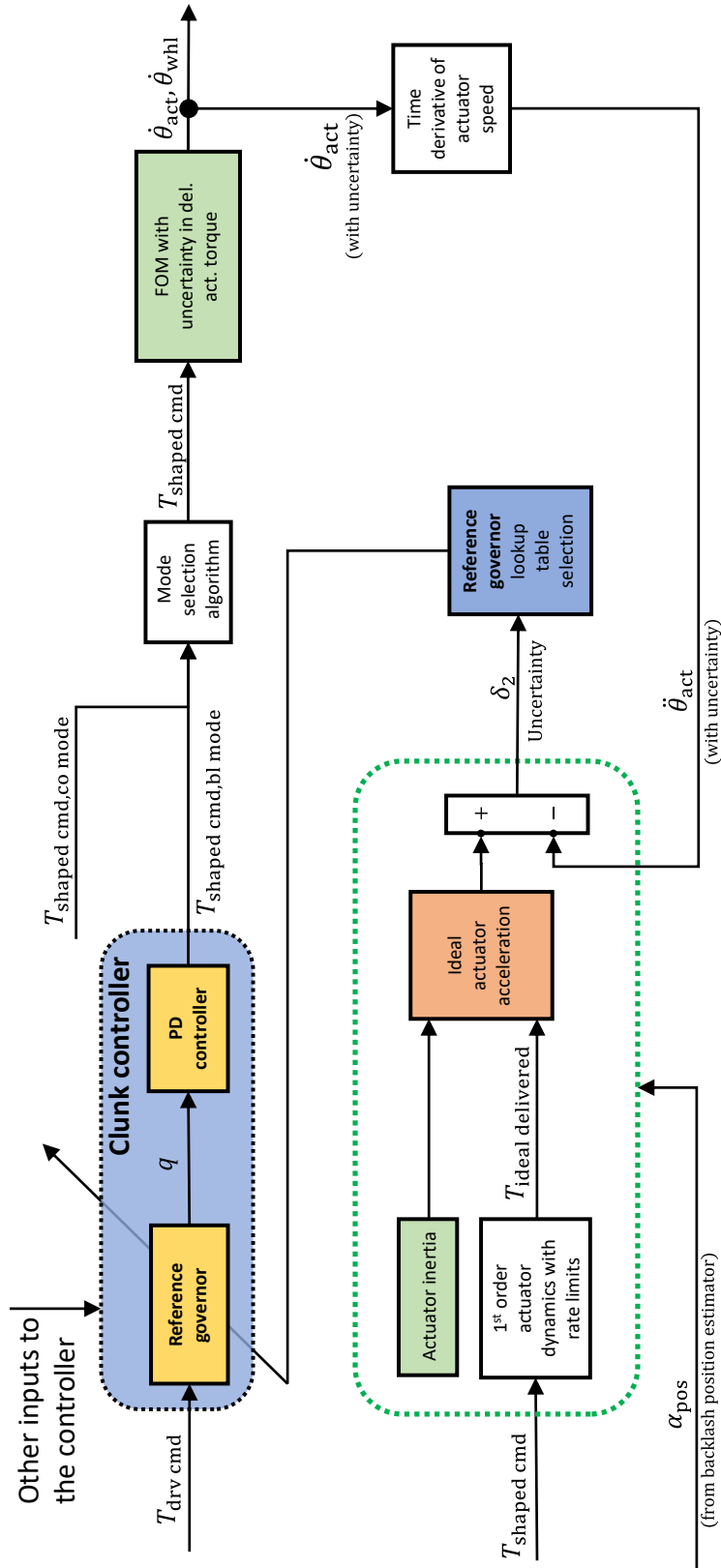


Figure 4.8: Schematic of the proposed adaptive clunk controller. In this schematic, the uncertainty in the delivered actuator torque is being calculated. Note that the remaining elements of the clunk controller as same as shown in Fig. 4.2.

An MOAS is calculated for 10% and 40% uncertainty each in the delivered actuator torque and generate appropriate LUTs. Using the calculated uncertainty from Eq. (4.31), the appropriate LUT is chosen. In Fig. 4.9, the first tip-in has 10% uncertainty in the actuator delivered torque while the second has 40% uncertainty. The performance of the clunk controller is compared for three scenarios: (i) the clunk controller is unaware of the uncertainty in the delivered actuator torque, (ii) the clunk controller has a single LUT generated for 40% uncertainty in the delivered actuator torque, and (iii) the clunk controller has two LUTs generated for 10% and 40% uncertainty and adaptively switches between these tables based on the calculated uncertainty in the delivered actuator torque. In Fig. 4.9(b), it is noticed that when the clunk controller compensates for only 40% uncertainty, the time taken to traverse lash is comparatively higher. This may cause the vehicle to be perceived as sluggish and lead to a potential drivability issue. Therefore, the benefit of the adaptive clunk controller is clear in such scenarios.

The presence of a switching system in the adaptive clunk controller could lead to controller stability concerns. However, it should be noted that the lash traversal event, during which the clunk controller is active, is a fast event in the order of milliseconds. Moreover, the design of the reference governor aims to push the system towards positive contact. Therefore, even if the dwell-time [54] between consecutive switching events is relatively small, the transition to contact mode controller will ensure stability of the system.

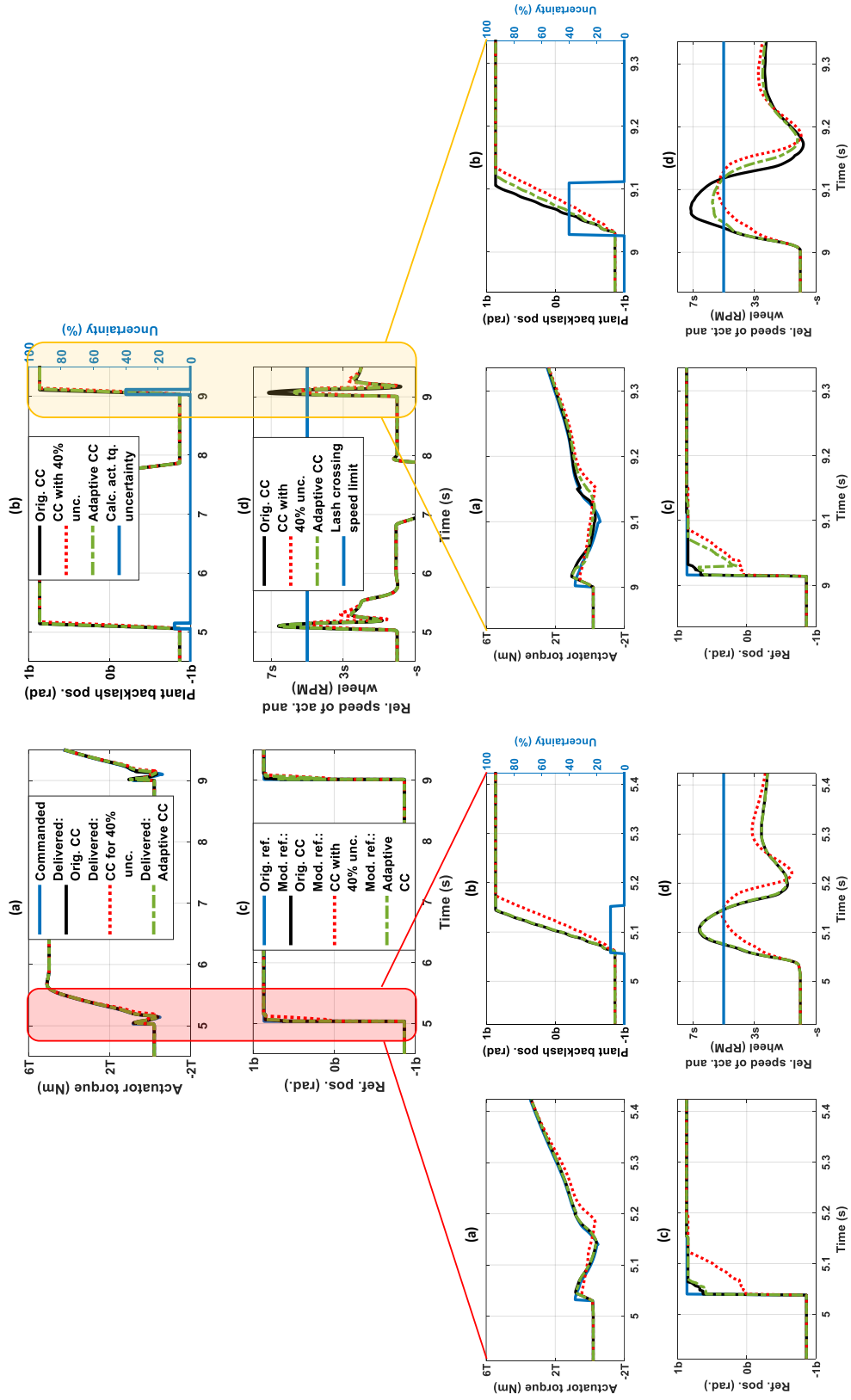


Figure 4-9: Comparison of clunk controller (CC) behavior with 10% and 40% uncertainty in the delivered actuator torque. The performance of the clunk controller is shown for three cases: (i) with original clunk controller, (ii) with clunk controller developed for 40% uncertainty in the delivered actuator torque, and (iii) with clunk controller developed for 10% and 40% uncertainty in the delivered actuator torque. Additional plots show zoomed portions of the tip-ins.

4.5 Robustness analysis of clunk controller

During normal operation of an automobile, it is expected that the designed clunk controller will need to meet the impact velocity constraints for various user inputs and operating conditions. In this section, the robustness of the designed clunk controller is analyzed for some common operating conditions that may have an effect on the performance of the controller.

4.5.1 Robustness to various driver torque requests

During real-world driving, the driver can request torque at a variety of ramp rates. These ramp rates of the driver requested torque can be categorized as small, medium and large tip-in scenarios based on the rate of change of the driver requested torque (see Table 4.3). An acceptable impact velocity is chosen through vehicle testing for these three tip-in scenarios. Consequently, the MOAS is recalculated for these new impact velocity constraints, and new LUTs are generated. The gains of the PD controller, and all other calibration parameters remain the same. Four ramp rates, including the case shown in Fig. 4.4, were considered in this analysis. In Table 4.3 it can be observed that the controller is able to meet the impact velocity constraint in all these cases, with the observed maximum lash crossing velocity during lash traversal

Table 4.3

Summary of performance of the designed clunk controller for variations in ramp rate of driver torque request. Note that the impact velocities are reported in alphanumerical representation ('s') to keep test vehicle parameters confidential.

Torque ramp rate (Nm/s)	Impact velocity constraint (RPM)	Observed impact velocity with clunk controller (RPM)	Maximum lash crossing velocity during lash traversal (RPM)
300	2 s	1.4 s	5 s
1000	5 s	4.9 s	7 s
1700	5 s	4.2 s	6.5 s
Step	7 s	5.5 s	7 s

going above the constraint. This shows that it is possible to achieve fast lash traversal, while keeping clunk within the desired limits just by changing the impact velocity constraint alone.

4.5.2 Robustness to variations in backlash size

The size of backlash in the drivetrain is one of the input parameters (see Eq. (22)) that is used in the OCP to calculate the MOAS. However, the size of the backlash can increase over the lifetime of the vehicle due to wear and it can also vary from vehicle to vehicle due to manufacturing tolerances. Therefore, it is important that the backlash size information is periodically updated in the designed clunk controller for obtaining optimal clunk control. The backlash size estimator from Chapter 3 is able to estimate the backlash size without any prior knowledge of the backlash in the drivetrain. However, it might not be possible for the clunk controller to have

the latest backlash size information at all times. Therefore, the robustness of the controller is tested for scenarios where the true backlash size is not known to the clunk controller.

In Fig. 4.10, the size of the backlash in the plant model increases (see Fig. 4.10 (b)) but the clunk controller is unaware of the change and is unable to compensate for it immediately. In the first two tip-in scenarios neither the backlash position estimator nor the reference governor are aware of the increase in plant backlash size. In these cases a violation of impact velocity constraint can be noticed. In the third tip-in, the change in backlash size is updated inside the backlash position estimator only and it can be clearly observed that the clunk controller meets the impact velocity constraint. Therefore, the clunk controller is robust to the change in backlash size without any modification of the MOAS and the LUTs of the reference governor as long as the backlash position estimator is updated according to the change in backlash size.

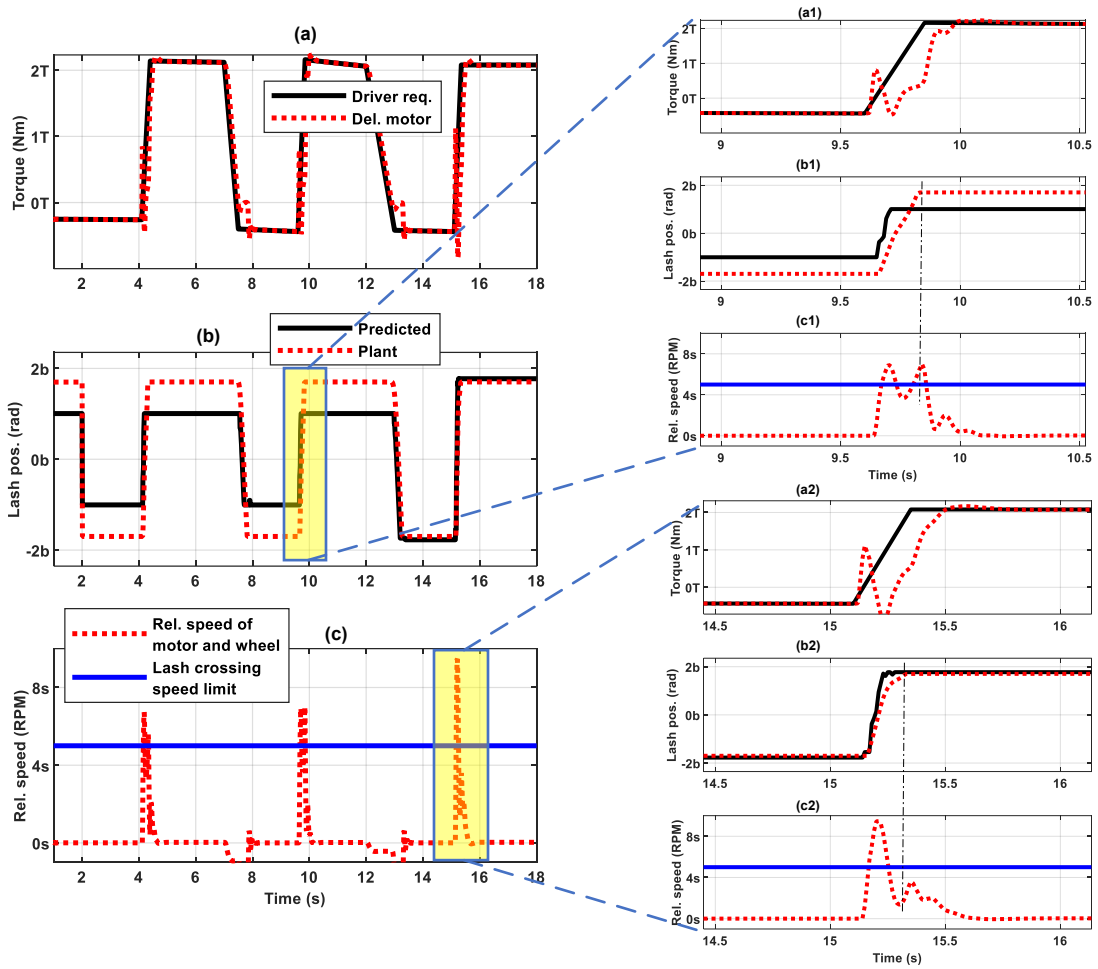


Figure 4.10: Performance of the designed clunk controller when backlash size changes in the vehicle but the controller does not have the updated backlash size information. During the first and second tip-in events, the size of the backlash in the vehicle is larger than the size of the backlash known to the controller. This leads to a violation of the impact velocity constraint (as evident in plot (c1)). The backlash size estimator learns the increase in the backlash size and updates the known backlash size (observed in plot (b2)) by the third tip-in event between $t = 14$ s and $t = 16$ s. Even though the reference governor's MOAS is not updated, the impact velocity constraint is met as seen in plot (c2).

Chapter 5

Integrating the torque shaping controller with other automotive controllers¹

In this chapter, the torque shaping control system developed in the previous chapters (consisting of the backlash position estimator + clunk and shuffle controller) is separately integrated with two other model-based, optimal controllers. In the first section, a model predictive controller developed to reduce ‘torque lag’ in automotive torque converters is added to the torque shaping clunk and shuffle controller. From Chapters 2 through 4 of this thesis, it was assumed that the torque converter lock-up

¹The first half of this chapter first appeared in an SAE journal paper[9]. Letter of permission to republish from SAE is included in Appendix C.

clutch remains locked as this is the standard operating scenario for the driveline torque shaping controller. Through this integration, the application of the torque shaping clunk and shuffle controller is being expanded to the cases where the torque converter lock-up clutch starts slipping. In the second half of this chapter (Section 5.2), an economic-nonlinear model predictive engine controller designed to track engine torque requests while reducing fuel consumption and oxides of Nitrogen (NO_x) emissions is integrated with the torque shaping clunk and shuffle controller. Through this integration, a proof of concept showing coordinated control between two complex control systems is demonstrated.

5.1 Integration with the torque converter torque lag (TCTL) controller

In automobiles with an IC engine actuator and a torque converter with lock-up clutch functionality, certain driving scenarios with the lock-up clutch locked could cause engine speed vibrations to be transmitted to the driveline and affect the drivability of the vehicle. E.g., at lower engine speeds with a locked TCC, when the driver demand increases rapidly during a tip-in event, it is possible for low frequency engine vibrations to propagate through the driveline [55, 56]. These low frequency vibrations most commonly originate due to the discrete firing of engine cylinders. The amplitude

and frequency of these vibrations vary with engine speed, and depend on the number and configuration of the engine cylinders [56]. During such scenarios, it is desirable to allow the torque converter to slip for a brief period of time to increase the damping in the driveline due to the fluid path of the torque converter. This increased damping can reduce the unwanted vibrations from the IC engine. However, when the TCC starts to slip, there is an abrupt reduction in the torque delivered to the wheels which can be attributed to the fluid path dynamics of the torque converter. This reduction in the torque at the torque converter turbine, and subsequently at the wheels, is called “torque lag” in this work. This is illustrated in Fig. 5.1, when the driver rapidly requests torque and the TCC starts to slip while the engine is delivering the requested torque. While the actuator delivers the commanded torque (see Fig. 5.1(a)), it is evident in Fig. 5.1(b) and (c) that the turbine and propeller shaft torque significantly different for the cases when the TCC is locked and slipping while delivering the driver requested torque. The torque lag phenomenon causes the driver to perceive the vehicle as feeling sluggish and, therefore, it is necessary to optimally control the slip of the TCC while delivering the shaped torque request and for keeping the drivability of the vehicle close to the case when the TCC is locked. To that end, a model predictive controller (MPC) is designed to reduce the torque lag and its operation with the torque shaping clunk and shuffle controller is demonstrated. This controller is referred to as the torque converter torque lag (TCTL) controller in this thesis.

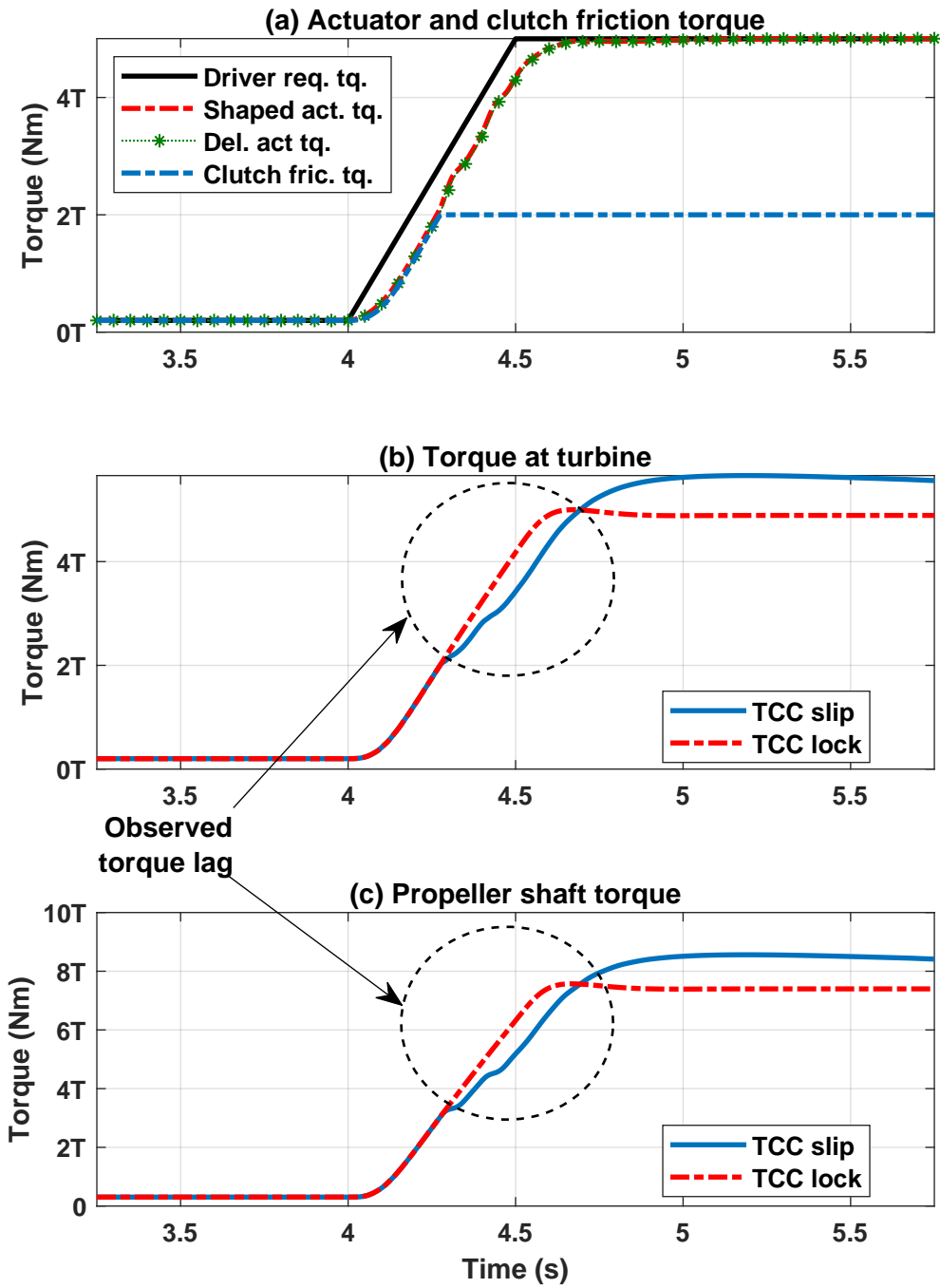


Figure 5.1: Torque lag in a vehicle powertrain due to a slipping torque converter.

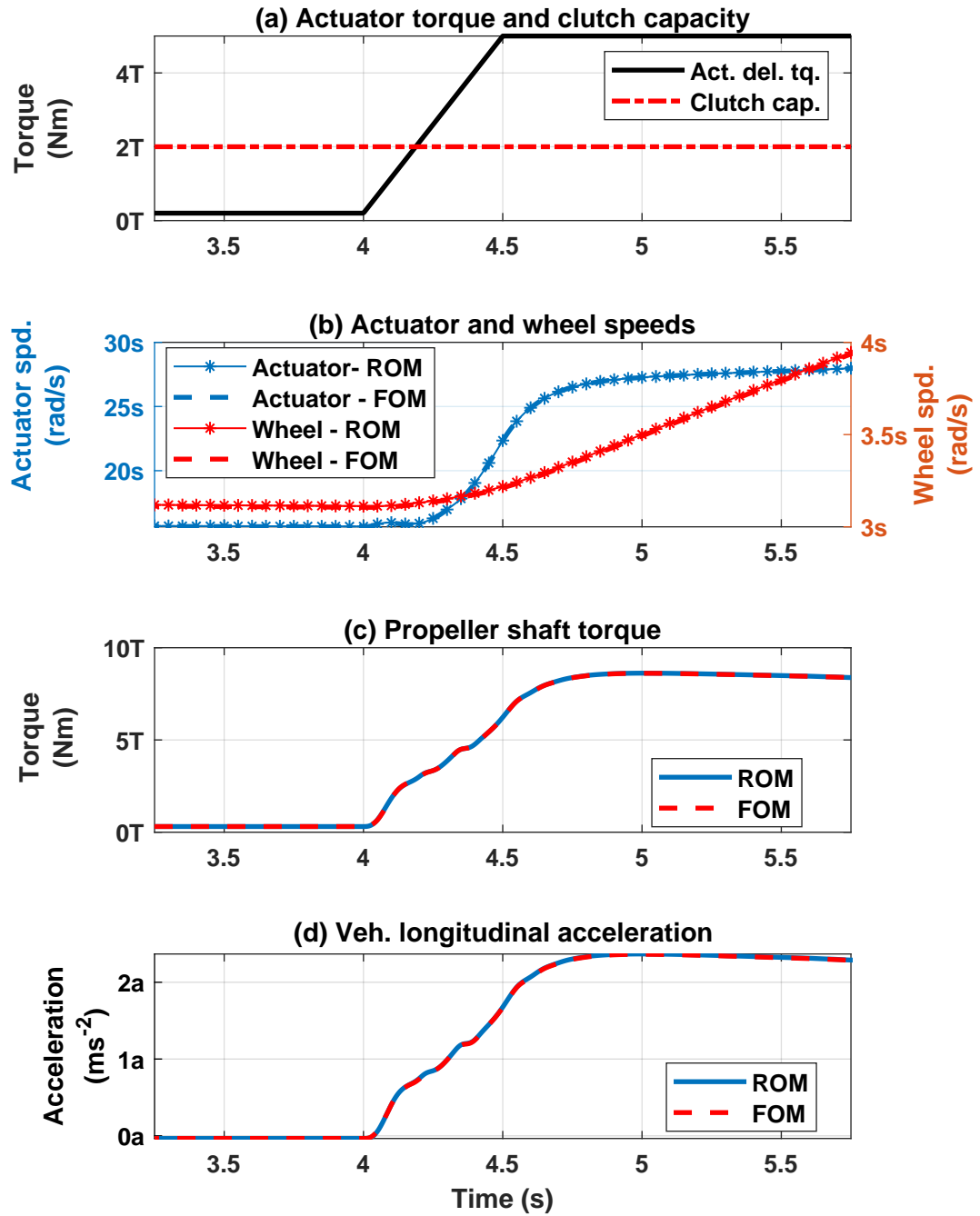


Figure 5.2: Comparison of FOM and ROM outputs with a slipping torque converter.

Previous work in this domain can be split into: (i) torque converter modeling for controls applications, and (ii) estimation and control algorithms for torque converters with a lock-up clutch. A physics based torque converter model was introduced in [57], which uses first-order differential equations for the impeller, turbine and the working fluid of the torque converter. In [58], a detailed bond graph-based torque converter model is developed. In [59], a lookup table-based method is used to represent the dynamics of the torque converter. Experimental testing is performed with the torque converter to capture relations between the speed ratio (SR), torque ratio (TR) and capacity factor (K_{cap}) and these are stored as lookup tables. In [60], algebraic equations are used to capture the torque converter dynamics. Other researchers (e.g., [61, 62]) propose application specific models of the torque converter. For MPC, the Kotwicki-based modeling approach [60] is found to be most suitable and, therefore, is chosen for this work.

Some of the estimation and control algorithms mentioned in the previous chapters could also be used for controlling TCC slip. Since the goal here is to reduce the torque lag in the torque converter by manipulating the actuator torque request and the slip in the TCC while staying within the constraints of the system, an MPC approach is chosen as the desired control algorithm.

The dynamics of the torque converter are split into mechanical friction and fluid paths. The mechanical friction path transmits torque through the torque converter

clutch and the fluid path transmits through hydrokinetics between the impeller and turbine. These paths are illustrated in Fig. 5.3. The dynamics of the fluid path are modeled using TR vs. SR, and TR vs. K_{cap} maps. Additionally, the transient dynamics of the fluid path are included as first order dynamics in the model (e.g., refer [63],[64]), while also including the hysteresis of the lock up clutch. The capacity of the lock up clutch is defined in terms of the amount of torque that the clutch can transfer.

The full-order plant model used for model-in-the-loop (MIL) testing and validation of the integrated control system in this section is the same as that developed in Chapter 2, with the torque converter lock up clutch allowed to slip in this case.

5.1.1 Control-oriented model for slipping torque converter

The control-oriented model (COM) developed in Chapter 2 and its driveline equations (2.35 to 2.42) are slightly modified to include the dynamics of a slipping torque converter lock-up clutch. The modified schematic of the COM is illustrated in Fig. 5.4. Accordingly, the equations of motion of the COM from Chapter 2 are modified as shown below:

$$T_{act} - T_{imp,fluid} - T_{TCC} = J_1 \ddot{\theta}_{act}, \quad (5.1)$$

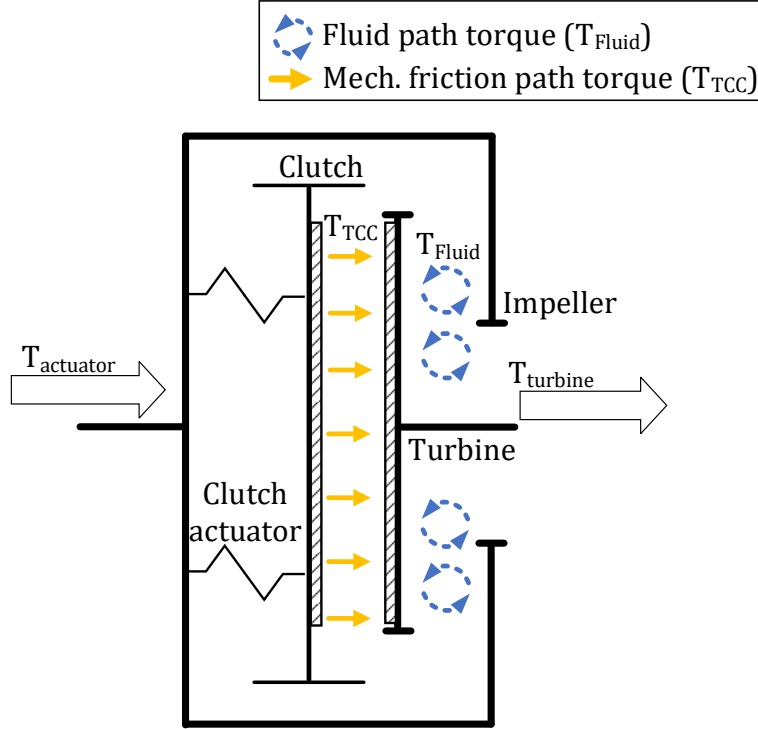


Figure 5.3: Schematic of a torque converter equipped with a lock-up clutch. The fluid path and the mechanical path of torque transmission are illustrated.

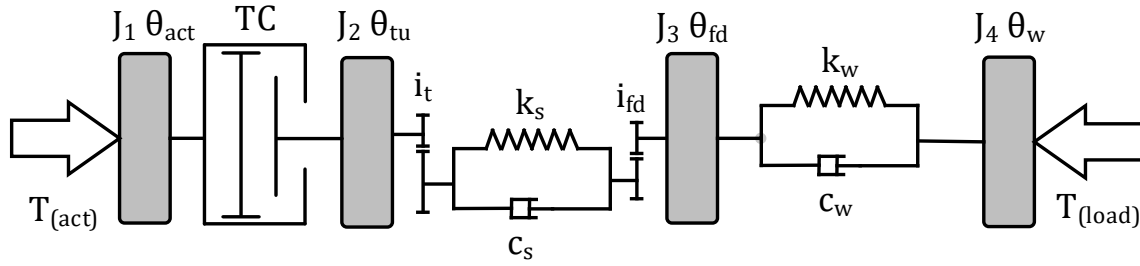


Figure 5.4: Schematic of the COM designed to capture the torque lag dynamics.

Torque multiplication mode ($\frac{\dot{\theta}_{tu}}{\dot{\theta}_{imp}} \leq 0.95$):

$$T_{imp,fluid} = \alpha_{1,act} \dot{\theta}_{act}^2 + \alpha_{2,act} \dot{\theta}_{act} \dot{\theta}_{tu} + \alpha_{3,act} \dot{\theta}_{tu}^2, \quad (5.2)$$

$$T_{\text{tu,fluid}} = \alpha_{1,\text{tu}}\dot{\theta}_{\text{act}}^2 + \alpha_{2,\text{tu}}\dot{\theta}_{\text{act}}\dot{\theta}_{\text{tu}} + \alpha_{3,\text{tu}}\dot{\theta}_{\text{tu}}^2, \quad (5.3)$$

Fluid coupling mode ($0.95 < \frac{\dot{\theta}_{\text{tu}}}{\dot{\theta}_{\text{imp}}} \leq 1$):

$$\begin{aligned} T_{\text{imp,fluid}} &= T_{\text{tu,fluid}} \\ &= \alpha_{1,\text{fc}}\dot{\theta}_{\text{act}}^2 + \alpha_{2,\text{fc}}\dot{\theta}_{\text{act}}\dot{\theta}_{\text{tu}} + \alpha_{3,\text{fc}}\dot{\theta}_{\text{tu}}^2, \end{aligned} \quad (5.4)$$

$$T_{\text{tu,fluid}} + T_{\text{TCC}} - \frac{T_{\text{s}}}{i_{\text{t}}} = J_2\ddot{\theta}_{\text{tu}}, \quad (5.5)$$

$$T_{\text{s}} = k_{\text{s}}\left(\frac{\theta_{\text{tu}}}{i_{\text{t}}} - \theta_{\text{fd}}i_{\text{fd}}\right) + c_{\text{s}}\left(\frac{\dot{\theta}_{\text{tu}}}{i_{\text{t}}} - \dot{\theta}_{\text{fd}}i_{\text{fd}}\right), \quad (5.6)$$

$$T_{\text{s}}i_{\text{fd}} - T_{\text{w}} = J_3\ddot{\theta}_{\text{fd}}, \quad (5.7)$$

$$T_{\text{w}} = k_{\text{w}}(\theta_{\text{fd}} - \theta_{\text{w}}) + c_{\text{w}}(\dot{\theta}_{\text{fd}} - \dot{\theta}_{\text{w}}), \quad (5.8)$$

$$T_{\text{w}} - F_{\text{load}}r_{\text{T}} = (J_4 + M_{\text{rT}}^2)\ddot{\theta}_{\text{w}}, \quad (5.9)$$

where $\alpha_{1,\text{act}}, \alpha_{2,\text{act}}, \alpha_{3,\text{act}}, \alpha_{1,\text{tu}}, \alpha_{2,\text{tu}}, \alpha_{3,\text{tu}}, \alpha_{1,\text{fc}}, \alpha_{2,\text{fc}}, \alpha_{3,\text{fc}}$ are the Kotwicki coefficients, and are obtained using simulation data from the FOM and the parameter estimation tool in MATLAB.

The above equations (5.1 - 5.9) are used to develop a state space model of the driveline such that it can predict the performance of the system with sufficient accuracy over the prediction horizon in MPC. First, the nonlinear model equations of the torque converter are linearized for known equilibrium points using Equations (5.1)

to (5.5). Each equilibrium point is defined using the impeller and turbine speed measurements from the FOM for each time step. The equations (5.10) and (5.11) below are obtained from the linearization of the nonlinear torque converter model for torque multiplication mode:

$$\begin{aligned} \delta T_{\text{act}} - (2\alpha_{1,\text{act}}\dot{\theta}_{\text{act,eq}} + \alpha_{2,\text{act}}\dot{\theta}_{\text{tu,eq}})\delta\dot{\theta}_{\text{act}} - (2\alpha_{3,\text{act}}\dot{\theta}_{\text{tu,eq}} + \alpha_{2,\text{act}}\dot{\theta}_{\text{act,eq}})\delta\dot{\theta}_{\text{tu}} - \delta T_{\text{TCC}} \\ = J_1\delta\ddot{\theta}_{\text{act}}, \end{aligned} \quad (5.10)$$

$$\begin{aligned} (2\alpha_{1,\text{tu}}\dot{\theta}_{\text{act,eq}} + \alpha_{2,\text{tu}}\dot{\theta}_{\text{tu,eq}})\delta\dot{\theta}_{\text{act}} + (2\alpha_{3,\text{tu}}\dot{\theta}_{\text{tu,eq}} + \alpha_{2,\text{tu}}\dot{\theta}_{\text{act,eq}})\delta\dot{\theta}_{\text{tu}} + \delta T_{\text{TCC}} - \frac{\delta T_{\text{s}}}{i_T} \\ = J_2\delta\ddot{\theta}_{\text{tu}}, \end{aligned} \quad (5.11)$$

Similarly, for fluid coupling mode the Equations (5.12) and (5.13) are derived as:

$$\begin{aligned} \delta T_{\text{act}} - (2\alpha_{1,\text{fc}}\dot{\theta}_{\text{act,eq}} + \alpha_{2,\text{fc}}\dot{\theta}_{\text{tu,eq}})\delta\dot{\theta}_{\text{act}} - (2\alpha_{3,\text{fc}}\dot{\theta}_{\text{tu,eq}} + \alpha_{2,\text{fc}}\dot{\theta}_{\text{act,eq}})\delta\dot{\theta}_{\text{tu}} - \delta T_{\text{TCC}} \\ = J_1\delta\ddot{\theta}_{\text{act}}, \end{aligned} \quad (5.12)$$

$$\begin{aligned} (2\alpha_{1,\text{fc}}\dot{\theta}_{\text{act,eq}} + \alpha_{2,\text{fc}}\dot{\theta}_{\text{tu,eq}})\delta\dot{\theta}_{\text{act}} + (2\alpha_{3,\text{fc}}\dot{\theta}_{\text{tu,eq}} + \alpha_{2,\text{fc}}\dot{\theta}_{\text{act,eq}})\delta\dot{\theta}_{\text{tu}} + \delta T_{\text{TCC}} - \frac{\delta T_{\text{s}}}{i_T} \\ = J_2\delta\ddot{\theta}_{\text{tu}}, \end{aligned} \quad (5.13)$$

where the prefix δ represents a small linear variation of the variable from its

equilibrium point value, and the subscript ‘eq’ denotes the equilibrium point.

The linearized equations (5.10 to 5.13) are combined with the remaining equations (5.6 to 5.9) of the drivetrain. The final state space representation of the driveline system with a slipping TCC is given by:

$$\delta\mathbf{X}_{k+1} = \mathbf{A}\delta\mathbf{X}_k + \mathbf{B}\delta\mathbf{u}_k + \mathbf{G}\delta\mathbf{d}_k, \quad (5.14)$$

$$\delta\mathbf{Y}_{k+1} = \mathbf{C}\delta\mathbf{X}_{k+1} + \mathbf{D}\delta\mathbf{u}_{k+1}, \quad (5.15)$$

where δX_k represents the small linear variation of the states from their corresponding equilibrium point value, at any k^{th} time step. Further, the small linear differences in states (δX), inputs (δu), outputs (δY) and disturbances (δd) to the state space model in Equations (5.14) and (5.15) are given as

$$\delta\mathbf{X} = \begin{bmatrix} \delta\dot{\theta}_{\text{act}} & \delta T_{\text{imp,fluid}} & \delta T_{\text{tu,fluid}} & \delta\dot{\theta}_{\text{tu}} & \dots \\ \dots & \left(\frac{\delta\theta_{\text{tu}}}{i_t} - \delta\theta_{\text{fd}}i_{\text{fd}}\right) & (\delta\theta_{\text{fd}} - \delta\theta_{\text{w}}) & \delta\dot{\theta}_{\text{fd}} & \delta\dot{\theta}_{\text{w}} \end{bmatrix}^T, \quad (5.16)$$

$$\delta\mathbf{Y} = \begin{bmatrix} \delta T_{\text{tu}} \end{bmatrix}, \quad (5.17)$$

$$\delta\mathbf{u} = \begin{bmatrix} \delta T_{\text{act}} & \delta T_{\text{TCC}} \end{bmatrix}^T, \quad (5.18)$$

$$\delta\mathbf{d} = \begin{bmatrix} \delta F_{\text{load}} \end{bmatrix}. \quad (5.19)$$

Furthermore, the \mathbf{A} , \mathbf{B} , \mathbf{C} , \mathbf{D} and \mathbf{G} matrices from Equations (5.14) and (5.15) are

shown in the continuous domain below. These are discretized using Tustin approach at a time step of 10 ms for implementing within the rapid prototyping controller.

$$\mathbf{A} = \begin{bmatrix} 0 & \frac{-1}{J_1} & 0 & 0 & 0 & 0 & 0 & 0 \\ \frac{a_1}{\tau} & \frac{-1}{\tau} & 0 & \frac{a_2}{\tau} & 0 & 0 & 0 & 0 \\ \frac{b_1}{\tau} & 0 & \frac{-1}{\tau} & \frac{b_2}{\tau} & 0 & 0 & 0 & 0 \\ 0 & 0 & \frac{1}{J_2} & \frac{-c_s}{J_2 i_t^2} & \frac{-k_s}{J_2 i_t} & 0 & \frac{c_s i_{fd}}{J_2 i_t} & 0 \\ 0 & 0 & 0 & \frac{1}{i_t} & 0 & 0 & -i_{fd} & 0 \\ 0 & 0 & 0 & 0 & 0 & 0 & 1 & -1 \\ 0 & 0 & 0 & \frac{c_s i_{fd}}{J_3 i_t} & \frac{k_s i_{fd}}{J_3} & \frac{-k_w}{J_3} & \frac{-a}{J_3} & \frac{c_w}{J_3} \\ 0 & 0 & 0 & 0 & 0 & \frac{k_w}{b} & \frac{c_w}{b} & \frac{-c_w}{b} \end{bmatrix}, \quad (5.20)$$

$$\mathbf{B} = \begin{bmatrix} \frac{1}{J_1} & 0 & 0 & 0 & 0 & 0 & 0 & 0 \\ -\frac{1}{J_1} & 0 & 0 & \frac{1}{J_2} & 0 & 0 & 0 & 0 \end{bmatrix}^T, \quad (5.21)$$

$$\mathbf{C} = \begin{bmatrix} 0 & 0 & 1 & 0 & 0 & 0 & 0 & 0 \end{bmatrix}, \quad (5.22)$$

$$\mathbf{D} = \begin{bmatrix} 0 & 1 \end{bmatrix}, \quad (5.23)$$

$$\mathbf{G} = \left[0 \quad 0 \quad 0 \quad 0 \quad 0 \quad 0 \quad 0 \quad -\frac{r_T}{b} \right]^T, \quad (5.24)$$

where a_1 , a_2 , b_1 and b_2 are defined for the two modes of torque converter operation as follows:

(i) Torque multiplication mode $\left(\frac{\dot{\theta}_{tu}}{\dot{\theta}_{imp}} \leq 0.95 \right)$:

$$a_1 = 2\alpha_{1,act}\dot{\theta}_{act,eq} + \alpha_{2,act}\dot{\theta}_{tu,eq}, \quad a_2 = 2\alpha_{3,act}\dot{\theta}_{tu,eq} + \alpha_{2,act}\dot{\theta}_{act,eq},$$

$$b_1 = 2\alpha_{1,tu}\dot{\theta}_{act,eq} + \alpha_{2,tu}\dot{\theta}_{tu,eq}, \quad b_2 = 2\alpha_{3,tu}\dot{\theta}_{tu,eq} + \alpha_{2,tu}\dot{\theta}_{act,eq},$$

(ii) Fluid coupling mode $\left(0.95 < \frac{\dot{\theta}_{tu}}{\dot{\theta}_{imp}} \leq 1 \right)$:

$$a_1 = b_1 = 2\alpha_{1,fc}\dot{\theta}_{act,eq} + \alpha_{2,fc}\dot{\theta}_{tu,eq}, \quad a_2 = b_2 = 2\alpha_{3,fc}\dot{\theta}_{tu,eq} + \alpha_{2,fc}\dot{\theta}_{act,eq}.$$

Additionally, in the state matrix \mathbf{A} in Eq. (5.20), τ represents the time constant of the first order dynamics for the fluid path of torque converter, while the constants a and b are given by

$$a = c_s i_{fd}^2 + c_w, \quad b = J_4 + M.r_T^2.$$

5.1.2 TCTL Controller design

The design of the TCTL controller can be split into: (i) setting up the prediction model, (ii) defining the constraints of the system, and (iii) setting up the optimization problem. The shuffle controller from Chapter 4 commands a shaped torque request, which the designed TCTL controller tracks by controlling the actuator torque command and the lock-up clutch capacity. The TCTL controller uses readily available driveline signals such as commanded actuator torque, available clutch capacity, measured speeds from the impeller, turbine and wheels as the measured variables. The schematic layout of the TCTL controller is shown in Fig. 5.5.

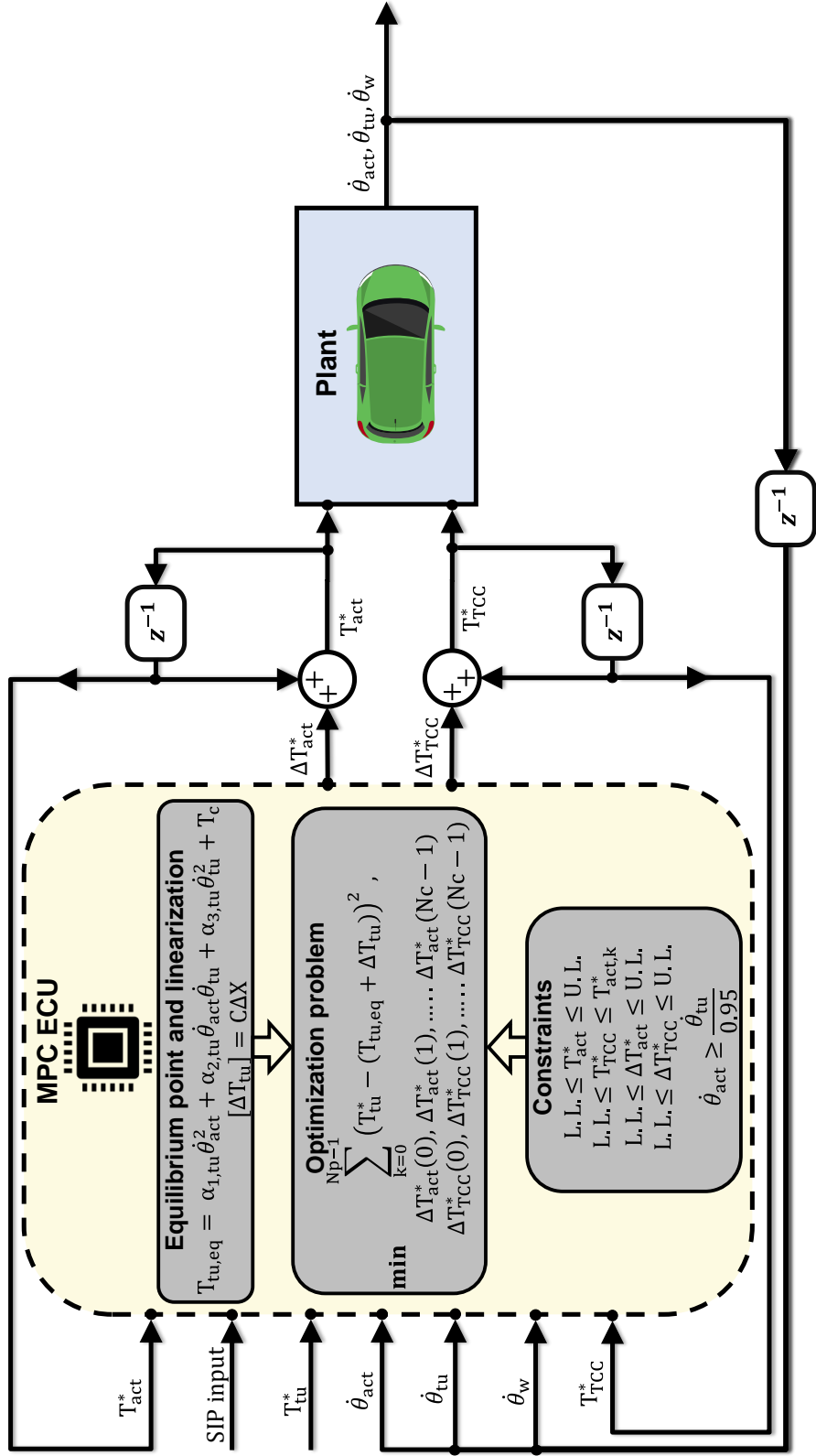


Figure 5.5: Schematic of torque converter torque lag (TCTL) controller designed in this work.

5.1.2.1 Augmentation of the state space model

The optimization problem is set up such that the optimal changes in the actuator torque, ΔT_{act} , and clutch capacity, ΔT_{TCC} , (also termed as manipulated variables) are determined. The optimization of change in actuator torque and clutch capacity is chosen because of the convenience in setting up the constrained optimization algorithm using this approach. To that end, the state space model developed in the previous section is augmented to consist of magnitude of state change (ΔX) and magnitude of input change (Δu). The state space model from Equations (5.14) and (5.15) is represented in terms of change of input, state and output vectors as:

$$\Delta X_{k+1} = A\Delta X_k + B\Delta u_k \quad (5.25)$$

$$Y_{k+1} = C\Delta X_{k+1} + D\Delta u_{k+1} + Y_k, \quad (5.26)$$

The road load, δd_k , is assumed to be constant over the linear prediction window and hence Δd_k is taken to be 0. Furthermore, the modified state space model represented by Equations (5.25) and (5.26) is written in the augmented form as

$$X_{\text{ag},k+1} = A_{\text{ag}}X_{\text{ag},k} + B_{\text{ag}}\Delta u_k \quad (5.27)$$

$$Y_{k+1} = C_{\text{ag}}X_{\text{ag},k+1} \quad (5.28)$$

where

$$X_{\text{ag},k} = \begin{bmatrix} \Delta X_k \\ Y_k \end{bmatrix}, \quad A_{\text{ag}} = \begin{bmatrix} A & 0 \\ CA & I \end{bmatrix}, \quad B_{\text{ag}} = \begin{bmatrix} B \\ CB \end{bmatrix}, \quad C_{\text{ag}} = \begin{bmatrix} 0 & I \end{bmatrix}.$$

5.1.2.2 Prediction model

The prediction model inside the MPC is based on the augmented state space model to predict the future outputs over the prediction horizon, $N_p = 10$ steps, and control

horizon, $N_c = 10$ steps. The final model is represented as:

$$\begin{bmatrix} Y_{k+1} \\ Y_{k+2} \\ \vdots \\ Y_{k+N_p} \end{bmatrix}_{10 \times 1} = \begin{bmatrix} C_{ag} A_{ag} \\ C_{ag} A_{ag}^2 \\ \vdots \\ C_{ag} A_{ag}^{N_p} \end{bmatrix}_{10 \times 1} \cdot X_{ag,k} + \begin{bmatrix} C_{ag} B_{ag} & 0 & \dots & 0 \\ C_{ag} A_{ag} B_{ag} & C_{ag} B_{ag} & \dots & 0 \\ \vdots & \vdots & \vdots & \vdots \\ C_{ag} A_{ag}^{N_p-1} B_{ag} & C_{ag} A_{ag}^{N_p-2} B_{ag} & \dots & C_{ag} A_{ag}^{N_p-N_c} B_{ag} \end{bmatrix}_{10 \times 10} \cdot \begin{bmatrix} \Delta u_k \\ \Delta u_{k+1} \\ \vdots \\ \Delta u_{k+N_c-1} \end{bmatrix}_{10 \times 1}. \quad (5.29)$$

The Equation (5.29) is denoted in the following shortened notation:

$$Y = P X_{ag,k} + H \Delta U. \quad (5.30)$$

5.1.2.3 Actuator and Driveline Constraints

Next, the physical constraints of the actuator and the driveline are set up in the optimization problem to make the controller aware of the physical limitations of the system.

Constraints on rate of input:

Both the IC engine and the torque converter clutch are physically rate limited in the amount of torque they are able to deliver, and this is captured as a constraint as shown below:

$$T_{\text{act rate,low}} \leq \dot{T}_{\text{act}} \leq T_{\text{act rate,up}}, \quad (5.31)$$

$$T_{\text{TCC rate,low}} \leq \dot{T}_{\text{TCC}} \leq T_{\text{TCC rate,up}}, \quad (5.32)$$

where $T_{\text{act rate,low}}$ and $T_{\text{act rate,up}}$ are the lower and upper limits on rate of delivered actuator torque, and $T_{\text{TCC rate,low}}$ and $T_{\text{TCC rate,up}}$ are the lower and upper limits for the rate of change of TCC capacity, respectively. These constraints can be set up in a matrix inequality form over the prediction horizon (N_p) and control horizon (N_c) as:

$$\begin{bmatrix}
\mathbf{I} & 0 & 0 & \dots & 0 \\
0 & \mathbf{I} & 0 & \dots & 0 \\
\vdots & \vdots & \vdots & \vdots & \vdots \\
0 & 0 & 0 & \dots & \mathbf{I} \\
-\mathbf{I} & 0 & 0 & \dots & 0 \\
0 & -\mathbf{I} & 0 & \dots & 0 \\
\vdots & \vdots & \vdots & \vdots & \vdots \\
0 & 0 & 0 & \dots & -\mathbf{I}
\end{bmatrix}_{20 \times 10}
\begin{bmatrix}
\Delta u_k \\
\Delta u_{k+1} \\
\vdots \\
\Delta u_{k+N_c-1}
\end{bmatrix}_{10 \times 1}
\leq
\begin{bmatrix}
\Delta u_{\max} \\
\Delta u_{\max} \\
\vdots \\
\Delta u_{\max} \\
-\Delta u_{\min} \\
-\Delta u_{\min} \\
\vdots \\
-\Delta u_{\min}
\end{bmatrix}_{20 \times 1}, \quad (5.33)$$

denoted by a shortened notation as:

$$\mathbf{M}_1 \Delta \mathbf{U} \leq \Gamma_1. \quad (5.34)$$

Constraints on magnitude of input:

The magnitude of the actuator torque and the TCC capacity torque are confined within the following range:

$$0 \leq T_{\text{act}} \leq 500 \text{ Nm}, \quad (5.35)$$

$$0 \leq T_{\text{TCC}} \leq T_{\text{act,eq}} \text{ Nm}. \quad (5.36)$$

Further, these inequalities are written in the matrix inequality form over N_p and N_c

as

$$\begin{bmatrix} \mathbf{I} & 0 & 0 & \dots & 0 \\ 0 & \mathbf{I} & 0 & \dots & 0 \\ \vdots & \vdots & \vdots & \vdots & \vdots \\ 0 & 0 & 0 & \dots & \mathbf{I} \\ -\mathbf{I} & 0 & 0 & \dots & 0 \\ 0 & -\mathbf{I} & 0 & \dots & 0 \\ \vdots & \vdots & \vdots & \vdots & \vdots \\ 0 & 0 & 0 & \dots & -\mathbf{I} \end{bmatrix}_{20 \times 10} \begin{bmatrix} \mathbf{u}_k \\ \mathbf{u}_{k+1} \\ \vdots \\ \mathbf{u}_{k+N_c-1} \end{bmatrix}_{10 \times 1} \leq \begin{bmatrix} \mathbf{u}_{\max} \\ \mathbf{u}_{\max} \\ \vdots \\ \mathbf{u}_{\max} \\ -\mathbf{u}_{\min} \\ -\mathbf{u}_{\min} \\ \vdots \\ -\mathbf{u}_{\min} \end{bmatrix}_{20 \times 1}, \quad (5.37)$$

where

$$\begin{bmatrix} \mathbf{u}_k \\ \mathbf{u}_{k+1} \\ \vdots \\ \mathbf{u}_{k+N_c-1} \end{bmatrix}_{10 \times 1} = \begin{bmatrix} \mathbf{I} \\ \mathbf{I} \\ \vdots \\ \mathbf{I} \end{bmatrix}_{10 \times 1} \mathbf{u}_{\text{eq}} + \begin{bmatrix} \mathbf{I} & 0 & 0 & \dots & 0 \\ \mathbf{I} & \mathbf{I} & 0 & \dots & 0 \\ \vdots & \vdots & \vdots & \vdots & \vdots \\ \mathbf{I} & \mathbf{I} & \mathbf{I} & \dots & \mathbf{I} \end{bmatrix}_{10 \times 10} \begin{bmatrix} \Delta \mathbf{u}_k \\ \Delta \mathbf{u}_{k+1} \\ \vdots \\ \Delta \mathbf{u}_{k+N_c-1} \end{bmatrix}_{10 \times 1}, \quad (5.38)$$

$$\mathbf{u}_{\text{eq}} = \begin{bmatrix} \mathbf{T}_{\text{act,eq}} & \mathbf{T}_{\text{TCC,eq}} \end{bmatrix}^T. \quad (5.39)$$

Equations (5.37) and (5.38) are shortened to:

$$\mathbf{M}_2 \mathbf{L} \Delta \mathbf{U} \leq \Gamma_2 - \mathbf{M}_2 \mathbf{E} \mathbf{u}_{\text{eq}}. \quad (5.40)$$

Constraints on impeller and turbine speed states:

A third constraint is applied on the states of impeller and turbine speed of the state space model. Unlike the previous two constraints, this is a soft constraint and it is implemented to make the torque converter operate in the torque multiplication mode, as torque amplification at the turbine will overcome the torque lag even more quickly.

Thus, mathematically this can be represented as:

$$\dot{\theta}_{\text{act},k+n} \geq \frac{\dot{\theta}_{\text{tu},k+n}}{0.95}, \quad n = 1, 2, 3, \dots, \text{Np} \quad (5.41)$$

Further, the overall constraint inequality is represented as:

$$-L_1\Psi\Delta U \leq (E_1\dot{\theta}_{\text{eq}} + L_1P_1X_{\text{ag},k} + \Phi), \quad (5.42)$$

where

$$L_1 = \begin{bmatrix} 1 & 0 & \dots & 0 \\ 1 & 1 & \dots & 0 \\ \vdots & \vdots & \vdots & \vdots \\ 1 & 1 & \dots & 1 \end{bmatrix}_{10 \times 10}, \quad (5.43)$$

$$\Psi = \begin{bmatrix} VB_{\text{ag}} & 0 & \dots & 0 \\ VA_{\text{ag}}B_{\text{ag}} & VB_{\text{ag}} & \dots & 0 \\ \vdots & \vdots & \vdots & \vdots \\ VA_{\text{ag}}^{\text{Np}-1}B_{\text{ag}} & VA_{\text{ag}}^{\text{Np}-2}B_{\text{ag}} & \dots & VA_{\text{ag}}^{\text{Np}-\text{Nc}}B_{\text{ag}} \end{bmatrix}_{10 \times 10}, \quad (5.44)$$

$$\mathbf{E}_1 = \begin{bmatrix} 1 & 1 & \dots & 1 \end{bmatrix}_{1 \times 10}^T, \quad (5.45)$$

$$\dot{\theta}_{\text{eq}} = \left(\dot{\theta}_{\text{act,eq}} - \frac{\dot{\theta}_{\text{tu,eq}}}{0.95} \right), \quad (5.46)$$

$$\mathbf{P}_1 = \begin{bmatrix} \text{VA}_{\text{ag}} & \text{VA}_{\text{ag}}^2 & \dots & \text{VA}_{\text{ag}}^{N_p} \end{bmatrix}_{1 \times 10}^T, \quad (5.47)$$

$$\mathbf{V} = \begin{bmatrix} 1 & 0 & 0 & -\frac{1}{0.95} & 0 & 0 & 0 & 0 & 0 \end{bmatrix}, \quad (5.48)$$

and Φ is the slack variable vector.

5.1.3 Optimization problem

Based on the framed mathematical model and constraints, the optimization problem for the designed TCTL MPC is formulated as:

$$\begin{aligned} \min_{\Delta \mathbf{T}_{\text{act}}^*, \Delta \mathbf{T}_{\text{TCC}}^*} & \sum_k^{k+N_p-1} \mathbf{J}(\mathbf{T}_{\text{tu}}^*, \mathbf{T}_{\text{tu}}) \\ \text{s.t.} & \mathbf{M}' \Delta \mathbf{U} \leq \Gamma \end{aligned} \quad (5.49)$$

where the cost function \mathbf{J} is defined as:

$$\mathbf{J} = (\mathbf{T}_{\text{tu}}^* - \mathbf{T}_{\text{tu}})^T \mathbf{Q} (\mathbf{T}_{\text{tu}}^* - \mathbf{T}_{\text{tu}}) + \Delta \mathbf{U}^T \mathbf{S} \Delta \mathbf{U}, \quad (5.50)$$

and

$$M' = \begin{bmatrix} M_1 & M_2L & -L_1\Psi \end{bmatrix}^\top, \quad (5.51)$$

$$\Gamma = \begin{bmatrix} \Gamma_1 \\ \Gamma_2 - M_2E u_{\text{eq}} \\ E_1\dot{\theta}_{\text{eq}} + L_1P_1X_{\text{ag},k} + \Phi \end{bmatrix}. \quad (5.52)$$

In Equation (5.50), Q is the weight matrix and S is a block diagonal matrix containing the tuning parameters for manipulated variables, ΔT_{act} and ΔT_{TCC} .

5.1.4 Control Results

The performance of the designed model predictive controller is verified through MIL and PIL experiments. The modified FOM, discussed in the beginning of this chapter, is used as the virtual plant for assessing the TCTL controller's performance in both these experiments.

5.1.4.1 MIL results

For performing MIL experimentation, the same co-simulation approach that was used in Chapter 4 for the torque shaping clunk and shuffle controller is used. The designed

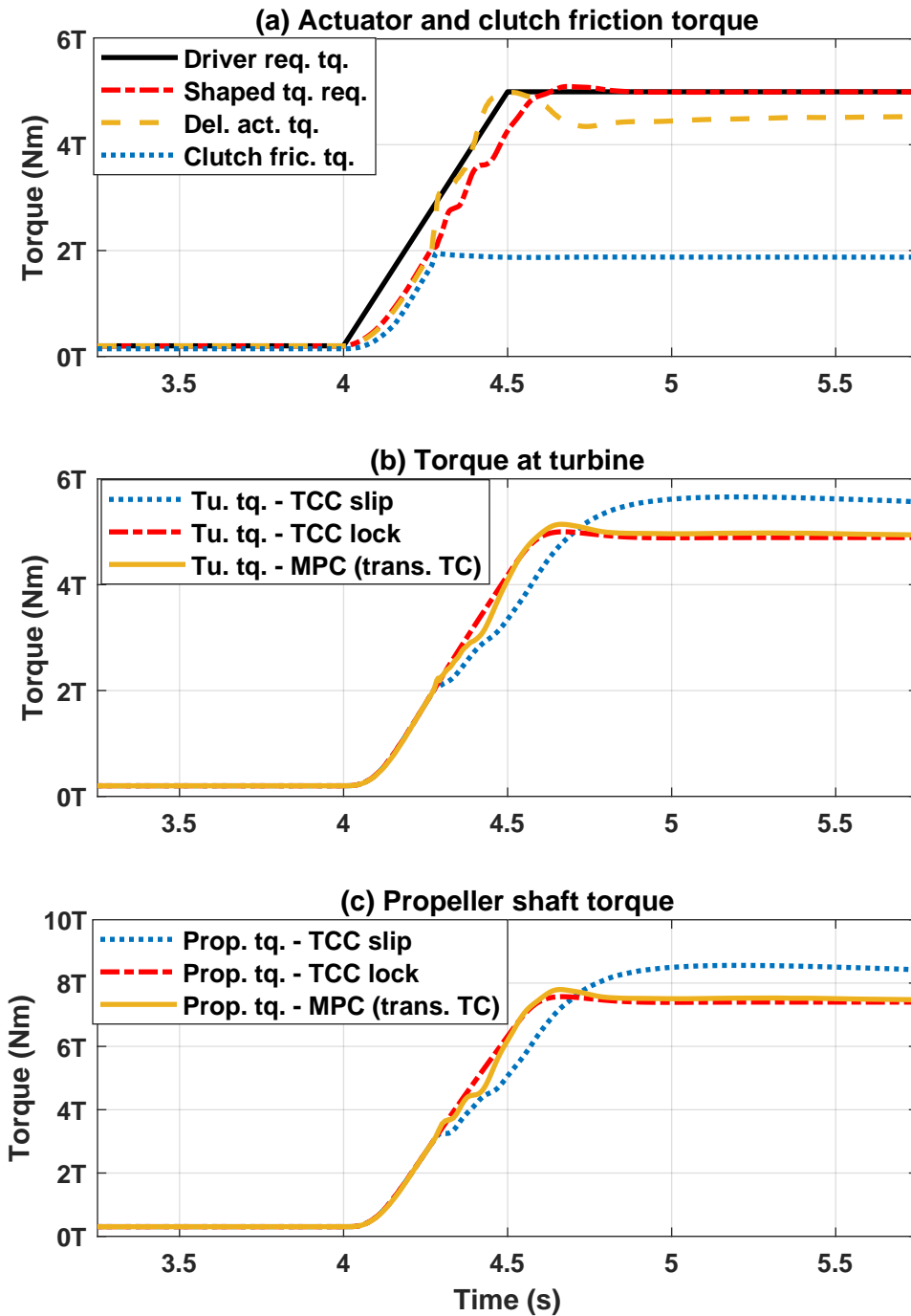


Figure 5.6: Response of a drivetrain during torque delivery with locked and slipping torque converter clutch (TCC).

MPC is implemented in MATLAB while the full order plant model is implemented in AMESim. The results obtained through the implementation of the designed controller are shown in Fig. 5.6. The actuator torque and the clutch torque capacity, shown in Fig. 5.6(a) are governed by the controller such that turbine torque delivered (Fig. 5.6(b)) and the propeller shaft torque delivered (Fig. 5.6(d)) at wheels overcome the torque lag.

Fig. 5.7 and Table 5.1 show an approximate improvement of 83% in the driveline response with the implementation of the developed TCTL controller against no TCC slip control implementation. Furthermore, metrics such as *expediency*, which is defined as the time taken by the vehicle to reach an acceleration of 0.4 m/s^2 , and *connectedness*, which is defined as the maximum acceleration attained within 1 second of the tip-in occurring, also show an improvement with the TCTL controller. The designed control algorithm controls the actuator torque and clutch capacity in such a way that the torque delivered at the turbine during the TCC slip is close to the torque that would have been delivered if the TCC was locked, thus, overcoming the torque lag in the process.

5.1.4.2 PIL results

Similar to the setup used in Chapter 4, a dSPACE MicroAutoBox II system is used for implementing the designed TCTL controller and the virtual plant. dSPACE

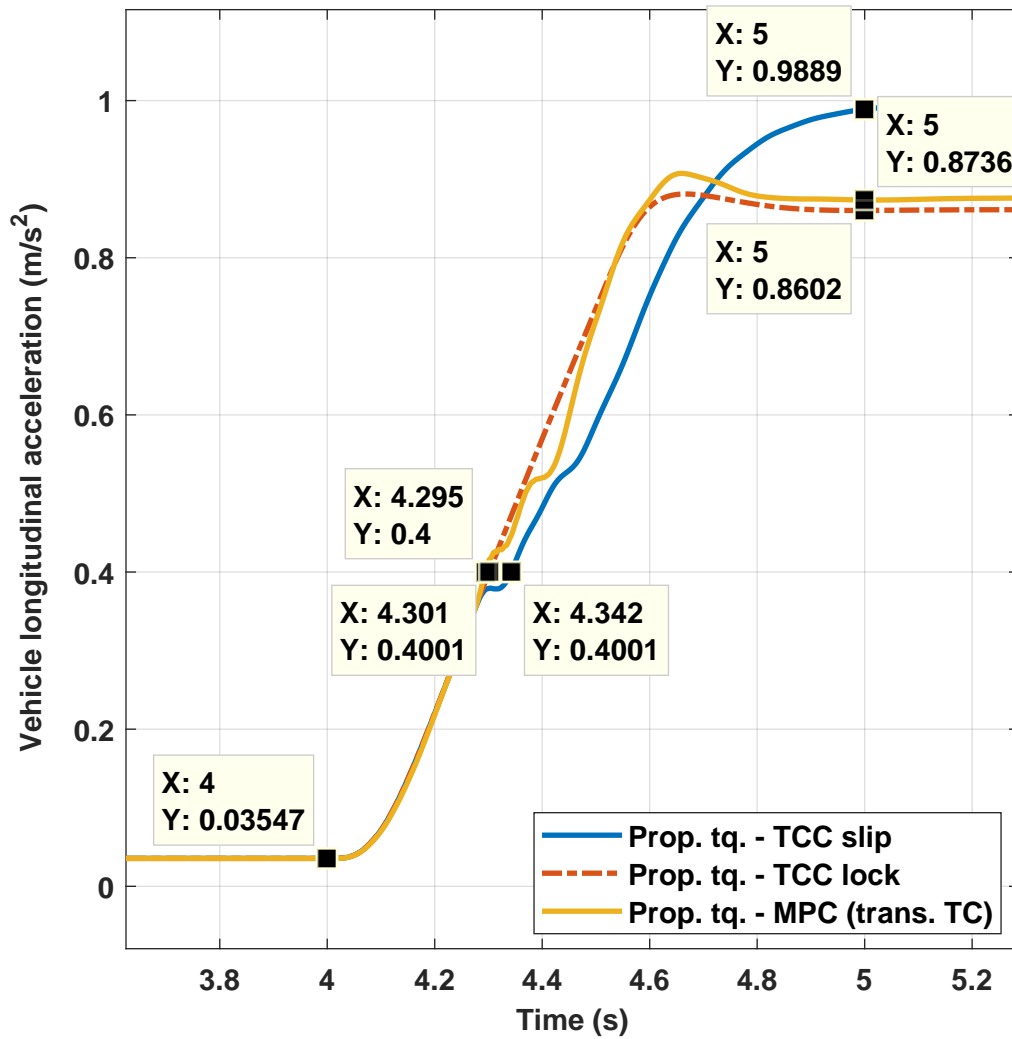


Figure 5.7: Comparison of the observed expediency and connectedness with the designed drivetrain controller for slipping torque converters.

Control Desk software is used for recording the real-time commands sent to the TCTL controller and the response of the plant model. The schematic of the PIL setup is shown in Fig. 5.8. In this analysis, two different sample times are chosen for the controller. The turnaround time for these sample times is obtained using dSPACE

Table 5.1

Performance comparison of driveline metrics with and without the developed controller. The term *Expediency* is defined as the time taken by the vehicle to reach an acceleration of 0.4 m/s^2 and the term *Connectedness* is defined as the maximum acceleration attained within 1 second of the tip-in occurring. Moreover, the percentage difference is computed with respect to the corresponding variables for the locked TCC scenario.

Parameter	Average difference w.r.t. locked TCC	
	Without control	With MPC
Turbine torque	13.5%	2.1%
Prop. shaft torque	13.5%	2.1%
Expediency	13.6%	1.9%
Connectedness	14.9%	1.5%

Profiler and tabulated in Table 4.1. When the controller and plant have a sample time of 10 ms and 5 ms, respectively, it is observed that the performance of the controller in PIL tests is similar to the performance observed and shown in MIL results (see Fig. 5.6). As the sample time of the controller is increased to 50 ms, it is observed that the turnaround time starts to reduce but the performance of the controller also starts to deteriorate. This is expected because the reduction in sample interval reduces the intervention by the controller to overcome the torque lag. Therefore, the designed TCTL controller is effective at a sample time of 10 ms or less.

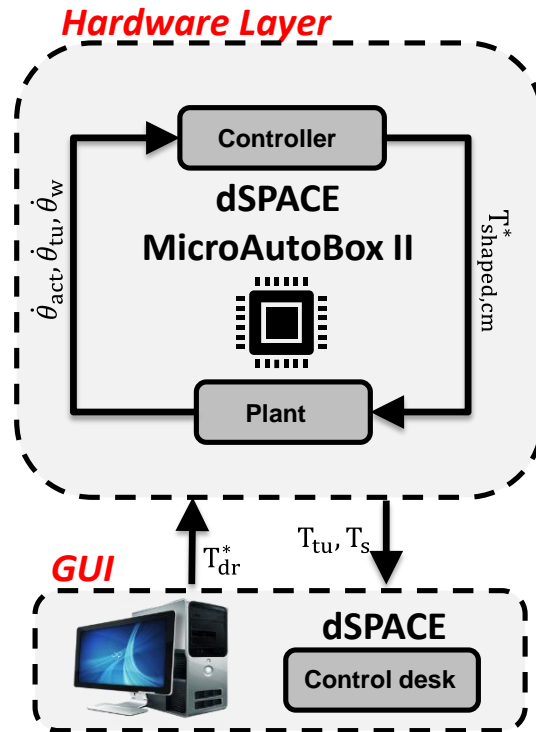


Figure 5.8: Schematic showing the PIL test setup for the TCTL controller

5.1.5 Robustness Analysis of TCTL controller

The robustness of the designed TCTL controller is verified for variations in the transient first order fluid path dynamics of the torque converter, and changes in the available capacity of the torque converter clutch.

5.1.5.1 Variation in transient fluid path dynamics

The torque converters used in different vehicles can have fluids with different properties (e.g., density, viscosity etc.). These variations in the fluids combined with aging and variations in operating conditions might lead to variability in the transient dynamics of fluid path torque transfer across the torque converter. If these dynamics are represented by a first order system, these variations could cause a change in the time constants of the first order dynamics. Therefore, the robustness of the TCTL controller is verified for different time constants of this first order dynamics. This is analogous to verifying the performance of the controller with different torque converters or with a torque converter that has varying fluid properties due to aging effects.

The performance of the controller is verified for three different time constants: 10 ms, 20 ms and 50 ms. Fig. 5.9 shows the turbine and propeller shaft torque for the three cases. It is noticed that the delivered torque difference for the locked and the controlled TCC slip scenarios increases with the time constant. Consequently, the torque difference for a 10 ms time constant is computed to be 2.1% and that for a 50 ms time constant is computed to be 3.7%. Therefore, it is concluded that the designed TCTL controller is able to handle variations in clutch engagement dynamics well.

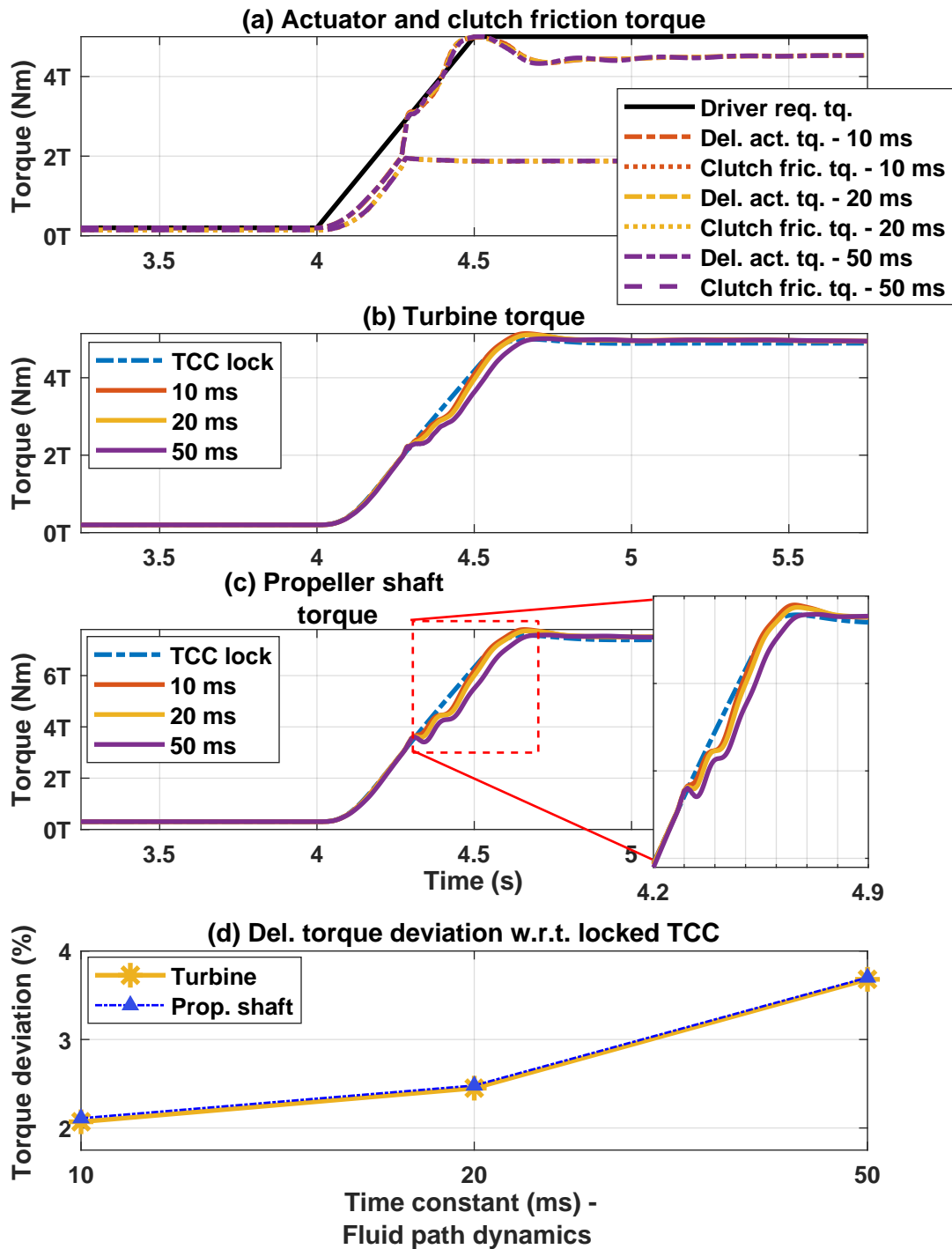


Figure 5.9: Comparison of the drivetrain controller with varying first order lag constants for the fluid dynamics of the torque converter.

Table 5.2
TCC slipping positions for robustness analysis

Clutch slip initiation point (SIP)	Time instant	Clutch capacity at slip initiation
SIP 1	4.43 s	330 Nm
SIP 2	4.27 s	196 Nm
SIP 3	4.23 s	130 Nm

5.1.5.2 Variation in clutch slip initiation

The supervisory controller can decide, based on operating conditions, to start slipping the clutch at any point of actuator torque delivery. Therefore, the TCTL controller needs to be robust to different clutch slip initiation points (SIPs). The performance of the designed TCTL controller is verified at three different points where the clutch slipping is initiated. The specifications of the three tested SIPs are listed in Table 5.2.

Figure 5.10 shows the performance of the controller for the three SIPs. It is observed that the controller is able to work well in all three cases with a maximum turbine torque deviation of 4.1% for the case where slip starts to occur at SIP 3 (see Fig. 5.10(d)). It is also observed that the deviation is greater when the clutch slip is initiated at lower TCC capacities when compared to higher capacity clutch slip initiation. This is expected because it is more difficult for the controller to compensate when a larger amount of torque is required from the fluid path.

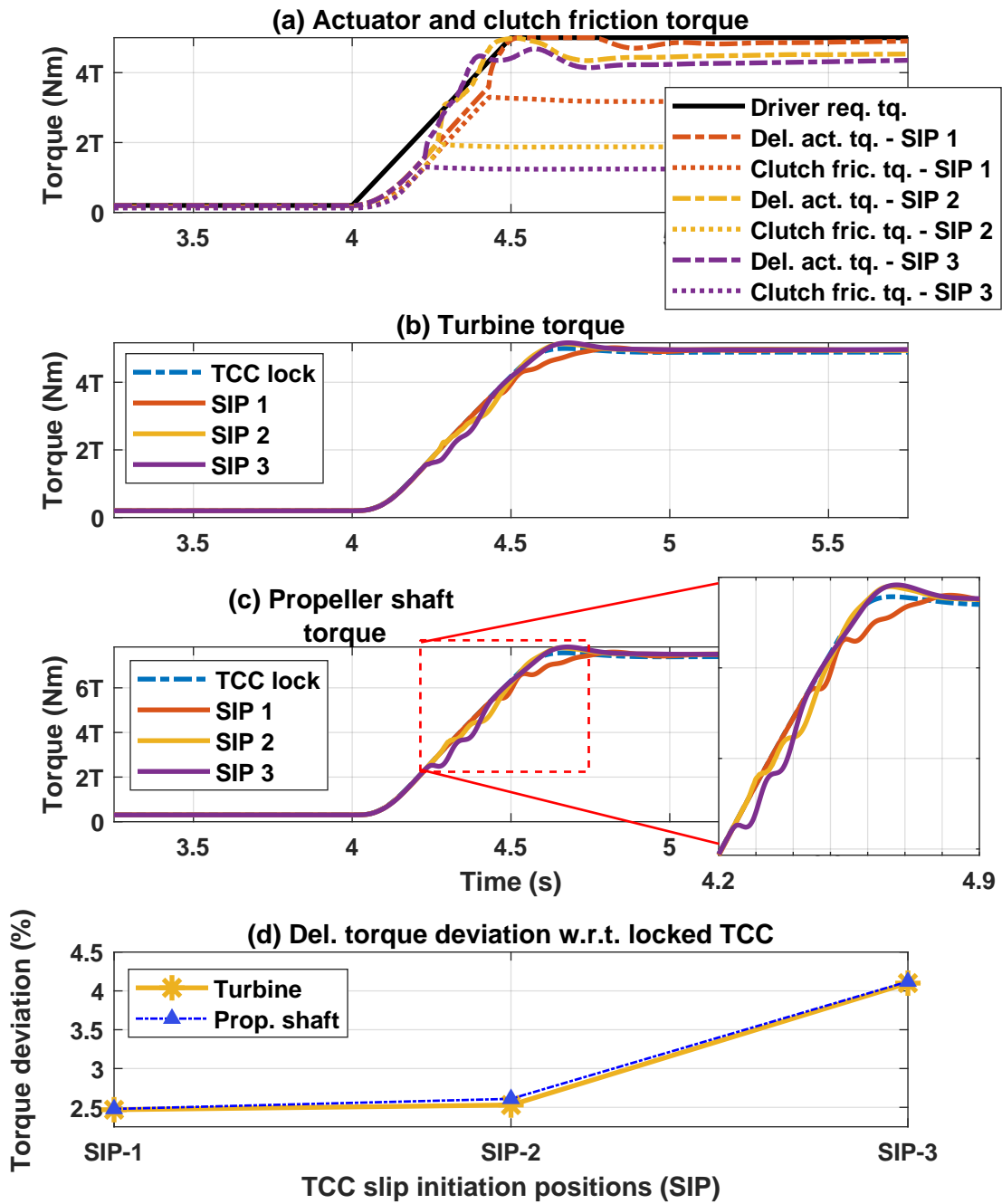


Figure 5.10: Comparison of the drivetrain controller for different clutch slip positions.

5.2 Integration with an economic nonlinear MPC torque tracking engine controller

The shaped torque commanded by the clunk and shuffle torque shaping controller is typically sent to the actuator controller which controls the torque delivered by the actuator while taking other operational parameters (e.g., combustion stability in IC engine) into account. When the actuator is an IC engine, there are multiple sub-components that need to be controlled and coordinated in order to quickly deliver the requested torque while operating within the physical limits of the engine. Traditionally, electronic engine control has utilized map-based and rule-based controllers or using empirical control techniques such as PID control [65, 66]. These approaches typically have many calibration parameters and require significant development and calibration efforts. Further, these traditional approaches are not easily adaptable to changes in the plant model. In modern IC engines, the number of individual parts that need to be coordinated has increased (e.g., additional control required for operating the turbocharger, variable timing of valves, variable exhaust gas recirculation ratio, etc.). Therefore, model-based, optimal engine controllers are more suitable for modern engine controls. They are less calibration intensive and provide better overall performance by allowing multi-objective optimization while meeting various actuator and engine operational constraints. In model-based engine

controls, torque-based control [67] is common since it is easy for other dependent controllers to work in the torque domain.

In this section, an economic-nonlinear model predictive engine controller (E-NMPC) that tracks torque requests while reducing fuel consumption and oxides of Nitrogen (NO_x) emissions is integrated with the clunk and shuffle torque shaping controller to demonstrate a proof of concept of the two controllers coordinating and working together. The motivation behind this integration is to show that proper coordination between the two optimal controllers is needed for meeting their control objectives without violating their design constraints. This economic nonlinear model predictive controller (E-NMPC) was developed as part of a doctoral thesis by Dr. Xin Wang, a former PhD student of Michigan Technological University [3].

A 2.0L Gasoline Turbocharged Direct Injection (GTDI) spark ignition (SI) Ford engine was modeled in GT-Power and used as the plant model for developing the E-NMPC algorithm. This plant model was calibrated and validated using testbed data from an experimental 2.0L Ford Ecoboost engine. The control objective of the E-NMPC algorithm was to track required engine torque via a indicated mean effective pressure (IMEP) command and minimizing specific fuel consumption and NO_x emissions, while adhering to a comprehensive set of engine operating constraints. The E-NMPC algorithm was developed in MATLAB/Simulink and a co-simulation was set up between the controller (Simulink) and the plant model (GT-Power). The

development and validation of the high-fidelity engine model in GT-Power and the design of the engine controller have been discussed in detail in [3]. For completeness, the parameters of the plant model and the design of the torque (or IMEP) tracking E-NMPC algorithm are briefly discussed in the following subsections.

5.2.1 GT-Power engine model development and validation

The GT-Power engine plant model that was developed for MIL testing consists of the complete airpath system including the intake, exhaust and turbocharger models. Detailed 3D CAD models of the intake components, cylinder head, and exhaust components were used for modeling the fluid flow in GT-Power. The turbocharger model was developed using manufacturer-provided maps and was used to predict the mass flow rate, output power, temperatures and pressures inside the turbocharging system. For accurately modeling the combustion dynamics and for simulating the flame propagation inside the engine, the turbulent flame combustion model was used in conjunction with 3D CAD models of the cylinders and pistons. Further, the NO_x emissions were predicted using the extended Zeldovich mechanism to capture the net NO_x produced in the engine.

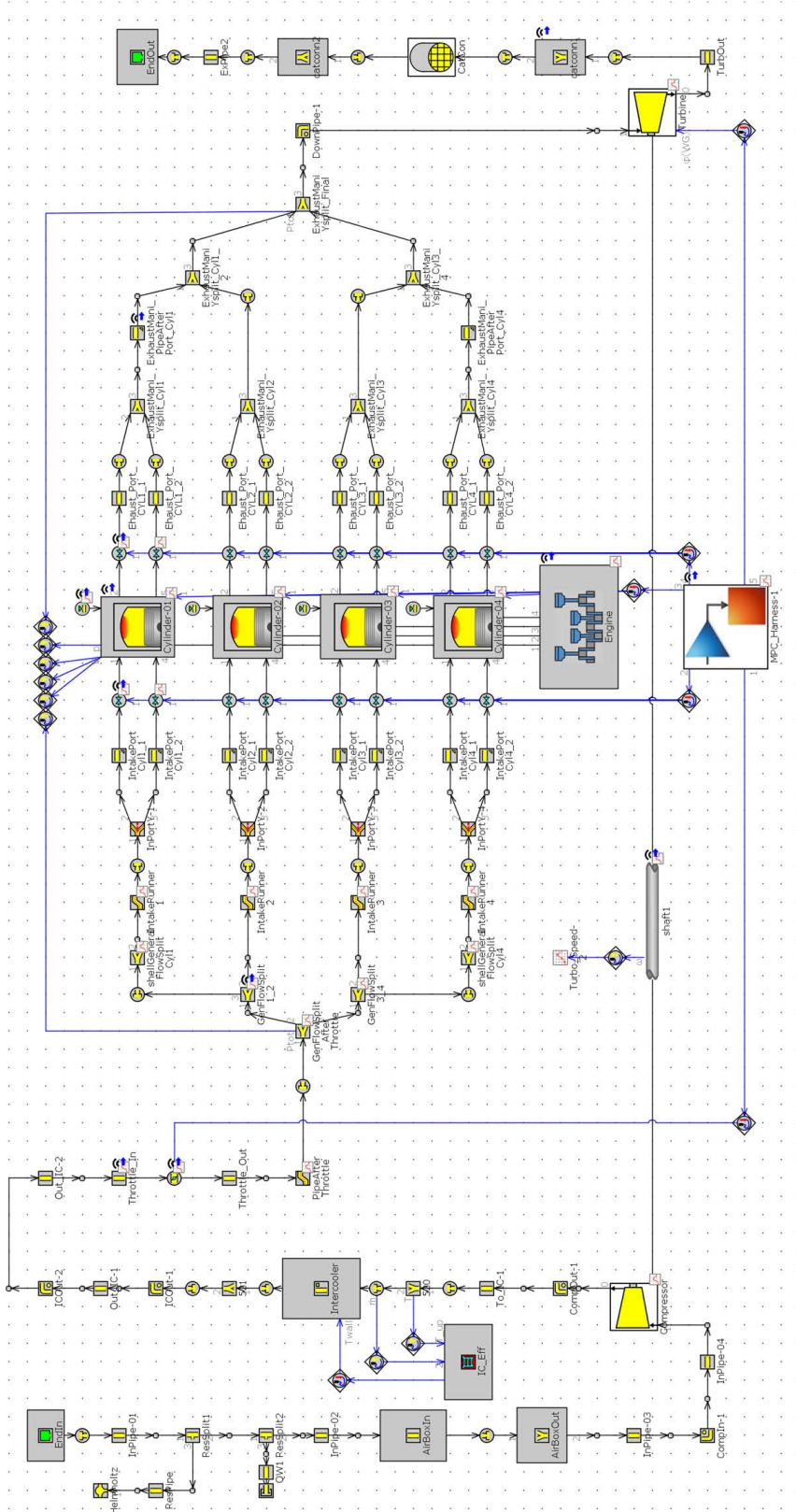


Figure 5.11: High-fidelity engine model developed in GT-Power for use in MIL testing of the E-NMPC engine controller [3].

The GT-Power engine model was calibrated using experimental test data obtained from engine dynamometer tests. Initially, the overall in-cylinder heat transfer coefficient was calibrated by comparing experimental in-cylinder pressure traces and air flow with the simulated results. Next, closed volume pressure analysis and in-cylinder quantities were used to calibrate the predictive turbulent SI combustion and the NO_x calculations. Later, the root mean squared errors between the experimental and simulated burn rate were used for calibrating the combustion model.

For validating this high-fidelity engine model transient test data, including engine control inputs for valve timing and spark timing, and engine speed, operating temperatures, etc., was obtained from experimental tests on the engine. These inputs were provided to the GT-Power model and the outputs were compared to the experimental test data. It was observed that the signals from the experimental tests and the simulation matched well, with an average error in combustion phasing represented by crank angle of 50% of the fuel burned (CA50), manifold absolute pressure (MAP), and gross IMEP being -0.7 deg., 0.03 kPa and 2.2 kPa, respectively, indicating that the model was able to properly capture the nonlinear dynamics of the engine.

5.2.2 Design of the economic - nonlinear model predictive engine controller

For designing the economic - nonlinear model predictive controller (E-NMPC), a control-oriented model consisting of the airpath and in-cylinder dynamics is developed. To effectively capture the nonlinear dynamics, both physics-based and data driven approaches are used for building the control-oriented models. These models are then calibrated and validated using the same experimental data that was used for validating the GT-Power model. Five controllable components are defined for the engine, which include the throttle angle, θ_{th} , spark timing, θ_{IGN} , intake valve closing timing, θ_{IVC} , exhaust valve opening timing, θ_{EVO} , and the opening of the turbocharger wastegate, θ_{WG} . The feedback signals obtained from the engine through production sensor measurements include the engine speed, intake manifold temperature, intake manifold pressure, turbocharger speed, and lambda (air-fuel equivalence ratio) from the universal gas oxygen sensor.

The objective of the designed E-NMPC is to track a torque request while minimizing NOx emissions and fuel consumption, and operating within the physical limits of the engine actuators. This is formulated as an optimal control problem (OCP) with the cost function consisting of terms for tracking an IMEP (torque) request, reducing fuel consumption and engine out NOx emissions. Additionally, the cost function aims to

minimize control effects by minimizing rate of change of engine actuator functions such as throttle angle, valve timing, turbocharger wastegate opening, etc. These also help to reduce unwanted sudden changes in the combustion process that could lead to system instability. The cost function of the OCP is set up as:

$$\arg \min_{U(k)} \sum_{i=1}^{N_c} \left(\begin{array}{l} A \cdot (\text{IMEP}(k, i) - \text{IMEP}^{\text{ref}}(k, i))^2 + B \cdot (m_{\text{cyl fuel}})^2 \\ + C \cdot (\text{NO}_x(k, i))^2 + D_1 \cdot (\Delta\theta_{\text{thr}}(k, i))^2 \\ + D_2 \cdot (\Delta\theta_{\text{IVC}}(k, i))^2 + D_3 \cdot (\Delta\theta_{\text{CA50}}(k, i))^2 \\ + D_4 \cdot (\Delta\theta_{\text{EVO}}(k, i))^2 + D_5 \cdot (\Delta\theta_{\text{WG}}(k, i))^2 \end{array} \right) \quad (5.53)$$

subject to

$$0^\circ \leq \Delta\theta_{\text{thr}}(k, i) \leq 90^\circ, \quad (5.54)$$

$$0^\circ \leq \Delta\theta_{\text{IVC}}(k, i) \leq 50^\circ, \quad (5.55)$$

$$0^\circ \leq \Delta\theta_{\text{EVO}}(k, i) \leq 50^\circ, \quad (5.56)$$

$$0^\circ \leq \Delta\theta_{\text{WG}}(k, i) \leq 100^\circ, \quad (5.57)$$

$$5^\circ \leq \Delta\theta_{\text{CA50}}(k, i) \leq 20^\circ, \quad (5.58)$$

$$0 \leq \text{COV}_{\text{IMEP}}(k, i) \leq 3, \quad (5.59)$$

$$0 \leq \text{KI}(k, i) \leq 5, \quad (5.60)$$

$$0\text{kPa} \leq P_{\text{TIP}}(k, i) - P_{\text{Man}}(k, i) \leq 100\text{kPa}. \quad (5.61)$$

where the constraints (5.54) to (5.57) represent the physical constraints of the

actuators, and constraints (5.58) to (5.61) are for ensuring a stable combustion inside the cylinders. Control inputs $U(k)$ are defined as:

$$U(k) = \begin{bmatrix} \theta_{th}(k) & \theta_{IVC}(k) & \theta_{CA50}(k) & \dots \\ \dots & \theta_{EVO}(k) & \theta_{WG}(k) & \dots \end{bmatrix}^T \quad (5.62)$$

For solving this OCP, ACADO toolkit [68, 69] is used along with an active-set QP solver, qpOASES [70, 71]. Since the cost function consists of least squared terms, the Hessian matrices are approximated using the generalized Gauss-Newton method. ACADO uses the information on the control-oriented engine model and the OCP to build C-code for the E-NMPC. This is implemented in Simulink as an S-function, and a co-simulation is set up between the controller (Simulink) and the engine plant model (GT-Power). The actuator control inputs are sent from the Simulink model to the GT-Power model, while receiving feedback signals from the GT-Power model.

5.2.3 Coordinated control between E-NMPC and torque shaping powertrain controller

For setting up the coordinated control between the E-NMPC engine torque controller and the torque shaping powertrain controller, a co-simulation was set up between Simulink, AMESim and GT-Power. While AMESim contained the driveline plant

model and GT-Power contained the engine plant model, both the optimal controllers were set up in Simulink. Torque requested by the driver was provided as an input to the torque shaping controller which in turn provided shaped torque command as an input to the engine torque controller. Based on this command, the E-NMPC system provided actuator inputs to the GT-Power engine model and the torque output from the engine was provided to the AMESim driveline model. There are feedback loops between the GT-Power engine model and the engine controller and between the AMESim driveline model and the torque shaping controller. A schematic of the setup of this coordinated control is shown in Fig. 5.12.

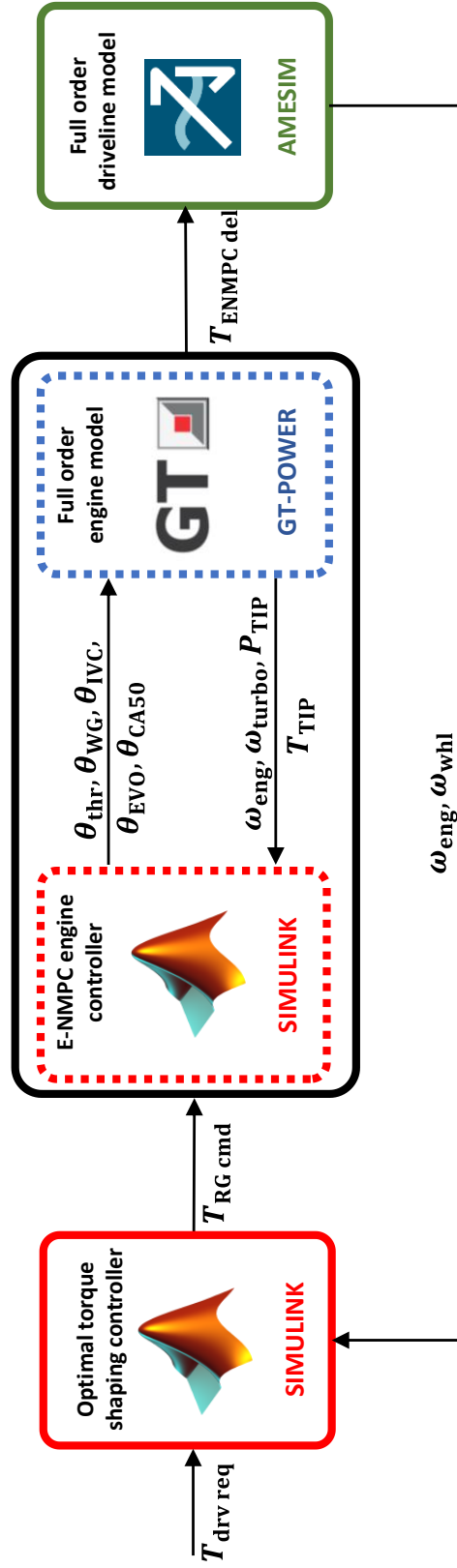


Figure 5.12: Schematic showing the coordinated control between the E-NMPC engine controller and the clunk and shuffle torque shaping driveline controller.

Initially, the engine and torque shaping driveline controllers do not have proper coordination. The driveline response in such a scenario is illustrated in Fig. 5.13. While the engine controller tries to deliver the commanded torque it is not able to respond at the rate needed by the driveline controller to momentarily reduce torque during lash crossing. Therefore, the control objective of the driveline controller, i.e., the backlash hitting positive contact within the constrained lash crossing speed, is not fulfilled (evident in Fig. 5.13 (b) and (c)). Further, the engine controller is sometimes restricted by its combustion stability constraints and is not able to deliver the torque commanded by the torque shaping controller. In these cases, the engine controller fails to reach convergence which causes the simulation to stop as the controller stops sending actuator commands (as seen in Fig. 5.13 at $t = 8.4$ sec).

Since the controllers were not developed together, certain modifications were made in both the controllers for them to work in a coordinated manner. In the E-NMPC engine controller, the costs associated with torque tracking, fuel consumption and NOx emissions had to be modified to cater to the sudden rise and drop in the commanded actuator torque received from the reference governor driveline controller. In the torque shaping driveline controller, the prediction steps used for predicting the backlash position had to be modified such that the change in backlash position is conveyed earlier to the driveline controller. This had the effect of modifying the reference backlash position earlier and giving the engine controller time to react to the changes in the torque command. Furthermore, the contact mode controller

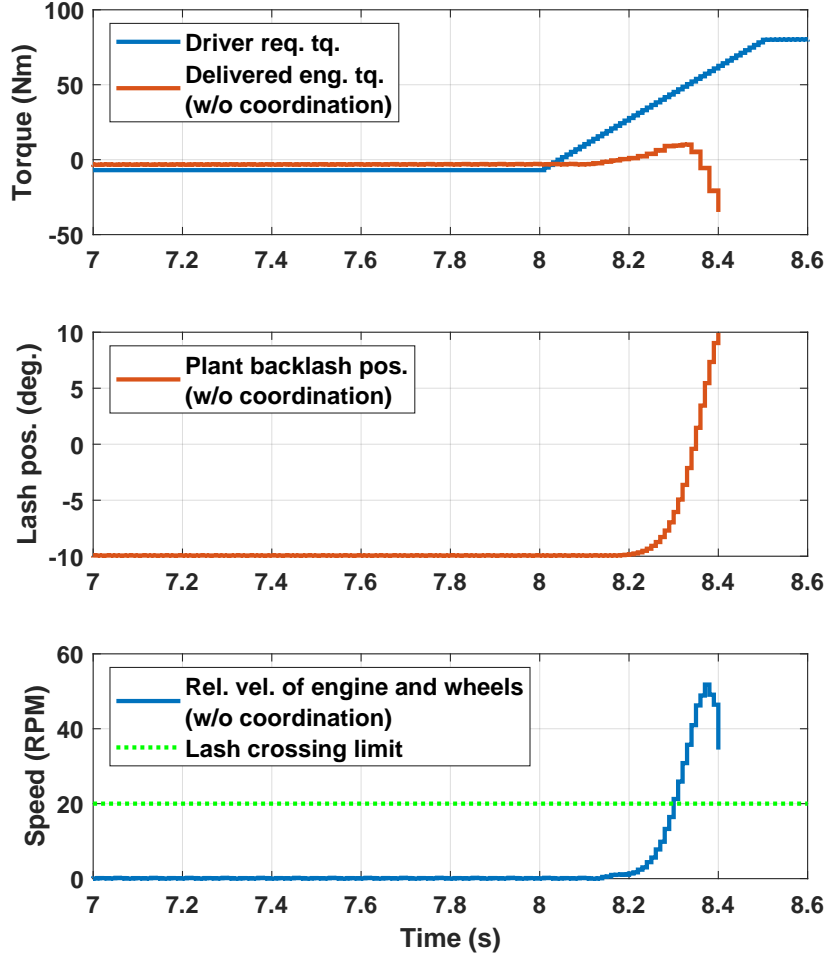


Figure 5.13: Driveline response when the engine and the driveline controllers do not have proper coordination. At $t = 8.4$ sec, the engine controller fails to reach convergence for the torque commanded by the driveline controller. The simulation abruptly stops at this point.

during pre-lash mode was commanded to deliver more torque than requested by the driver, to increase the velocity with which the initial lash crossing occurs. The integrated performance of both the controllers is illustrated in Figs. 5.14 and 5.15. To simultaneously show the benefit of the driveline torque shaping controller, the driveline signals without the torque shaping controller are also overlaid in all the

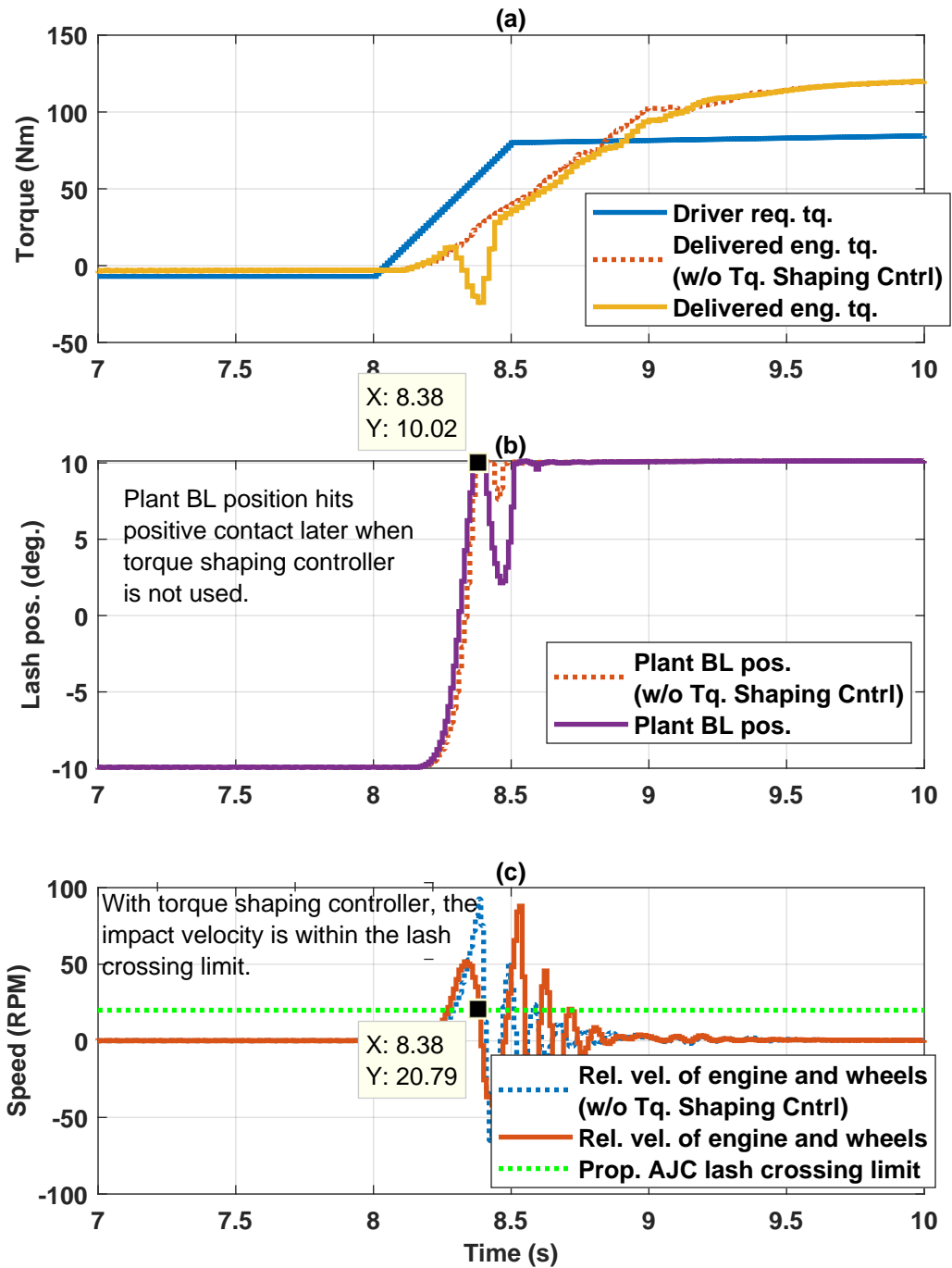


Figure 5.14: Plot showing the coordinated control between the engine and driveline controller to deliver the shaped torque command during a tip-in scenario.

subplots of these two figures. The driver requested torque and the corresponding engine delivered torque are shown in Fig. 5.14 (a), wherein the delivered torque shows the expected non-monotonic behavior that was previously observed with the clunk and shuffle driveline controller in Chapter 4. Fig. 5.14 (b) and (c) show the the plant backlash position, and relative speed between the engine and wheels, respectively. It can be clearly seen in the figure that the control objectives of the reference governor-based torque shaping controller are met, as the speed at which lash crossing takes place steadily increases initially, and then reduces to meet the impact velocity constraint as the backlash reaches positive contact at $t = 8.38$ sec. Correspondingly, Fig. 5.15 (a), (b) and (c) show the changes in the engine actuators to accomplish the torque commanded by the driveline torque shaping controller in Fig. 5.14. The results from the integrated controllers demonstrate the importance of proper coordination between the two optimal controllers in meeting their individual control objectives.

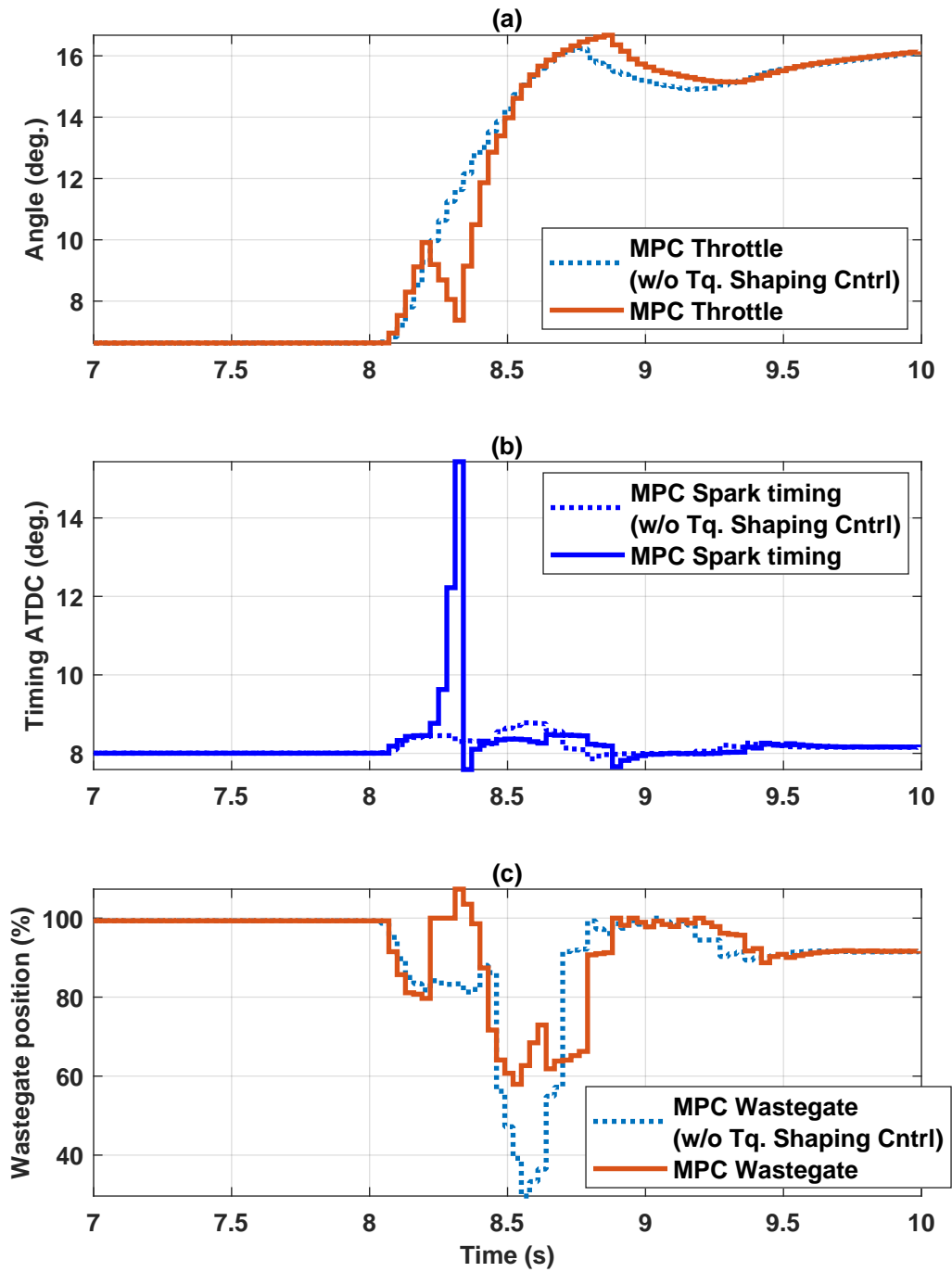


Figure 5.15: Plot showing the engine controller commands in the engine actuators to deliver the driveline controller commanded torque shown in Fig. 5.14.

Chapter 6

Conclusions and future work

6.1 Summary and Conclusions

This thesis presented the design of a novel, model-based torque shaping system which makes use of readily available sensors on a vehicle to significantly improve the drivability of a vehicle. The main highlights of this work are:

1. The design and analysis of a high-fidelity driveline plant model and control oriented driveline models for use in driveline control applications.
2. The design of model-based estimation algorithms for estimating driveline backlash position and backlash size without any previous information.

3. The design of a soft landing reference governor-based clunk controller and a per-compensator and lead compensator-based shuffle controller that provides smooth torque delivery with minimal driveline oscillations.
4. The coordinated control of two optimal, model-based control systems that meet their individual control objectives while providing smooth torque output.

In Chapter 2, a full-order driveline plant model and a control-oriented model are designed and validated using experimental test vehicle data. The major findings and conclusions from Chapter 2 are:

- † The designed full-order model and control-oriented model are able to satisfactorily capture the clunk and shuffle dynamics of an experimental test vehicle. The frequency and phase of shuffle in the full-order model (FOM) and control-oriented model (COM) signals matches the shuffle in the test vehicle with an average error of less than 10%.
- † The designed control-oriented model reduces the required computation cost to $\frac{1}{4}$ th of the computation required by the full-order model, without any compromise in the representation of clunk and shuffle dynamics in the driveline.
- † The contact mode subsystem of the control-oriented model is both controllable and observable. The backlash mode subsystem of the control-oriented model can be made observable and controllable through certain assumptions depending

on their operating points.

In Chapter 3, a backlash position estimator and a backlash size estimator are designed and validated using experimental test vehicle data. The major findings and conclusions from Chapter 3 are:

† The model-based backlash position estimator is able to accurately estimate the position in backlash with a time delay of 10 ms (or 1 sample time). The estimated actuator and wheel speed signals show good agreement with model-in-the-loop data, with an average error of less than 0.1%. With test vehicle data, the same estimator is able to estimate the backlash position with a time delay of 20 ms (or 2 sample time). Further, this estimator is verified to be robust to a variety of use cases through model-in-the-loop tests.

† The model-based backlash size estimator is able to accurately estimate the backlash size in the vehicle using readily available sensors and without any previous information about the backlash. The estimator shows an error of less than 2% in estimating the backlash size in both model-in-the-loop tests and experimental test vehicle data. The size estimator is also robust to a variety of use cases with a maximum observed error of 9% in the estimated backlash size.

† Both the backlash position estimator and the backlash size estimator are easily implementable in real-time systems. Both estimators have very low

computational load when tested in rapid controls prototyping equipment.

In Chapter 4, a model-based clunk and shuffle controller is developed and integrated to be used with the backlash position estimator and the backlash size estimator. The performance of the controller is verified through model-in-the-loop tests and processor-in-the-loop tests. Uncertainty and robustness analyses are discussed for the reference governor-based clunk controller. The major findings and conclusions from Chapter 4 are:

- † The designed model-based torque shaping controller reduces the number of calibration parameters used in conventional, rule-based torque shaping controllers by more than 90%, while improving the drivability of the vehicle by providing smooth and connected vehicle feel to the driver.
- † The designed torque shaping controller works well in model-in-the-loop tests and in processor-in-the-loop tests. The controller is easily implementable on embedded processors and is able to work with a sample time as low as 5 ms on a rapid control prototyping equipment.
- † The reference governor-based clunk controller is able to robustly meet the impact velocity constraints in multiple use cases while reducing the lash crossing time.
- † The performance of the reference governor-based clunk controller can be

improved in systems with additive and multiplicative uncertainties by utilizing MRAC-based techniques.

In Chapter 5, the model-based torque shaping control system from Chapter 4 is integrated with two independent, optimal controllers. These controllers were designed to solve different control objectives, but by integrating them with the torque shaping controller the coordinated control between these complex systems is demonstrated. The main findings and conclusions from Chapter 5 are:

- † The torque shaping system integrates well with a model predictive controller designed to reduce torque lag in a driveline with a slipping torque converter clutch. The error in torque delivered at the propeller shaft could be reduced from 13.5% to 2.1% through the integration of these two controllers.
- † The designed model predictive torque lag controller is able to work on embedded processors for a sample time of up to 10 ms. The controller is robust to various use case scenarios and the maximum torque delivery error in these robustness cases was up to 4.1%.
- † The torque shaping controller works in an integrated platform with an economic-nonlinear model predictive engine controller that is designed to optimally deliver the commanded engine torque while minimizing fuel consumption and oxides of Nitrogen (NO_x) emissions. Without the coordinated control between these two

complex controllers, it is observed that the nonlinear model predictive engine controller is either unable to deliver the commanded torque or unable to meet the control objectives of the torque shaping system.

6.2 Recommendations for future work

The work done in this thesis can be extended and improved upon in the following ways:

- † The estimation and control algorithms could be implemented and tested on an actual vehicle. While there are extensive model-in-the-loop, processor-in-the-loop and vehicle field test data sets and analyses in this thesis, implementation on a real vehicle always brings additional challenges due to the complex interactions of the sensors and actuators on the vehicle.
- † The adaptive reference governor-based clunk controller proposed in this thesis can be improved by using estimation algorithms to estimate the uncertainty in the driveline parameters. This can make determining the magnitude of uncertainty much more robust than the current implementation in this thesis.
- † The coordinated control between the engine torque delivery controller and the torque shaping controller could be further improved by the design of a

centralized controller so that it is much more robust in different test scenarios. Due to the complex nature of interaction between the two controllers, there are significant efforts involved in ensuring that the shaped torque commands from the shuffle and clunk controller are delivered satisfactorily by the engine controller.

References

- [1] Statista, “U.S. Car and Truck retail sales between 2011 - 2021,” 2021. Accessed at <https://www.statista.com/statistics/199981/us-car-and-truck-sales-since-1951/> on 2022-09-19.
- [2] J.P. Morgan, “Global EV penetration targets,” 2020. Accessed at <https://www.jpmorgan.com/insights/research/future-is-electric> on 2022-09-19.
- [3] X. Wang, *A study of model-based control strategy for a gasoline turbocharged direct injection spark ignited engine*. PhD thesis, Michigan Technological University, 2020.
- [4] P. Reddy, K. Darokar, D. Robinette, M. Shahbakhti, J. Blough, M. Ravichandran, M. Farmer, and J. Doering, “Control-oriented modeling of a vehicle drivetrain for shuffle and clunk mitigation,” *SAE Technical Paper 2019-01-0345*, 2019.
- [5] P. Reddy, K. Darokar, D. Robinette, M. Shahbakhti, M. Ravichandran, and

- J. Doering, “Backlash size estimation in automotive drivelines,” in *2020 IEEE Conference on Control Technology and Applications (CCTA)*, pp. 201–206, IEEE, 2020.
- [6] K. Darokar, P. Reddy, J. Furlich, D. Robinette, M. Shahbakhti, M. Ravichandran, and J. Doering, “Automotive backlash position estimator for driveline jerk control,” in *2020 IEEE Conference on Control Technology and Applications (CCTA)*, pp. 88–93, IEEE, 2020.
- [7] P. Reddy, M. Shahbakhti, M. Ravichandran, and J. Doering, “Real-time estimation of backlash size in automotive drivetrains,” *IEEE/ASME Transactions on Mechatronics*, 2022.
- [8] P. Reddy, M. Shahbakhti, M. Ravichandran, and J. Doering, “Drivetrain clunk control via a reference governor,” *IFAC-PapersOnLine*, vol. 54, no. 20, pp. 846–851, 2021.
- [9] S. A. Nadeem, P. Reddy, M. Shahbakhti, M. Ravichandran, and J. Doering, “Model predictive control of an automotive driveline for optimal torque delivery with minimal oscillations during torque converter slipping conditions,” *SAE International Journal of Passenger Cars-Mechanical Systems*, vol. 14, no. 06-14-01-0004, pp. 51–66, 2021.
- [10] R. Krenz, “Vehicle response to throttle tip-in/tip-out,” *SAE Technical Paper 850967*, 1985.

- [11] C. Mo, A. Beaumont, and N. Powell, “Active control of driveability,” tech. rep., SAE Technical Paper, 1996.
- [12] T. Wellmann, K. Govindswamy, E. Braun, and K. Wolff, “Aspects of driveline integration for optimized vehicle nvh characteristics,” tech. rep., SAE Technical Paper, 2007.
- [13] M. J. Griffin, *Handbook of human vibration*. Academic press, 2012.
- [14] D. Cho and J. K. Hedrick, “Automotive powertrain modeling for control,” *Journal of dynamic systems, measurement, and control*, vol. 111, no. 4, pp. 568–576, 1989.
- [15] J. Karlsson and J. Fredriksson, “Cylinder-by-cylinder engine models vs mean value engine models for use in powertrain control applications,” 1999. SAE Technical Paper 1999-01-0906.
- [16] M. Pettersson, *Driveline modeling and control*. Department of Electrical Engineering, Linköping University, 1997.
- [17] D. Hrovat and W. Tobler, “Bond graph modeling of automotive power trains,” *Journal of the Franklin Institute*, vol. 328, no. 5-6, pp. 623–662, 1991.
- [18] S. Dridi, I. B. Salem, and L. El Amraoui, “Dynamic modeling of nonlinear longitudinal automotive system using graphically based techniques,” in *2017*

- International Conference on Information and Digital Technologies (IDT)*, pp. 349–354, IEEE, 2017.
- [19] G. Sun, M. Wei, J. Shao, and M. Pei, “Automotive powertrain modeling and simulation based on AMESim,” 2007. SAE Technical Paper 2007-01-3464.
- [20] O. Hayat, M. Lebrun, and E. Domingues, “Powertrain driveability evaluation: analysis and simplification of dynamic models,” 2003. SAE Technical paper 2003-01-1328.
- [21] A. Sorniotti, “Driveline modeling, experimental validation and evaluation of the influence of the different parameters on the overall system dynamics,” 2008. SAE Technical Paper 2008-01-0632.
- [22] M. Bartram, G. Mavros, and S. Biggs, “A study on the effect of road friction on driveline vibrations,” *Proceedings of the Institution of Mechanical Engineers, Part K: Journal of Multi-body Dynamics*, vol. 224, no. 4, pp. 321–340, 2010.
- [23] M. Nordin, J. Galic’, and P.-O. Gutman, “New models for backlash and gear play,” *International journal of adaptive control and signal processing*, vol. 11, no. 1, pp. 49–63, 1997.
- [24] A. Lagerberg and B. Egardt, “Backlash estimation with application to automotive powertrains,” *IEEE Transactions on Control Systems Technology*, vol. 15, no. 3, pp. 483–493, 2007.

- [25] P. Templin and B. Egardt, “A powertrain LQR-torque compensator with backlash handling,” *Oil & Gas Science and Technology—Revue d’IFP Energies nouvelles*, vol. 66, no. 4, pp. 645–654, 2011.
- [26] M. Canova, C. Rostiti, L. D’Avico, S. Stockar, G. Chen, M. Prucka, and H. Dourra, “Model-based wheel torque and backlash estimation for drivability control,” *SAE International Journal of Engines*, vol. 10, pp. 1318–1327, 2017.
- [27] G. R. Guercioni, E. Galvagno, A. Tota, A. Vigliani, and T. Zhao, “Driveline backlash and half-shaft torque estimation for electric powertrains control,” tech. rep., SAE Technical Paper, 2018.
- [28] K. Tindell, H. Hanssmon, and A. J. Wellings, “Analysing real-time communications: controller area network (can).,” in *RTSS*, pp. 259–263, Citeseer, 1994.
- [29] P. Templin, “Simultaneous estimation of driveline dynamics and backlash size for control design,” in *IEEE International conference on Control Applications*, 2008. San Antonio, Texas, USA.
- [30] G. Hovland, S. Hanssen, E. Gallestey, S. Moberg, T. Brogardh, S. Gunnarsson, and M. Isaksson, “Nonlinear identification of backlash in robot transmissions,” in *Proceedings of the 33rd ISR (International Symposium on Robotics)*, pp. 1–6, Citeseer, 2002.

- [31] G. P. Prajapat, P. Bhui, N. Senroy, and I. N. Kar, “Modelling and estimation of gear train backlash present in wind turbine driven dfig system,” *IET Generation, Transmission & Distribution*, vol. 12, no. 14, pp. 3527–3535, 2018.
- [32] R. Merzouki, J. Davila, L. Fridman, and J. Cadiou, “Backlash phenomenon observation and identification in electromechanical system,” *Control Engineering Practice*, vol. 15, no. 4, pp. 447–457, 2007.
- [33] D. Papageorgiou, M. Blanke, H. H. Niemann, and J. H. Richter, “Backlash estimation for industrial drive-train systems,” *IFAC-PapersOnLine*, vol. 50, no. 1, pp. 3281–3286, 2017.
- [34] J. L. Stein and C.-H. Wang, “Estimation of gear backlash: Theory and simulation,” *Journal of Dynamic Systems, Measurement, and Control*, vol. 120, no. 1, pp. 74–82, 1998.
- [35] T. Tjahjowidodo, F. Al-Bender, and H. Van Brussel, “Experimental dynamic identification of backlash using skeleton methods,” *Mechanical Systems and Signal Processing*, vol. 21, no. 2, pp. 959–972, 2007.
- [36] M. Ravichandran, J. Doering, R. Johri, and K. Ruybal, “Design and evaluation of EV drivetrain clunk and shuffle management control system,” in *2020 American Control Conference (ACC)*, pp. 4905–4912, IEEE, 2020.
- [37] C. Lv, J. Zhang, Y. Li, and Y. Yuan, “Synthesis of a hybrid-observer-based active controller for compensating powetrain backlash nonlinearity of an electric

- vehicle during regenerative braking,” *SAE International Journal of Alternative Powertrains*, vol. 4, no. 1, pp. 190–198, 2015.
- [38] H. Yonezawa, I. Kajiwara, S. Sato, C. Nishidome, M. Sakata, T. Hatano, and S. Hiramatsu, “Vibration control of automotive drive system with nonlinear gear backlash,” *Journal of Dynamic Systems, Measurement, and Control*, vol. 141, no. 12, 2019.
- [39] A. Lagerberg and B. Egardt, “Model predictive control of automotive powertrains with backlash,” in *16th IFAC world congress*, pp. 4–8, Prague Prague, Czech Republic, 2005.
- [40] A. Formentini, A. Oliveri, M. Marchesoni, and M. Storace, “A switched predictive controller for an electrical powertrain system with backlash,” *IEEE Transactions on Power Electronics*, vol. 32, no. 5, pp. 4036–4047, 2016.
- [41] C. Rostiti, Y. Liu, M. Canova, S. Stockar, G. Chen, H. Dourra, and M. Prucka, “A backlash compensator for drivability improvement via real-time model predictive control,” *Journal of Dynamic Systems, Measurement, and Control*, vol. 140, no. 10, p. 104501, 2018.
- [42] S. Di Cairano, J. Doering, I. V. Kolmanovsky, and D. Hrovat, “Model predictive control of engine speed during vehicle deceleration,” *IEEE transactions on control systems technology*, vol. 22, no. 6, pp. 2205–2217, 2014.

- [43] M. Schwab, “Electronically-controlled transmission systems-current position and future developments,” in *Vehicle Electronics in the 90’s: Proceedings of the International Congress on Transportation Electronics*, pp. 335–342, IEEE, 1990.
- [44] H. B. Pacejka, “The tyre as a vehicle component,” in *26th FISITA Congress, 16-13 June 1996, Prague, Czechoslovakia*, 1996.
- [45] Siemens Industry Software NV, *Amehelp - User Manual for Simcenter Amesim*. Plano, TX, 2019.
- [46] D. Simon, *Optimal state estimation: Kalman, H infinity, and nonlinear approaches*, pp. 252–257. John Wiley & Sons, 2006.
- [47] H. Sakai, “Theoretical and experimental studies on the dynamic properties of tyres. part 4: investigations of the influences of running conditions by calculation and experiment,” *International Journal of Vehicle Design*, vol. 3, no. 3, pp. 333–375, 1982.
- [48] E. Bakker, L. Nyborg, and H. B. Pacejka, “Tyre modelling for use in vehicle dynamics studies,” *SAE Transactions*, pp. 190–204, 1987.
- [49] C. R. Carlson and J. C. Gerdes, “Identifying tire pressure variation by nonlinear estimation of longitudinal stiffness and effective radius,” in *Proceedings of AVEC 2002 6th International Symposium of Advanced Vehicle Control*, 2002.

- [50] A. Crowther and N. Zhang, “Applied numerical modelling of gear impacts in powertrains-driveline shuffle and clunk,” in *4th Australasian Congress on Applied Mechanics, ACAM 2005*, 2005.
- [51] M. K. Mandal, A. Asif, *et al.*, *Continuous and discrete time signals and systems/Mrinal Mandal and Amir Asif*. Cambridge, UK; New York: Cambridge University Press,, 2007.
- [52] E. G. Gilbert and K. T. Tan, “Linear systems with state and control constraints: The theory and application of maximal output admissible sets,” *IEEE Transactions on Automatic control*, vol. 36, no. 9, pp. 1008–1020, 1991.
- [53] P. A. Ioannou and J. Sun, *Robust adaptive control*, ch. 6. Courier Corporation, 2012.
- [54] J. P. Hespanha and A. S. Morse, “Stability of switched systems with average dwell-time,” in *Proceedings of the 38th IEEE conference on decision and control*, vol. 3, pp. 2655–2660, IEEE, 1999.
- [55] K. Kono, H. Itoh, S. Nakamura, K. Yoshizawa, and M. Osawa, “Torque converter clutch slip control system,” *SAE transactions*, pp. 1354–1364, 1995.
- [56] T. Reinhart, “NVH considerations in Engine Development,” in *Encyclopedia of automotive engineering* (D. Crolla, ed.), John Wiley & Sons, 2015.

- [57] T. Ishihara and R. I. Emori, "Torque converter as a vibration damper and its transient characteristics," *SAE Transactions*, pp. 501–512, 1967.
- [58] D. Hrovat and W. Tobler, "Bond graph modeling and computer simulation of automotive torque converters," *Journal of the Franklin institute*, vol. 319, no. 1-2, pp. 93–114, 1985.
- [59] K. Hebbale, C. Lee, F. Samie, C.-K. Kao, X. Chen, J. Horgan, and S. Hearld, "Model based torque converter clutch slip control," tech. rep., SAE Technical Paper, 2011.
- [60] A. J. Kotwicki, "Dynamic models for torque converter equipped vehicles," *SAE Transactions*, pp. 1595–1609, 1982.
- [61] B. Yang, L. Keqiang, H. Ukawa, and M. Handa, "Modelling and control of a non-linear dynamic system for heavy-duty trucks," *Proceedings of the Institution of Mechanical Engineers, Part D: Journal of Automobile Engineering*, vol. 220, no. 10, pp. 1423–1435, 2006.
- [62] J. Li and X. Wang, "Study on transfer function and dynamic characteristic of hydraulic converter," in *2008 IEEE Vehicle Power and Propulsion Conference*, pp. 1–5, IEEE, 2008.
- [63] J.-H. Lee and H. Lee, "Dynamic simulation of nonlinear model-based observer for hydrodynamic torque converter system," 2004. SAE Technical Paper No. 2004-01-1228.

- [64] A. Tugcu, K. Hebbale, A. Alexandridis, and A. Karmel, “Modeling and simulation of the powertrain dynamics of vehicles equipped with automatic transmission,” in *Proceedings of Symposium on Simulation of Ground Vehicles and Transportation Systems, ASME Winter Annual Meeting*, no. 2, pp. 39–61, 1986.
- [65] A. Triwiyatno, M. Nuh, A. Santoso, and I. N. Sutantra, “Engine torque control of spark ignition engine using fuzzy gain scheduling,” *TELKOMNIKA (Telecommunication Computing Electronics and Control)*, vol. 10, no. 1, pp. 83–90, 2012.
- [66] S. A. Kolyubin, D. V. Efimov, V. O. Nikiforov, and A. A. Bobtsov, “Two-channel adaptive hybrid control of the air-to-fuel ratio and torque of automobile engines,” *Automation and Remote Control*, vol. 73, no. 11, pp. 1794–1807, 2012.
- [67] K. Reif, “Gasoline engine management,” *Bosch Professional Automotive Information, DOI*, vol. 10, pp. 978–3, 2015.
- [68] B. Houska, H. Ferreau, and M. Diehl, “ACADO Toolkit – An Open Source Framework for Automatic Control and Dynamic Optimization,” *Optimal Control Applications and Methods*, vol. 32, no. 3, pp. 298–312, 2011.
- [69] D. Ariens, B. Houska, and H. Ferreau, “Acado for matlab user’s manual.” <http://www.acadotoolkit.org>, 2010–2011.

- [70] H. Ferreau, H. Bock, and M. Diehl, “An online active set strategy to overcome the limitations of explicit mpc,” *International Journal of Robust and Nonlinear Control*, vol. 18, no. 8, pp. 816–830, 2008.
- [71] H. Ferreau, A. Potschka, and C. Kirches, “qpOASES webpage.” <http://www.qpOASES.org/>, 2007–2014.
- [72] R. Anjum, A. Yar, I. Yousufzai, Q. Ahmed, and A. I. Bhatti, “Second order sliding mode based speed tracking control for torque management of gasoline engines,” in *2019 12th Asian Control Conference (ASCC)*, pp. 555–560, IEEE, 2019.
- [73] T. Karikomi, K. Itou, T. Okubo, and S. Fujimoto, “Development of the shaking vibration control for electric vehicles,” in *2006 SICE-ICASE International Joint Conference*, 2006. Busan, Korea.
- [74] M. Grotjahn, L. Quernheim, and S. Zemke, “Modelling and identification of car driveline dynamics for anti-jerk controller design,” in *2006 IEEE International Conference on Mechatronics*, 2006. Budapest, Hungary.
- [75] H. Kawamura, K. Ito, T. Karikomi, and T. Kume, “Highly-responsive acceleration control for the nissan leaf electric vehicle,” pp. 1–6, 2011. SAE Technical Paper 2011-01-0397.
- [76] A. Lagerberg, “A literature survey on control of automotive powertrains with

- backlash,” *Technical report no R013/2001; Department of Signals and Systems, Chalmers University of Technology, Gothenburg, Sweden*, pp. 1–15, 2001.
- [77] S. De La Salle, M. Jansz, and D. Light, “Design of a feedback control system for damping of vehicle shuffle,” in *Proceedings of the EAEC conference*, 1999.
- [78] M. Batra, A. Maitland, J. McPhee, and N. L. Azad, “Non-linear model predictive anti-jerk cruise control for electric vehicles with slip-based constraints,” in *2018 Annual American Control Conference (ACC)*, pp. 3915–3920, IEEE, 2018.
- [79] A. Lagerberg and B. Egardt, “Evaluation of control strategies for automotive powertrains with backlash,” in *6th International Symposium on Advanced Vehicle Control at Hiroshima, Japan*, 2002.
- [80] A. Lagerberg and B. Egardt, “Estimation of backlash with application to automotive powertrains,” in *Proceedings of 42nd IEEE International Conference on Decision and Control*, 2003. Maui, HI, USA.
- [81] J. Baumann, A. Swarnakar, U. Kiencke, and T. Schlegl, “A robust controller design for anti-jerking,” 2005. SAE Technical Paper 2005-01-0041.
- [82] J. Baumann, D. D. Torkzadeh, A. Ramstein, U. Kiencke, and T. Schlegl, “Model-based predictive anti-jerk control,” *Control Engineering Practice*, vol. 14, no. 3, pp. 259–266, 2006.

- [83] E. Rabeih and D. Crolla, “Coupling of driveline and body vibrations in trucks,” 1996. SAE Technical Paper 962206.
- [84] P. Templin and B. Egardt, “An LQR torque compensator for driveline oscillation damping,” in *IEEE Conference on Control Applications*, 2009. St. Petersburg, Russia.
- [85] A. Lagerberg and B. Egardt, “Estimation of backlash in automotive powertrains—an experimental validation,” *IFAC Proceedings Volumes*, vol. 37, no. 22, pp. 47–52, 2004.
- [86] C. A. M. Makosi, S. Rinderknecht, R. Binz, F. Uphaus, and F. Kirschbaum, “Implementation of an open-loop controller to design the longitudinal vehicle dynamics in passenger cars,” *SAE Technical Paper 2017-01-1107*, 2017.
- [87] S. G. Mohinder and P. A. Angus, *Kalman filtering: Theory and practice using MATLAB*. John Wileys and Sons, 2001.
- [88] M. Ravichandran, J. Doering, R. Johri, and K. Ruybal, “Design and evaluation of EV drivetrain clunk and shuffle management control system,” in *2020 American Control Conference (ACC)*, pp. 4905–4912, IEEE, 2020.
- [89] D. Hao, C. Zhao, Y. Huang, L. Yang, and G. G. Zhu, “Adaptive optimal control for suppressing vehicle longitudinal vibrations,” in *2019 American Control Conference (ACC)*, pp. 1736–1741, 2019.

- [90] J. M. Mohit Batra, Anson Maitland and N. L. Azad, “Non-linear model predictive anti-jerk cruise control for electric vehicles with slip-based constraints,” in *American Control Conference*, 2018. Milwaukee, USA.
- [91] J. Sun and I. V. Kolmanovsky, “Load governor for fuel cell oxygen starvation protection: A robust nonlinear reference governor approach,” *IEEE Transactions on Control Systems Technology*, vol. 13, no. 6, pp. 911–920, 2005.
- [92] A. Chakrabarty, K. Berntorp, and S. Di Cairano, “Learning-based parameter-adaptive reference governors,” in *2020 American Control Conference (ACC)*, pp. 956–961, IEEE, 2020.
- [93] M. Berriri, P. Chevrel, and D. Lefebvre, “Active damping of automotive powertrain oscillations by a partial torque compensator,” *Control Engineering Practice*, vol. 16, no. 7, pp. 874–883, 2008.
- [94] D. Wehrwein and Z. P. Mourelatos, “Optimization of engine torque management under uncertainty for vehicle driveline clunk using time-dependent metamodels,” *Journal of Mechanical Design*, vol. 131, no. 5, 2009.
- [95] I. Kolmanovsky and E. G. Gilbert, “Landing reference governor,” in *Proceedings of the 2001 American Control Conference.(ACC)*, vol. 1, pp. 374–375, IEEE, 2001.
- [96] E. Garone, S. Di Cairano, and I. Kolmanovsky, “Reference and command

governors for systems with constraints: A survey on theory and applications,”
Automatica, vol. 75, pp. 306–328, 2017.

[97] N. E. Kahveci and I. V. Kolmanovsky, “Control design for electromagnetic actuators based on backstepping and landing reference governor,” *IFAC Proceedings Volumes*, vol. 43, no. 18, pp. 393–398, 2010.

[98] J. Fredriksson, H. Weiefors, and B. Egardt, “Powertrain control for active damping of driveline oscillations,” *Vehicle System Dynamics*, vol. 37, no. 5, pp. 359–376, 2002.

Appendix A

PhD publications

A.1 Peer reviewed journal papers

A.1.1 Published journal papers

† P Reddy, M Shahbakhti, M Ravichandran, J Doering, “Real-time estimation of backlash size in automotive drivetrains”, *IEEE/ASME Transactions on Mechatronics*, 11 pages, Early Access, doi: 10.1109/TMECH.2021.3137461., 2022. (Ref. [7])

† S A Nadeem, P Reddy, M Shahbakhti, M Ravichandran, J Doering, “Optimal torque delivery with minimal oscillations during torque converter slipping

conditions”, SAE International Journal of Passenger Cars - Mechanical Systems, 14, pg. 51-66, 2021. (Ref. [9])

A.1.2 Journal paper in review

† P Reddy, M Shahbakhti, M Ravichandran, J Doering, “Real-time predictive clunk control using a reference governor”, Submitted to Controls Engineering Practice (Minor revision resubmitted on Oct. 24, 2022), 28 pages, 2022.

A.2 Refereed conference papers

† P Reddy, M Shahbakhti, M Ravichandran, J Doering, “Drivetrain clunk control via a reference governor”, IFAC Modeling, Estimation and Control Conference 2021, Oct 24 - 27, 2021, Austin, TX, IFAC PapersOnline, 2021. (Ref. [8])

† P Reddy, K Darokar, M Shahbakhti, M Ravichandran, J Doering, “Backlash size estimation in automotive drivelines”, 2020 IEEE Conference on Control Technology and Applications, August 24 - 26, 2020, Montreal, Canada, pg. 201-206, 2020. (Ref. [5])

† K Darokar, P Reddy, M Shahbakhti, M Ravichandran, J Doering, “Automotive backlash position estimator for driveline jerk control”, 2020 IEEE Conference on

Control Technology and Applications, August 24 - 26, 2020, Montreal, Canada
pg. 88-93, 2020. (Ref. [6])

† P Reddy, K Darokar, D Robinette, M Shahbakhti, J Blough, M Ravichandran,
M Farmer, J Doering, “Control-Oriented Modeling of a Vehicle Drivetrain for
Shuffle and Clunk Mitigation”, SAE World Congress, April 9 - 11, 2019, Detroit,
USA, SAE Technical Paper No: 2019-01-0345, 13 pages, 2019. (Ref. [4])

A.2.1 Conference paper in preparation

† P Reddy, X Wang, M Shahbakhti, J Naber, M Ravichandran, J Doering,
“Integration of optimal engine and driveline controllers to minimize driveline
clunk and shuffle”, In preparation for submission to IFAC Modeling, Estimation
and Controls Conference, Lake Tahoe, Nevada, Oct 2 - 5, 2023.

Appendix B

Implementation and testing of the backlash size estimator and the clunk controller in real vehicles

As part of his Summer 2021 internship work at Ford Motor Company, the author was able to implement a proof of concept for the backlash size estimator and the reference governor-based clunk controller in a test vehicle. The model-based code for the backlash size estimator and the reference governor-based clunk controller developed in Simulink was manually hand coded in C language. With help from calibrators and test drivers, both the algorithms were shown to provide promising results in a HIL environment and in the test vehicle. Additional effort was not spent

on calibrating the algorithms for the test vehicle due to the time limitation in the internship. Due to program confidentiality, these results are not being included in this thesis.

Appendix C

Letters of permission to republish

Letters of permission and publisher policies to reuse material from previously published journal and conference papers is included in this section:

For contents in Chapter 2



This is a License Agreement between Prithvi Reddy ("User") and Copyright Clearance Center, Inc. ("CCC") on behalf of the Rightsholder identified in the order details below. The license consists of the order details, the Marketplace Order General Terms and Conditions below, and any Rightsholder Terms and Conditions which are included below.

All payments must be made in full to CCC in accordance with the Marketplace Order General Terms and Conditions below.

Order Date	26-Oct-2022	Type of Use	Republish in a thesis/dissertation
Order License ID	1283257-1	Publisher	SOCIETY OF AUTOMOTIVE ENGINEERS,
ISSN	0148-7191	Portion	Chapter/article

LICENSED CONTENT

Publication Title	SAE technical paper series	Language	English
Article Title	Control-Oriented Modeling of a Vehicle Drivetrain for Shuffle and Clunk Mitigation	Country	United States of America
Author/Editor	SOCIETY OF AUTOMOTIVE ENGINEERS.	Rightsholder	SAE International
Date	01/01/1970	Publication Type	Monographic Series

REQUEST DETAILS

Portion Type	Chapter/article	Rights Requested	Main product
Page Range(s)	1-11	Distribution	Worldwide
Total Number of Pages	13	Translation	Original language of publication
Format (select all that apply)	Electronic	Copies for the Disabled?	No
Who Will Republish the Content?	Author of requested content	Minor Editing Privileges?	No
Duration of Use	Life of current edition	Incidental Promotional Use?	No
Lifetime Unit Quantity	Up to 499	Currency	USD

NEW WORK DETAILS

Title	Design and real-time implementation of optimal model-based torque shaping automotive control systems	Institution Name	Michigan Technological University
Instructor Name	Prithvi Reddy	Expected Presentation Date	2022-11-15

ADDITIONAL DETAILS

Order Reference Number	N/A	The Requesting Person/Organization to Appear on the License	Prithvi Reddy
------------------------	-----	---	---------------

REUSE CONTENT DETAILS

Title, Description or Numeric Reference of the Portion(s)	Full-order model development, Full-order model validation, Model order reduction	Title of the Article/Chapter the Portion Is From	Control-Oriented Modeling of a Vehicle Drivetrain for Shuffle and Clunk Mitigation
Editor of Portion(s)	Reddy, Prithvi; Darokar, Kaushal; Robinette, Darrell; Shahbakhti, Mahdi; Blough, Jason; Ravichandran, Maruthi; Farmer, Mary; Doering, Jeff	Author of Portion(s)	Reddy, Prithvi; Darokar, Kaushal; Robinette, Darrell; Shahbakhti, Mahdi; Blough, Jason; Ravichandran, Maruthi; Farmer, Mary; Doering, Jeff
Volume of Serial or Monograph	2019-01-0345	Issue, if Republishing an Article From a Serial	N/A
Page or Page Range of Portion	1 - 11	Publication Date of Portion	2019-04-02

Marketplace Order General Terms and Conditions

The following terms and conditions ("General Terms"), together with any applicable Publisher Terms and Conditions, govern User's use of Works pursuant to the Licenses granted by Copyright Clearance Center, Inc. ("CCC") on behalf of the applicable Rightsholders of such Works through CCC's applicable Marketplace transactional licensing services (each, a "Service").

1) **Definitions.** For purposes of these General Terms, the following definitions apply:

"License" is the licensed use the User obtains via the Marketplace platform in a particular licensing transaction, as set forth in the Order Confirmation.

"Order Confirmation" is the confirmation CCC provides to the User at the conclusion of each Marketplace transaction. "Order Confirmation Terms" are additional terms set forth on specific Order Confirmations not set forth in the General Terms that can include terms applicable to a particular CCC transactional licensing service and/or any Rightsholder-specific terms.

"Rightsholder(s)" are the holders of copyright rights in the Works for which a User obtains licenses via the Marketplace platform, which are displayed on specific Order Confirmations.

"Terms" means the terms and conditions set forth in these General Terms and any additional Order Confirmation Terms collectively.

"User" or "you" is the person or entity making the use granted under the relevant License. Where the person accepting the Terms on behalf of a User is a freelancer or other third party who the User authorized to accept the General Terms on the User's behalf, such person shall be deemed jointly a User for purposes of such Terms.

"Work(s)" are the copyright protected works described in relevant Order Confirmations.


2) **Description of Service.** CCC's Marketplace enables Users to obtain Licenses to use one or more Works in accordance with all relevant Terms. CCC grants Licenses as an agent on behalf of the copyright rightsholder identified in the relevant Order Confirmation.


3) **Applicability of Terms.** The Terms govern User's use of Works in connection with the relevant License. In the event of any conflict between General Terms and Order Confirmation Terms, the latter shall govern. User acknowledges that Rightsholders have complete discretion whether to grant any permission, and whether to place any limitations on any grant, and that CCC has no right to supersede or to modify any such discretionary act by a Rightsholder.

4) **Representations; Acceptance.** By using the Service, User represents and warrants that User has been duly authorized by the User to accept, and hereby does accept, all Terms.

5) **Scope of License; Limitations and Obligations.** All Works and all rights therein, including copyright rights, remain the sole and exclusive property of the Rightsholder. The License provides only those rights expressly set forth in the terms and

For contents in Chapter 3

Home Help ▾ Email Support Sign in Create Account



Requesting permission to reuse content from an IEEE publication

Automotive backlash position estimator for driveline jerk control
Conference Proceedings: 2020 IEEE Conference on Control Technology and Applications (CCTA)
Author: Kaushal Darokar
Publisher: IEEE
Date: August 2020
Copyright © 2020, IEEE

Thesis / Dissertation Reuse

The IEEE does not require individuals working on a thesis to obtain a formal reuse license, however, you may print out this statement to be used as a permission grant:

Requirements to be followed when using any portion (e.g., figure, graph, table, or textual material) of an IEEE copyrighted paper in a thesis:

- 1) In the case of textual material (e.g., using short quotes or referring to the work within these papers) users must give full credit to the original source (author, paper, publication) followed by the IEEE copyright line © 2011 IEEE.
- 2) In the case of illustrations or tabular material, we require that the copyright line © [Year of original publication] IEEE appear prominently with each reprinted figure and/or table.
- 3) If a substantial portion of the original paper is to be used, and if you are not the senior author, also obtain the senior author's approval.

Requirements to be followed when using an entire IEEE copyrighted paper in a thesis:

- 1) The following IEEE copyright/ credit notice should be placed prominently in the references: © [year of original publication] IEEE. Reprinted, with permission, from [author names, paper title, IEEE publication title, and month/year of publication]
- 2) Only the accepted version of an IEEE copyrighted paper can be used when posting the paper or your thesis on-line.
- 3) In placing the thesis on the author's university website, please display the following message in a prominent place on the website: In reference to IEEE copyrighted material which is used with permission in this thesis, the IEEE does not endorse any of [university/educational entity's name goes here]'s products or services. Internal or personal use of this material is permitted. If interested in reprinting/republishing IEEE copyrighted material for advertising or promotional purposes or for creating new collective works for resale or redistribution, please go to http://www.ieee.org/publications_standards/publications/rights/rights_link.html to learn how to obtain a License from RightsLink.

If applicable, University Microfilms and/or ProQuest Library, or the Archives of Canada may supply single copies of the dissertation.

BACK

CLOSE WINDOW

For contents in Chapter 3



Home

Help ▾

Email Support

Sign in

Create Account



Backlash size estimation in automotive drivelines

Conference Proceedings: 2020 IEEE Conference on Control Technology and Applications (CCTA)

Author: Prithvi Reddy

Publisher: IEEE

Date: August 2020

Copyright © 2020, IEEE

Thesis / Dissertation Reuse

The IEEE does not require individuals working on a thesis to obtain a formal reuse license, however, you may print out this statement to be used as a permission grant:

Requirements to be followed when using any portion (e.g., figure, graph, table, or textual material) of an IEEE copyrighted paper in a thesis:

- 1) In the case of textual material (e.g., using short quotes or referring to the work within these papers) users must give full credit to the original source (author, paper, publication) followed by the IEEE copyright line © 2011 IEEE.
- 2) In the case of illustrations or tabular material, we require that the copyright line © [Year of original publication] IEEE appear prominently with each reprinted figure and/or table.
- 3) If a substantial portion of the original paper is to be used, and if you are not the senior author, also obtain the senior author's approval.

Requirements to be followed when using an entire IEEE copyrighted paper in a thesis:

- 1) The following IEEE copyright/ credit notice should be placed prominently in the references: © [year of original publication] IEEE. Reprinted, with permission, from [author names, paper title, IEEE publication title, and month/year of publication]
- 2) Only the accepted version of an IEEE copyrighted paper can be used when posting the paper or your thesis on-line.
- 3) In placing the thesis on the author's university website, please display the following message in a prominent place on the website: In reference to IEEE copyrighted material which is used with permission in this thesis, the IEEE does not endorse any of [university/educational entity's name goes here]'s products or services. Internal or personal use of this material is permitted. If interested in reprinting/republishing IEEE copyrighted material for advertising or promotional purposes or for creating new collective works for resale or redistribution, please go to http://www.ieee.org/publications_standards/publications/rights/rights_link.html to learn how to obtain a License from RightsLink.

If applicable, University Microfilms and/or ProQuest Library, or the Archives of Canada may supply single copies of the dissertation.

BACK

CLOSE WINDOW

For contents in Chapter 3

Home Help ▾ Email Support Sign in Create Account



Requesting permission to reuse content from an IEEE publication

Real-Time Estimation of Backlash Size in Automotive Drivetrains

Author: Prithvi Reddy
Publication: IEEE/ASME Transactions on Mechatronics
Publisher: IEEE
Date: Dec 31, 1969

Copyright © 1969, IEEE

Thesis / Dissertation Reuse

The IEEE does not require individuals working on a thesis to obtain a formal reuse license, however, you may print out this statement to be used as a permission grant:

Requirements to be followed when using any portion (e.g., figure, graph, table, or textual material) of an IEEE copyrighted paper in a thesis:

- 1) In the case of textual material (e.g., using short quotes or referring to the work within these papers) users must give full credit to the original source (author, paper, publication) followed by the IEEE copyright line © 2011 IEEE.
- 2) In the case of illustrations or tabular material, we require that the copyright line © [Year of original publication] IEEE appear prominently with each reprinted figure and/or table.
- 3) If a substantial portion of the original paper is to be used, and if you are not the senior author, also obtain the senior author's approval.

Requirements to be followed when using an entire IEEE copyrighted paper in a thesis:

- 1) The following IEEE copyright/ credit notice should be placed prominently in the references: © [year of original publication] IEEE. Reprinted, with permission, from [author names, paper title, IEEE publication title, and month/year of publication]
- 2) Only the accepted version of an IEEE copyrighted paper can be used when posting the paper or your thesis on-line.
- 3) In placing the thesis on the author's university website, please display the following message in a prominent place on the website: In reference to IEEE copyrighted material which is used with permission in this thesis, the IEEE does not endorse any of [university/educational entity's name goes here]'s products or services. Internal or personal use of this material is permitted. If interested in reprinting/republishing IEEE copyrighted material for advertising or promotional purposes or for creating new collective works for resale or redistribution, please go to http://www.ieee.org/publications_standards/publications/rights/rights_link.html to learn how to obtain a License from RightsLink.

If applicable, University Microfilms and/or ProQuest Library, or the Archives of Canada may supply single copies of the dissertation.

BACK

CLOSE WINDOW

For contents in Chapter 4

Prithvi Reddy

From: IFAC Secretariat <secretariat@ifac-control.org> on behalf of IFAC Secretariat
Sent: Monday, October 10, 2022 7:58 AM
To: Prithvi Reddy
Subject: Re: Permission to reuse published material in PhD thesis

Dear Prithvi Reddy,

Thank you for contacting the IFAC Secretariat. I have checked and yes the permission is granted with acknowledgment to original publication:
so the text is:

©2021 The Authors. Reproduced from Prithvi Reddy, Mahdi Shahbakhti, Maruthi Ravichandran, Jeff Doering, "Drivetrain clunk control via a reference governor." IFAC-PapersOnLine, Volume 54, Issue 20 (2021).

Best regards,

Elske Haberl, IFAC Secretariat

On 09.10.2022 22:13, Prithvi Reddy wrote:

> Hello Sir/Madam,

>

> I am a PhD student at Michigan Technological University and the author

> of an IFAC conference paper titled, "Drivetrain clunk control via a

> reference governor". I am currently writing my PhD thesis and would

> like to reuse material from this paper in my thesis. I reached out to

> the Elsevier Copyrights Coordinator and I was directed to you. I

> request you to kindly grant permission to do the same. Full details of

> the paper and the DOI link are provided below:

>

> Title: Drivetrain clunk control via a reference governor

> Authors: Prithvi Reddy, Mahdi Shahbakhti, Maruthi Ravichandran, Jeff

> Doering

> Year: 2021

> From page: 846

> To page: 851

> ISSN: 2405-8963

> Volume: 54

> Issue: IFAC-PapersOnLine

> DOI link: <https://doi.org/10.1016/j.ifacol.2021.11.277>

> <<https://doi.org/10.1016/j.ifacol.2021.11.277>>

>

> Please let me know if you need any other information from me.

>

> Thank you,

>

> Prithvi Reddy,

>

> Mechanical Engineering – Engineering Mechanics department,

For contents in Chapter 5



This is a License Agreement between Prithvi Reddy ("User") and Copyright Clearance Center, Inc. ("CCC") on behalf of the Rightsholder identified in the order details below. The license consists of the order details, the Marketplace Order General Terms and Conditions below, and any Rightsholder Terms and Conditions which are included below. All payments must be made in full to CCC in accordance with the Marketplace Order General Terms and Conditions below.

Order Date	26-Oct-2022	Type of Use	Republish in a
Order License ID	1283259-1	Publisher	thesis/dissertation
ISSN	1946-4002	Portion	SAE International Chapter/article

LICENSED CONTENT

Publication Title	SAE International journal of passenger cars. Mechanical systems	Publication Type	Journal
Article Title	Model Predictive Control of an Automotive Driveline for Optimal Torque Delivery with Minimal Oscillations during Torque Converter Slipping Conditions	Start Page	51
Author/Editor	Society of Automotive Engineers.	End Page	66
Date	01/01/2009	Issue	1
Language	English	Volume	14
Country	United States of America	URL	http://saepcmec.saejournals.org
Rightsholder	SAE International		

REQUEST DETAILS

Portion Type	Chapter/article	Rights Requested	Main product
Page Range(s)	51 - 66	Distribution	Worldwide
Total Number of Pages	16	Translation	Original language of publication
Format (select all that apply)	Electronic	Copies for the Disabled?	No
Who Will Republish the Content?	Author of requested content	Minor Editing Privileges?	No
Duration of Use	Life of current edition	Incidental Promotional Use?	No
Lifetime Unit Quantity	Up to 99,999	Currency	USD

NEW WORK DETAILS

Institution Name	Michigan Technological University
Expected Presentation Date	2022-11-15

Title DESIGN AND REAL-TIME IMPLEMENTATION OF OPTIMAL MODEL-BASED TORQUE SHAPING AUTOMOTIVE CONTROL SYSTEM

Instructor Name Prithvi Reddy

ADDITIONAL DETAILS

Order Reference Number	N/A	The Requesting Person/Organization to Appear on the License	Prithvi Reddy
------------------------	-----	---	---------------

REUSE CONTENT DETAILS

Title, Description or Numeric Reference of the Portion(s)	Introduction, Drivetrain modeling, Controller Design, Control Results	Title of the Article/Chapter the Portion Is From	Model Predictive Control of an Automotive Driveline for Optimal Torque Delivery with Minimal Oscillations during Torque Converter Slipping Conditions
Editor of Portion(s)	Nadeem, Syed Ahmad; Reddy, Prithvi; Shahbakhti, Mahdi; Ravichandran, Maruthi; Doering, Jeffrey	Author of Portion(s)	Nadeem, Syed Ahmad; Reddy, Prithvi; Shahbakhti, Mahdi; Ravichandran, Maruthi; Doering, Jeffrey
Volume of Serial or Monograph	14	Issue, if Republishing an Article From a Serial	1
Page or Page Range of Portion	51-66	Publication Date of Portion	2021-04-30

Marketplace Order General Terms and Conditions

The following terms and conditions ("General Terms"), together with any applicable Publisher Terms and Conditions, govern User's use of Works pursuant to the Licenses granted by Copyright Clearance Center, Inc. ("CCC") on behalf of the applicable Rightsholders of such Works through CCC's applicable Marketplace transactional licensing services (each, a "Service").

1) **Definitions.** For purposes of these General Terms, the following definitions apply:

"License" is the licensed use the User obtains via the Marketplace platform in a particular licensing transaction, as set forth in the Order Confirmation.

"Order Confirmation" is the confirmation CCC provides to the User at the conclusion of each Marketplace transaction. "Order Confirmation Terms" are additional terms set forth on specific Order Confirmations not set forth in the General Terms that can include terms applicable to a particular CCC transactional licensing service and/or any Rightsholder-specific terms.

"Rightsholder(s)" are the holders of copyright rights in the Works for which a User obtains licenses via the Marketplace platform, which are displayed on specific Order Confirmations.

"Terms" means the terms and conditions set forth in these General Terms and any additional Order Confirmation Terms collectively.

"User" or "you" is the person or entity making the use granted under the relevant License. Where the person accepting the Terms on behalf of a User is a freelancer or other third party who the User authorized to accept the General Terms on the

Appendix D

Image and data file summary

D.1 Chapter 1

Table D.1
Chapter 1 figure files

File name	File description
Driveline_schematic.pdf	Figure 1.1
clunkShuffle.pdf	Figure 1.2
Pickup_truck_sales.pdf	Figure 1.3
Electric_Vehicle_Sales_Forecast.pdf	Figure 1.4
Overview_lit_review.pdf	Figure 1.5
BL_pos_lit_review.pdf	Figure 1.6
Estimators_lit_summary.pdf	Figure 1.7
Thesis_structure.pdf	Figure 1.9

D.2 Chapter 2

Table D.2
Chapter 2 figure files

File name	File description
FOM_schematic_rev.pdf	Figure 2.1
Sensor_placement.pdf	Figure 2.2
FOM_validation_Pacejka.pdf	Figure 2.3
Expdata_vs_simpletire_vs_Pacejka.pdf	Figure 2.4
Backlash_comparison_ROM.pdf	Figure 2.5
ROM_Intro_2backlash.pdf	Figure 2.6
ROM2.pdf	Figure 2.7
ROMvsFOMvsTestVeh.pdf	Figure 2.8
Residuals.pdf	Figure 2.9
2DOFvsMultiDOF_2.pdf	Figure 2.10

Table D.3
Chapter 2 model files

File name	File description
AMESim_FOM.ame	Full-order model AMESim file
AMESim_3DOF_ROM.ame	3 degree of freedom control-oriented AMESim file
AMESim_2DOF_ROM.ame	2 degree of freedom control-oriented AMESim file
MATLAB_actuator_model.slx	Engine and e-motor models with co-simulation interface

D.3 Chapter 3

Table D.4
Chapter 3 figure files

File name	File description
PredictionAndEstimation.pdf	Figure 3.1
Backlash_pos_est_overview.pdf	Figure 3.2
Sim_validation.pdf	Figure 3.3
Exp_validation_final.pdf	Figure 3.4
Jitter_PDF.pdf	Figure 3.5
CAN_jitter_eng_wheel_comb_zoom.pdf	Figure 3.6
Backlash_size_est_overview.pdf	Figure 3.7
Activation_criteria_Stateflow.pdf	Figure 3.8
Residuals.pdf	Figure 2.9
Primary_use_plot_final.pdf	Figure 3.9
Experimental_data_results_final.pdf	Figure 3.10
PIL_sim_overview.pdf	Figure 3.11
PIL_validation.pdf	Figure 3.12
RoadLoadRobustness.pdf	Figure 3.14
CANjitter_robustness.pdf	Figure 3.15
Robustness_lashsizechange.pdf	Figure 3.16
Magic_formula_slipping_robustness.pdf	Figure 3.17
sampleTime_Robustness.pdf	Figure 3.18

Table D.5
Chapter 3 model files

File name	File description
AMESim_FOM.ame	Full-order model AMESim file
MATLAB_bl_pos_est_model.slx	Backlash position estimator Simulink model with co-simulation interface
MATLAB_bl_size_est_model.slx	Backlash size estimator Simulink model with co-simulation interface
Bl_pos_est_parameters.m	Backlash position estimator parameters
Bl_size_est_parameters.m	Backlash size estimator parameters

D.4 Chapter 4

Table D.6
Chapter 4 figure files

File name	File description
ShuffleCntrl_BodePlot.pdf	Figure 4.1
Controller_schematic.pdf	Figure 4.2
MOAS.pdf	Figure 4.3
Sim_validation.pdf	Figure 4.4
PIL_schematic.pdf	Figure 4.5
Comp_MOAS.pdf	Figure 4.6
UncAnalysis_Comp.pdf	Figure 4.7
Adaptive_controller_schematic.pdf	Figure 4.8
10_40_unc_comp.pdf	Figure 4.9
NoBLSIZEInfor.pdf	Figure 4.10

Table D.7
Chapter 4 model files

File name	File description
AMESim_FOM.ame	Full-order model AMESim file
MATLAB_clunk_shuffle_model.slx	Shuffle and Clunk controller Simulink model with backlash position and size estimators with co-simulation interface
Clunk_shuffle_cntrl_parameters.m	Clunk and shuffle controller parameters
MOAS_calculations.m	Code for calculating the maximal output admissible set
RG_table_calculations.m	Calculation of reference governor clunk controller tables from MOAS

D.5 Chapter 5

Table D.8
Chapter 5 figure files

File name	File description
tcc_slip_response_comp_no_control.pdf	Figure 5.1
ROM2_TCslip_val.pdf	Figure 5.2
torque_conv_schematic.pdf	Figure 5.3
ROM2_TCslip.pdf	Figure 5.4
MPC_controller_schematic.pdf	Figure 5.5
tcc_slip_final_response_for_no_control_ with_10ms_lag.pdf	Figure 5.6
Accn_plot_comparison_expediency_ and_connectedness.pdf	Figure 5.7
MPC_TCTL_PIL_schematic.pdf	Figure 5.8
robustness_to_varying_first_order_ lag_constants.pdf	Figure 5.9
robustness_to_clutch_slip_positions.pdf	Figure 5.10
GTPowerModel.pdf	Figure 5.10
Controller_int_schematic_paper.pdf	Figure 5.12
Thesis_result_NoCoord.pdf	Figure 5.13
Thesis_Comp_result_Coord_p1.pdf	Figure 5.14
Thesis_Comp_result_Coord_p2.pdf	Figure 5.15

Table D.9
Chapter 5 model files

File name	File description
AMESim_FOM.ame	Full-order model AMESim file
MATLAB_clunk_shuffle_TCTL_model.slx	Shuffle and Clunk controller Simulink model with backlash position and size estimators and TCTL controller with co-simulation interface
MATLAB_clunk_shuffle_ENMPC_model.slx	Shuffle and Clunk controller Simulink model with backlash position estimator and E-NMPC engine controller with two co-simulation interfaces
Clunk_shuffle_cntrl_parameters.m	Clunk and shuffle controller parameters
MOAS_calculations.m	Code for calculating the maximal output admissible set
RG_table_calculations.m	Calculation of reference governor clunk controller tables from MOAS